DISSERTATION / DOCTORAL THESIS

Titel der Dissertation /Title of the Doctoral Thesis

„Mass spectrometry-based functional proteomics for characterizing (patho-) physiological mechanisms in complex biological systems "

verfasst von / submitted by

Lukas Janker, MSc

angestrebter akademischer Grad / in partial fulfilment of the requirements for the degree of

Doktor der Naturwissenschaften (Dr.rer.nat.)

Wien, 2022 / Vienna, 2022

Acknowledgements

First and foremost, I want to express my sincere gratitude to Christopher Gerner, my supervisor and mentor who accompanied me through my early scientific career. Without him, I would not have had the opportunities which led to the career I am pursuing now.

I want to thank Astrid Slany, my co-supervisor, for having an open ear and helping me through sometimes challenging situations or times.

I want to thank Samuel Meier-Menches for the most interesting and philosophical and scientific discussions, often at late hour. These discussions nurtured and challenged my understanding of scientific problem solving and made me to the scientist I am today

I want to thank Andrea Bileck and Rupert Mayer for their excellent support at the start and at the end of my doctorate, without them the last 4 years would have been much harder.

I am grateful to my fellow PhD colleagues Laura Niederstätter, Julia Brunmair and Benjamin Neuditschko who accompanied me through almost all of my doctorate and with whom I have spent countless fun hours in the lab and in discussions.

Furthermore, I want to thank all the people helping to keep the labs up and running, including Peter Frühauf, Johanna Mader, Günter Walder, and last but not least Andrea Hilbert.

My gratitude goes to all the cooperation partners from diverse backgrounds and expertises, including Giorgia del Favero, Sabine Taschner-Mandl, Thomas Feichtenschlager, Tobias Pukrop, Albrecht Reichle, Katharina Rebay-Salisbury, and Fabian Kanz. Without them, this dissertation would not have been possible.

A special thank goes to my dear friends Samuel and Sophie Walter. They both had an open ear and sometimes beer for me. It is a pleasure spending time with them and finding the balance between work and private life.

My sincere gratitude goes to my family and especially to my parents Daniela and Michael, who supported me throughout my whole life and enabled me to pursue my dreams.

Last but not least, I want to dedicate this work to two important persons who helped me to be my best in moments where I did not know how to proceed or what to do next –

my sister Viktoria and my partner in life Patricia. They both helped me to see light when there was darkness and helped me regain my strength in difficult times.

For that I am most grateful.

"What we know is not much. What we do not know is immense."

- Pierre-Simon Laplace

from "Éloge historique de M. le Marquis de Laplace" (1829)

<u>This doctoral thesis is based on the following publications or manuscripts:</u>

Metabolic, Anti-apoptotic and Immune Evasion Strategies of Primary Human Myeloma Cells Indicate Adaptations to Hypoxia

Janker & Mayer et al.

Molecular & Cellular Proteomics 18: 936– 953, **2019**

DOI: 10.1074/mcp.RA119.001390

Octenidine-based hydrogel shows anti-inflammatory and protease-inhibitory capacities in wounded human skin

Janker & Seiser et al.

Scientific Reports 11:32, **2021**

DOI: 10.1038/s41598-020-79378-9

Exploring the dermotoxicity of the mycotoxin deoxynivalenol: combined morphologic and proteomic profiling of human epidermal cells reveals alteration of lipid biosynthesis machinery and membrane structural integrity relevant for skin barrier function

Janker & Del Favero et al.

Archives of Toxicology 95:2201–2221, **2021**

DOI: 10.1007/s00204-021-03042-y

Schwann cell plasticity regulates neuroblastic tumor cell differentiation via epidermal growth factor-like protein 8

Weiss & Taschner-Mandl et al.

Nature Communications 12:1624, **2021**

DOI: 10.1038/s41467-021-21859-0

Multi-omics empowered deep phenotyping of ulcerative colitis

Janker et al.

medRxiv 2022.05.25.22275502, **2022**

DOI: 10.1101/2022.05.25.22275502

Manuscript under revision

Table of Contents

1 Abstract

Proteomic research made remarkable advances during the last two decades, enabling a detailed analysis of proteins responsible for phenotypical changes in complex biological systems. The capability to identify and quantify thousands of proteins in parallel allowed an unbiased and more holistic view on the role of the proteome. Mass spectrometry-based in-depth profiling of PTMs such as protein phosphorylation, a modification highly relevant for protein activity, localization, or interaction, allow to further "functionalize" the measured proteome and add additional layers of information relevant for causal interpretations. Assessing the actual distribution of proteoforms for a protein present in a biological system can give valuable insights and relevant information for the emergence and progression of (patho-) physiological processes. In addition to proteins, the analysis of biochemically relevant molecules such as amino acids, eicosanoids, lipids and organic acids can complement the interpretation of proteome data by linking alterations on protein level to effects observed on the metabolome level. Focusing on said effector molecules, important questions regarding disease progression and metabolic impact of stromal tissue in multiple myeloma were successfully addressed, supplementing genetic screening approaches. The analysis of plasma cells from multiple myeloma patients in different disease stages, as well as probing of the tumor microenvironment enabled insights which could have implications for patient stratification and novel therapeutic concepts. In other disease models, the combination of MS-based screenings with transcriptomics allowed the characterization of wound-healing signatures triggered by antiseptic molecules, or elucidate intricate receptor signalling cascades *via* temporal phosphoproteomics profiling which are relevant for disease escalation and metastatic potential. Testing an environmental mycotoxin, the exogenous small molecule deoxynivalenol, we explored potential dermotoxicity in an *in vitro* setup and applied a combination of imaging techniques with phospho-/proteomics datasets to unravel potential implications relevant for dermal exposure. These analysis strategies can also give vital information about clinical status and elucidate disease mechanisms of patients with autoimmune diseases with no obvious underlying genetic driver mutations. Complementary biomarkers from different molecule classes can help to identify driving (patho-) physiological processes and possible interventions in order to achieve not only phenotypical but also remission on a molecular level. To summarize the in this thesis presented studies, the application of unbiased MS based methods can aid the understanding of mostly postgenomically driven biological processes in complex systems and reveal novel functional aspects. Furthermore, the versatility and power of combination of said methods enabled the application to a diverse set of important scientific questions, once more demonstrating the power of comprehensive mass spectrometry-based -omics technologies.

1.1 Zusammenfassung

Das wissenschaftliche Feld der Proteomik machte in den letzten zwei Jahrzehnten erstaunliche Fortschritte, welche eine detaillierte Analyse von Proteinen, verantwortlich für phänotypische Veränderungen in komplexen biologischen Systemen, ermöglichte. Das Potential der Identifizierung und Quantifizierung von tausenden Proteinen in Parallel ermöglichte eine unvoreingenommene und ganzheitliche Sichtweise auf die Rolle des Proteoms. Die massenspektrometrische Analyse von post-translationalen Modifikationen wie Protein Phosphorylierung, welche für Protein Aktivität, Lokalisierung oder Interaktion äußerst wichtig ist, erlaubt eine weitere „Funktionalisierung" des gemessenen Proteoms und fügt eine zusätzliche Ebene von Information, relevant für eine kausale Interpretation, hinzu. Die Beurteilung der Diversität von vorliegenden Proteoformen, welche in biologischen Systemen präsent sind, können wichtige Erkenntnisse und Informationen zur Entstehung und den Verlauf von (patho-) physiologischen Prozessen liefern. In Ergänzung zu Proteinen kann die Analyse von biochemisch relevanten Molekülen wie Aminosäuren, Fettsäuren, Lipiden und organischen Säuren die Interpretation von proteomischen Daten durch die Verknüpfung von Effekten mit metabolomischen Veränderungen komplementieren. Mit Fokus auf erwähnte Effektor Moleküle konnten wichtige Fragen im Bezug auf Krankheitsverlauf und metabolischen Einfluss von stromalen Gewebe in multiplen Myelom adressiert werden, welche das vorhandene Wissen *via* genetische Analysen ergänzen. Die Analyse von Plasmazellen und Tumormikroumgebung von multpiplen Myelom Patienten in verschiedenen Stadien der Erkrankung ermöglichte Erkenntnisse, welche Implikationen für Patientenstratifizierung und neue therapeutische Konzepte haben könnte. In anderen Krankheitsmodellen konnte die Kombination von MS basierten Proteomanalysen mit transkriptomischen Analysen eine Charakterisierung von Wundheilungssignaturen ausgelöst durch antiseptische Moleküle ermöglichen oder die Betrachtung komplexer Signaltransduktionskaskaden *via* ergänzenden temporalen phosphoproteomischen Analysen das metastatische Potential und daraus folgender Krankheitseskalation aufgeklärt werden. Die *in vitro* Testung des Mycotoxins Deoxynivalenol, ein exogenes kleines Molekül, ermöglichte die Bestimmung von potentiellen Wirkmechanismen im Bezug auf dermale Toxizität mittels (phospho-) proteomischen Analysen. Die erwähnten Analysestrategien können auch bei der Bestimmung des klinischen Status und treibenden Krankheitsmechanismen von Autoimmunerkrankungen helfen, wo keine offensichtlichen genetischen Treibermutationen vorhanden sind. Die Bestimmung von komplementären Biomarker kann die Identifizierung von treibenden (patho-) physiologischen Prozessen und somit mögliche Therapiestrategien für eine Remission auf molekularer Ebene ermöglichen. Die in dieser Thesis präsentierten Publikationen sollen zeigen, dass die Anwendung von unvoreingenommenen Massenspektrometrie basierten Methoden das Potential haben, das Verständnis von hauptsächlich postgenomisch bestimmten biologischen

Prozessen in komplexen Systemen zu verbessern und neue funktionale Aspekte aufzuzeigen. Darüber hinaus ermöglichten die Vielseitigkeit und Kombinationskraft dieser Methoden die Anwendung auf eine Vielzahl wichtiger wissenschaftlicher Fragestellungen, was einmal mehr die Leistungsfähigkeit umfassender, auf Massenspektrometrie basierender Omics-Technologien demonstriert.

2 Introduction and Methodological Background

Mass spectrometry-based techniques, which aim to detect, identify and quantify biologically relevant analytes are becoming more prominent and relevant in basic and translational research.[1-4] The translation of knowledge created by basic research into appropriate clinical applications of said methods still remains in its infancy. With massive developments in the last two decades in the field of mass spectrometry-based post-genomic research, the time has come for new concepts and ideas focusing on basic research questions not accessible for conventional methods. This work aims to elucidate aspects of multiple "Omics" research fields including the combination of complementary datasets and approaches to enhance the functional states of the proteome by probing dynamic alterations of post-translational modifications. In the following chapters, applied methods and theoretical concepts are described.

2.1 "Omics"

"Omics" can be defined as a term for particular research fields, mainly related to biology or biochemistry and aims to characterize and monitor the entirety of a given biomolecule class, such as genes (genomics), transcripts (transcriptomics), proteins (proteomics) or metabolites (metabolomics). In relation to cellular or molecular biology, the often-used suffix "-ome" describes exactly this molecule class in their totality[5] – the term genome was coined in 1920 by botanist Hans Winkler, trying to combine the words gene and chromosome to describe the collectivity of all genes.[6]

2.1.1 The Central Dogma

The dependence between different biomolecule classes and their interfaces can be illustrated by the "Central dogma of molecular biology", initially described by Francis Crick.[7]

Figure 1 | The central dogma of molecular biology showing residue dependent flow of information in protein direction. Contributing biological processes such as transcription, reverse transcription and translation are illustrated at the appropriate sites.

Starting with the hypothesis, that proteins are formed by enzymes, which themselves are proteins raised some obvious questions which needed explanation. How are enzymes initially formed, if enzymes are responsible for protein synthesis? What set of enzymes is necessary to cover the heterogeneity of proteins found in nature? The answer to these questions had to

be a radical new way of thinking about protein synthesis, involving a process which should be relatively simple yet universal in nature. Crick described the essence of the protein synthesis problem in three distinct parts comprising of individual fluxes: i) the flow of energy ii) the flow of matter iii) and the flow of information. Focusing on the third part, he describes information as the specific sequence of amino acid in a given protein. The process of correct sequentialization and joining of amino acid for polypeptide synthesis, so the correct transfer of matter, was at the time heavily discussed and no definitive mechanism was previously given.[7-9] The collected ideas and experimental evidence pointed into the direction of the todays known "Central dogma of molecular biology" describing the flow of information. As depicted in **Figure 1**, this transfer of information can occur from nucleic acid to nucleic acid, or nucleic acid to protein, but information that reaches the protein level cannot be transferred backwards.[7]

2.1.2 Beginnings of "Omics" Research

The year 1953 was pivotal for the advancements of molecular research areas dealing with sequence information of DNA and proteins. The elucidation of double helix structure of DNA [10-12] by Watson, Crick, Franklin and Wilkins, describing an irregular sequence of bases with no obvious sequential restrictions along the chains [10], marked the early beginnings of the first big omics field, namely genomics. Although genomics was the first well established sequencing-based omics field, it was actually Sanger who first sequenced the two chains of the insulin protein before the sequencing of any deoxyribonucleic acid.[13,14] The first DNA sequencing method followed in 1977 [15], but it took almost three decades of further progress in order to provide applications offering a more holistic approach, allowing genome wide association studies.[16-18] This development paved the way for novel omics areas such as transcriptomics and proteomics to come into existence by creating reference points for extensive mapping efforts.[19] Based on Sanger sequencing, early steps were taken in the field of transcriptomics in 1995 with the development of serial analysis of gene expression (SAGE), which provided the possibility of profiling novel transcripts but was limited in terms of scope and quantitative capability.[20] Further developments include microarray analysis and RNA-Seq, cutting the cost and time per transcript massively.[21-23] First approaches towards a systematic analysis of proteins were initiated with sequencing efforts via Edman-degradation.[24] With the beginning of the new millennium, the novel field of proteomics emerged. Starting with "protein spots" excised from 2D-SDS-PAGE and analysed with an MALDI-ToF approach, multiple proteins could be profiled from a complex protein mixture. Striving for better proteome coverage and throughput, as well as a higher degree of automation, different approaches had to be developed. Big advances were achieved when Fenn et al.[25] developed a technique called electrospray ionization, enabling a soft but highly efficient ionization of analytes with the additional potential for on-line coupling to liquid chromatography instruments. Applying

flowrates in the nanoliter-per-minute range, the gain in sensitivity and reduction of complexity *via* LC separation allowed, for the first time, an automated in-depth profiling of bulk proteomes and pathed the way for further technological improvements which shape our current understanding of protein function.[26] Previously mentioned advancements in ionization techniques also strongly influenced the field of metabolomics, but first proof-of-concept experiments were already performed in the 1960s, employing GC-MS instruments for the characterization of metabolites in urine and biological tissue extracts.[27]

2.2 Proteomics

In this thesis, the focus lays on the generation of biological relevant functional readout of proteome data. To achieve this goal, multiple approaches had to be combined in order to sufficiently enable a discussion on functional implications of presented datasets. The measurement of protein abundance in a given sample can give meaningful insights into protein turnover and synthesis rates and general composition of the proteome but is limited in the readout of functional states of a given protein. To further investigate protein function, additional assays may be performed in order to elucidate protein-protein interactions or modifications of proteins on single amino acids indicative of a given proteoform.

2.2.1 Protein Chemistry, Post Translational Modifications and Proteoforms

Amino acids are the essential building blocks of every protein. As the terminology "building block" suggests, these organic compounds contain an amino and a carboxylate functional group allowing a condensation reaction *via* the process of ribosomal translation into a polypeptide chain, as shown in **Figure 2**.
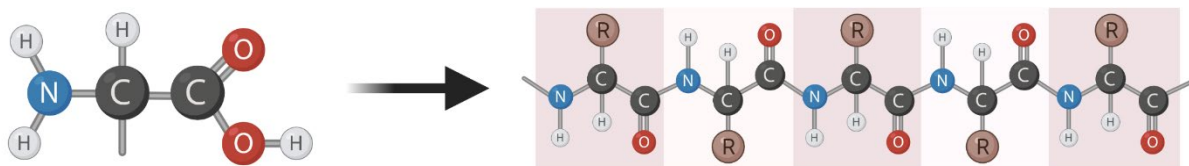
Figure 2 | Schematic illustration of chemical structure of amino acids without functional residue assignment (left) and formation of a polypeptide chain via ribosomal transcription with simplified residue groups (right).

Different residue groups located at the α-carbon allow the formation of chemically diverse polypeptides. To date, a total of over 500 naturally occurring amino acids could be identified, although only 21 amino acids can be found in the genetic code[28], with selenocysteine as a special case.[29]

When comparing simple numbers between proteomics and other omics fields such as metabolomics or lipidomics with factor 2 or factor 5 less distinct molecules, respectively (**Figure 2**), one could be prone to a premature conclusion that proteins do not share the

observed complexity. Indeed, estimates by the Human Proteome Project predict about 20.000 proteins encoded by the genome, with around 18.000 already detected.[19] As depicted in **Figure 3**, the perspective onto the proteome without any post-translational modifications or alternative splicing isoforms is only part of the "truth".
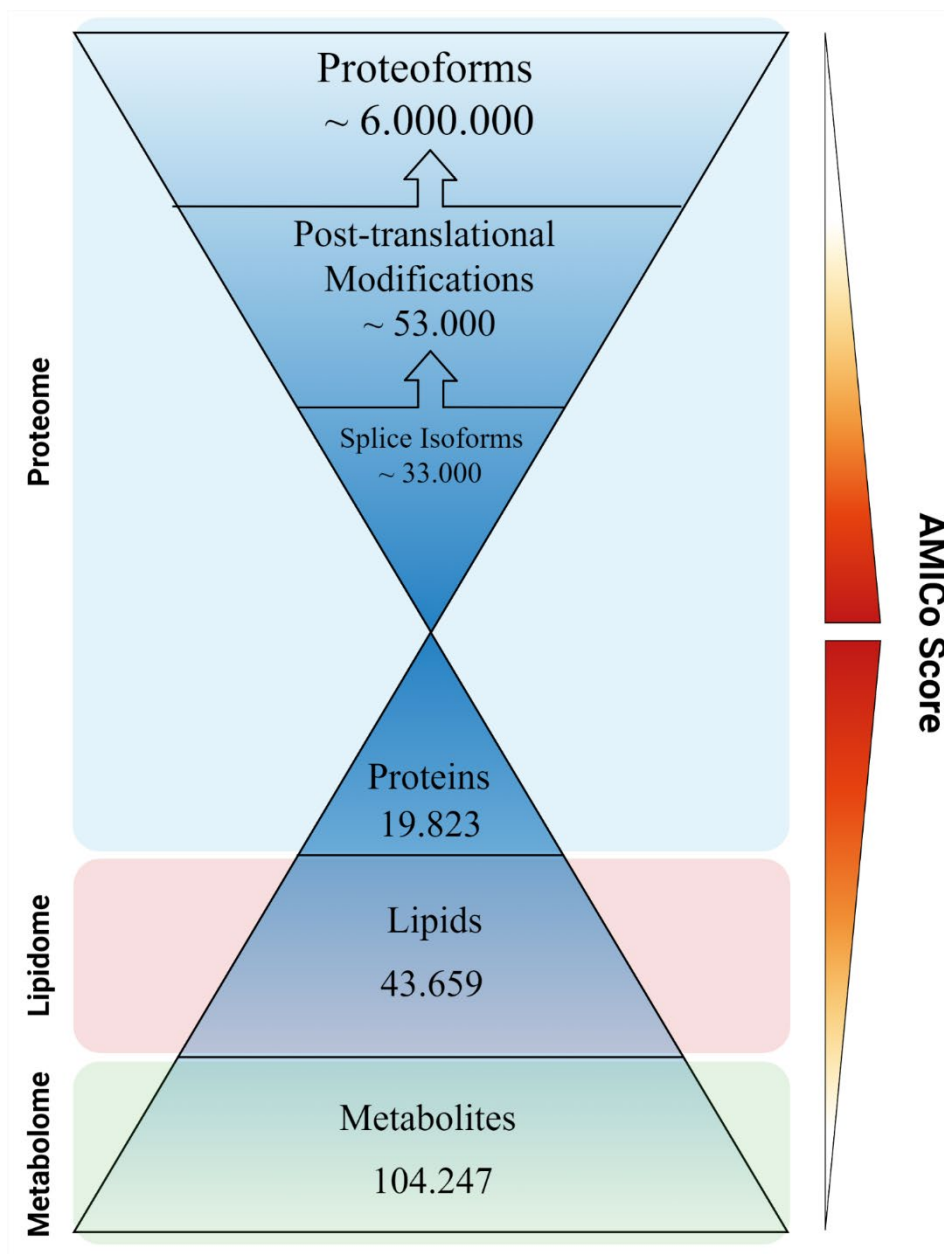
Figure 3 | Overview over chemical diversity of different "Omics" fields with important key figures. Multiple parameters and features are combined into a theoretical "AMICo Score". (Numeric values and concept based on Aebersold et al.[30]. HPP[19], LipidMaps[31], HMDB[32] - accessed 2018)

The shown diagram summarizes relevant molecule classes and their complexity in form of an hourglass. Introducing a theoretical score called "AMICo", an acronym originating from the Italian word "friend", trying to summarize key features as analyte Abundance, Metabolic stability, certainty of Identification and experimental capability to Control or monitor quantitative fluctuations in complex systems *via* MS-based bioanalytical methods.

Looking at the "friendliness or relatability" of a given molecule class determined by above mentioned metrics and parameters, unmodified proteins can be a favorable choice for investigation, with the downside of losing essential information on the exact functional state of the protein, hence possibly diminishing the quality of data interpretation. Proteoforms are distinct protein "phenotypes" consisting of combinations of splice isoforms and/or different post-translational modifications.[33] Assessing the actual distribution of proteoforms for a protein present in a biological system can give valuable insights and relevant information for the emergence and progression of (patho-) physiological processes. Roughly 400 distinct post-translational modifications are known in biology as described on Unimod (www.unimod.org), with only few being mapped extensively. Including data provided in the 10/2017 release of Human SwissProt database with approx. 33.000 splice isoforms, approx. 78.000 site-specific amino acid variants and approx. 53.000 mapped post-translational modifications of which around 38.000 are protein phosphorylations, the number of possible combinations exceeds the processing capabilities of any currently available bioinformatic approach. s some post-translational modifications can only occur under certain circumstances or on specific amino acids, one can differentiate between "binary" modifications such as phosphorylation or acetylation where certain amino acids are either modified or not, or modifications like methylation, where amino acids such as lysine could be modified *via* methylation, demethylation or trimethylation. These properties allow the following equation for the calculation of possible proteoforms[30]:

Equation 1

$$\# \ theoretical \ proteoforms = \prod_{i=1}^{n}(potential \ PTMs \ at \ AA_i + 1)$$

Applying these theoretical calculations to the example of histone H4 *(P62805)* including only the 13 most common PTM sites and one additional SNP variant creates 98.304 possible proteoforms.[30] The same protein was also extensively profiled by multiple labs and only 75 proteoforms with a relative abundance of >0.01% could be experimentally validated.[34] These findings suggest that although the theoretical proteoform space can be immensely vast, biologically relevant proteoforms which can be detected with state-of-the-art technology, may seem to only represent a small but not negligible fraction.

The role of proteoforms in biology and challenges for MS-based bioanalytical methods can be summarized as seen in ***Figure 4***. Mapping of proteoform heterogeneity with increasing structural complexity allows better assignment of molecular function, hence assessing physiological relevance (green wedges). With increasing complexity also come downsides like decreased identification certainty, especially when looking at site specific modifications and their localization probability. Molecular stability of intermediate complexes or chemical instable

modifications can influence the robustness of obtained datasets greatly, making it harder to bioanalytically access and monitor those proteoforms.[30]
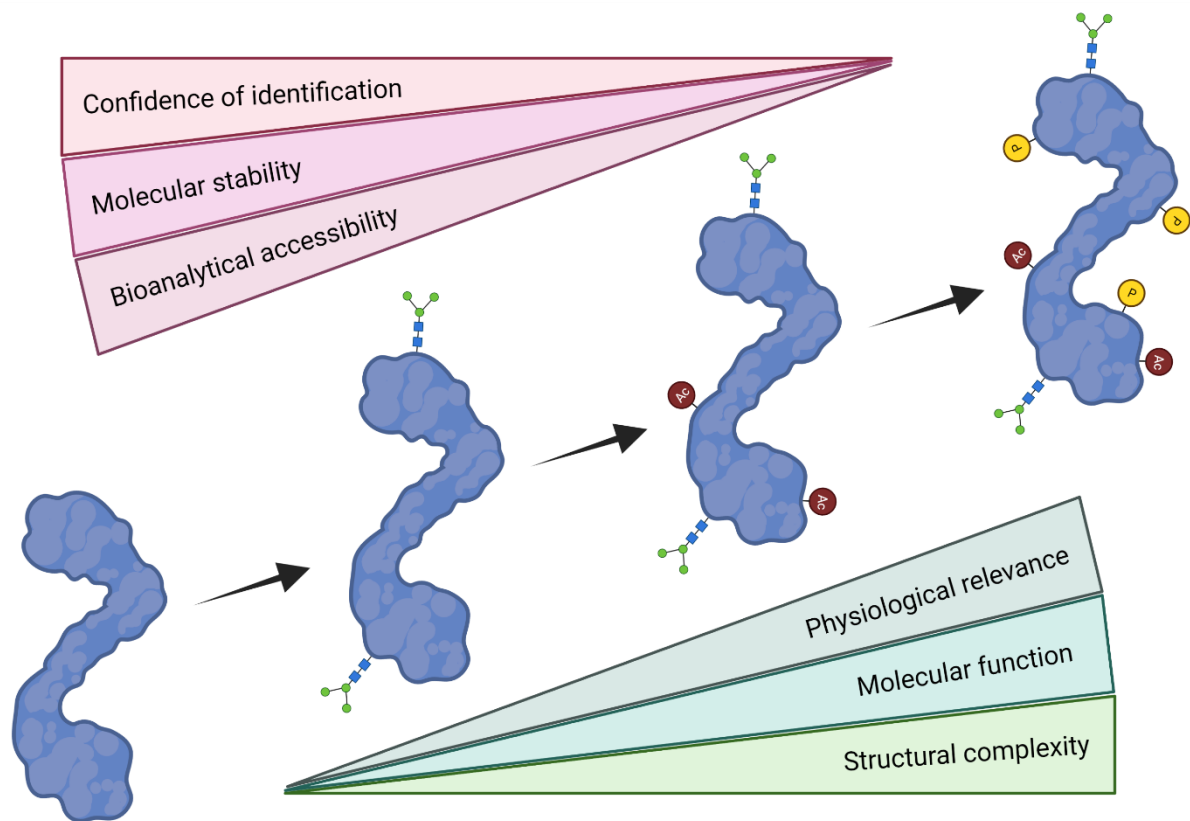
Figure 4 | Summary of protein proteoform exemplified via different stages of PTM (glycosylation, acetylation and phosphorylation) complexity.

2.2.2 Bottom-up Shotgun Proteomics

In order to facilitate and enhance the detection of proteins *via* mass spectrometry, multiple steps of protein sample preparation must be performed. ***Figure 5*** illustrates one of the most commonly applied workflows in proteomics, the bottom-up approach. Due to the favourable properties of peptides regarding charge distribution, molecule complexity relevant for identification *via* MS2 scan and chromatographic behaviour compared to intact proteins, this approach paved the way for the first reference proteomes.[26]
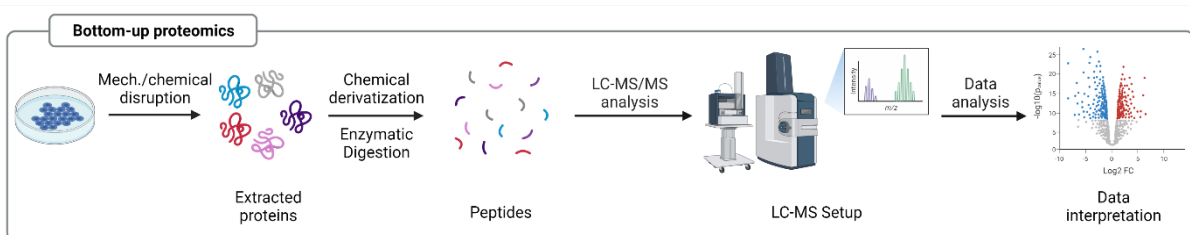
Figure 5 | General bottom-up proteomics workflow illustrated in simplistic steps. Initial disruption of cells via mechanical or chemical stress is followed by chemical derivatization and enzymatic digestion. Digested peptides are measured via MS, often coupled to LC instrument. Interpretation of resulting data of peptide spectra is later performed via search algorithms, resulting in protein identification and, if possible, quantification.

Extraction and solubilization of protein complexes can be enhanced *via* addition of ionic or non-ionic detergents such as SDS or Triton-X. Besides extraction, removal of unwanted analytes such as sugars, nucleic acids or lipids should be performed in order to allow a reproducible analysis of mentioned proteome. This purification can be performed *via* precipitation of proteins *via* organic solvents, often methanol or ethanol, but also acetonitrile. As complexity is increased upon peptide digestion, it must be ensured that resulting cleavage sites are created in a controlled fashion. Degradation with a specific enzyme such as the endopeptidase trypsin allows the C-terminal cleavage of Lysine or Arginine residues, as this positively charged residues stabilize a selective complex with the negatively charged Aspartate residue in the trypsin binding site. The resulting C-terminally protonated amino acid already provides an ionization advantage.[26] To guarantee a nearly complete digestion of a protein, higher order structures must be eliminated to allow the enzyme unhindered access to every relevant amino acid. A derivatization of reactive thiol residues of cysteine *via* carbamidomethylation should be performed to ensure the inhibition of refolding. With increasing complexity of possible analytes that could be present in a sample also come drawbacks and limitations. Chromatographic separation *via* nano-UHPLC setups can mitigate some of the drawbacks, including a massive reduction of sample complexity in a temporal manner, as well as enabling more accurate quantification approaches. The majority of bottom-up experiments performed are based on a label-free quantification (LFQ) method utilizing MS1 information for the (semi-)quantification of peptides, whereas MS2 information is used to obtain amino acid sequence information. As throughput and reproducibility of LFQ experiments may limit larger scale experiments or direct comparisons of samples in one acquisition, additional labelling techniques such as SILAC or TMT were developed. SILAC, so-called stable isotope labelling by amino acids in cell culture, utilizes the metabolic amino acid turnover by incorporation of heavy lysine or heavy arginine isotopes into newly synthesised proteins and therefore creating a distinct mass shift detectable by MS. This technique can be used to study protein turnover but also aids the interpretation of complex biological interactions in co-incubation cell culture experiments.[35] Another well established technique utilizes the possibility of isobaric labelling of tryptic peptides *via* tandem mass tags (TMT). This approach allows the identification and quantification of peptides originating from multiple samples in a single MS run by applying different mass tags to each sample, increasing throughput and eliminating measurement or chromatography related differences or artefacts.[36] Distinct signals, so-called reporter ions, can be detected in MS2 scans and their relative intensity should in theory reflect the relative abundance of the analyte, although it has been shown that phenomenon called "ratio compression" can influence the signal intensity of reporter ions through co-fragmentation causing skewed ratios.[37,38]

2.2.3 The Dark Matter of the Proteome

As described in chapter 2.2.1, the importance of post-translational modifications (PTMs) cannot be stressed enough. Recent advances in mass spectrometry-based in-depth profiling of PTMs such as protein phosphorylation[39-41], a modification highly relevant for protein activity, localization, or interaction, allow to further "functionalize" the measured proteome and add additional layers of information relevant for causal interpretations.[42] With increasing data density, intricate signalling networks could be profiled in detail. It became clear that perturbations of single kinases or phosphatases resulted in off-target phosphoproteome modulation suggesting highly interconnected phosphorylation signalling networks which differs greatly from previously described linear pathways.[43] This assumption is further strengthened when looking at in literature described kinase-to-substrate relations and the 20:80 rule, meaning that 20% of known kinases account for modulation of over 80% of annotated substrates. This bias is strongly reflected by the number of mapped substrates per kinase – with 80% of kinases having 20 or fewer substrates and 30% of kinases only having one substrate assigned.[44] Besides protein phosphorylation, there are only a dozen of other PTMs which are profiled in a highly coordinated fashion with comparable database standards and scientific community guidelines for the improvement of data traceability and overall quality. With the above-mentioned points, it becomes apparent that with incomplete identification and mapping of key regulators and network nodes or interactions, the so called "dark matter", an unbiased and complete analysis of biological networks may only be partially possible. MS-based methods for the elucidation and probing of this "dark matter" are important tools to enhance and improve our understanding of (patho-) physiological processes and their relevance in complex systems.

2.3 Metabolomics as Complementary Readout

Metabolomics deals with the entirety of metabolites (small molecules) derived from endogenous processes or exogenous origin and includes amino acids, peptides, lipids, nucleic acids, sugars, vitamins, organic acids and many more.[32] Recent advances in metabolite research allow in-depth analysis of complex physiological processes and associated metabolic pathways.[45-48] In manuscripts relevant to this thesis, we took advantage of said advances and probed relevant metabolic pathways covering eicosanoids and more than 500 metabolites, including amino acids, lipids and bile acids in order to complement proteome datasets from matching samples. In *Janker et al.*[4] the analysis of plasma samples from ulcerative colitis and healthy control patients aided, in conjuncture with proteome data, the stratification of disease state and differentiation from healthy controls.
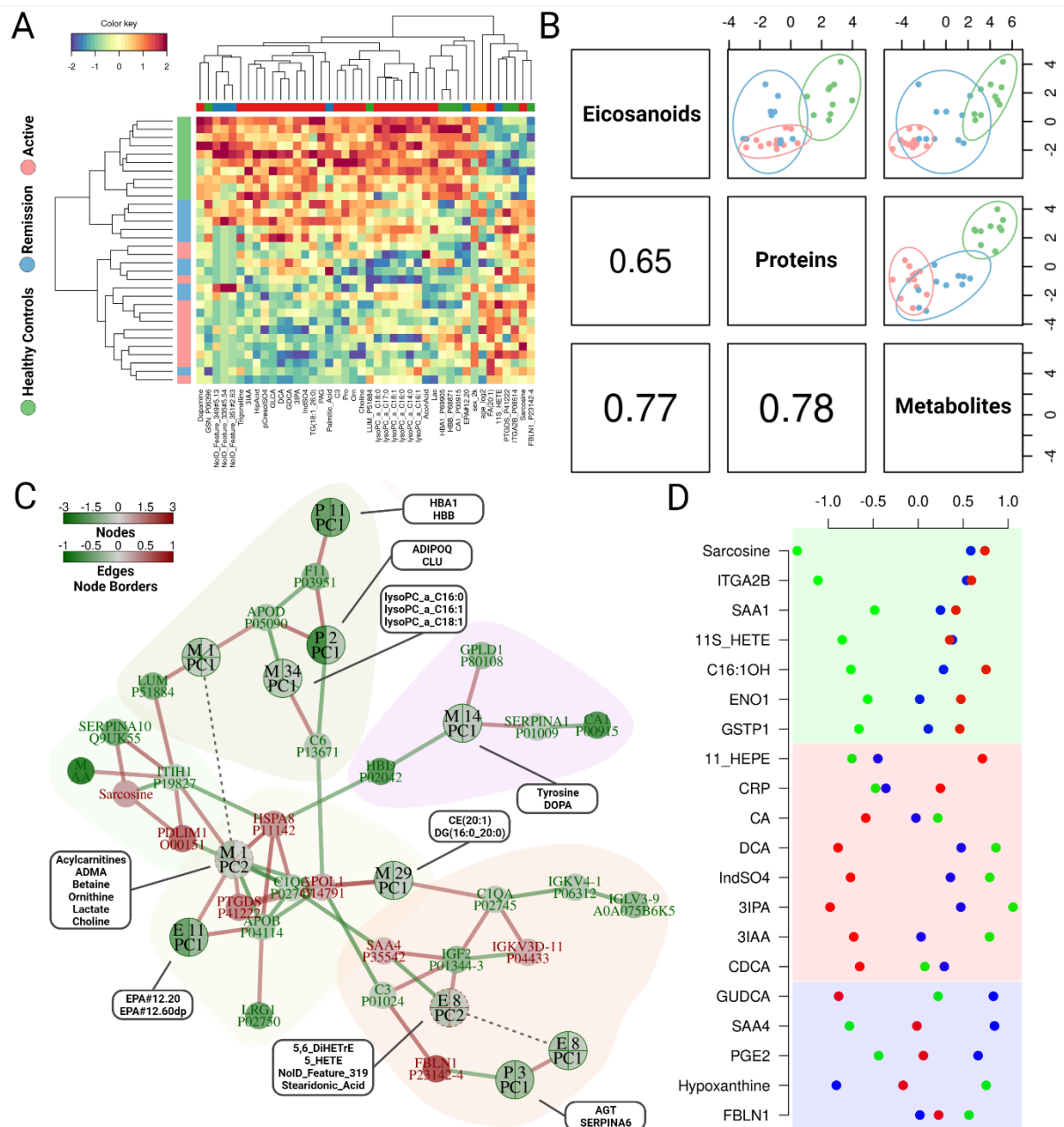
Figure 6 | Multi-omics analysis of plasma samples taken from ulcerative colitis patients as well as healthy controls. The bioinformatical combination of multiple datasets originating including proteome, eicosanoid and metabolite data allowed patient stratification according to disease state. Figure taken from *Janker et al*[4]

Figure 6 illustrates the combination of above-mentioned datasets and can be summarized in a panel (D) of key molecules determining the stratification of disease state. Most interestingly, it must be pointed out that clinically validated biomarkers such as CRP did show normalization in remission state as expected, but certain eicosanoids relevant for promotion or attenuation of inflammatory processes did not show a similar trend, demonstrating the potential prognostic power and significance of in-depth metabolic profiling.

2.4 Mass Spectrometry-based Analysis of Biological Analytes

As this work mainly highlights different parts of the proteomic research in combination with complementing fields, this introduction on mass spectrometry-based analysis strategies will focus on proteins, their role in complex biological systems and how to measure them using mass spectrometry. An often-mentioned challenge in post-genomic research is the complexity of any given biological class of molecules, without the possibility of direct analyte amplification. The following chapters capture main methods and applications commonly used in proteome research.

2.4.1 Orbitrap-based Mass Spectrometry

Many different instruments employing different types of mass analyzers and detectors such as Time-of-flight (TOF), Fourier-transform ion cyclotron resonance (FT-ICR) or quadrupole mass analyzer. The variety of existing analyzers and detectors allowed the design of complex mass spectrometers, but where often limited in terms of resolution, scan rate or simply the cost of operating a system at near null temperature.

Mass spectrometers containing orbitrap analyzers became commercially available in 2005, after years of development from Makarov et al, overcoming most of the above-mentioned drawbacks.[49] The orbitrap consists of a spindle-shaped central electrode and a barrel-shaped outer electrode. Ions are injected into the analyzer at high speed, trapped by the electrostatic field applied along the inner electrode and forced onto circular orbits, performing corkscrew-like motions. While pushing the entering ions towards the electrode, the electric field is decreased to enable trapping of the ions, only to be raised again afterwards to approximately +/- 3200V, depending on the operation in positive or negative ion mode. In order to ensure unperturbed ion movement, high vacuum of approximately 10^{-10} mbar is applied in the orbitrap. Current is induced upon ion packages flying past the outer electrode, measured, amplified and Fourier transformed into sine waves. Their frequency is related to the m/z value of the ion whereas its intensity provides information on the number of ions present at this specific m/z value.[50] The Q Exactive[TM] product line features hybrid instruments employing quadrupole-based ion pre-selection in combination with an orbitrap mass analyzer. Before ions can be analyzed and detected, a transfer from liquid to gas phase *via* electrospray ionization in a closed source interface must be applied. Ions travelling through the transfer capillary reach a S-lens ion-optics device, allowing efficient ion capturing and focusing without the need of a DC gradient. After focusing the ion stream in a first step, a second step of focusing with additional filtering of neutrals and ion clusters through orthogonal deflection, in most instruments *via* bent flatapole, is performed. As above described, an ion pre-selection with a quadrupole mass analyzer can be applied to narrow the m/z window of passing ions. After this first selection

steps, the ions of interest must be bundled and cooled in order to allow a transfer into the orbitrap. The C-trap, a curved linear trap, allows bundling and cooling of ions by ramping down RF amplitude and applying a DC gradient. Enabled by the curved shape of the linear trap, subsequent orthogonal injection of ions into the orbitrap detector can happen within the spatial/temporal requirements for successful measurement. For MS/MS experiments from instruments employing CID or HCD, ions can be linearly transferred into a collision chamber, applying an inert gas and high voltage in order to cause collisions between ions and gas molecules to produce fragment ions. These fragment ions can be reintroduced to the C-trap and subsequently be measured. With the enablement of ion guidance through the C-trap, accumulation, fragmentation and measurement of ions can be performed in a parallel fashion.

2.4.2 Ion Mobility Time-of-Flight Mass Spectrometry

Ion mobility describes the differential migration behaviour of molecules through a gas phase, under the influence of an electrical field. Differing sizes and shapes of molecules result in distinct retention and thereof allow separation of similar molecules or even isomers. Collisional cross section (CCS) properties, dependent on the used gas and instrument type, provide the possibility to map and compare CCS values of molecules and may increase, besides the reduction of complexity also confidence regarding identification.[51]

Adding ion mobility (IM) as a separation dimension to conventional LC-MS setups enables the separation of isomeric and isobaric compounds, not differing in molecular weight but molecular structure or molecular composition, eventually allowing for the deconvolution of chimeric MS spectra, containing co-eluting analytes resulting in co-fragmentation and mixed spectra.[52] The technique of trapped ion mobility spectrometry (TIMS) was developed by Park et al. in 2011.[53] In TIMS instruments, ions are pushed forward by an electrical field against a counteracting gas flow in a drift cell, holding them stationary and allowing for a significant reduction of the IM analyzer dimensions compared to the initially developed drift tube devices.[54] The ions adopt a steady state drift velocity v_d which is the product of the applied electric field E and the ion mobility K. (**Equation 2**) K is influenced, among other parameters, by ion size, shape and charge as well as parameters such as composition, pressure (p), temperature (T) and polarizability of the employed gas. By replacing p and T with standard-pressure (p_0) and -temperature (T_0), K can be standardized and described as the reduced ion mobility K_0 (**Equation 3**). The collisional cross section (CCS) of an ion, being characteristic for its interaction with the gas, can be calculated *via* the Mason Schamp equation (**Equation 4**) implementing the ion charge z and the collision gas mass m as well as the ion mass M, both determined *via* MS in ion mobility mass spectrometry hybrid instruments (IMMS).[54]

Equation 2

$$v_d = K \cdot E$$

Equation 3

$$K_0 = K \cdot \frac{T_0}{T} \cdot \frac{p_0}{p}$$

Equation 4

$$CCS = 18500 \cdot \frac{z}{K_0} \cdot \sqrt{T \cdot \frac{M \cdot m}{M + m}}$$

TIMS analyzers are usually hyphenated with (nano)-ESI or atmospheric pressure photoionization (APPI). Several modes of action such as sequential analysis, gated methods and parallel or selected accumulation can be implemented with TIMS, allowing for a broad variety of analysis techniques. IMMS devices have so far been equipped with Fourier-transform – ion cyclotron resonance (FT-ICR) or time-of-flight (TOF) mass analyzers.[54] As IM based separation usually only takes tens of milliseconds, TOF instruments with their high scan speeds of approximately 0.1ms per spectrum are well compatible with this technology.[55]
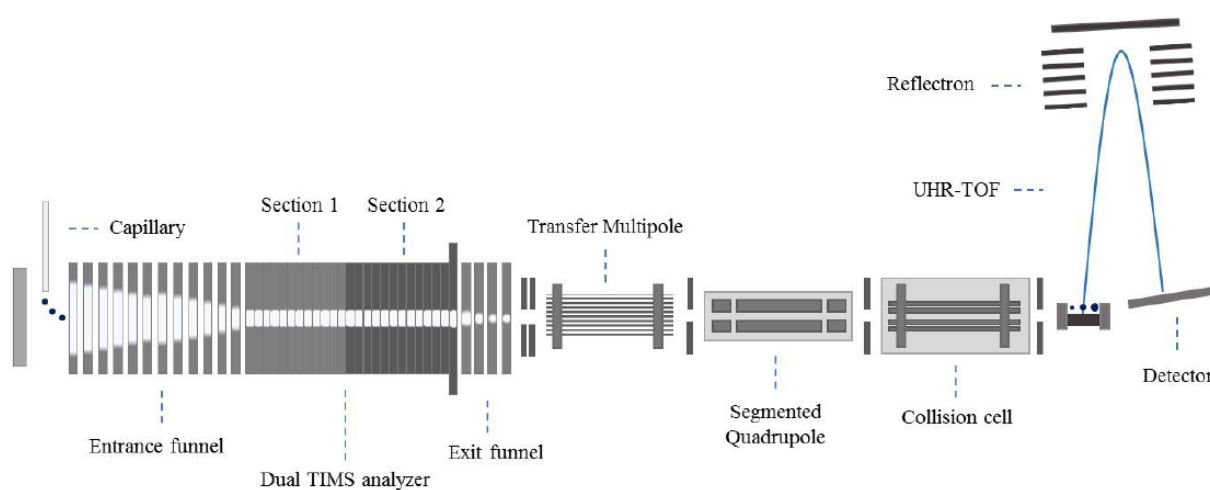
Figure 7 | Schematic overview of main building blocks of timsTOF™ Pro instrument. (Copyright with permission from Patricia Bortel[56])

An IMMS device that combines an ESI source with a dual TIMS analyzer and an ultra-high resolution-TOF (UHR-TOF) is the timsTOF™ by Bruker Daltonics Inc.. In the TIMS analyzer, sitting between an ion funnel and segmented quadrupole (**Figure 7**), a gas flow pushes the injected ions forward while a counteracting electrical field gradient is applied. As a result, each ion comes to rest at the position where the force of the gas flow and the opposing electric field are equal, depending on the unique CCS value of the ion and its charge. The duality of the TIMS tunnel enables ion pre-separation and storage in the first section while IM-based analysis

separation takes places in the second section, enabling duty cycles of up to 100%. Ions are eluted from the TIMS cell by gradually lowering the electric field gradient, with low mobility ions being released first due to their small collisional cross sections. The parallel accumulation-serial fragmentation (PASEF) mode facilitates the accumulation of up to hundreds of MS2 scans per second without compromising sensitivity. In the TOF section of the device, ion packages are formed in the accelerator unit, ejected into the orthogonal drift tube and reflected by the two-stage reflectron before they are finally detected by a multi-channel plate ion detector (MCP).[52,55]

2.4.3 Electrospray Ionization

In 1989, Fenn et al.[25] developed electrospray ionization (ESI), enabling a soft but highly efficient ionization of analytes with the additional potential for on-line coupling to liquid chromatography instruments. In the field of proteomics, ESI is one of the most commonly employed ionization techniques. A characteristic of soft ionization techniques is that molecules are efficiently ionized with less in-source fragmentation compared to harder ionization methods. In ESI, the analyte solution is passed through a fine needle while a high potential (usually 2-5kV) is applied at atmospheric pressure, creating a so-called Taylor cone.[57] Charged droplets are formed driven by the charge accumulation on the surface of the liquid. Due to evaporation, the droplets shrink, their charge density increases and by Coulomb explosions, the drop size is continuously decreased until the analyte ions are transferred into the gas phase. The evaporation and ionization process can be assisted by applying a drying gas such as nitrogen at the capillary entrance, adjusting the flow rate or lowering the surface tension by the addition of organic solvents. For proteomics applications, ionization is usually performed in positive mode with acidified sample solutions.[58]

2.5 Separation and Enrichment Techniques

Chromatographic or capturing-based technologies are essential tools in state-of-the-art bioanalytical experiments. With rising sensitivity of MS instruments, the complexity of measured signals can exceed the capability of said instruments to detect all signals with high quality at one point in time. Additional limiting factors can be the dynamic range of analytes exceeding the dynamic range of a detector, or the presence of post-translational modifications. Therefore, separation and enrichment techniques must be applied to allow a temporal reduction of complexity to mitigate matrix effects and enhance the identification and quantification of analytes *via* their respective chromatographic behaviour.

2.5.1 Reversed Phase Liquid Chromatography

With the development of on-line coupling interfaces like the ESI source, the application of chromatographic devices for bioanalytical methods became a valuable tool, nowadays used in almost every mass spectrometry laboratory. Todays most implemented LC separation technique for proteomic and metabolomic applications is reversed phase (RP) chromatography, utilizing a non-polar stationary phase and polar, mostly aqueous mobile phase.[59] In this chromatographic method, the analytes, e.g. peptides, are separated based on their partition between a hydrophobic stationary phase and a more hydrophilic mobile phase. In order to separate and gradually elute the analyte species, the hydrophobicity of the liquid phase is increased over time employing a gradient. Following this technique, hydrophilic peptides elute earlier while more hydrophobic peptide species interact with the hydrophobic solid phase and elute later within the applied elution gradient. RP column beads are functionalized with aliphatic chains of typically C_8 or C_{18} length while eluents often consist of water and acetonitrile acidified with formic acid.[50] Additional parameters such as column diameter, column length, particle size, particle size distribution or particle pore size can strongly influence the chromatographic behaviour and analytical performance of a given system.[60] Due to the highly complex nature of the proteome, and the increase of complexity of to-be-measured analytes caused by tryptic digestion in bottom-up approaches, novel LC systems had to be developed in order to allow an acceptable coverage of the proteome. Nano-UHPLC systems allow relatively low flow rates of about 100 to 500 nL·min^{-1} whilst keeping the column pressure at around 600 to 1000 bar, depending on column length, diameter, and particle size. With decreasing column diameter to about 100 µm, column length up to 500 mm, and ESI needle diameters around 20 µm, a massive increase in ionization efficiency and sensitivity can be achieved.[61] Downsides to this setup are reduced retention stability of analytes, broader peak shapes, and of course a massive increase in gradient time with a realistic minimum of 30 minutes when compared to normal flow systems.

2.5.2 Enrichment of Phosphorylated Peptides *via* TiO$_2$ MOAC, Fe-IMAC and Antibody-based Enrichment Strategies

In order to selectively enrich phosphorylated peptide species and increase sensitivity towards them, different phosphopeptide enrichment strategies can be applied. Metal-based strategies include the immobilized metal oxide affinity chromatography (IMAC) and the metal oxide affinity chromatography (MOAC).[62] In IMAC, the oldest affinity chromatography-based phosphopeptide enrichment technique[63], chelators are used to non-covalently immobilize metal ions on a solid matrix such as beads and the enrichment mechanism is based on the interaction between the metal ions and the phosphate groups.[62]

The first metal ions implemented in IMAC included Fe^{3+} and Ga^{3+} in combination with chelating groups such as nitriloacetate (NTA) and iminoadiacetate (IDA).[64] As these IMAC materials exhibited affinity to acidic non-phosphorylated peptides, the provided insufficient specificity led to the development of novel IMAC materials.[65,66] Novel, highly phosphopeptide-selective IMAC materials include for example Ti^{4+} with a phosphonate residue for immobilization[63], or Ti^{4+} or Zr^{4+} metal ions in combination with poly(GMA-co-TMPTMA), a flexible linker.[65,66] As acidic, basic, mono- and multi- phosphorylated peptides all exhibit different binding affinities to metal ions, combining different metal ion types into a sequential workflow could also improve phosphopeptide enrichment efficiency.[62]

In MOAC, phosphopeptides are selectively enriched by metal oxides as phosphopeptides exhibit a high affinity to them and bind to their surface in a bidentate mode. The mechanism is based on Lewis acid-base interactions and each metal oxide exhibits a different selectivity for different types of phosphopeptides based on their Lewis acidity.[67] One of the most commonly used metal oxides in MOAC is TiO_2, but the range of MOAC materials also includes Fe_3O_4, ZrO_2, SnO_2, Ga_2O_3, HfO_2 and $Al(OH)_3$. While ZrO_2 shows a high selectivity for monophosphorylated peptides, Fe_3O_4 preferably binds to multiphosphorylated peptides. In general, MOAC based phosphopeptide enrichment workflows are usually more robust than those based on IMAC as MOAC materials are less likely to interact with buffers and detergents.[62]

Another alternative is the use of composite materials such as TiO_2-ZrO_2 microspheres which show enhanced phosphopeptide enrichment specificity compared to TiO_2.[68] Due to its good commercial availability and high enrichment specificity, TiO_2 remains the most widely used MOAC material.[67] MOAC based workflows implementing TiO_2 can also be improved by optimizing the experimental conditions, for example performing the enrichment at a low pH protonates the acidic residues of aspartic and glutamic acid, reducing their affinity to IMAC and MOAC materials.[62] Another type of phosphopeptide enrichment method is the highly efficient and specific antibody-based strategy termed immunoprecipitation. Immunoprecipitation based phopshopeptide enrichment is mainly used in order to increase sensitivity towards tyrosine-phosphorylated species. As phosphorylation of tyrosine residues occurs at substoichiometric level, tyrosine-phosphorylated peptides are usually underrepresented in metal-based enrichment workflows.[62,69] The antibody-based enrichment of tyrosine-phosphorylated peptides is also limited by the required amount of protein/peptide-input, as appropriate input is in the mg range.[63] As immunoprecipitation approaches are cost-intensive and the availability of specific antibodies is limited, this method is predominantly employed for specific research questions and MOAC and IMAC still remain most commonly used phosphopeptide enrichment strategies.[62,63,69]

2.6 Bioinformatical analysis strategies for proteomics

The analysis of data *via* bioinformatical tools is an essential requirement of modern MS-based "Omics" experiments. Hardware improvements primarily focused on the enhancement of sensitivity but also acquisition speed, resulting in previously unseen data density and complexity.[70] Confronted with this new obstacle, advances in bioinformatic approaches had to develop solutions for comprehensive and automated analysis of data in a parallelized fashion. One fundamental steppingstone to allow automated algorithms to become a viable option for data analysis were the establishment of comprehensive databases. The Human Proteome Project[19] laid the foundation with databases like UniProt (www.uniprot.org) or mass spectrometry focused repositories like PeptideAtlas, ProteomeXchange or Protein Identification Database (PRIDE) allowing high confident mapping of the human proteome. At the beginning of the last decade, the development of search algorithms such as Andromeda, integrated into the MaxQuant software suite, accelerated proteomics research by enabling end users with limited bioinformatical knowledge to perform calculations needed for the interpretation of complex spectra.[71,72]

2.6.1 Interpretation of Fragmentation Spectra and Peptide Spectral Matching

MS^2, MS/MS or tandem mass spectrometry describes the measurement of fragment ions deriving from a previously isolated precursor ion. This additional information can be used to further investigate molecule properties which would otherwise not be accessible. When looking at metabolites, fragmentation spectra can help with structural elucidation and exact identification.[73] Dealing with tryptic peptides, a certain precursor mass can already inform about possible peptides, but the exact composition (order of amino acids) and eventual occurrence of PTMs can only be elucidated *via* peptide fragmentation. Different ion activation techniques such as collisional induced dissociation (CID), higher-energy collisional dissociation (HCD) or electron transfer dissociation (ETD) can be used to induce fragmentation of the analyte. Depending on the molecule of interests' chemical properties, different activation techniques can result e.g., in the conservation of PTMs on the fragment ion (ETD) or the complete fragmentation of more stable compounds (HCD).[26,74] ***Figure 8*** illustrates typical peptide backbone fragmentation routes shown on a dipeptide, annotated according to the Roepstorff–Fohlmann–Biemann nomenclature.[75,76] As the fragmentation process of peptides is often induced *via* collision with residual gas, the cleavage occurs at the most energetically favourable bond, the amide bond, resulting in b and y fragments. Typically, a doubly positive charged tryptic peptide will fragment into singly charged b- and y-ions. Depending on ion activation types, additional "satellite" fragment ions with loss of NH_3 or H_2O as well as immonium ions can occur.[77]
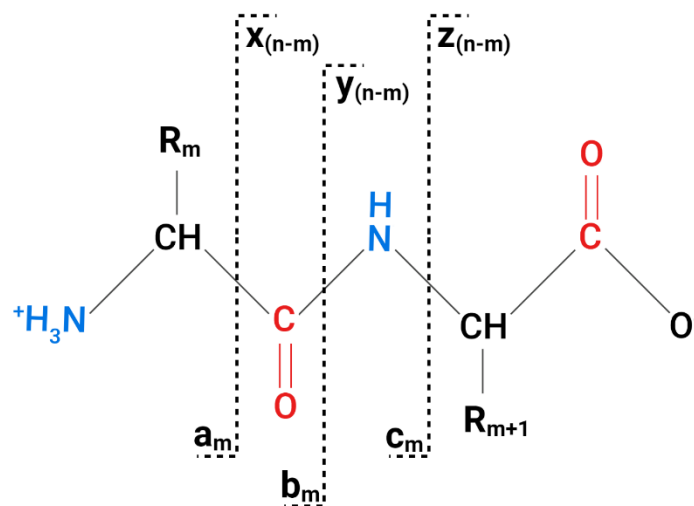
Figure 8 | Schematic overview of different peptide fragmentation routes. Positions of fragmentation are labelled according to the Roepstorff–Fohlmann–Biemann nomenclature. Fragments a, b, and c are counted from their respective position of their adjacent amino acid (m), whereas fragments x, y; and z are annotated in a counter wise fashion, subtracting the number of the most adjacent amino acid from the total number of amino acids in the peptide (n-m). Figure was adapted from Steen et al.[77]

The resulting fragment spectra can then be matched to *in silico* generated fragment databases which contain, depending on the settings applied to the dataset, all possible combinations of delta masses of fragments mapped to intact precursor masses. The process of aligning and matching experimental spectra with *in silico* generated spectra is called "peptide spectra matching" resulting in PSMs. Factors such as isolation efficiency, mass accuracy or not considered PTMs can influence the quality of matching. To estimate the quality of a dataset, PSMs must be scored and cut-offs must be defined to avoid false positive peptide identifications.[78]

2.6.2 False Discovery Rate

When dealing with proteomics data, one of the first obstacles can be to distinguish true peptide identifications from misinformed hits which can lead to false protein assignments. A typical proteomics experiment can consist of more than 10^6 spectra per experiment, making it highly probable that false assignments will happen by chance.[79] In addition to high data density, factors such as interfering background noise and experimental variations can, especially in the case of low abundant signals, lead to additional wrong assignments which can ultimately lead to an unacceptable dilution of data quality.[80] Algorithms like Andromeda or Mascot[81] employ a probability-based ranking and scoring of PSMs, enabling the calculation of p-values for single observations. Although these scoring algorithms only give arbitrary values as scores, the rule of higher scores as better match can be formulated. To control for unwanted false positive assignments, mathematical models had to be developed to enable the calculation of false discovery rates, as proposed by Benjamini and Hochberg in 1995.[82] The application of false discovery rates (FDR) to proteomics data was made possible through the introduction of decoy

databases, for the first time allowing an adequate correction for multiple observations by comparison of PSM scores.[83] Decoy databases consist of non-naturally occurring peptide sequences generated *via* reversing, shuffling or sequence randomizations of true target databases.
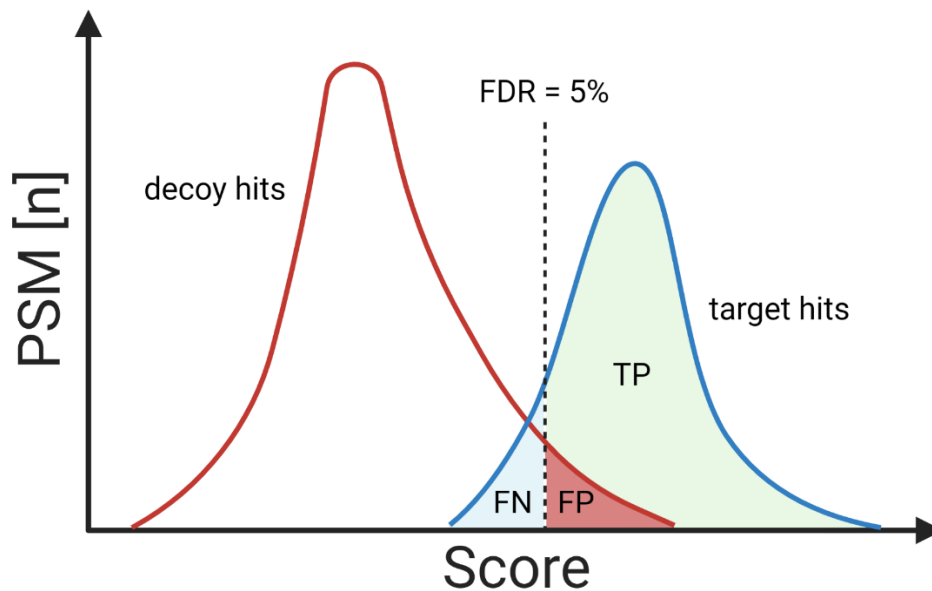

Figure 9 | Visualization of FDR calculation for proteomics data. X-axis is showing ascending search algorithm score for certain PSMs, Y-axis is showing the frequency (number) of PSMs at a given score. An FDR of 5% is indicated via the dashed ling. On the left side, hits that are generated against a decoy database are mapped in red. Target hits with intrinsic higher score are mapped via blue distribution. True-positive (TP), false-positive (FP) and false-negative (FN) hits are indicated via the colored areas under the curves in green, red and turquoise, respectively.

As depicted in *Figure 9* the FDR is dependent on the quality, hence score, of target and decoy hits. Experimental data is searched against both target and decoy database and generated hits are assigned accordingly. Normally, high scoring decoy hits can overlap with low scoring target hits. Setting the FDR to 5% for example, relates to an acceptance of 5% false-positive hits (red) in our final dataset which should ideally only consist of true-positive hits (green). In order to not lose to many target hits to a false-negative hit (turquoise) assignment, the cut-off must be chosen carefully. An acceptance rate of 0% false-positive hits would unproportionally diminish the quality of data as the rate of false-negative hit assignments would escalate.

2.6.3 Data Analysis Strategies for Protein Phosphorylation

The process of reversible protein phosphorylation plays a central role in many physiological processes and can lead to changes in protein conformation, enzymatic activity, or surface charge.[84] As shown in *Figure 10*, the highly dynamic process of phosphorylation and dephosphorylation of certain amino acids like serine, threonine or tyrosine is catalysed *via* kinases and phosphates employing adenosine 5'-triphosphate (ATP) as substrate.[85] Taking the sub-stoichiometric and highly dynamic nature together with incomplete annotation of phosphorylation sites into consideration, phosphoproteomics could be coined as one of the

most challenging mass spectrometry related post-genomic research fields.[41,44] Identifying main signalling networks and the interconnection between them can aid the efforts to tackle diseases dependent on aberrant signalling cascades (*Figure 10*). In order to understand those signalling events, the proteomics community developed tools to probe this low-abundant and highly dynamic proteoforms. Combining standard bottom-up approaches with subsequent enrichment of phosphorylated peptide species employing for example metal oxide affinity chromatography allowed an in-depth profiling.[39,40,86-88]
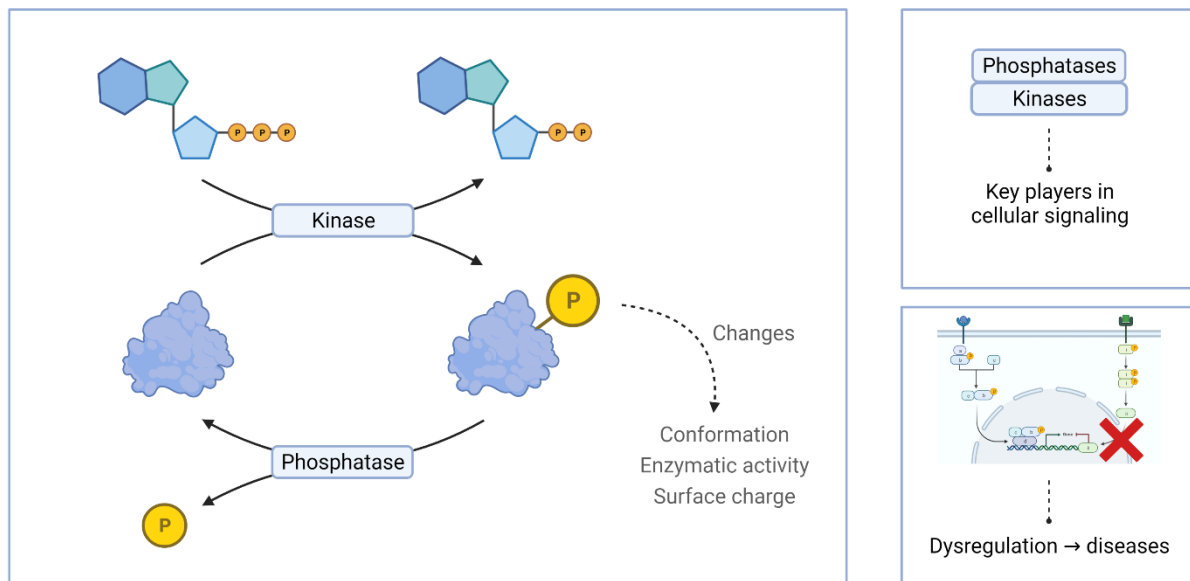
Figure 10 | Simplified key points addressing protein phosphorylation and de-phosphorylation via kinases and phosphatases. Dysregulation of kinase and phosphatase activity can strongly influence physiological processes possibly leading to diseases.

Data analysis of differentially phosphorylated substrates from proteomics experiments may allow a preliminary view on perturbations. To understand underlying biological processes, an indirect analysis of kinase activity through the elucidation of probable kinase substrate relations *via* investigation of binding domain specificity is pivotal.[89,90] Exemplified by phosphotyrosine signalling, the concept of writer/reader/eraser is critical for the understanding of intricate signalling networks.[91] Taking this one step further, it must be mentioned that not only the kinase activity per se, but also the pattern of multiple phosphosites in near vicinity to each other can influence binding affinities and create binding pockets for protein interactions.[92] As already mentioned in chapter 2.2.3, to our current understanding, a disproportionally small number of kinases is responsible, or at least mapped, for the bulk of phosphorylated substrates introducing the 80:20 rule. This bias is currently limiting most of the approaches trying to causally link kinase activation/function to the observed data. To mitigate these bias effects, tools were developed to, either rank kinase activity not solely on substrate overrepresentation but also perturbations of those, or completely rethink the mapping of established kinase-substrate relations and implement additional criteria. Kinase-substrate enrichment analysis (KSEA) leverages a peptide-centric analysis approach focusing on perturbations observed in

case-control scenario and allows a generalized comparison of positive or negative regulation of kinase activity.[93] A similar but more elaborate approach to investigate phosphoproteome-wide effects can be performed *via* the PhosR analysis pipeline, aiming to tackle bioinformatical challenges regarding the missing value problem and often observed batch variations.[93-95] Highly dynamic phosphorylation events of low abundant peptide species create, in addition to above mentioned challenges, an additional bioanalytical challenge which must be addressed later in the bioinformatic analysis by adapted data normalization, missing value imputation and batch correction.[96] In addition to peptide-centric analysis of the data, PhosR also enables a protein-centric analysis aiding a causal interpretation by creating protein modules, which bin proteins showing similar phosphorylation dynamics.[95]

2.6.4 Correlation and Causation

Correlation is a statistical entity describing the association between two independent variables which covary, meaning if one variable is changing the other also changes, leading to positive or negative correlation. In contrast to correlation, causation implies that a change of one variable brings also change to another, linked variable.[97] An often-underappreciated aspect of bioanalytical sciences is the discrimination between correlation and cause-and-effect relations. As Buchanan stated correctly: "Not only does correlation not imply causality, but lack of correlation needn't imply a lack of causality either"[98].
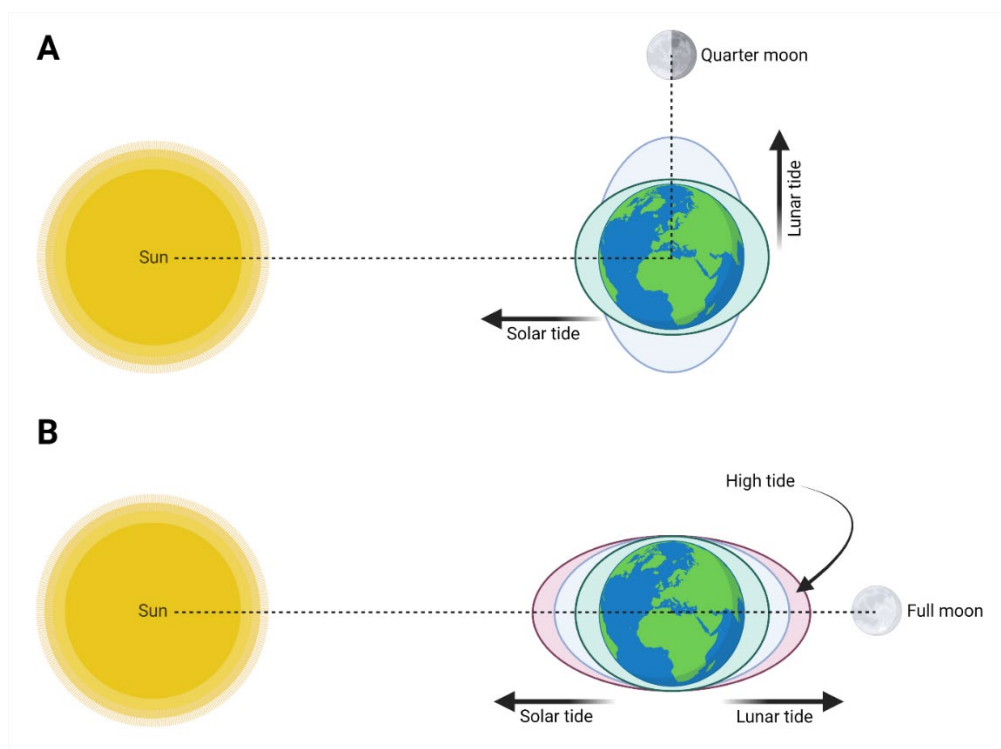
Figure 11 | Correlation and causation differentiation demonstrated via the astronomical example of tidal heights and the illumination of the lunar surface.

Showing an example from astronomy in *Figure 11*, it demonstrates that the understanding for observed bodies (in this case variables) and their influence on each other as well as surrounding factors is necessary to distinguish between simple correlation and causal reasoning. The simplified illustration only takes the influence of sun and moon into account, showing that, in theory, one could attribute the height of tides to the lunar surface brightness as tides are higher at full moon than compared to e.g., quarter moon. This assumption would suggest that the correlation of mentioned variables would be predictive and thus should possibly be causative. Of course, this correlation only holds true if local maxima are considered in the measurement, as seen in *Figure 12*. Here it seems that the local maxima and surrounding slopes (green box) show a good fit and positive correlation. But looking beyond the observed areas, one can see an anti-correlation clearly showing that lunar surface brightness cannot be directly responsible for tidal heights, but rather the position of celestial bodies in respect to earth.
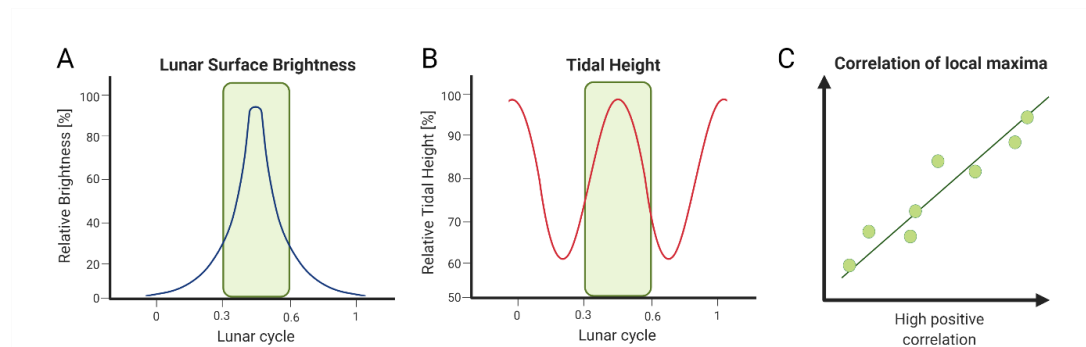
Figure 12 | Comparison of measured variables, lunar surface brightness and tidal height, showing high positive correlation when only observed around their local maxima.

Even in ancient Rome, philosopher Seneca describes in an essay called "De Providentia" an undisputable correlation between the position of the moon and observed tidal heights. Through the centuries, many theories were postulated to be dismissed later. Even famous thinkers and early scientists such as Galileo Galilei, Newton, Bernoulli, or Laplace tried to mathematically predict exact tidal heights and times but only had limited success. It took scientists a few hundred years to arrive at the concept of harmonic analysis with the usage of Fourier transformations to develop the concept of tide-generating potential, distinguishing over 300 frequencies which allow a prediction of tides.[99] This example should demonstrate the importance of multi-dimensionality in the analysis of complex systems. In most mass spectrometry based "omics" experiments, the combination of low number of samples with a multitude of observed variables can create potentially problematic data artefacts or randomly distributed differences leading to significant correlations which may have no direct relation to causal changes. The combination of multiple omics datasets as well as the in-depth elucidation of phosphorylation events can promote these efforts towards a causality driven analysis of data.

2.7 Research Justification

The aim of this thesis is to tackle challenges associated with conventional approaches applied in proteomics or even multi-omics studies. Focusing on post-genomic effector molecules and their influence on complex (patho-) physiological processes, it was of utmost importance to demonstrate the power of combination of multiple complementary mass spectrometry based methods to aid the understanding of disease development and progression, wound-healing processes, influence of toxins on cellular integrity, profiling of ligand-dependent signalling cascades in malignant diseases and last but not least, the elucidation of clinically relevant autoimmune disease signatures in different stages *via* multi-omic profiling.

Today's most prevalent "Omics" research fields cover the areas of the genome, transcriptome, proteome and most recently also metabolome. Data integration and combined interpretation of multiple Omics datasets from distinct samples is currently one of the most challenging tasks.[100] The generation of high-throughput in-depth datasets created, in theory, the possibility to monitor systemic alterations of individual molecule classes, and to infer their function by causal reasoning. Early studies were based on correlative observations, many researchers know strive to strengthen their observations with state-of-the-art approaches combining multiple bioanalytical approaches.[101,102] A big focus in the bioanalytical research community lies on the improvement of in-depth analysis of individual molecule classes, improving sensitivity and overall quality of datasets [103], but an often-overseen problem is the sheer complexity of possible variables in each subset of molecule classes resulting in datasets which are difficult to interpret in a causal setting. These generated datasets bring additional caveats, such as a higher dimensionality which may be difficult to comprehend and monitor in an unbiased fashion. Illustrated in *Figure 13*, one can see an example of oversimplification of higher-dimensional datasets and its potential consequences. Simplification, and therefore reduction of dimensionality can be a helpful tool to comprehend and communicate complex data, trying to create coherent and consistent observations. These observations ideally fit into binary systems only allowing one "truth", potentially ignoring alternative interpretations when looking from a wider or different perspective and therefore distorting, often unconsciously, possible outcomes.
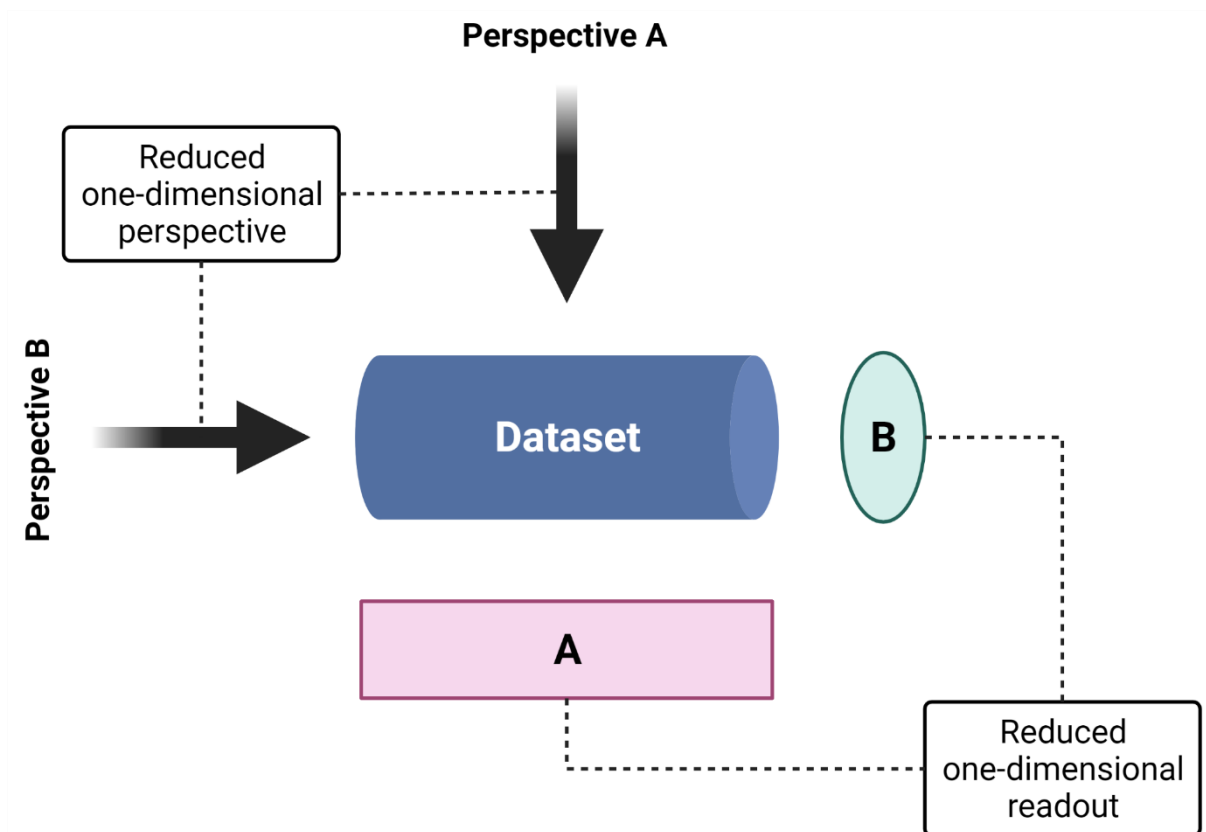
Figure 13 | Dimensionality reduction of a higher-dimensional datasets. Two distinct perspectives resulting in two different (reduced) readouts creating a potential distortion of the measured datasets.

Interestingly, research of cancer and related diseases is most commonly structured around genetics, even today this scheme does not seem to have changed. Voices from researchers with leading opinions promote the idea that cancer is primarily a signalling disease.[104] When looking at cancer research historically, genetics delivered astonishing novel insights into tumour biology when biochemistry and cell biology simply could not keep up with the pace.[105] Even state-of-the-art MS-based methods cannot, to this point in time, keep up with the sensitivity and throughput of methods in the geneticist's toolbox. Nevertheless, one must point out, that not all questions can be answered by genetics alone, as demonstrated by research on the most famous tumour repressor protein p53. The five most commonly found mutations in *TP53* are not determining a strong loss-of-function phenotype but arise in tumour tissues through favourable mutagenic conditions which drive these mutations.[106]

Applying said methods, we aimed to investigate (patho-) physiological processes from a post-genomic point-of-view with state-of-the-art technology and combine multiple complementary datasets to strengthen the analytical power of our analysis.

Focusing on effector molecules, namely proteins, metabolites and lipids, questions such as disease progression and metabolic impact of stromal tissue in multiple myeloma could be partially answered, whereas genetic screening allowed a general diagnosis and categorization into sub-types.[3] Combinations of MS-based screenings with transcriptomics allowed the characterization of wound-healing signatures triggered by antiseptic molecules[107], or elucidate

intricate receptor signalling cascades *via* phosphoproteomics which are relevant for disease escalation and metastatic potential.[108] This analysis strategies can give vital information about clinical status and elucidate disease mechanisms of patients with autoimmune diseases with no obvious underlying genetic driver. Complementary biomarkers from different molecule classes can help to identify driving pathophysiological processes and possible interventions in order to achieve not only phenotypical but also remission on a molecular level.[4]

2.8 Abbreviations

2D – two dimensional, **AA** – amino acid, **CCS** – collisional cross section, **CID** – collisional induced dissociation, **DC** – direct current, **EGFL8** – epidermal growth factor-like protein 8, **ESI** – electrospray ionization, **FDR** – false discovery rate, **GC** – gas chromatography, **GN** – ganglioneuromas, **IDA** – iminoadiacetate, **IMAC** – immobilized metal affinity chromatography, **KSEA** – kinase substrate enrichment analysis, **LC** – liquid chromatography, **LFQ** – label free quantification, **m/z** – mass-to-charge ratio, **MALDI** - matrix-assisted laser desorption/ionisation, **MAPK** – mitogen-activated protein kinase, **MM** – multiple myeloma, **MOAC** – metal oxide affinity chromatography, **MS** – mass spectrometry, **MS2 (MS/MS)** – fragmentation mass spectrum, **NB** – neuroblastoma, **NTA** – nitriloacetate, **OCT** – octenidine, **PAGE** – polyacrylamide gel electrophoresis, **PSM** – peptide spectral match, **PTM** – post translational modification, **RP** – reversed phase, **RT** – retention time, **SC** – schwann cells, **SDS** – sodium dodecyl sulfate, **SILAC** - stable isotope labeling by amino acids in cell culture, **TIMS** – trapped ion mobility separation, **TMT** – tandem mass tag, **TOF** – time-of-flight, **UC** – ulcerative colitis

3 References

1   Ahmed, Z. Multi-omics strategies for personalized and predictive medicine: past, current, and future translational opportunities. *Emerg Top Life Sci* **6**, 215-225, doi:10.1042/ETLS20210244 (2022).
2   Geyer, P. E. *et al.* Plasma Proteome Profiling to Assess Human Health and Disease. *Cell Syst* **2**, 185-195, doi:10.1016/j.cels.2016.02.015 (2016).
3   Janker, L. *et al.* Metabolic, Anti-apoptotic and Immune Evasion Strategies of Primary Human Myeloma Cells Indicate Adaptations to Hypoxia. *Mol Cell Proteomics* **18**, 936-953, doi:10.1074/mcp.RA119.001390 (2019).
4   Janker, L. *et al.* Multi-omics empowered deep phenotyping of ulcerative colitis. *medRxiv*, 2022.2005.2025.22275502, doi:10.1101/2022.05.25.22275502 (2022).
5   Oxford University Press.   (Oxford University Press, Oxford, England, 2002).
6   Winkler, H. *Verbreitung und Ursache der Parthenogenesis im Pflanzen- und Tierreiche*. (G. FIscher, 1920).
7   Crick, F. H. On protein synthesis. *Symp Soc Exp Biol* **12**, 138-163 (1958).
8   Gierer, A. & Schramm, G. Infectivity of ribonucleic acid from tobacco mosaic virus. *Nature* **177**, 702-703, doi:10.1038/177702a0 (1956).
9   Fraenkel-Conrat, H. THE ROLE OF THE NUCLEIC ACID IN THE RECONSTITUTION OF ACTIVE TOBACCO MOSAIC VIRUS1. *Journal of the American Chemical Society* **78**, 882-883, doi:10.1021/ja01585a055 (1956).
10   Watson, J. D. & Crick, F. H. Molecular structure of nucleic acids; a structure for deoxyribose nucleic acid. *Nature* **171**, 737-738, doi:10.1038/171737a0 (1953).
11   Franklin, R. E. & Gosling, R. G. Molecular configuration in sodium thymonucleate. *Nature* **171**, 740-741, doi:10.1038/171740a0 (1953).
12   Wilkins, M. H., Stokes, A. R. & Wilson, H. R. Molecular structure of deoxypentose nucleic acids. *Nature* **171**, 738-740, doi:10.1038/171738a0 (1953).
13   Sanger, F. & Thompson, E. O. The amino-acid sequence in the glycyl chain of insulin. II. The investigation of peptides from enzymic hydrolysates. *Biochem J* **53**, 366-374, doi:10.1042/bj0530366 (1953).
14   Sanger, F. & Thompson, E. O. The amino-acid sequence in the glycyl chain of insulin. I. The identification of lower peptides from partial hydrolysates. *Biochem J* **53**, 353-366, doi:10.1042/bj0530353 (1953).
15   Sanger, F. & Coulson, A. R. A rapid method for determining sequences in DNA by primed synthesis with DNA polymerase. *J Mol Biol* **94**, 441-448, doi:10.1016/0022-2836(75)90213-2 (1975).
16   Venter, J. C. *et al.* The sequence of the human genome. *Science* **291**, 1304-1351, doi:10.1126/science.1058040 (2001).
17   Lander, E. S. *et al.* Initial sequencing and analysis of the human genome. *Nature* **409**, 860-921, doi:10.1038/35057062 (2001).
18   Klein, R. J. *et al.* Complement factor H polymorphism in age-related macular degeneration. *Science* **308**, 385-389, doi:10.1126/science.1109557 (2005).
19   Omenn, G. S. *et al.* Research on the Human Proteome Reaches a Major Milestone: >90% of Predicted Human Proteins Now Credibly Detected, According to the HUPO Human Proteome Project. *J Proteome Res* **19**, 4735-4746, doi:10.1021/acs.jproteome.0c00485 (2020).
20   Velculescu, V. E., Zhang, L., Vogelstein, B. & Kinzler, K. W. Serial analysis of gene expression. *Science* **270**, 484-487, doi:10.1126/science.270.5235.484 (1995).
21   Wang, Z., Gerstein, M. & Snyder, M. RNA-Seq: a revolutionary tool for transcriptomics. *Nat Rev Genet* **10**, 57-63, doi:10.1038/nrg2484 (2009).
22   Ozsolak, F. & Milos, P. M. RNA sequencing: advances, challenges and opportunities. *Nat Rev Genet* **12**, 87-98, doi:10.1038/nrg2934 (2011).
23   Nelson, N. J. Microarrays have arrived: gene expression tool matures. *J Natl Cancer Inst* **93**, 492-494, doi:10.1093/jnci/93.7.492 (2001).

24   Edman, P. A method for the determination of amino acid sequence in peptides. *Arch Biochem* **22**, 475 (1949).

25   Fenn, J. B., Mann, M., Meng, C. K., Wong, S. F. & Whitehouse, C. M. Electrospray ionization for mass spectrometry of large biomolecules. *Science* **246**, 64-71, doi:10.1126/science.2675315 (1989).

26   Aebersold, R. & Mann, M. Mass spectrometry-based proteomics. *Nature* **422**, 198-207, doi:10.1038/nature01511 (2003).

27   Dalgliesh, C. E., Horning, E. C., Horning, M. G., Knox, K. L. & Yarger, K. A gas-liquid-chromatographic procedure for separating a wide range of metabolites occuring in urine or tissue extracts. *Biochem J* **101**, 792-810, doi:10.1042/bj1010792 (1966).

28   Flissi, A. *et al.* Norine: update of the nonribosomal peptide resource. *Nucleic Acids Res* **48**, D465-D469, doi:10.1093/nar/gkz1000 (2020).

29   Bock, A., Forchhammer, K., Heider, J. & Baron, C. Selenoprotein synthesis: an expansion of the genetic code. *Trends Biochem Sci* **16**, 463-467, doi:10.1016/0968-0004(91)90180-4 (1991).

30   Aebersold, R. *et al.* How many human proteoforms are there? *Nat Chem Biol* **14**, 206-214, doi:10.1038/nchembio.2576 (2018).

31   Bowden, J. A. *et al.* Harmonizing lipidomics: NIST interlaboratory comparison exercise for lipidomics using SRM 1950-Metabolites in Frozen Human Plasma. *J Lipid Res* **58**, 2275-2288, doi:10.1194/jlr.M079012 (2017).

32   Wishart, D. S. *et al.* HMDB 4.0: the human metabolome database for 2018. *Nucleic Acids Res* **46**, D608-D617, doi:10.1093/nar/gkx1089 (2018).

33   Smith, L. M., Kelleher, N. L. & Consortium for Top Down, P. Proteoform: a single term describing protein complexity. *Nat Methods* **10**, 186-187, doi:10.1038/nmeth.2369 (2013).

34   Dang, X. *et al.* The first pilot project of the consortium for top-down proteomics: a status report. *Proteomics* **14**, 1130-1140, doi:10.1002/pmic.201300438 (2014).

35   Ong, S. E. *et al.* Stable isotope labeling by amino acids in cell culture, SILAC, as a simple and accurate approach to expression proteomics. *Mol Cell Proteomics* **1**, 376-386, doi:10.1074/mcp.m200025-mcp200 (2002).

36   Thompson, A. *et al.* Tandem mass tags: a novel quantification strategy for comparative analysis of complex protein mixtures by MS/MS. *Anal Chem* **75**, 1895-1904, doi:10.1021/ac0262560 (2003).

37   Ow, S. Y., Salim, M., Noirel, J., Evans, C. & Wright, P. C. Minimising iTRAQ ratio compression through understanding LC-MS elution dependence and high-resolution HILIC fractionation. *Proteomics* **11**, 2341-2346, doi:10.1002/pmic.201000752 (2011).

38   Savitski, M. M. *et al.* Measuring and managing ratio compression for accurate iTRAQ/TMT quantification. *J Proteome Res* **12**, 3586-3598, doi:10.1021/pr400098r (2013).

39   Ficarro, S. B. *et al.* Phosphoproteome analysis by mass spectrometry and its application to Saccharomyces cerevisiae. *Nat Biotechnol* **20**, 301-305, doi:10.1038/nbt0302-301 (2002).

40   Beausoleil, S. A. *et al.* Large-scale characterization of HeLa cell nuclear phosphoproteins. *Proc Natl Acad Sci U S A* **101**, 12130-12135, doi:10.1073/pnas.0404720101 (2004).

41   Olsen, J. V. *et al.* Global, in vivo, and site-specific phosphorylation dynamics in signaling networks. *Cell* **127**, 635-648, doi:10.1016/j.cell.2006.09.026 (2006).

42   Humphrey, S. J., James, D. E. & Mann, M. Protein Phosphorylation: A Major Switch Mechanism for Metabolic Regulation. *Trends Endocrinol Metab* **26**, 676-687, doi:10.1016/j.tem.2015.09.013 (2015).

43   Bodenmiller, B. *et al.* Phosphoproteomic analysis reveals interconnected system-wide responses to perturbations of kinases and phosphatases in yeast. *Sci Signal* **3**, rs4, doi:10.1126/scisignal.2001182 (2010).

44   Needham, E. J., Parker, B. L., Burykin, T., James, D. E. & Humphrey, S. J. Illuminating the dark phosphoproteome. *Sci Signal* **12**, doi:10.1126/scisignal.aau8645 (2019).

45 Brunmair, J. *et al.* Metabolic phenotyping of tear fluid as a prognostic tool for personalised medicine exemplified by T2DM patients. *EPMA J* **13**, 107-123, doi:10.1007/s13167-022-00272-7 (2022).

46 Brunmair, J. *et al.* Metabo-tip: a metabolomics platform for lifestyle monitoring supporting the development of novel strategies in predictive, preventive and personalised medicine. *EPMA J* **12**, 141-153, doi:10.1007/s13167-021-00241-6 (2021).

47 Brunmair, J. *et al.* Finger sweat analysis enables short interval metabolic biomonitoring in humans. *Nat Commun* **12**, 5993, doi:10.1038/s41467-021-26245-4 (2021).

48 Reichl, B. *et al.* Determination of a Tumor-Promoting Microenvironment in Recurrent Medulloblastoma: A Multi-Omics Study of Cerebrospinal Fluid. *Cancers (Basel)* **12**, doi:10.3390/cancers12061350 (2020).

49 Makarov, A. Electrostatic axially harmonic orbital trapping: a high-performance technique of mass analysis. *Anal Chem* **72**, 1156-1162, doi:10.1021/ac991131p (2000).

50 Lovric, J. *Introducing proteomics : from concepts to sample separation, mass spectrometry and data analysis.* (Wiley-Blackwell, 2011).

51 Harvey, D. J. in *Encyclopedia of Analytical Science (Third Edition)* (eds Paul Worsfold, Colin Poole, Alan Townshend, & Manuel Miró) 473-482 (Academic Press, 2019).

52 Meier, F. *et al.* Online Parallel Accumulation-Serial Fragmentation (PASEF) with a Novel Trapped Ion Mobility Mass Spectrometer. *Mol Cell Proteomics* **17**, 2534-2545, doi:10.1074/mcp.TIR118.000900 (2018).

53 Fernandez-Lima, F. A., Kaplan, D. A. & Park, M. A. Note: Integration of trapped ion mobility spectrometry with mass spectrometry. *Rev Sci Instrum* **82**, 126106, doi:10.1063/1.3665933 (2011).

54 Ridgeway, M. E., Lubeck, M., Jordens, J., Mann, M. & Park, M. A. Trapped ion mobility spectrometry: A short review. *International Journal of Mass Spectrometry* **425**, 22-35, doi:10.1016/j.ijms.2018.01.006 (2018).

55 Meier, F. *et al.* Parallel Accumulation-Serial Fragmentation (PASEF): Multiplying Sequencing Speed and Sensitivity by Synchronized Scans in a Trapped Ion Mobility Device. *J Proteome Res* **14**, 5378-5387, doi:10.1021/acs.jproteome.5b00932 (2015).

56 Bortel, P. Evaluation of phosphopeptide enrichment strategies for perturbation studies on in vitro systems employing ion mobility mass spectrometry. doi:10.25365/thesis.63429 (2020).

57 Taylor, G. I. Disintegration of water drops in an electric field. *Proceedings of the Royal Society of London. Series A. Mathematical and Physical Sciences* **280**, 383-397, doi:doi:10.1098/rspa.1964.0151 (1964).

58 Matthiesen, R. & Bunkenborg, J. Introduction to Mass Spectrometry-Based Proteomics. *Methods Mol Biol* **2051**, 1-58, doi:10.1007/978-1-4939-9744-2_1 (2020).

59 Molnar, I. & Horvath, C. Reverse-phase chromatography of polar biological substances: separation of catechol compounds by high-performance liquid chromatography. *Clin Chem* **22**, 1497-1502 (1976).

60 Gritti, F. & Guiochon, G. Comparative study of the performance of columns packed with several new fine silica particles. Would the external roughness of the particles affect column properties? *J Chromatogr A* **1166**, 30-46, doi:10.1016/j.chroma.2007.06.064 (2007).

61 Wilm, M. *et al.* Femtomole sequencing of proteins from polyacrylamide gels by nano-electrospray mass spectrometry. *Nature* **379**, 466-469, doi:10.1038/379466a0 (1996).

62 Li, X.-S., Yuan, B.-F. & Feng, Y.-Q. Recent advances in phosphopeptide enrichment: Strategies and techniques. *TrAC Trends in Analytical Chemistry* **78**, 70-83, doi:10.1016/j.trac.2015.11.001 (2016).

63 von Stechow, L. Phospho-Proteomics - Methods & Protocols. *Methods Mol Biol* **1355**, v, doi:10.1007/978-1-4939-3049-4 (2016).

64 Posewitz, M. C. & Tempst, P. Immobilized gallium(III) affinity chromatography of phosphopeptides. *Anal Chem* **71**, 2883-2892, doi:10.1021/ac981409y (1999).

65   Zhou, H. *et al.* Robust phosphoproteome enrichment using monodisperse microsphere-based immobilized titanium (IV) ion affinity chromatography. *Nat Protoc* **8**, 461-480, doi:10.1038/nprot.2013.010 (2013).

66   Feng, S. *et al.* Immobilized zirconium ion affinity chromatography for specific enrichment of phosphopeptides in phosphoproteome analysis. *Mol Cell Proteomics* **6**, 1656-1665, doi:10.1074/mcp.T600071-MCP200 (2007).

67   Leitner, A. Phosphopeptide enrichment using metal oxide affinity chromatography. *TrAC Trends in Analytical Chemistry* **29**, 177-185, doi:10.1016/j.trac.2009.08.007 (2010).

68   Yan, J., Li, X., Cheng, S., Ke, Y. & Liang, X. Facile synthesis of titania-zirconia monodisperse microspheres and application for phosphopeptides enrichment. *Chem Commun (Camb)*, 2929-2931, doi:10.1039/b901424a (2009).

69   Fila, J. & Honys, D. Enrichment techniques employed in phosphoproteomics. *Amino Acids* **43**, 1025-1047, doi:10.1007/s00726-011-1111-z (2012).

70   Richards, A. L., Merrill, A. E. & Coon, J. J. Proteome sequencing goes deep. *Curr Opin Chem Biol* **24**, 11-17, doi:10.1016/j.cbpa.2014.10.017 (2015).

71   Cox, J. *et al.* Andromeda: a peptide search engine integrated into the MaxQuant environment. *J Proteome Res* **10**, 1794-1805, doi:10.1021/pr101065j (2011).

72   Cox, J. & Mann, M. MaxQuant enables high peptide identification rates, individualized p.p.b.-range mass accuracies and proteome-wide protein quantification. *Nat Biotechnol* **26**, 1367-1372, doi:10.1038/nbt.1511 (2008).

73   Xue, J., Guijas, C., Benton, H. P., Warth, B. & Siuzdak, G. METLIN MS(2) molecular standards database: a broad chemical and biological resource. *Nat Methods* **17**, 953-954, doi:10.1038/s41592-020-0942-5 (2020).

74   Frese, C. K. *et al.* Improved peptide identification by targeted fragmentation using CID, HCD and ETD on an LTQ-Orbitrap Velos. *J Proteome Res* **10**, 2377-2388, doi:10.1021/pr1011729 (2011).

75   Roepstorff, P. & Fohlman, J. Proposal for a common nomenclature for sequence ions in mass spectra of peptides. *Biomed Mass Spectrom* **11**, 601, doi:10.1002/bms.1200111109 (1984).

76   Biemann, K. Mass spectrometry of peptides and proteins. *Annu Rev Biochem* **61**, 977-1010, doi:10.1146/annurev.bi.61.070192.004553 (1992).

77   Steen, H. & Mann, M. The ABC's (and XYZ's) of peptide sequencing. *Nat Rev Mol Cell Biol* **5**, 699-711, doi:10.1038/nrm1468 (2004).

78   Hubler, S. L. *et al.* Challenges in Peptide-Spectrum Matching: A Robust and Reproducible Statistical Framework for Removing Low-Accuracy, High-Scoring Hits. *J Proteome Res* **19**, 161-173, doi:10.1021/acs.jproteome.9b00478 (2020).

79   Cargile, B. J., Bundy, J. L. & Stephenson, J. L., Jr. Potential for false positive identifications from large databases through tandem mass spectrometry. *J Proteome Res* **3**, 1082-1085, doi:10.1021/pr049946o (2004).

80   Shen, C. *et al.* On the estimation of false positives in peptide identifications using decoy search strategy. *Proteomics* **9**, 194-204, doi:10.1002/pmic.200800330 (2009).

81   Perkins, D. N., Pappin, D. J., Creasy, D. M. & Cottrell, J. S. Probability-based protein identification by searching sequence databases using mass spectrometry data. *Electrophoresis* **20**, 3551-3567, doi:10.1002/(SICI)1522-2683(19991201)20:18<3551::AID-ELPS3551>3.0.CO;2-2 (1999).

82   Benjamini, Y. & Hochberg, Y. Controlling the False Discovery Rate: A Practical and Powerful Approach to Multiple Testing. *Journal of the Royal Statistical Society: Series B (Methodological)* **57**, 289-300, doi:10.1111/j.2517-6161.1995.tb02031.x (1995).

83   Kall, L., Storey, J. D., MacCoss, M. J. & Noble, W. S. Assigning significance to peptides identified by tandem mass spectrometry using decoy databases. *J Proteome Res* **7**, 29-34, doi:10.1021/pr700600n (2008).

84   Hunter, T. Protein kinases and phosphatases: the yin and yang of protein phosphorylation and signaling. *Cell* **80**, 225-236, doi:10.1016/0092-8674(95)90405-0 (1995).

85   Cohen, P. The origins of protein phosphorylation. *Nat Cell Biol* **4**, E127-130, doi:10.1038/ncb0502-e127 (2002).

86   Gruhler, A. *et al.* Quantitative phosphoproteomics applied to the yeast pheromone signaling pathway. *Mol Cell Proteomics* **4**, 310-327, doi:10.1074/mcp.M400219-MCP200 (2005).

87   Ballif, B. A., Villen, J., Beausoleil, S. A., Schwartz, D. & Gygi, S. P. Phosphoproteomic analysis of the developing mouse brain. *Mol Cell Proteomics* **3**, 1093-1101, doi:10.1074/mcp.M400085-MCP200 (2004).

88   Blagoev, B., Ong, S. E., Kratchmarova, I. & Mann, M. Temporal analysis of phosphotyrosine-dependent signaling networks by quantitative proteomics. *Nat Biotechnol* **22**, 1139-1145, doi:10.1038/nbt1005 (2004).

89   Horn, H. *et al.* KinomeXplorer: an integrated platform for kinome biology studies. *Nat Methods* **11**, 603-604, doi:10.1038/nmeth.2968 (2014).

90   Akella, R., Moon, T. M. & Goldsmith, E. J. Unique MAP Kinase binding sites. *Biochim Biophys Acta* **1784**, 48-55, doi:10.1016/j.bbapap.2007.09.016 (2008).

91   Lim, W. A. & Pawson, T. Phosphotyrosine signaling: evolving a new cellular communication system. *Cell* **142**, 661-667, doi:10.1016/j.cell.2010.08.023 (2010).

92   Seet, B. T., Dikic, I., Zhou, M. M. & Pawson, T. Reading protein modifications with interaction domains. *Nat Rev Mol Cell Biol* **7**, 473-483, doi:10.1038/nrm1960 (2006).

93   Wiredja, D. D., Koyuturk, M. & Chance, M. R. The KSEA App: a web-based tool for kinase activity inference from quantitative phosphoproteomics. *Bioinformatics* **33**, 3489-3491, doi:10.1093/bioinformatics/btx415 (2017).

94   Casado, P. *et al.* Kinase-substrate enrichment analysis provides insights into the heterogeneity of signaling pathway activation in leukemia cells. *Sci Signal* **6**, rs6, doi:10.1126/scisignal.2003573 (2013).

95   Kim, H. J. *et al.* PhosR enables processing and functional analysis of phosphoproteomic data. *Cell Rep* **34**, 108771, doi:10.1016/j.celrep.2021.108771 (2021).

96   Tyanova, S. *et al.* The Perseus computational platform for comprehensive analysis of (prote)omics data. *Nat Methods* **13**, 731-740, doi:10.1038/nmeth.3901 (2016).

97   John, A. Correlations Genuine and Spurious in Pearson and Yule. *Statistical Science* **10**, 364-376, doi:10.1214/ss/1177009870 (1995).

98   Buchanan, M. Cause and correlation. *Nature Physics* **8**, 852-852, doi:10.1038/nphys2497 (2012).

99   Doodson, A. T. & Lamb, H. The harmonic development of the tide-generating potential. *Proceedings of the Royal Society of London. Series A, Containing Papers of a Mathematical and Physical Character* **100**, 305-329, doi:10.1098/rspa.1921.0088 (1921).

100   Misra, B. B., Langefeld, C. D., Olivier, M. & Cox, L. A. Integrated Omics: Tools, Advances, and Future Approaches. *J Mol Endocrinol*, doi:10.1530/JME-18-0055 (2018).

101   Lohmueller, K. E., Pearce, C. L., Pike, M., Lander, E. S. & Hirschhorn, J. N. Meta-analysis of genetic association studies supports a contribution of common variants to susceptibility to common disease. *Nat Genet* **33**, 177-182, doi:10.1038/ng1071 (2003).

102   Lay, J. O., Liyanage, R., Borgmann, S. & Wilkins, C. L. Problems with the "omics". *TrAC Trends in Analytical Chemistry* **25**, 1046-1056, doi:10.1016/j.trac.2006.10.007 (2006).

103   Meier, F., Park, M. A. & Mann, M. Trapped Ion Mobility Spectrometry (TIMS) and Parallel Accumulation – Serial Fragmentation (PASEF) in Proteomics. *Molecular & Cellular Proteomics*, 100138, doi:10.1016/j.mcpro.2021.100138 (2021).

104   Yaffe, M. B. Why geneticists stole cancer research even though cancer is primarily a signaling disease. *Sci Signal* **12**, doi:10.1126/scisignal.aaw3483 (2019).

105   Weinberg, R. A. Racing to the Beginning of the Road: The Search for the Origin of Cancer. 263 (1998).

106   Giacomelli, A. O. *et al.* Mutational processes shape the landscape of TP53 mutations in human cancer. *Nat Genet* **50**, 1381-1387, doi:10.1038/s41588-018-0204-y (2018).

107 Seiser, S. *et al.* Octenidine-based hydrogel shows anti-inflammatory and protease-inhibitory capacities in wounded human skin. *Sci Rep* **11**, 32, doi:10.1038/s41598-020-79378-9 (2021).

108 Weiss, T. *et al.* Schwann cell plasticity regulates neuroblastic tumor cell differentiation via epidermal growth factor-like protein 8. *Nat Commun* **12**, 1624, doi:10.1038/s41467-021-21859-0 (2021).

„Ich habe mich bemüht, sämtliche Inhaber der Bildrechte ausfindig zu machen und ihre Zustimmung zur Verwendung der Bilder in dieser Arbeit eingeholt. Sollte dennoch eine Urheberrechtsverletzung bekannt werden, ersuche ich um Meldung bei mir."

Janker Lukas, Mai 2022

4 Results

4.1 Metabolic, Anti-apoptotic and Immune Evasion Strategies of Primary Human Myeloma Cells Indicate Adaptations to Hypoxia

Lukas Janker[1]*, Rupert L Mayer[1]*, Andrea Bileck[1], Dominique Kreutz[1], Johanna C Mader[1], Kirsten Utpatel[2], Daniel Heudobler[3], Hermine Agis[4], Christopher Gerner[1], Astrid Slany[1]

1   Department of Analytical Chemistry, Faculty of Chemistry, University of Vienna, Vienna, Austria

2   Department of Pathology, University Regensburg, Regensburg, Germany

3   Department of Internal Medicine III, Hematology and Oncology, University Hospital Regensburg, Regensburg, Germany
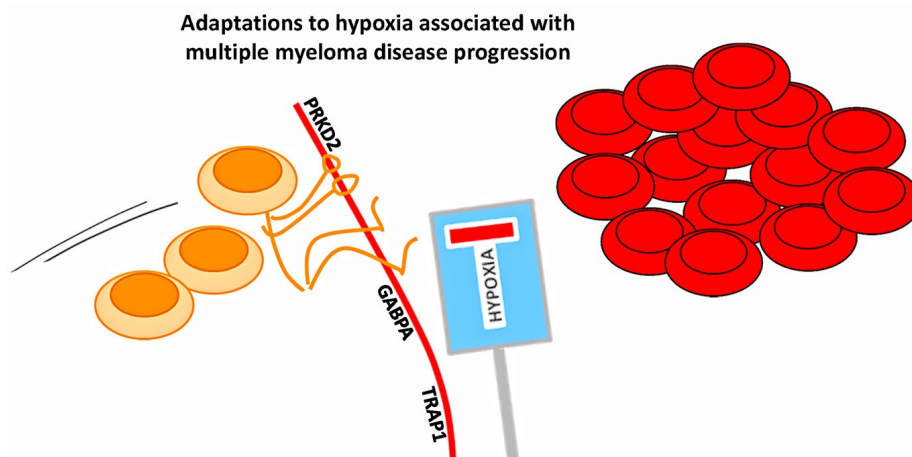
4   Department of Oncology, University Clinic for Internal Medicine I, Medical University of Vienna, Vienna, Austria

*   Contributed equally

Adaptations to hypoxia associated with multiple myeloma disease progression

Contributions to this publication:

- Performing research and MS measurements
- Analysis and interpretation of data
- Preparation of figures and writing of manuscript

Metabolic, Anti-apoptotic and Immune Evasion Strategies of Primary Human Myeloma Cells Indicate Adaptations to Hypoxia

Authors

Lukas Janker, Rupert L. Mayer, Andrea Bileck, Dominique Kreutz, Johanna C. Mader, Kirsten Utpatel, Daniel Heudobler, Hermine Agis, Christopher Gerner, and Astrid Slany

Correspondence

astrid.slany@univie.ac.at

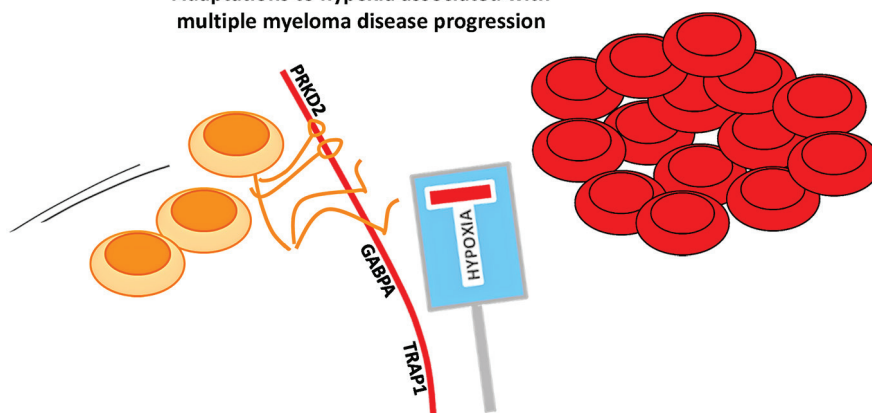## Graphical Abstract

In Brief

In-depth proteome profiling of primary human CD138-positive plasma cells, derived from bone marrow biopsies from patients with different stages of multiple myeloma, have been performed on a Q Exactive orbitrap. Analysis of the 6218 identified proteins using label-free quantification with the MaxQuant software revealed strategies adopted by myeloma cells to overcome limitations imposed by hypoxic conditions in the bone marrow microenvironment, including specific immune evasion mechanisms and metabolic adaptations.

Highlights

- In-depth proteome profiling of primary human myeloma cells

- Characteristics of myeloma cells are related to hypoxic bone marrow conditions

- Myeloma cells show specific immune evasion strategies

- Metabolic adaptations involve tumor and stroma cells

Metabolic, Anti-apoptotic and Immune Evasion Strategies of Primary Human Myeloma Cells Indicate Adaptations to Hypoxia*⑤

Lukas Janker‡‡‡, Rupert L. Mayer‡‡‡, Andrea Bileck‡, Dominique Kreutz‡, Johanna C. Mader‡, Kirsten Utpatel§, Daniel Heudobler¶, Hermine Agis‖, Christopher Gerner‡, and Astrid Slany‡**

Multiple Myeloma (MM) is an incurable plasma cell malignancy primarily localized within the bone marrow (BM). It develops from a premalignant stage, monoclonal gammopathy of undetermined significance (MGUS), often via an intermediate stage, smoldering MM (SMM). The mechanisms of MM progression have not yet been fully understood, all the more because patients with MGUS and SMM already carry similar initial mutations as found in MM cells. Over the last years, increased importance has been attributed to the tumor microenvironment and its role in the pathophysiology of the disease. Adaptations of MM cells to hypoxic conditions in the BM have been shown to contribute significantly to MM progression, independently from the genetic predispositions of the tumor cells. Searching for consequences of hypoxia-induced adaptations in primary human MM cells, CD138-positive plasma cells freshly isolated from BM of patients with different disease stages, comprising MGUS, SMM, and MM, were analyzed by proteome profiling, which resulted in the identification of 6218 proteins. Results have been made fully accessible via ProteomeXchange with identifier PXD010600. Data previously obtained from normal primary B cells were included for comparative purposes. A principle component analysis revealed three clusters, differentiating B cells as well as MM cells corresponding to less and more advanced disease stages. Comparing these three clusters pointed to the alteration of pathways indicating adaptations to hypoxic stress in MM cells on disease progression. Protein regulations indicating immune evasion strategies of MM cells were determined, supported by immunohistochemical staining, as well as transcription factors involved in MM development and progression. Protein regulatory networks related to metabolic adaptations of the cells became apparent. Results were strengthened by targeted analyses of a selected panel of metabolites in MM cells and MM-associated fibroblasts. Based on our data, new opportunities may arise for developing therapeutic strategies targeting myeloma disease progression. *Molecular & Cellular Proteomics 18: 936–953, 2019. DOI: 10.1074/mcp.RA119.001390.*

Multiple myeloma (MM)[1] is a hematological tumor localized primarily in the bone marrow (BM), characterized by the proliferation of malignant antibody-secreting plasma cells. The disease is accompanied by severe health problems such as bone lesions, hypercalcemia, renal failure, anemia and immunodeficiency (1). Even though several new therapeutic strategies extending the survival time of patients have been developed over the last years, MM remains an incurable disease (2). Further, genetic alterations in MM cells are heterogeneous and it is difficult to predict disease course or therapeutic response for individual patients (3). Even though first-line treatments may be successful, relapses are to be expected and tumors then typically become more aggressive and more difficult to treat. MM develops from a premalignant stage, monoclonal gammopathy of undetermined significance (MGUS), and typically progresses through an intermediary stage, smoldering MM (SMM). It is still not completely understood what drives this progression, as patients with MGUS and SMM already carry similar mutations as found in MM cells, suggesting that these mutations are necessary but not enough for tumor development (4–6).

Over the last years, the tumor microenvironment has been recognized to play an important role in MM progression, as well as in immune evasion and drug resistance of MM cells (7, 8). New therapeutic approaches have thus been developed, targeting not only the tumor itself but also tumor-supporting stromal cells such as fibroblasts and endothelial cells, as well as cells of the immune system (9, 10). Further, significance has been attributed to hypoxic conditions in the BM and the role of hypoxia in MM biology, offering novel possibilities for treatment strategies (11–13). MM cells encountering hypoxic

environments in the BM apparently enhance pathways that allow them to survive and proliferate under these conditions. Consequently, processes such as angiogenesis and anti-apoptotic survival and proliferation strategies may be induced, and alternative metabolic pathways may be activated in the tumor cells (14–16). As a result, hypoxia-surviving MM cells may become more aggressive and more resistant to therapies (17).

Recent advances in proteomics technologies have given us the opportunity to better understand cellular processes involved in development and progression of diseases (18–22). Proteomics has already been used by others to assess specific aspects of MM such as development of drug resistance (23–26). In line with a recent work on chronic lymphocytic leukemia (CLL) B cells (22), in the present study we have investigated primary human multiple myeloma (MM) cells. The aim was to apply proteome profiling to get deeper insights into pathways MM cells follow in response to hypoxic conditions in the BM microenvironment. Hypoxia-related proteome signatures of MM cells, associated with survival, proliferation and mechanisms to escape apoptosis and immune response were investigated, as well as new targets for therapeutic interventions. To this end, we analyzed primary human CD138-positive plasma cells freshly isolated from the BM of patients with different disease stages, comprising MGUS, SMM, and MM. Another aim was to find out if, like chronic lymphocytic leukemia cells (22), MM cells of individual donors, despite MM being associated with a rather heterogeneous genotype, would show consistent protein patterns indicating pathways commonly adapted by MM cells. The study design should also allow investigating whether there were differences in the proteome of cells from premalignant and earlier stages compared with more advanced stages of the disease, which could provide insights into the pathogenesis and progression of multiple myeloma.

EXPERIMENTAL PROCEDURES

Study Cohort and Bone Marrow Sampling—For proteome profiling experiments, bone marrow (BM) samples from thirteen patients with different stages of multiple myeloma (MM), including monoclonal gammopathy of undetermined significance (MGUS), smoldering MM (SMM) and diagnosed MM, were obtained from routinely taken BM aspirates at the Vienna General Hospital. Written informed consent was obtained from all patients, as well as approval of the Ethics Committee of the Medical University of Vienna (application nr. 1181/2013). In the same way another five BM aspirates were taken from patients with diagnosed MM for targeted analyses of a selected panel

---

[1] The abbreviations used are: MM, multiple myeloma; BM, bone marrow; ER, endoplasmic reticulum; FASP, filter aided sample preparation; GO, gene ontology; HCD, high-energy collisional dissociation; IR, infiltration rate; LDL, low density lipoprotein; LFQ, label-free quantification; MACS, magnetic activated cell sorting; MGUS, monoclonal gammopathy of undetermined significance; MHC, major histocompatibility complex; MWCO, molecular weight cut off; PCA, principle component analysis; SMM, smoldering multiple myeloma; TF, transcription factor.

of metabolites (described below). From three of these samples, plasma cells were isolated. From the two other samples, as well as from two biopsies also used for proteomics experiments (indicated in Table I), BM fibroblasts were prepared as described below. Both, BM plasma cells and BM fibroblasts were subjected to the analysis of selected metabolites.

For immunohistochemical staining, BM biopsies from eight patients with different stages of MM were used. These biopsies were obtained for routine diagnostics at the University Hospital of Regensburg. No additional biopsies for research purposes were taken. After routine diagnostics, remaining material was used for immunohistochemistry (IHC) with approval of the Ethics Committee of the University of Regensburg (application nr. 051097). Clinical parameters, as well as if patients have obtained MM-specific treatments or not, are indicated in Table I for all patients included in the present study.

Plasma Cell Isolation—Bone marrow aspirates were filtered through 40 μm filter (40 μm Nylon Cell Stainer, BD Falcon), diluted 1:2 with PBS, overlaid on Ficoll Paque (GE Healthcare, Bio-Sciences AB, Uppsala, Sweden), and centrifuged at 720 $\times$ g for 20 min at room temperature with minimal acceleration and deceleration settings. Mononuclear cells were collected from the resulting interface, were washed with PBS, then resuspended in PBS. Plasma cells were isolated using magnetic activated cell sorting (MACS). To this end, mononuclear cells were incubated at 4 °C for 15 min, after adding magnetic bead-coupled anti-CD138 antibody (Miltenyi Biotec, Bergisch Gladbach, Germany). After another PBS washing step, cells were resuspended in MACS buffer (1$\times$ PBS, 0.5% FBS, 2 mM EDTA) and pipetted onto a preconditioned MACS LS column mounted on a magnetic holder (both Miltenyi Biotec, Bergisch Gladbach, Germany). Cells were washed with MACS buffer and CD138-positive plasma cells eluted by removing the MACS LS column from the magnet and pressing 4 ml of MACS buffer through the column. The plasma cell-containing eluate was diluted to 10 ml and cell number as well as viability was determined using the MOXI Z Mini Automated Cell Counter (ORFLO Technologies, Ketchum, ID). Cells were then pelleted by centrifugation at 590 $\times$ g for 5 min at 4 °C.

Cell Lysis and Subcellular Fractionation of Primary Human Bone Marrow Plasma Cells—Cell lysis and subcellular fractionation were performed applying a previously established protocol (27). In short, CD138-positive cells were resuspended in lysis buffer supplemented with protease inhibitors at 4 °C to achieve cell lysis. After centrifugation, the cytoplasmic fraction was collected in the supernatant. The pellet was dissolved in 500 mM NaCl solution and subsequently diluted in NP40-buffer; after centrifugation, nuclear protein extracts were collected in the supernatant. Cytoplasmic and nuclear proteins were precipitated in ice-cold ethanol overnight and solubilized in sample buffer (7.5 M urea, 1.5 M thiourea, 4% CHAPS. 0.05% SDS, 100 mM DTT). Protein concentrations were assessed by applying a Bradford assay (Bio-Rad-Laboratories, Vienna, Austria).

Proteolytic Digestion and Sample Clean-up for LC-MS/MS Analysis—Protein fractions were subjected to a filter-assisted proteolytic digestion with a modified version of the FASP protocol (28, 29). In short, 20 μg of proteins were loaded onto a prewetted MWCO filter (Pall Austria Filter GmbH, Vienna, Austria) with a pore size of 3 kDa, followed by reduction of disulfide bonds with dithiothreitol (DTT), alkylation with iodoacetamide (IAA) and washing steps with 50 mM ammonium bicarbonate buffer. Digestion of proteins was achieved by applying two times Trypsin/Lys-C with Mass Spec Grade quality (Promega, Mannheim, Germany), at first overnight, and in a second step for 4 h. Resulting peptides were eluted through the filter by centrifugation, and clean-up was performed using C-18 spin columns (Pierce, Thermo Fisher Scientific, Austria).

LC-MS/MS Analysis—For LC-MS/MS analyses, samples were reconstituted in 5 μl 30% formic acid (FA), supplemented with four

41

synthetic peptide standards for internal quality control, and diluted with 40 μl mobile phase A (97.9% H_2O, 2% ACN, 0.1% FA). Of this solution 10 μl were injected into a Dionex Ultimate 3000 nano LC-system coupled to a Q Exactive orbitrap mass spectrometer equipped with a nanospray ion source (Thermo Fisher Scientific, Austria). All samples were analyzed as technical replicates. As a preconcentration step, peptides were loaded on a 2 cm × 75 μm C18 Pepmap100 pre-column (Thermo Fisher Scientific, Austria) at a flow rate of 10 μl/min using mobile phase A. Elution from the precolumn to a 50 cm × 75 μm Pepmap100 analytical column (Thermo Fisher Scientific, Austria) and subsequent separation was achieved at a flow rate of 300 nl/min using a gradient of 8% to 40% mobile phase B (79.9% ACN, 2% H_2O, 0.1% FA) over 235 min with a total chromatographic run time of 280 min. For mass spectrometric detection, MS scans were performed in the range from m/z 400–1400 at a resolution of 70000 (at m/z = 200). MS/MS scans of the eight most abundant ions were achieved through HCD fragmentation at 30% normalized collision energy and analyzed in the orbitrap at a resolution of 17,500 (at m/z = 200).

Data Analysis—The MaxQuant software (version 1.6.0.1), including the Andromeda search engine, was used for data analysis (30). For positive protein identification, as a minimum two peptides, at least one of them being unique, had to be detected. Trypsin/P was specified in the digestion mode. Peptide mass tolerance was set to 50 and 25 ppm for the first and the main search, respectively. The false discovery rate (FDR) was set to 0.01 both on peptide and protein level. The database applied for the search was the human Uniprot database (version 06/2017, with 20100 reviewed entries and 22088 isoforms). Carbamidomethylation was set as fixed modification, methionine oxidation and N-terminal acetylation as variable modifications. Each peptide could have a maximum of two missed cleavages and two modifications. "Match between runs" was enabled and the alignment and match time window set to 25 and 1 min, respectively.

In parallel, to allow data submission to the ProteomeXchange Consortium via the PRIDE partner repository (31), raw files were analyzed using Proteome Discoverer 1.4 (Thermo Fisher Scientific, Austria) using Mascot 2.5 (Matrix Science, UK). Protein identification was performed by searching raw files against the SwissProt Database (version 11/2015 with 20 193 entries), applying a mass tolerance of 50 ppm at MS1 level and 100 mmu at MS2 level, and allowing for up to two missed cleavages per peptide. Fixed and variable modifications were set in the same way as for the MaxQuant search described above. Resulting data were submitted to the ProteomeXchange Consortium via the PRIDE partner repository and can be accessed via www.proteomeexchange.org with the identifier PXD010600.

Experimental Design and Statistical Rationale—Plasma cells isolated from bone marrow of ten patients with multiple myeloma (MM) and three patients with premalignant stages of MM (MGUS or SMM), as indicated in Table I, were used for proteome profiling experiments. Only patients diagnosed according to the guidelines provided by the International Myeloma Working Group (32) were included. Patients suffering from severe comorbidities were excluded. In addition to the MM cell data set, data previously obtained from six biological replicates of peripheral B cells (22), isolated from six healthy donors by applying magnetic activated cell sorting with anti-CD19 antibodies, were included for comparative purposes. B cells were used as reference cell system, representing precursors of plasma cells which have hardly experienced hypoxia. All biological samples were measured as technical replicates with LC-MS/MS, which resulted in 19 independent data sets and a total of 38 measurements. The MaxQuant software (version 1.6.0.1), including the Andromeda search engine, was used for data analysis (30). For statistical data evaluation, the Perseus software (version 1.6.0.2) was used (30, 33). Reverse sequences, potential contaminants as well as proteins identified only by site were

removed. Additionally, the normal distribution of data points was manually checked via the histogram function implemented in the Perseus software. Label-free quantification (LFQ) values were logarithmized to base 2, and technical replicates were averaged. Protein groups were filtered for valid values, keeping only those identified in at least 70% of B cell or MM cell samples. Missing values were then replaced from a normal distribution with a down shift of 1.8 and a width of 0.3 in order to enable t-testing and volcano plots. A principle component analysis (PCA), based on label-free quantification of cytoplasmic proteins, was performed. To determine protein groups significantly regulated between resulting clusters, two-sided t-tests employing multiparameter correction with a q-value ≤0.01 (permutation-based FDR correction with s0 = 0.5) were applied. For selected proteins, heat maps representing LFQ values determined in each sample were generated by a custom R (https://www.r-project.org) script. Protein groups found to be significantly regulated were further submitted to the oPOSSUM software (version 3.0) (34), which allowed the detection of over-represented conserved transcription factor binding sites in the corresponding sets of genes.

Targeted Analyses of a Selected Panel of Metabolites—For targeted analyses of a selected panel of metabolites, one million of CD138-positive plasma cells isolated from BM biopsy material of three patients with diagnosed MM (Table I) was suspended in lysis buffer (10 mM phosphate buffer in 85% ethanol) and lysed by three freeze-thaw cycles. The obtained cell lysates were analyzed with the AbsoluteIDQ p180 kit (Biocrates Life Sciences AG, Innsbruck, Austria), as described previously (20). In short, LC-MS and flow injection (FIA)-MS analyses were carried out on a 4000 QTRAP MS system (AB Sciex, Framingham, MA) coupled to a 1200 RR HPLC system (Agilent, Palo Alto, CA), using the Analyst 1.6.2 software (also AB SCIEX). Data evaluation was performed with the software supplied with the kit (MetIDQ, version 5–4-8-DB100-Boron-2607, Biocrates Life Sciences). Results were again compared with data obtained previously from the analysis of B cells (22).

In parallel, from BM samples of four MM patients (Table I), fibroblasts were prepared as previously described (8). In short, BM samples were filtered through a 40 μm mesh (40 μm Nylon Cell Stainer, BD Falcon), the residue in the filter was transferred into a culture flask with fibroblast basal medium (FBM, Lonza Clonetics, # CC-3131) supplemented with one FGM BulletKit (Lonza Clonetics, # CC-3130) and 10% FCS. The culture flask was placed in an incubator at 37 °C in a humidified atmosphere containing 5% CO_2, refreshing the medium after 24 h. For comparative purposes, three biological replicates of human mesenchymal stem cells (hMSC, passage 4 to 5; Lonza), cultured in mesenchymal stem cell growth medium (Lonza) supplemented with the associated Bulletkit and 100 U/ml penicillin/streptomycin (ATCC/LGC Standards, London, UK), were used. After reaching 75% confluence, fibroblasts and hMSC were detached by trypsin-EDTA (Sigma-Aldrich) treatment. Cells were washed twice with PBS and one million of each of these cells was processed and used for targeted analyses of a selected panel of metabolites as described above for CD138-positive plasma cells.

Immunohistochemistry—Immunohistochemical stainings were performed on 3 μm thick formalin-fixed, paraffin-embedded tissue sections. Antigen retrieval was performed with Ventana cell conditioning solution 1 (Tris-EDTA buffer pH 8 at 100 °C 32 min) (Ventana Medical Systems, Tucson, AZ). Subsequently, the slides were incubated with primary antibodies against SDC1 (CD138; mouse monoclonal, dilution 1:100, Dako, Denmark), SIGIRR (rabbit polyclonal, dilution 1:500, abcam, United Kingdom), CD46 (rabbit monoclonal, dilution 1:750, abcam, United Kingdom), SLAM7 (rabbit polyclonal, dilution 1:150, Sigma Aldrich, Germany) for 32 min at 36 °C. The immunoreactivity was visualized with the Optiview DAB IHC Detection Kit (Ventana Medical Systems). Slides were counterstained with hematoxylin.

RESULTS

In-depth Proteome Profiling of Primary Human Myeloma Cells—Primary human CD138-positive plasma cells were isolated from freshly isolated bone marrow (BM) biopsy material of ten patients with diagnosed MM, one patient with monoclonal gammopathy of undetermined significance (MGUS), the premalignant stage of MM, and two patients with smoldering multiple myeloma (SMM), an intermediary stage of MM (Table I). Cells were fractionated into cytoplasm and nuclear extracts and analyzed by in-depth proteome profiling using a Q Exactive orbitrap. In total, 6038 and 3415 proteins were identified in cytoplasmic and nuclear fractions of the cells, respectively, (supplemental Tables S1 and S2) by means of the MaxQuant Andromeda search engine (30). A principle component analysis (PCA), based on label-free quantification of cytoplasmic proteins, distinguished three groups: (1) B cells; (2) premalignant stages of MM, and diagnosed MM with BM plasma cell infiltration rates up to 20%, termed MM_{low}; (3) diagnosed and more advanced stages of MM which match to BM plasma cell infiltration rates of at least 40%, termed MM_{high} (Fig. 1*A*). Remarkably, in both groups, MM_{high} and MM_{low}, patients who had obtained MM-specific therapies and patients who had not been specifically treated before were included (indicated in Table I). Therefore, it was particularly relevant to observe that proteome profiles were that homogeneous in each of these groups, and displayed more commonalities than differences, indicating that protein expression profiles of MM cells were more dependent on the disease stage and hardly on patient treatments. In total, 637 and 605 cytoplasmic proteins were found significantly regulated between MM cells and B cells, and between MM_{high} and MM_{low} cells, respectively, illustrated by volcano plots in Fig. 1*B* and listed in supplemental Table S1. In the nuclear extracts, 414 proteins were found significantly regulated between MM cells and B cells, and 158 proteins between MM_{high} and MM_{low} cells (supplemental Table S2). MGUS, SMM, and MM cells, when compared all together to B cells, were referred to as "MM cells." Several well-known differentiation markers of plasma cells, such as CD19, MS4A1 (CD20) and CD38, as well as marker proteins characteristic for myeloma cells, such as CD37, PTPRC (CD45), and SDC1 (CD138) (35, 36), were found regulated as expected in MM *versus* B cells (Fig. 1*C*).

Proteins Involved in Apoptosis Regulated in MM Cells—To determine biological processes regulated in MM cells and possibly related to the hallmarks of cancer (37), we used different resources such as DAVID functional annotation tool (38, 39), UniProt information about proteins (40), and performed thorough research of scientific literature. In this way, first, we determined pathways that point to suppression of apoptosis in MM cells, including upregulation of anti-apoptotic proteins and downregulation of pro-apoptotic proteins (Fig. 1*D*). Some of these proteins were found regulated in all MM cells relative to B cells, exemplified by apoptosis regula-

tor BAX, whereas others were only regulated at advanced stages of the disease, such as, for example, CASP10 (Fig. 1*E*).

Proteins Involved in ER Activities Regulated in MM Cells—Further, several proteins related to biological activities in the endoplasmic reticulum (ER) such as folding and modification of newly synthesized proteins, as well as degradation of incorrectly folded proteins, and transport processes from the ER to the Golgi apparatus, were found at significantly elevated levels in MM cells (Fig. 2*A*). Most of these proteins were upregulated in a progressive way between B and MM_{low} cells, and further between MM_{low} and MM_{high} cells (Fig. 2*B* and 2*C*), consistent with the increasing amounts of immunoglobulins produced by malignant plasma cells on disease progression. This was further accompanied by a significant upregulation of proteins involved in translational processes, according to GO terms (highlighted in Fig. 1*B*). Similarly, upregulation of proteins involved in control of redox stress caused by disulfide bond formation, such as PRDX4 and TXNDC11 (41, 42), was observed (Figs. 2*A*–2*C*). In parallel, pathways that limit ER stress-induced apoptosis seemed to be enhanced especially in MM_{high} cells, involving downregulation of BAX, TRAF2, ITPR1, and PRAF2 (43–45) and upregulation of SDF2L1, MYDGF, SDF4, RCN1, and TXNDC5 (46–49) (Figs. 1*D*, 1*E*, 2*A* and 2*C*).

Regulation of Proteins Related to Respiratory Activities and to Hypoxia—Numerous mitochondrial proteins were found deregulated in MM cells. Although reduced levels of proteins of the respiratory chain, such as COX6C, $MT-CO_2$, or ATP5L, were determined in all MM cells compared with B cells (supplemental Table S1), several other proteins of the respiratory chain, especially chaperones necessary for the assembly of respiratory complexes, were found at significant higher levels in MM_{high} than in B cells and MM_{low} cells (Fig. 3*A*). These findings may point to a downshift of respiratory activities in MM_{low} cells and a reactivation in MM_{high} cells. In line with this, proteins involved in mitochondrial translation, according to GO terms, appeared to be significantly upregulated in MM_{high} *versus* MM_{low} cells (highlighted in Fig. 3*B*). Additionally, several proteins related to hypoxia were found regulated. HIF1AN and VHL (Fig. 3*C*), known to prevent activation of hypoxia-inducible factor (14, 50–53), were determined at reduced levels in MM cells, similarly to TP53I11 and PTPN1, described to be targets of hypoxia-induced micro-RNA-210 (54). Remarkably, DIMT1, described to be downregulated by micro-RNA-210 likewise (16), was found at lower levels only in MM_{low} cells, but was upregulated again in MM_{high} cells. Similarly, higher levels of FYN and SRC, two tyrosine-protein kinases of the same family, were determined at higher levels only in MM_{low} cells; hypoxia has been shown to activate FYN either by phosphorylation or by upregulation of protein expression (55, 56). Also consistent with this, GTF2F2, reported to be downregulated under hypoxic conditions (57), was found at lower levels in MM_{low} than in MM_{high} cells. These findings indicate that MM cells activate mechanisms in re-

43

TABLE I
Clinical parameters for patients included in the present study and type of experiment performed with the respective biopsy sample

Patient #	Diagnosis	MM-specific treatment	Experiments			
			Proteomics	PC-Metabolites	Fib-Metabolites	IHC
MM1	cyclin D1-neg. MGUS; IR 5%	no	x			
MM2	κ-pos., cyclin D1-neg. IgA-SMM; IR 50%	no	x			
MM3	λ-pos., cyclin D1-neg., IgH-MAF/t(14,16)-pos., monosomy 14 & 16-pos. IgA-SMM; IR 40%	no	x			
MM4	λ-pos., cyclin D1-neg. plasma cell myeloma recidive; IR 20%	yes	x			
MM5	λ-pos., cyclin D1-neg. plasma cell myeloma recidive; IR 10–15%	yes	x			
MM6	λ-pos., cyclin D1-pos. secondary plasma cell myeloma after ASCT; IR 70%	yes	x			
MM7	κ-pos., cyclin D1-neg., low-secretory plasma cell myeloma recidive after ASCT; IR 60%	yes	x			
MM8	λ-pos., cyclin D1-neg. newly diagnosed plasma cell myeloma; IR 70%	no	x			
MM9	λ-pos., IgA-positive, newly diagnosed plasma cell myeloma; IR 70%	no	x			
MM10	κ-pos., cyclin D1-neg., IgH-MAF/t(14,16)-pos., TP53 Deletion-pos., polysomy 4, 14 & 16-pos., trisomy 17-pos. newly diagnosed light-chain plasma cell myeloma; IR 85%	no	x		x	
MM11	λ-pos., cyclin D1-neg., polysomy 14-pos., trisomy 17-pos., newly diagnosed light-chain plasma cell myeloma; IR >90%	no	x		x	
MM12	κ-pos., bcl1-pos., low-secretory plasma cell myeloma; IR 80%	yes	x			
MM13	λ-pos., heterozygous IgH and p53 deletion-pos., ATM amplification-pos., newly diagnosed plasma cell myeloma; IR 50%	no	x			
MM14	λ-pos., cyclin D1-neg. newly diagnosed plasma cell myeloma; IR 70%	no		x		
MM15	IgG-κ-pos. plasma cell myeloma; IR 40%	yes		x		
MM16	IgG-λ-pos., bcl1-pos. plasma cell myeloma; advanced stage; IR N/A	yes		x		
MM17	λ-pos., cyclin D1-neg., plasma cell myeloma; IR 50%	yes			x	
MM18	IgD-λ-pos., cyclin D1-neg., newly diagnosed plasma cell myeloma; IR 50%	no			x	
MM19	κ-pos, cyclin-D1-neg., newly diagnosed IgG-myeloma; IR:10%	no				x
MM20	κ-pos, cyclin-D1-neg.,13q14 deletion, newly diagnosed IgA-myeloma; IR:15%	no				x
MM21	λ-pos, cyclin-D1-neg., newly diagnosed IgA-myeloma; IR:20%	no				x
MM22	λ-pos, cyclin-D1-neg., newly diagnosed IgA-myeloma; IR:40%	no				x
MM23	κ-pos, cyclin-D1-neg., 13q14 deletion, trisomy 3,9,11, newly diagnosed IgA-myeloma; IR:60%	no				x
MM24	λ-pos, cyclin-D1-neg., newly diagnosed light chain-myeloma; IR:70%	no				x
MM25	κ-pos, cyclin-D1-neg., 13q14-delation, TP53-deletion, newly diagnosed IgA-myeloma; IR:70%	no				x
MM26	λ-pos, cyclin-D1-neg., newly diagnosed IgG-myeloma; IR:80%	no				x
MM27	κ-pos, cyclin-D1-neg.,13q14-deletion, 17p-deletion, newly diagnosed IgG-myeloma; IR:80%	no				x

PC-Metabolites, targeted analyses of amino acids performed with BM plasma cells (PCs); Fib- Metabolites, targeted analyses of amino acids performed with MM-associated BM fibroblasts; IHC, immunohistochemistry; IR, BM infiltration rate with PCs; ASCT, autologous stem cell transplantation.

sponse to hypoxic conditions in the BM and that adaptation processes take place in MM$_{high}$ cells.

Regulation of Proteins Involved in Metabolic Processes—In addition, mitochondrial and cytoplasmic proteins involved in several metabolic processes appeared to be deregulated in myeloma cells. Fig. 4*A* shows metabolic pathways in which proteins were found significantly up- or downregulated between B cells, MM$_{low}$ cells and MM$_{high}$ cells, the most impor-
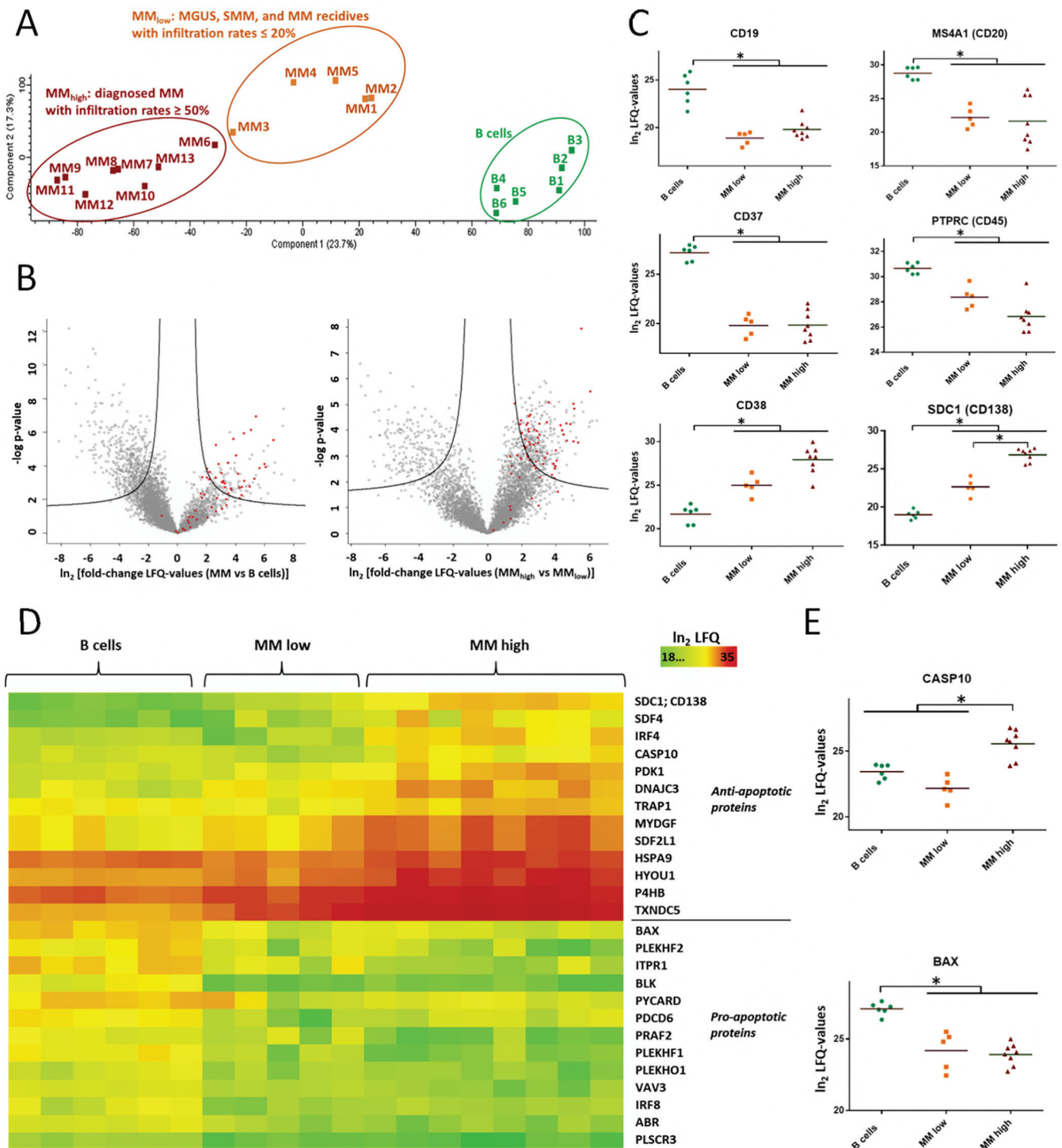
FIG. 1. **Proteome profiling of primary human MM cells and comparison to B cells.** The Perseus software (30, 33) was used to perform statistical data analyses. *A*, PCA based on label-free quantification (LFQ) of 6038 cytoplasmic proteins detected in B cells and MM cells, showing three groups: B cells; MM$_{low}$ cells from patients with MGUS or SMM, as well as from patients with MM with BM infiltration rates with MM cells $\leq$ 20%; and MM$_{high}$ cells from patients with diagnosed MM and BM infiltration rates $\geq$ 40%. *B*, Volcano plots comparing the abundance levels of the same proteins in MM *versus* B cells (left panel) and in MM$_{high}$ *versus* MM$_{low}$ cells (right panel). Proteins, which were found significantly up- or downregulated, are delineated in each plot in the right and in the left area above the black curves, respectively. Proteins involved in translational processes, according to GO terms, are highlighted in red. *C*, Levels of typical markers for B cell differentiation and/or for MM cells. *D*, Heat maps representing LFQ values of proteins involved in pro- or anti-apoptotic processes. *E*, Levels of two proteins involved in apoptosis. Significant regulations are indicated by asterisks.
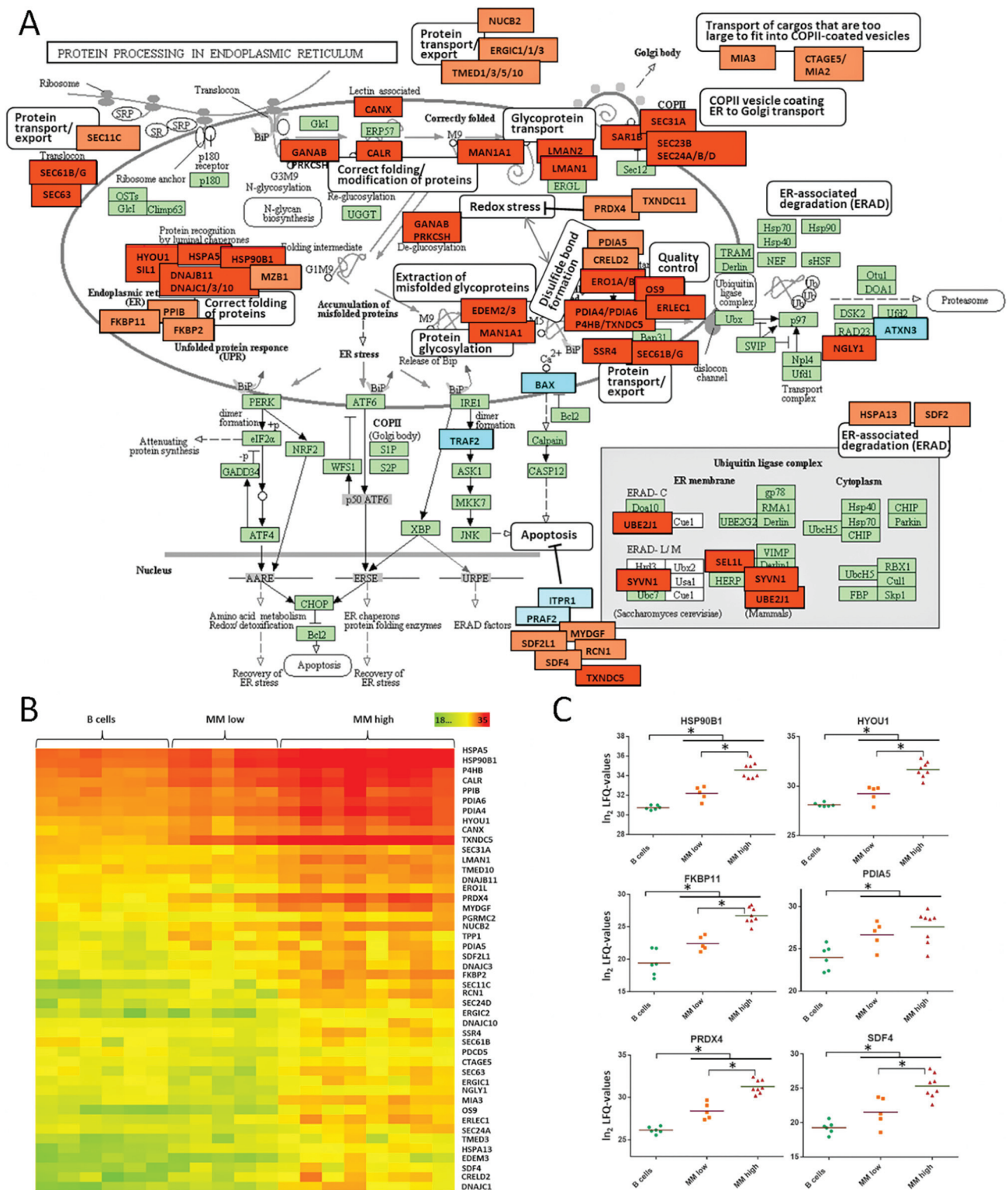
Fig. 2. **Protein processing in the in endoplasmic reticulum (ER) of MM cells.** *A*, Based on the KEGG database for pathway analysis, proteins significantly upregulated in MM cells and related to ER activities were highlighted in red, downregulated proteins in blue. Lighter colors were used when proteins were associated to ER activities based on other references such as the UniProt database (40). Reproduction of the KEGG pathway map image "Protein processing in endoplasmic reticulum" (hsa04141) (127) with permission of Kanehisa Laboratories. *B*, Heat maps representing LFQ values of ER related proteins, demonstrating a progressive upregulation from B cells to MM$_{low}$ and moreover to MM$_{high}$ cells. *C*, For selected proteins, corresponding LFQ values are represented as dot plots. Significant regulations are indicated by asterisks.

46
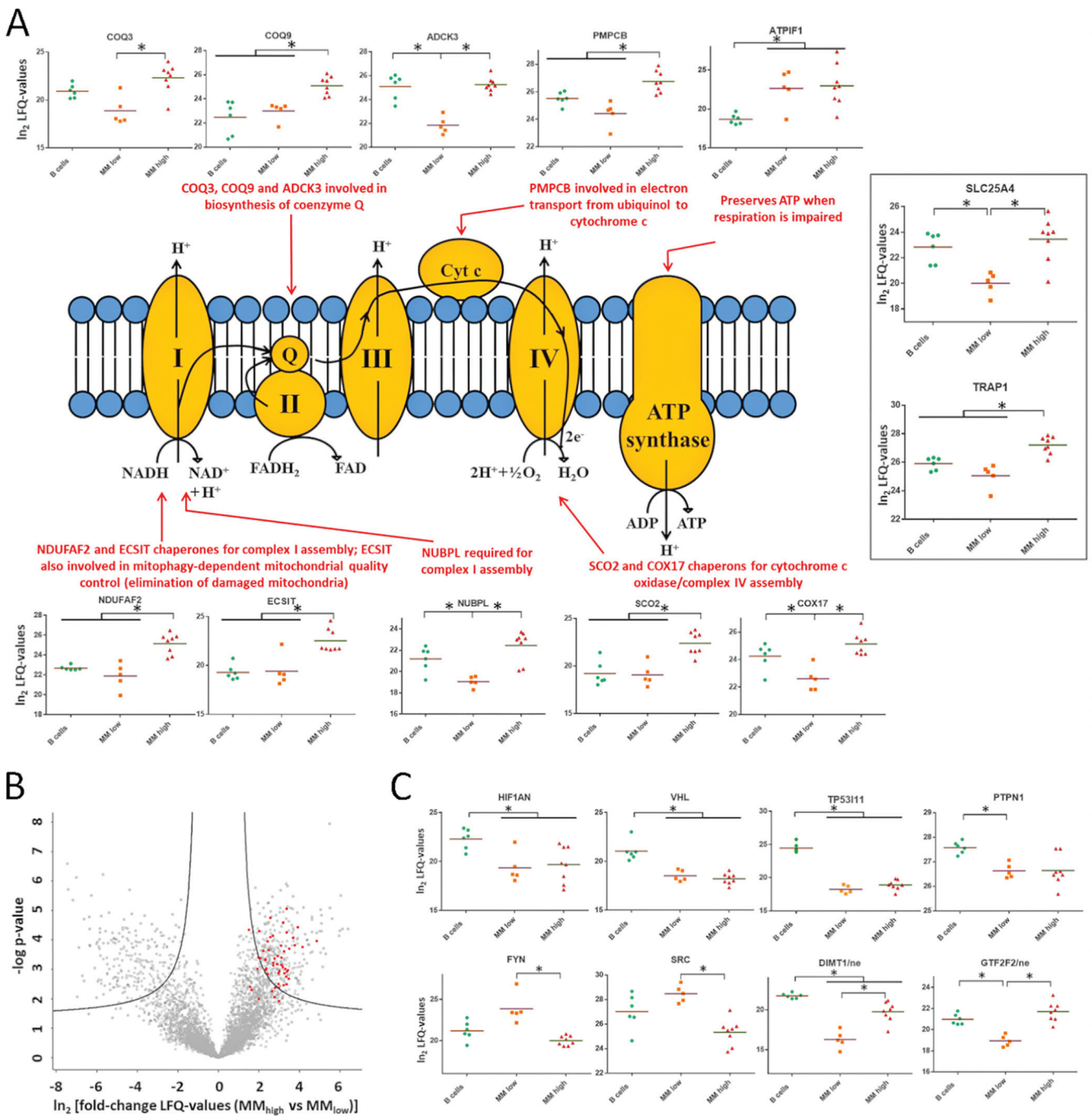
FIG. 3. **Regulation of proteins related to respiration and protein regulation by hypoxia.** *A*, Levels of selected proteins related to the respiratory chain are represented, and biological functions are indicated for some proteins. *B*, Volcano plot comparing the protein levels in MM$_{high}$ *versus* MM$_{low}$ cells. Proteins involved in mitochondrial translation processes, according to GO terms, are highlighted in red. *C*, Levels of selected proteins regulated by hypoxia, detected in the nuclear (ne) or in the cytoplasmic fraction (not specified). Significant regulations are indicated by asterisks.

tant regulatory events occurring between MM$_{low}$ and MM$_{high}$ cells. Most strikingly, the hexosamine pathway, amino acid interconversion reactions and degradation processes, the folate and the methionine cycle, cholesterol uptake and metabolism, and mitochondrial fatty acid synthesis were found upregulated in myeloma cells of advanced disease stages.

These pathways seem thus to play an important role in the progression of multiple myeloma.

To support these results, we also performed targeted analyses of amino acids with both, plasma cells and MM-associated fibroblasts isolated from the BM of patients with advanced disease stages, using B cells and human mesen-
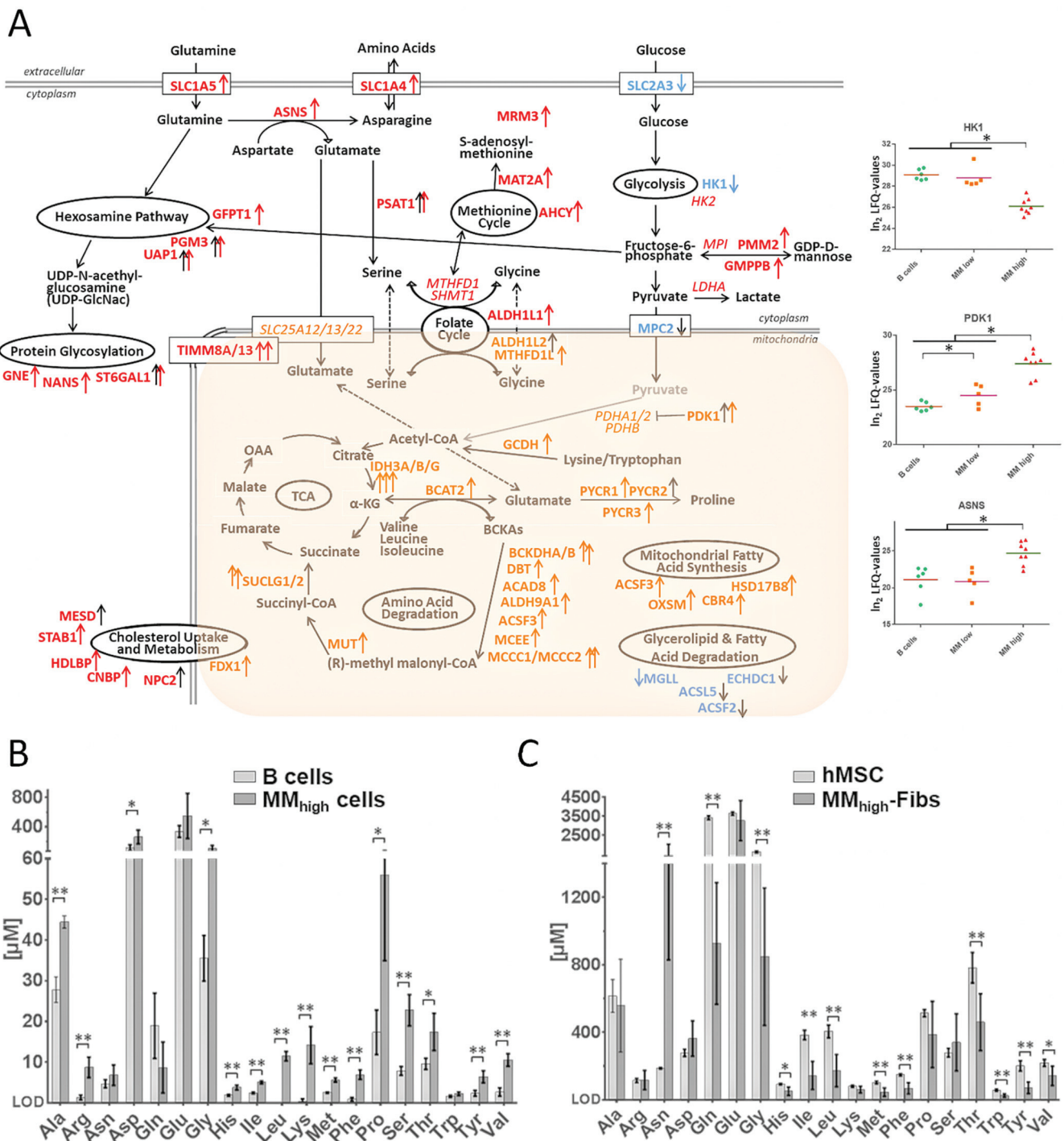
FIG. 4. **Regulation of proteins related to metabolic processes taking place in MM cells and results of metabolomics experiments.** *A*, Metabolic pathways for which enzymes were found significantly up- or downregulated in MM *versus* B cells (black arrows) and in MM$_{high}$ *versus* MM$_{low}$ cells (red and orange arrows for proteins upregulated in the cytoplasm and in mitochondria, respectively, blue arrows for downregulated proteins). Some proteins found at high levels but not regulated are indicated in italics. For three selected proteins, determined LFQ values are represented as dot plots. *B*, Levels of amino acids in B and MM$_{high}$ cells. *C*, Levels of amino acids in MM-associated BM fibroblasts (MM-Fibs) and in mesenchymal cells of the BM (hMSC) that were used as reference system. Significant regulations are indicated by asterisks. For metabolomics experiments: ** p-values < 0.01; * p-values < 0.05.

chymal stem cells of the BM (hMSCs) as reference cell system, respectively. In this way, higher amounts of several amino acids were determined in MM$_{high}$ cells compared with B cells (Fig. 4*B*), strengthening our proteomics data, which suggest that MM cells may use amino acids not primarily for the synthesis of immunoglobulins, but possibly also for other

48

purposes such as catabolism. In parallel, MM-associated fibroblasts, essential supporters of MM cells in the BM microenvironment (8), proved to have rather low levels of amino acids, except for asparagine, which was present at extremely high levels in these cells when compared with hMSCs (Fig. 4C). Fibroblasts seem thus to be deregulated in a concerted fashion to MM cells.

Protein Regulation Associated with Immune Evasion Strategies—Several pathways leading to immune evasion are known for MM cells. Our data independently confirmed upregulation of SLAMF7 and CD46 (10, 58), and downregulation of MHC-IIs such as HLA-DQB1 (35), together with positive expression of MHC-I molecules such as HLA-C in MM cells (Fig. 5A). Moreover, we were able to determine new candidates possibly involved in immune escape mechanisms of MM cells likewise. Regulation of such candidates, including STAB1, SIGIRR, DAPP1 as well as VSIR (Fig. 5B), have been described to suppress immune responses and to be involved in the patho-mechanisms of different diseases (59–63). Immunohistochemistry independently verified the relative expression levels of the proteins SLAM7, CD46, and SIGIRR together with SDC1 (CD138), which depend on the disease stage (Fig. 5C).

Transcription Factors Involved in Regulating Proteins in Primary Human Myeloma Cells—Finally, in order to determine over-represented conserved transcription factor binding sites and, thus, the main transcription factors responsible for the observed proteome alterations in MM cells, the corresponding sets of genes were submitted to the oPOSSUM software version 3.0 (34). This allowed us to find out transcription factors apparently playing an important role in the development and/or progression of multiple myeloma. Besides transcription factors known to be activated in MM, such as MYC, HIF1A, and ARNT (13, 64, 65), or to be suppressed in MM, such as SPI1 (PU.1) and KLF4 (66, 67), we were able to determine also NFYA, GABPA, ELK4, and PAX4 as transcription factors that may play an important role in the pathogenesis of MM (Fig. 6A). Levels of GABPA and NFYA determined in the nuclear fractions of MM cells are represented in Fig. 6B, together with the nuclear levels of two other transcriptions factors, PAX5 and IRF4, known to be involved in MM likewise. Downregulation of PAX5 is commonly associated with plasma cell differentiation and was related to multiple myeloma cell survival (68, 69). IRF4, originally identified as the product of a proto-oncogene involved in chromosomal translocations in multiple myeloma (70), has been described to be transcribed by MYC, whereas SPI1 seems to suppress the expression of IRF4 (64, 66). Finally, levels of two target proteins, PRKD2 and BLK are also shown in Fig. 6B. PRKD2 expression depends on the activity of transcription factor GABPA (71). BLK has been shown to be suppressed by MYC via downregulation of PAX5 (72).

DISCUSSION

Myeloma Cells are Adapted to Hypoxic Conditions in the Bone Marrow Microenvironment—It is generally recognized that the bone marrow (BM) is rather hypoxic compared with peripheral blood (13, 73). Silva and Gatenby have demonstrated using computer simulation that adaptation to hypoxic conditions in the BM microenvironment is essential for myeloma cells to progress to an aggressive stage (74). HIF1A and ARNT have been described to be upregulated by tumor cells including myeloma cells under low oxygen conditions (13, 65). Both transcription factors seem to be responsible for the induction of relevant proteins in MM cells (Fig. 6A). The observed downregulation of HIF1AN and VHL (Fig. 3C) also points to hypoxic conditions in the BM microenvironment of the cells (11, 14). Remarkably, even though expression of HIF1AN and VHL may also be affected by typical anti-myeloma treatments such as Bortezomid or Dexamethasone (52, 75), levels of these proteins were rather similar in all MM cells and apparently independent on patient treatments. Further, reduced levels of proteins of the respiratory chain, such as COX6C, MT-CO$_2$ or ATP5L (supplemental Table S1) indicate a limited oxygen consumption rate in MM cells. In line with this, ATPase inhibitory factor ATPIF1 was found highly induced in MM cells (Fig. 3A); this protein is necessary to preserve ATP at the expense of the mitochondrial membrane potential when respiration is impaired, and protects cells from ATP depletion in response to hypoxia and glucose deprivation (76, 77).

However, a trend of increased synthesis of proteins of the respiratory complexes in MM$_{high}$ relative to MM$_{low}$ cells was also observed, together with upregulation of the ADP/ATP translocase SLC25A4 (Fig. 3A). Further, proteins involved in mitochondrial translation, as well as TRAP1, an important mitochondrial chaperon that directly interacts with respiratory complexes and contributes to their stability and activity (78) were found at significantly elevated levels in MM$_{high}$ cells (Figs. 3A and 3B). Although its role in carcinogenesis is controversial, TRAP1 has been found highly expressed in several cancers, as reviewed by Matassa *et al.* (79), providing tumor cells the ability to use spare respiratory capacity when oxygen and glucose are limited (80). Additionally, mitochondrial enzymes of the folate cycle, highly relevant for mitochondrial translation and described to be strongly upregulated in proliferating lymphocytes (81), were found upregulated in MM$_{high}$ cells as well (Fig. 4A). Thus, it seems that, at advanced stages of the disease, myeloma cells get access to more oxygen, consistent with the "angiogenic switch" necessary for MM progression, as claimed by Silva and Gatenby (74), and with the pro-angiogenic phenotype associated with MM-related endothelial cells (15).

Metabolic Adaptations in MM Cells as Response to Hypoxic Conditions in the Bone Marrow—Myeloma cells have to adapt their metabolic pathways to be able to survive hypoxia. PDK1
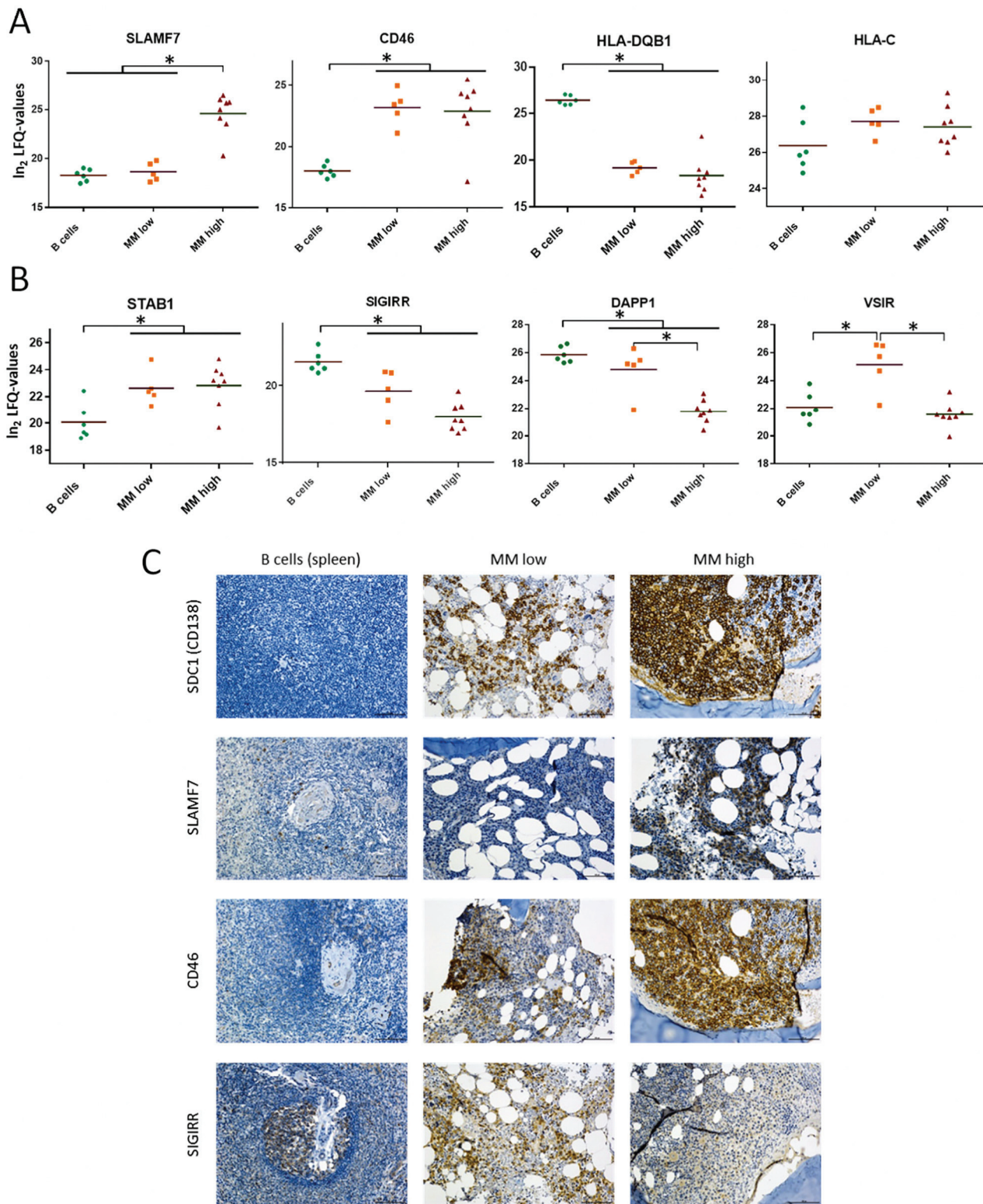
FIG. 5. **Regulation of proteins related to immune evasion strategies of MM cells.** *A*, Levels of selected proteins known to be involved in immune evasion strategies of MM cells. *B*, Levels of selected proteins potentially contributing to immune evasion strategies of MM cells likewise. *C*, Selected proteins were verified by immunohistochemistry (IHC). Stainings were performed on BM biopsies of patient MM19–27, MM19–21 representing MM$_{low}$ and MM22–27 MM$_{high}$ cases. Infiltration rates (IR) were assessed by evaluation of the entire tissue section. Because of focal infiltrates, the IR might vary within one section. Depicted image sections resemble representative areas. B cells in germinal centers of the spleen were used as reference system.
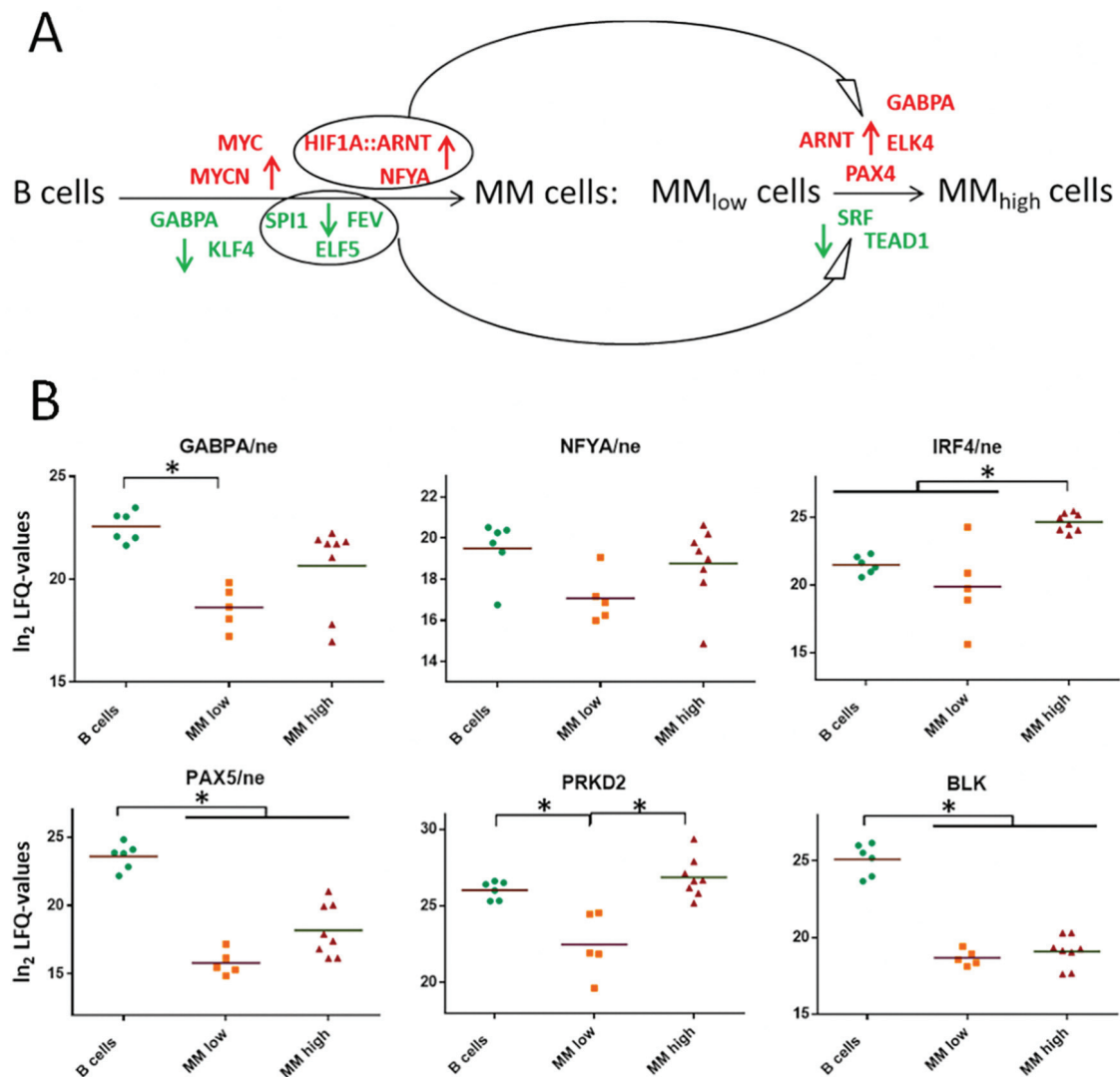
FIG. 6. **Tanscription factors (TFs) mainly responsible for the observed up- and downregulations of proteins in MM cells.** *A*, Well-known and newly determined TFs that may play an important role in MM development and/or progression. Red, TFs involved in upregulation of proteins; green, TFs involved in downregulation of proteins. HIF1A, ARNT, FYA, SPI1, FEV and ELF5 may be responsible for both, regulation of proteins in MM relative to B cells and in MM_{high} relative to MM_{low} cells. *B*, Levels of TFs detected in nuclear fractions (ne), and of two known TF targets, PRKD2 and BLK, detected in cytoplasmic fractions. Significant regulations are indicated by asterisks.

is one of the key enzymes regulating metabolic adaptations in response to hypoxia, allowing cell proliferation under these conditions (82). We have found this enzyme significantly up-regulated in MM *versus* B cells, and further in MM_{high} *versus* MM_{low} cells (Fig. 4*A*). This kinase prevents the formation of acetyl-coenzyme A from pyruvate by inhibiting the activity of pyruvate dehydrogenase, thus disconnecting glycolysis and citric acid cycle. This strategy is well-known as Warburg-effect, a strategy commonly used by tumor cells, as reviewed by Nissim Hay (83). Inhibition of PDK1 has been proposed as target for MM therapy (84). Further, we found mitochondrial pyruvate carrier MPC2 significantly downregulated in MM cells (Fig. 4*A*); loss of MPC has been associated with carci-nogenicity as well as with a stem cells phenotype (85, 86). Consistent with this, hypoxia has been shown to induce a

stem cell-like phenotype in MM cells (87), and GABPA and its target PRKD2 (Figs. 6*A* and 6*B*) have been described to control proliferation of hematopoietic stem cells as well as development of leukemia (71).

Moreover, glucose import and the glycolytic enzyme HK1 appeared to be significantly downregulated in MM_{high} cells (Fig. 4*A*), pointing to a reduced glycolysis rate in MM cells of advanced stages of the disease. This is in accordance with the already discussed upregulation of ATPIF1 and TRAP1 in MM_{high} cells. On the other hand, uptake of glutamine seems to be highly increased in MM_{high} cells (Fig. 4*A*), consistent with the observed glutamine dependence of MM cells (88). Glutamine is required for the hexosamine pathway, which is highly upregulated in MM_{high} cells (Fig. 4*A*). This pathway leads to protein glycosylation as part of the completion proc-

51

ess of newly synthesized proteins. Multiple myeloma is characterized by aberrantly glycosylated immunoglobulins (89), which are synthesized in high amounts by MM cells. Most importantly, glutamine can also be interconverted into asparagine, which might be used for the import of other amino acids via reciprocal exchange (90); levels of glutamine-hydrolyzing asparagine synthetase ASNS and transporter proteins involved in these processes, SLC1A4 and SLC1A5, were found significantly increased in MM_{high} cells (Fig. 4A). Results of the targeted analyses of amino acids further point to the likelihood that BM fibroblasts may supply MM cells with several of the necessary amino acids, probably in exchange for asparagine (Figs. 4B and 4C). This view is supported by the fact that BM stromal cells such as fibroblasts are widely used as feeder layers for MM cells in cell culture experiments (91). Remarkably, asparagine synthesis has been associated with survival of glutamine-dependent tumor cells, and expression of ASNS was correlated with poor prognosis in several tumors (92). Studies have indeed suggested good anti-myeloma activity of asparaginase (93).

Glutamate arising from the interconversion of glutamine to asparagine may be used for the synthesis of serine, which feeds into the folate cycle (Fig. 4A). Interfering with the serine metabolism has been proposed to improve anti-myeloma therapies (94). Alternatively, glutamate may be transported into mitochondria to be channeled into the citric acid cycle, directly or via interconversion into other amino acids (Fig. 4A). As depicted above, it appears that myeloma cells of advanced stages of the disease are capable of increasing respiration again. Our data indicate that fuels for oxidative phosphorylation in MM_{high} cells may arise from degradation of amino acids (Fig. 4A). Remarkably, we also observed increased mitochondrial fatty acid synthesis and upregulation of proteins involved in the methionine cycle (Fig. 4A). These two pathways give rise to lipoic acid, a cofactor of the enzyme BCKDH, which is necessary for branched chain amino acid degradation (95) and was found upregulated in MM_{high} cells (Fig. 4A). There is, furthermore, evidence that mitochondrial fatty acid synthesis is essential for respiration and mitochondrial biogenesis (96).

Two proteins involved in mitochondrial fusion, CLPP and CLPX (97), were also found significantly upregulated in MM_{high} cells, whereas OMA1, which prevents fusion (98) and SLC25A46, which is involved in mitochondrial fission (99) were found significantly downregulated in MM cells (supplemental Table S1). Mitochondria, which are metabolically challenged when cells switch to use amino acids or fatty acids for ATP production, have been described to undergo active fusion to avoid oxidative stress and mitochondrial damage (100). Enlarged mitochondria in multiple myeloma cells have already been described in the 1980s by Ghadially et al. (101). Further, we also found upregulation of ECSIT in MM_{high} cells relative to MM_{low} and B cells (Fig. 3A); this protein, besides being involved in the assembly of mitochondrial complex I, also plays an essential role in mitophagy-dependent mito-

chondrial quality control, preventing accumulation of damaged mitochondria (102).

In addition, cholesterol uptake as well as cholesterol metabolic processes were found upregulated in MM cells and especially in MM_{high} cells (Fig. 4A). This is in accordance with observations about hypocholesterinemia in the plasma of MM patients, associated with increased LDL clearance and use of cholesterol by MM cells, which seem to be necessary for MM cell survival (103, 104).

Responsible for deregulation of metabolic processes in MM_{high} versus MM_{low} cells may be the activation of transcription factor NFYA, which appeared to be involved in protein regulation in MM cells and showed a trend of upregulation in MM_{high} cells (Figs. 6A and 6B). This transcription factor promotes the expression of proteins fueling metabolic pathways commonly altered in cancer cells, such as the serine, the one carbon, the glycine, the glutamine pathways and the cholesterol pathway (105). Further, MYC is involved in regulating glutamine metabolism as well. Very recently, Gonsalves et al. have demonstrated that higher levels of MYC in smoldering myeloma cells correlate with an increased use of glutamine for the citric acid cycle and a shorter time to progression to MM (106). This is consistent with our data indicating an increased uptake of glutamine in MM_{high} cells, which apparently channel this amino acid into the citric acid cycle (Fig. 4A).

Myeloma Cells Adapt ER Activities to Hypoxic Conditions in the Bone Marrow—Stress proteins of the endoplasmic reticulum (ER) such as glucose-regulated and heat-shock proteins have been shown to be involved in resistance against environmental stress such as that caused by hypoxia, in avoidance of stress-induced apoptosis, and in cancer development (107, 108). It has also been demonstrated that protein-disulfide isomerases are upregulated in response to hypoxia and are critical for cell viability under these conditions (109). In line with this, we found massive upregulation of HSP90B1 (GRP94), HSPA5 (GRP78), HYOU1 (GRP170), and HSPA13 in MM versus B cells, and moreover in MM_{high} versus MM_{low} cells; the same trend was observed for protein-disulfide isomerases such as P4HB, PDIA4, PDIA5, and PDIA6 (Figs. 2A–2C). Azoitei et al. have shown that signals from hypoxia and HSP90 pathways are interconnected via PRKD2 (Figs. 6A and 6B), which is apparently necessary to prevent apoptosis and promote tumor angiogenesis and tumor growth (110). Activation of transcription factor PAX4 (Fig. 6A), proposed as candidate oncogene in hematologic malignancies (111), has also shown to contribute to protect against ER stress-induced apoptosis (112).

Myeloma Cells Have Strategies to Prevent Apoptosis Under Hypoxic and Normoxic Conditions—Ikeda et al. have demonstrated that myeloma cells are compatible with both hypoxic and normoxic conditions (16). Under hypoxic conditions, HIF apparently activates micro-RNA-210 that blocks the DIMT1-IRF4 axis and leads to glycolysis and to quiescence of the cells. Under normoxic conditions, active DIMT1 and IRF4

induce myeloma cell maturation and proliferation. Remarkably, we found IRF4 and DIMT1 to be present at significantly higher levels in MM$_{high}$ than in MM$_{low}$ cells (Figs. 3C and 6B). This fits to our model in which MM$_{low}$ cells are confronted with more hypoxic conditions than MM$_{high}$ cells, and that glycolysis is rather downregulated in MM$_{high}$ versus MM$_{low}$ cells. Most importantly, myeloma cells are obviously capable of preventing apoptosis under both conditions (16). In line with this, we were able to determine several proteins that may support cell death escaping mechanisms in MM$_{low}$ and MM$_{high}$ cells (Fig. 1D). In MM$_{low}$ cells hypoxia-induced anti-apoptotic factors such as SRC and FYN (55, 113) were found upregulated (Fig. 3C). This was accompanied by downregulation of pro-apoptotic proteins such as hypoxia-regulated proteins BAX (114), TP53I11 (115), and BLK (116) (Figs. 1E, 3C, and 6B). In MM$_{high}$ cells, elevated levels of anti-apoptotic proteins such as HYOU1 (117), SDF4 (47, 118), TRAP1 (119), and the ADP/ATP translocase SLC25A4 (120) (Figs. 1D, 2C, and 3A) were detected, together with IRF4 (121), which may also act indirectly in an anti-apoptotic way via induction of CASP10 (122) (Figs. 1E and 6B).

Myeloma Cells Develop Hypoxia-driven Strategies to Escape Immune Response—Besides evading intrinsic apoptosis, MM cells have pathways that limit extrinsic apoptosis induced by the immune system, involving for example up-regulation of CD38, CD46, SLAMF7 (CS1), and MHC-I molecules (Figs. 1C, 5A, and 5C) (10, 58). In case of CD38 and SLAM7 therapeutic antibodies are already tested in clinical trials for combination therapies (123). Remarkably, SLAM7, showed different expression levels depending on the disease stage (Figs. 5A and 5C), and may thus be applied as stratification marker of use in antibody therapy. Reduced levels of MHC-II molecules, as well as MHC-II-associated proteins such as CD37 (Figs. 1C and 5A), may also contribute to immune evasion by impeding the antigen presentation capacity of MM cells and their interactions with T cells (124, 125). Upregulation of MYC (Fig. 6A) has been shown to disrupt MHC-II-mediated immune recognition of human B cell tumors (126).

The presently applied untargeted method also revealed novel candidates potentially involved in immune escape mechanisms of MM cells, such as DAPP1 and STAB1 (Fig. 5B) (59, 62). Further, VSIR (Fig. 5B) may negatively regulate T cell functions, at least at earlier stages of the disease. This protein has been found highly expressed in tumor microenvironments where it seems to suppress the proliferation of T cells without affecting B cells, as described by Lines *et al.* (63). Reduced levels of SIGIRR (Figs. 5B and 5C) may also be involved in immune escape mechanisms of MM cells. This protein has also been found downregulated in chronic lymphocytic leukemia (61). It is however worth mentioning that, when comparing immune evasion strategies of MM cells with those of CLL cells described in a previous study of our group (22), more differences than similarities became evident.

Remarkably, hypoxic conditions in the BM microenvironment may induce mechanisms leading to immune evasion of MM cells. As mentioned before, Ikeda *et al.* have shown that under hypoxic conditions micro-RNA-210 is activated in MM cells (16). Noman *et al.* have demonstrated that, in lung cancer and melanoma, high levels of micro-RNA-210 dramatically decrease tumor cell susceptibility to cytotoxic T cell-mediated lysis via coordinate silencing of PTPN1, HOXA1 and TP53I11 (54). Our data indicate that PTPN1 is significantly reduced in MM$_{low}$ relative to B cells and a similar trend was observed for MM$_{high}$ versus B cells (Fig. 3C). HOXA1 was not detected in any sample investigated in the present study. TP53I11 was found significantly downregulated in both MM$_{low}$ and MM$_{high}$ cells (Fig. 3C), and the higher oxygen availability of MM$_{high}$ cells seems not to be sufficient to restore high levels of this protein.

Conclusion and Outlook—The present proteome profiling data strongly support that adaptation of MM cells to hypoxia accompanies myeloma disease progression. Our results demonstrate that in-depth proteome profiling is very well suited to give deep insights into processes that are contributing to tumor development and progression. The data clearly reproduced established knowledge on myeloma cells, but also present novel findings and causal relations of relevant pathways taking place in these tumor cells. Importantly, it seems that strategies exploited by myeloma cells to allow survival and proliferation, including immune evasion mechanisms and metabolic adaptations, are more dependent on the disease state than on the genetic background. This study may thus support the development of improved stratification and anti-myeloma treatment strategies.

DATA AVAILABILITY

Proteomics data were submitted to the ProteomeXchange Consortium via the PRIDE partner repository. Results are fully accessible via www.proteomeexchange.org with the identifier PXD010600.

** To whom correspondence should be addressed: Department of Analytical Chemistry, University of Vienna, Waehringer Strasse 38, 1090 Vienna, Austria. Tel.: +43-1-4277-52315; E-mail: astrid.slany@univie.ac.at.

‡‡ Authors contributed equally to this work.

REFERENCES

1. Kyle, R. A., and Rajkumar, S. V. (2008) Multiple myeloma. *Blood* **111,** 2962–2972

2. Terpos, E., and Soc, I. M. (2018) Multiple myeloma: clinical updates from the American Society of Hematology Annual Meeting, 2017. *Cl. Lymph. Myelom. Leuk.* **18,** 321–334

3. du Pont, S. R., Cleynen, A., Fontan, C., Attal, M., Munshi, N., Corre, J., and Avet-Loiseau, H. (2017) Genomics of multiple myeloma. *J. Clin. Oncol.* **35,** 963–967

4. van de Donk, N. W. C. J., Mutis, T., Poddighe, P. J., Lokhorst, H. M., and Zweegman, S. (2016) Diagnosis, risk stratification and management of monoclonal gammopathy of undetermined significance and smoldering multiple myeloma. *Int. J. Lab. Hematol.* **38,** 110–122

5. Bianchi, G., and Munshi, N. C. (2015) Pathogenesis beyond the cancer clone (s) in multiple myeloma. *Blood* **125,** 3049–3058

6. Dutta, A. K., Fink, J. L., Grady, J. P., Morgan, G. J., Mullighan, C. G., To, L. B., Hewett, D. R., and Zannettino, A. C. W. (2018) Subclonal evolution in disease progression from MGUS/SMM to multiple myeloma is characterised by clonal stability. *Leukemia* **33,** 457–468

7. Mitsiades, C. S., Mitsiades, N. S., Munshi, N. C., Richardson, P. G., and Anderson, K. C. (2006) The role of the bone microenvironment in the pathophysiology and therapeutic management of multiple myeloma: Interplay of growth factors, their receptors and stromal interactions. *Eur. J. Cancer* **42,** 1564–1573

8. Slany, A., Haudek-Prinz, V., Meshcheryakova, A., Bileck, A., Lamm, W., Zielinski, C., Gerner, C., and Drach, J. (2014) Extracellular matrix remodeling by bone marrow fibroblast-like cells correlates with disease progression in multiple myeloma. *J. Proteome Res.* **13,** 844–854

9. Gooding, S., and Edwards, C. M. (2016) New approaches to targeting the bone marrow microenvironment in multiple myeloma. *Curr. Opin. Pharmacol.* **28,** 43–49

10. Pittari, G., Vago, L., Festuccia, M., Bonini, C., Mudawi, D., Giaccone, L., and Bruno, B. (2017) Restoring natural killer cell immunity against multiple myeloma in the era of new drugs. *Front. Immunol.* **8,** 1444

11. Hu, J., Van Valckenborgh, E., Menu, E., De Bruyne, E., and Vanderkerken, K. (2012) Understanding the hypoxic niche of multiple myeloma: therapeutic implications and contributions of mouse models. *Dis. Model Mech.* **5,** 763–771

12. Filippi, I., Saltarella, I., Aldinucci, C., Carraro, F., Ria, R., Vacca, A., and Naldini, A. (2018) Different adaptive responses to hypoxia in normal and multiple myeloma endothelial cells. *Cell Physiol. Biochem.* **46,** 203–212

13. Colla, S., Storti, P., Donofrio, G., Todoerti, K., Bolzoni, M., Lazzaretti, M., Abeltino, M., Ippolito, L., Neri, A., Ribatti, D., Rizzoli, V., Martella, E., and Giuliani, N. (2010) Low bone marrow oxygen tension and hypoxia-inducible factor-1 alpha overexpression characterize patients with multiple myeloma: role on the transcriptional and proangiogenic profiles of CD138(+) cells. *Leukemia* **24,** 1967–1970

14. Martin, S. K., Diamond, P., Gronthos, S., Peet, D. J., and Zannettino, A. C. (2011) The emerging role of hypoxia, HIF-1 and HIF-2 in multiple myeloma. *Leukemia* **25,** 1533–1542

15. Vacca, A., Ria, R., Semeraro, F., Merchionne, F., Coluccia, M., Boccarelli, A., Scavelli, C., Nico, B., Gernone, A., Battelli, F., Tabilio, A., Guidolin, D., Petrucci, M. T., Ribatti, D., and Dammacco, F. (2003) Endothelial cells in the bone marrow of patients with multiple myeloma. *Blood* **102,** 3340–3348

16. Ikeda, S., Kitadate, A., Abe, F., Saitoh, H., Michishita, Y., Hatano, Y., Kawabata, Y., Kitabayashi, A., Teshima, K., Kume, M., Takahashi, N., and Tagawa, H. (2017) Hypoxia-inducible microRNA-210 regulates the DIMT1-IRF4 oncogenic axis in multiple myeloma. *Cancer Sci.* **108,** 641–652

17. Bhaskar, A., and Tiwary, B. N. (2016) Hypoxia inducible factor-1 alpha and multiple myeloma. *Int. J. Adv. Res.* **4,** 706–715

18. Groessl, M., Slany, A., Bileck, A., Gloessmann, K., Kreutz, D., Jaeger, W., Pfeiler, G., and Gerner, C. (2014) Proteome profiling of breast cancer biopsies reveals a wound healing signature of cancer-associated fibroblasts. *J. Proteome Res.* **13,** 4773–4782

19. Slany, A., Bileck, A., Kreutz, D., Mayer, R. L., Muqaku, B., and Gerner, C. (2016) Contribution of human fibroblasts and endothelial cells to the hallmarks of inflammation as determined by proteome profiling. *Mol. Cell. Proteomics* **15,** 1982–1997

20. Tahir, A., Bileck, A., Muqaku, B., Niederstaetter, L., Kreutz, D., Mayer, R. L., Wolrab, D., Meier, S. M., Slany, A., and Gerner, C. (2017) Combined proteome and eicosanoid profiling approach for revealing implications of human fibroblasts in chronic inflammation. *Anal. Chem.* **89,** 1945–1954

21. Muqaku, B., Eisinger, M., Meier, S. M., Tahir, A., Pukrop, T., Haferkamp, S., Slany, A., Reichle, A., and Gerner, C. (2017) Multi-omics analysis of serum samples demonstrates reprogramming of organ functions via systemic calcium mobilization and platelet activation in metastatic melanoma. *Mol. Cell. Proteomics* **16,** 86–99

22. Mayer, R. L., Schwarzmeier, J. D., Gerner, M. C., Bileck, A., Mader, J. C., Meier-Menches, S. M., Gerner, S. M., Schmetterer, K. G., Pukrop, T., Reichle, A., Slany, A., and Gerner, C. (2018) Proteomics and metabolomics identify molecular mechanisms of aging potentially predisposing for chronic lymphocytic leukemia. *Mol. Cell. Proteomics* **17,** 290–303

23. Dytfeld, D., Luczak, M., Wrobel, T., Usnarska-Zubkiewicz, L., Brzezniak-iewicz, K., Jamroziak, K., Giannopoulos, K., Przybylowicz-Chalecka, A., Ratajczak, B., Czerwinska-Rybak, J., Nowicki, A., Joks, M., Czechowska, E., Zawartko, M., Szczepaniak, T., Grzasko, N., Morawska, M., Bochenek, M., Kubicki, T., Morawska, M., Tusznio, K., Jakubowiak, A., and Komarnicki, M. (2016) Comparative proteomic profiling of refractory/relapsed multiple myeloma reveals biomarkers involved in resistance to bortezomib-based therapy. *Oncotarget* **7,** 56726–56736

24. Fernando, R. C., de Carvalho, F., Mazzotti, D. R., Evangelista, A. F., Braga, W. M. T., de Lourdes Chauffaille, M., Leme, A. F. P., and Colleoni, G. W. B. (2015) Multiple myeloma cell lines and primary tumors proteoma: protein biosynthesis and immune system as potential therapeutic targets. *Genes Cancer* **6,** 462–471

25. Xie, Z., Gunaratne, J., Cheong, L. L., Liu, S. C., Koh, T. L., Huang, G., Blackstock, W. P., and Chng, W. J. (2013) Plasma membrane proteomics identifies biomarkers associated with MMSET overexpression in T(4;14) multiple myeloma. *Oncotarget* **4,** 1008–1018

26. Ge, F., Xiao, C. L., Yin, X. F., Lu, C. H., Zeng, H. L., and He, Q. Y. (2010) Phosphoproteomic analysis of primary human multiple myeloma cells. *J. Proteomics* **73,** 1381–1390

27. Haudek-Prinz, V. J., Klepeisz, P., Slany, A., Griss, J., Meshcheryakova, A., Paulitschke, V., Mitulovic, G., Stockl, J., and Gerner, C. (2012) Proteome signatures of inflammatory activated primary human peripheral blood mononuclear cells. *J Proteomics* **76,** Spec No., 150–162

28. Bileck, A., Kreutz, D., Muqaku, B., Slany, A., and Gerner, C. (2014) Comprehensive Assessment of Proteins Regulated by Dexamethasone Reveals Novel Effects in Primary Human Peripheral Blood Mononuclear Cells. *J. Proteome Res.* **13,** 5989–6000

29. Wisniewski, J. R., Zougman, A., Nagaraj, N., and Mann, M. (2009) Universal sample preparation method for proteome analysis. *Nat. Methods* **6,** 359–362

30. Cox, J., and Mann, M. (2008) MaxQuant enables high peptide identification rates, individualized p.p.b.-range mass accuracies and proteome-wide protein quantification. *Nat. Biotechnol.* **26,** 1367–1372

31. Vizcaino, J. A., Csordas, A., del-Toro, N., Dianes, J. A., Griss, J., Lavidas, I., Mayer, G., Perez-Riverol, Y., Reisinger, F., Ternent, T., Xu, Q. W., Wang, R., and Hermjakob, H. (2016) 2016 update of the PRIDE database and its related tools. *Nucleic Acids Res.* **44,** D447–D456

32. Palumbo, A., Avet-Loiseau, H., Oliva, S., Lokhorst, H. M., Goldschmidt, H., Rosinol, L., Richardson, P., Caltagirone, S., Lahuerta, J. J., Facon, T., Bringhen, S., Gay, F., Attal, M., Passera, R., Spencer, A., Offidani, M., Kumar, S., Musto, P., Lonial, S., Petrucci, M. T., Orlowski, R. Z., Zamagni, E., Morgan, G., Dimopoulos, M. A., Durie, B. G., Anderson, K. C., Sonneveld, P., San Miguel, J., Cavo, M., Rajkumar, S. V., and Moreau, P. (2015) Revised international staging system for multiple myeloma: A report from international myeloma working group. *J. Clin. Oncol.* **33,** 2863–2869

33. Cox, J., and Mann, M. (2012) 1D and 2D annotation enrichment: a statistical method integrating quantitative proteomics with complementary high-throughput data. *BMC Bioinformatics* **13**

34. Ho Sui, S. J., Mortimer, J. R., Arenillas, D. J., Brumm, J., Walsh, C. J., Kennedy, B. P., and Wasserman, W. W. (2005) oPOSSUM: identification of over-represented transcription factor binding sites in co-expressed genes. *Nucleic Acids Res.* **33,** 3154–3164

54

35. Lohmeyer, J., Hadam, M., Santoso, S., Forster, W., Schulz, A., and Pralle, H. (1988) Establishment and characterization of a permanent human Iga2 kappa-myeloma cell-line. *Brit. J. Haematol.* **69,** 335–343

36. Rawstron, A. C., Owen, R. G., Davies, F. E., Johnson, R. J., Jones, R. A., Richards, S. J., Evans, P. A., Child, J. A., Smith, G. M., Jack, A. S., and Morgan, G. J. (1997) Circulating plasma cells in multiple myeloma: Characterization and correlation with disease stage. *Brit. J. Haematol.* **97,** 46–55

37. Hanahan, D., and Weinberg, R. A. (2011) Hallmarks of cancer: The next generation. *Cell* **144,** 646–674

38. Huang, D. W., Sherman, B. T., and Lempicki, R. A. (2009) Systematic and integrative analysis of large gene lists using DAVID bioinformatics resources. *Nat. Protoc.* **4,** 44–57

39. Huang, D. W., Sherman, B. T., and Lempicki, R. A. (2009) Bioinformatics enrichment tools: paths toward the comprehensive functional analysis of large gene lists. *Nucleic Acids Res.* **37,** 1–13

40. Bateman, A., Martin, M. J., O'Donovan, C., Magrane, M., Alpi, E., Antunes, R., Bely, B., Bingley, M., Bonilla, C., Britto, R., Bursteinas, B., Bye Jee, -A. -H., Cowley, A., Da Silva, A., De Giorgi, M., Dogan, T., Fazzini, F., Castro, L. G., Figueira, L., Garmiri, P., Georghiou, G., Gonzalez, D., Hatton-Ellis, E., Li, W. Z., Liu, W. D., Lopez, R., Luo, J., Lussi, Y., MacDougall, A., Nightingale, A., Palka, B., Pichler, K., Poggioli, D., Pundir, S., Pureza, L., Qi, G. Y., Rosanoff, S., Saidi, R., Sawford, T., Shypitsyna, A., Speretta, E., Turner, E., Tyagi, N., Volynkin, V., Wardell, T., Warner, K., Watkins, X., Zaru, R., Zellner, H., Xenarios, I., Bouguel-eret, L., Bridge, A., Poux, S., Redaschi, N., Aimo, L., Argoud-Puy, G., Auchincloss, A., Axelsen, K., Bansal, P., Baratin, D., Blatter, M. C., Boeckmann, B., Bolleman, J., Boutet, E., Breuza, L., Casal-Casas, C., de Castro, E., Coudert, E., Cuche, B., Doche, M., Dornevil, D., Duvaud, S., Estreicher, A., Famiglietti, L., Feuermann, M., Gasteiger, E., Gehant, S., Gerritsen, V., Gos, A., Gruaz-Gumowski, N., Hinz, U., Hulo, C., Jungo, F., Keller, G., Lara, V., Lemercier, P., Lieberherr, D., Lombardot, T., Martin, X., Masson, P., Morgat, A., Neto, T., Nouspikel, N., Paesano, S., Pedruzzi, I., Pilbout, S., Pozzato, M., Pruess, M., Rivoire, C., Roechert, B., Schneider, M., Sigrist, C., Sonesson, K., Staehli, S., Stutz, A., Sundaram, S., Tognolli, M., Verbregue, L., Veuthey, A. L., Wu, C. H., Arighi, C. N., Arminski, L., Chen, C. M., Chen, Y. X., Garavelli, J. S., Huang, H. Z., Laiho, K., McGarvey, P., Natale, D. A., Ross, K., Vinayaka, C. R., Wang, Q. H., Wang, Y. Q., Yeh, L. S., Zhang, J., and Consortium, U. (2017) UniProt: the universal protein knowledgebase. *Nucleic Acids Res.* **45,** D158–D169

41. Shimizu, Y., and Hendershot, L. M. (2009) Oxidative folding: cellular strategies for dealing with the resultant equimolar production of reactive oxygen species. *Antioxid. Redox Sign.* **11,** 2317–2331

42. Demasi, A. P., Martinez, E. F., Napimoga, M. H., Freitas, L. L., Vassallo, J., Duarte, A. S., Soares, A. B., Araujo, N. S., and Araujo, V. C. (2013) Expression of peroxiredoxins I and IV in multiple myeloma: association with immunoglobulin accumulation. *Virchows Arch.* **463,** 47–55

43. Scorrano, L., Oakes, S. A., Opferman, J. T., Cheng, E. H., Sorcinelli, M. D., Pozzan, T., and Korsmeyer, S. J. (2003) BAX and BAK regulation of endoplasmic reticulum Ca2+: A control point for apoptosis. *Science* **300,** 135–139

44. Zeng, T., Peng, L. F., Chao, H. C., Xi, H. B., Fu, B., Wang, Y. B., Zhu, Z. W., and Wang, G. X. (2015) IRE1 alpha-TRAF2-ASK1 complex-mediated endoplasmic reticulum stress and mitochondrial dysfunction contribute to CXC195-induced apoptosis in human bladder carcinoma T24 cells. *Biochem. Bioph. Res. Co.* **460,** 530–536

45. Vento, M. T., Zazzu, V., Loffreda, A., Cross, J. R., Downward, J., Stoppelli, M. P., and Iaccarino, I. (2010) Praf2 is a novel Bcl-xL/Bcl-2 interacting protein with the ability to modulate survival of cancer cells. *Plos One* **5,** e15636

46. Tiwari, A., Schuiki, I., Zhang, L. L., Allister, E. M., Wheeler, M. B., and Volchuk, A. (2013) SDF2L1 interacts with the ER-associated degradation machinery and retards the degradation of mutant proinsulin in pancreatic beta-cells. *J. Cell Sci.* **126,** 1962–1968

47. Chen, L., Xu, S., Liu, L., Wen, X., Xu, Y., Chen, J., and Teng, J. (2014) Cab45S inhibits the ER stress-induced IRE1-JNK pathway and apoptosis via GRP78/BiP. *Cell Death Dis.* **5,** e1219

48. Xu, S., Xu, Y., Chen, L., Fang, Q., Song, S., Chen, J., and Teng, J. (2017) RCN1 suppresses ER stress-induced apoptosis via calcium homeostasis and PERK-CHOP signaling. *Oncogenesis* **6,** e304

49. Peng, F. S., Zhang, H. L., Du, Y. H., and Tan, P. Q. (2018) Cetuximab enhances cisplatin-induced endoplasmic reticulum stress-associated apoptosis in laryngeal squamous cell carcinoma cells by inhibiting expression of TXNDC5. *Mol. Med. Reports* **17,** 4767–4776

50. Lando, D., Peet, D. J., Gorman, J. J., Whelan, D. A., Whitelaw, M. L., and Bruick, R. K. (2002) FIH-1 is an asparaginyl hydroxylase enzyme that regulates the transcriptional activity of hypoxia-inducible factor. *Gene Dev.* **16,** 1466–1471

51. Maxwell, P. H., Wiesener, M. S., Chang, G. W., Clifford, S. C., Vaux, E. C., Cockman, M. E., Wykoff, C. C., Pugh, C. W., Maher, E. R., and Ratcliffe, P. J. (1999) The tumour suppressor protein VHL targets hypoxia-inducible factors for oxygen-dependent proteolysis. *Nature* **399,** 271–275

52. Shin, D. H., Chun, Y. S., Lee, D. S., Huang, L. E., and Park, J. W. (2008) Bortezomib inhibits tumor adaptation to hypoxia by stimulating the FIH-mediated repression of hypoxia-inducible factor-1. *Blood* **111,** 3131–3136

53. Mahon, P. C., Hirota, K., and Semenza, G. L. (2001) FIH-1: a novel protein that interacts with HIF-1alpha and VHL to mediate repression of HIF-1 transcriptional activity. *Genes Dev.* **15,** 2675–2686

54. Noman, M. Z., Buart, S., Romero, P., Ketari, S., Janji, B., Mari, B., Mami-Chouaib, F., and Chouaib, S. (2012) Hypoxia-inducible miR-210 regulates the susceptibility of tumor cells to lysis by cytotoxic T cells. *Cancer Res.* **72,** 4629–4641

55. Hu, H., Takano, N., Xiang, L., Gilkes, D. M., Luo, W., and Semenza, G. L. (2014) Hypoxia-inducible factors enhance glutamate signaling in cancer cells. *Oncotarget* **5,** 8853–8868

56. Razorenova, O. V., Finger, E. C., Colavitti, R., Chernikova, S. B., Boiko, A. D., Chan, C. K., Krieg, A., Bedogni, B., LaGory, E., Weissman, I. L., Broome-Powell, M., and Giaccia, A. J. (2011) VHL loss in renal cell carcinoma leads to up-regulation of CUB domain-containing protein 1 to stimulate PKC{delta}-driven migration. *Proc. Natl. Acad. Sci. U.S.A.* **108,** 1931–1936

57. Minchenko, O. H., Tsymbal, D. O., Minchenko, D. O., and Kubaychuk, O. O. (2016) Hypoxic regulation of MYBL1, MEST, TCF3, TCF8, GTF2B, GTF2F2 and SNAI2 genes expression in U87 glioma cells upon IRE1 inhibition. *Ukr. Biochem. J.* **88,** 52–62

58. Sherbenou, D. W., Aftab, B. T., Su, Y., Behrens, C. R., Wiita, A., Logan, A. C., Acosta-Alvear, D., Hann, B. C., Walter, P., Shuman, M. A., Wu, X. B., Atkinson, J. P., Wolf, J. L., Martin, T. G., and Liu, B. (2016) Antibody-drug conjugate targeting CD46 eliminates multiple myeloma cells. *J. Clin. Invest.* **126,** 4640–4653

59. Palani, S., Elima, K., Ekholm, E., Jalkanen, S., and Salmi, M. (2016) Monocyte stabilin-1 suppresses the activation of Th1 lymphocytes. *J. Immunol.* **196,** 115–123

60. Karikoski, M., Marttila-Ichihara, F., Elima, K., Rantakari, P., Hollmen, M., Kelkka, T., Gerke, H., Huovinen, V., Irjala, H., Holmdahl, R., Salmi, M., and Jalkanen, S. (2014) Clever-1/stabilin-1 controls cancer growth and metastasis. *Clin Cancer Res.* **20,** 6452–6464

61. Vilia, M. G., Fonte, E., Rodriguez, T. V., Tocchetti, M., Ranghetti, P., Scarfo, L., Papakonstantinou, N., Ntoufa, S., Stamatopoulos, K., Ghia, P., and Muzio, M. (2017) The inhibitory receptor toll interleukin-1R 8 (TIR8/IL-1R8/SIGIRR) is downregulated in chronic lymphocytic leukemia. *Leukemia Lymphoma* **58,** 2419–2425

62. Al-Alwan, M., Hou, S., Zhang, T. T., Makondo, K., and Marshall, A. J. (2010) Bam32/DAPP1 promotes B cell adhesion and formation of polarized conjugates with T cells. *J. Immunol.* **184,** 6961–6969

63. Lines, J. L., Pantazi, E., Mak, J., Sempere, L. F., Wang, L., O'Connell, S., Ceeraz, S., Suriawinata, A. A., Yan, S., Ernstoff, M. S., and Noelle, R. (2014) VISTA is an immune checkpoint molecule for human T cells. *Cancer Res.* **74,** 1924–1932

64. Shaffer, A. L., Emre, N. C. T., Lamy, L., Ngo, V. N., Wright, G., Xiao, W. M., Powell, J., Dave, S., Yu, X., Zhao, H., Zeng, Y. X., Chen, B. Z., Epstein, J., and Staudt, L. M. (2008) IRF4 addiction in multiple myeloma. *Nature* **454,** 226–231

65. Hassen, W., Kassambara, A., Reme, T., Sahota, S., Seckinger, A., Vincent, L., Cartron, G., Moreaux, J., Hose, D., and Klein, B. (2015) Drug metabolism and clearance system in tumor cells of patients with multiple myeloma. *Oncotarget* **6,** 6431–6447

66. Ueno, N., Nishimura, N., Ueno, S., Endo, S., Tatetsu, H., Hirata, S., Hata, H., Matsuoka, M., Mitsuya, H., and Okuno, Y. (2017) PU.1 acts as tumor

suppressor for myeloma cells through direct transcriptional repression of IRF4. *Oncogene* **36,** 4481–4497

67. Schoenhals, M., Kassambara, A., Veyrune, J. L., Moreaux, J., Goldschmidt, H., Hose, D., and Klein, B. (2013) Kruppel-like factor 4 blocks tumor cell proliferation and promotes drug resistance in multiple myeloma. *Haematologica* **98,** 1442–1449

68. Nera, K. P., Kohonen, P., Narvi, E., Peippo, A., Mustonen, L., Terho, P., Koskela, K., Buerstedde, J. M., and Lassila, O. (2006) Loss of Pax5 promotes plasma cell differentiation. *Immunity* **24,** 283–293

69. Proulx, M., Cayer, M. P., Drouin, M., Laroche, A., and Jung, D. (2010) Overexpression of PAX5 induces apoptosis in multiple myeloma cells. *Int. J. Hematol.* **92,** 451–462

70. Iida, S., Rao, P. H., Butler, M., Corradini, P., Boccadoro, M., Klein, B., Chaganti, R. S., and Dalla-Favera, R. (1997) Deregulation of MUM1/IRF4 by chromosomal translocation in multiple myeloma. *Nat. Genet.* **17,** 226–230

71. Yang, Z. F., Zhang, H. J., Ma, L. Y., Peng, C., Chen, Y. Y., Wang, J. L., Green, M. R., Li, S. G., and Rosmarin, A. G. (2013) GABP transcription factor is required for development of chronic myelogenous leukemia via its control of PRKD2. *Proc. Natl. Acad. Sci. U.S.A.* **110,** 2312–2317

72. Zhang, H. J., Peng, C., Hu, Y. G., Li, H. W., Sheng, Z., Chen, Y. Y., Sullivan, C., Cerny, J., Hutchinson, L., Higgins, A., Miron, P., Zhang, X. Q., Brehm, M. A., Li, D. G., Green, M. R., and Li, S. G. (2012) The Blk pathway functions as a tumor suppressor in chronic myeloid leukemia stem cells. *Nat. Genet.* **44,** 861–871

73. Harrison, J. S., Rameshwar, P., Chang, V., and Bandari, P. (2002) Oxygen saturation in the bone marrow of healthy volunteers. *Blood* **99,** 394–394

74. Silva, A. S., and Gatenby, R. A. (2011) Adaptation to survival in germinal center is the initial step in onset of indolent stage of multiple myeloma. *Mol. Pharm.* **8,** 2012–2020

75. Vettori, A., Greenald, D., Wilson, G. K., Peron, M., Facchinello, N., Markham, E., Sinnakaruppan, M., Matthews, L. C., McKeating, J. A., Argenton, F., and van Eeden, F. J. M. (2017) Glucocorticoids promote Von Hippel Lindau degradation and Hif-1alpha stabilization. *Proc. Natl. Acad. Sci. U.S.A.* **114,** 9948–9953

76. Campanella, M., Parker, N., Tan, C. H., Hall, A. M., and Duchen, M. R. (2009) IF(1): setting the pace of the F(1)F(o)-ATP synthase. *Trends Biochem. Sci.* **34,** 343–350

77. Campanella, M., Casswell, E., Chong, S., Farah, Z., Wieckowski, M. R., Abramov, A. Y., Tinker, A., and Duchen, M. R. (2008) Regulation of mitochondrial structure and function by the F1Fo-ATPase inhibitor protein, IF1. *Cell Metab.* **8,** 13–25

78. Altieri, D. C., Stein, G. S., Lian, J. B., and Languino, L. R. (2012) TRAP-1, the mitochondrial Hsp90. *Biochim. Biophys. Acta* **1823,** 767–773

79. Matassa, D. S., Agliarulo, I., Avolio, R., Landriscina, M., and Esposito, F. (2018) TRAP1 regulation of cancer metabolism: dual role as oncogene or tumor suppressor. *Genes* **9,** 195

80. Chae, Y. C., Angelin, A., Lisanti, S., Kossenkov, A. V., Speicher, K. D., Wang, H., Powers, J. F., Tischler, A. S., Pacak, K., Fliedner, S., Michalek, R. D., Karoly, E. D., Wallace, D. C., Languino, L. R., Speicher, D. W., and Altieri, D. C. (2013) Landscape of the mitochondrial Hsp90 metabolome in tumours. *Nat. Commun.* **4,** 2139

81. Morscher, R. J., Ducker, G. S., Li, S. H. J., Mayer, J. A., Gitai, Z., Sperl, W., and Rabinowitz, J. D. (2018) Mitochondrial translation requires folate-dependent tRNA methylation. *Nature* **554,** 128–132

82. Goto, M., Miwa, H., Suganuma, K., Tsunekawa-Imai, N., Shikami, M., Mizutani, M., Mizuno, S., Hanamura, I., and Nitta, M. (2014) Adaptation of leukemia cells to hypoxic condition through switching the energy metabolism or avoiding the oxidative stress. *BMC Cancer* **14**

83. Hay, N. (2016) Reprogramming glucose metabolism in cancer: can it be exploited for cancer therapy? *Nat. Rev. Cancer* **16,** 635–649

84. Fujiwara, S., Kawano, Y., Yuki, H., Okuno, Y., Nosaka, K., Mitsuya, H., and Hata, H. (2013) PDK1 inhibition is a novel therapeutic target in multiple myeloma. *Brit. J. Cancer* **108,** 170–178

85. Li, X. L., Ji, Y. S., Han, G. Y., Li, X. R., Fan, Z. R., Li, Y. Q., Zhong, Y. L., Cao, J., Zhao, J., Zhang, M. Z., Wen, J. G., Goscinski, M. A., Nesland, J. M., and Suo, Z. H. (2016) MPC1 and MPC2 expressions are associated with favorable clinical outcomes in prostate cancer. *BMC Cancer* **16**

86. Schell, J. C., Olson, K. A., Jiang, L., Hawkins, A. J., Van Vranken, J. G., Xie, J. X., Egnatchik, R. A., Earl, E. G., DeBerardinis, R. J., and Rutter, J.

(2014) A role for the mitochondrial pyruvate carrier as a repressor of the Warburg effect and colon cancer cell growth. *Molecular Cell* **56,** 400–413

87. Muz, B., de la Puente, P., Azab, F., Luderer, M., and Azab, A. K. (2014) Hypoxia promotes stem cell-like phenotype in multiple myeloma cells. *Blood Cancer J* **4,** e262

88. Bolzoni, M., Chiu, M., Accardi, F., Vescovini, R., Airoldi, I., Storti, P., Todoerti, K., Agnelli, L., Missale, G., Andreoli, R., Bianchi, M. G., Allegri, M., Barilli, A., Nicolini, F., Cavalli, A., Costa, F., Marchica, V., Toscani, D., Mancini, C., Martella, E., Dall'Asta, V., Donofrio, G., Aversa, F., Bussolati, O., and Giuliani, N. (2016) Dependence on glutamine uptake and glutamine addiction characterize myeloma cells: a new attractive target. *Blood* **128,** 667–679

89. Aurer, I., Lauc, G., Dumic, J., Rendic, D., Matisic, D., Milos, M., Heffer-Lauc, M., Flogel, M., and Labar, B. (2007) Aberrant glycosylation of Igg heavy chain in multiple myeloma. *Coll. Antropol.* **31,** 247–251

90. Krall, A. S., Xu, S., Graeber, T. G., Braas, D., and Christofk, H. R. (2016) Asparagine promotes cancer cell proliferation through use as an amino acid exchange factor. *Nat. Commun.* **7,** 11457

91. Degrassi, A., Hilbert, D. M., Rudikoff, S., Anderson, A. O., Potter, M., and Coon, H. G. (1993) In vitro culture of primary plasmacytomas requires stromal cell feeder layers. *Proc. Natl. Acad. Sci. U.S.A.* **90,** 2060–2064

92. Zhang, J., Fan, J., Venneti, S., Cross, J. R., Takagi, T., Bhinder, B., Djaballah, H., Kanai, M., Cheng, E. H., Judkins, A. R., Pawel, B., Baggs, J., Cherry, S., Rabinowitz, J. D., and Thompson, C. B. (2014) Asparagine plays a critical role in regulating cellular adaptation to glutamine depletion. *Mol. Cell* **56,** 205–218

93. Agrawal, N. R., Bukowski, R. M., Rybicki, L. A., Kurtzberg, J., Cohen, L. J., and Hussein, M. A. (2003) A Phase I-II trial of polyethylene glycol-conjugated L-asparaginase in patients with multiple myeloma. *Cancer* **98,** 94–99

94. Zaal, E. A., Wu, W., Jansen, G., Zweegman, S., Cloos, J., and Berkers, C. R. (2017) Bortezomib resistance in multiple myeloma is associated with increased serine synthesis. *Cancer Metab* **5,** 7

95. Hiltunen, J. K., Schonauer, M. S., Autio, K. J., Mittelmeier, T. M., Kastaniotis, A. J., and Dieckmann, C. L. (2009) Mitochondrial fatty acid synthesis type II: more than just fatty acids. *J. Biol. Chem.* **284,** 9011–9015

96. Kastaniotis, A. J., Autio, K. J., Keratar, J. M., Monteuuis, G., Makela, A. M., Nair, R. R., Pietikainen, L. P., Shvetsova, A., Chen, Z. J., and Hiltunen, J. K. (2017) Mitochondrial fatty acid synthesis, fatty acids and mitochondrial physiology. *Bba-Mol. Cell. Biol. L* **1862,** 39–48

97. Deepa, S. S., Bhaskaran, S., Ranjit, R., Qaisar, R., Nair, B. C., Liu, Y., Walsh, M. E., Fok, W. C., and Van Remmen, H. (2016) Down-regulation of the mitochondrial matrix peptidase ClpP in muscle cells causes mitochondrial dysfunction and decreases cell proliferation. *Free Radic. Biol. Med.* **91,** 281–292

98. Anand, R., Wai, T., Baker, M. J., Kladt, N., Schauss, A. C., Rugarli, E., and Langer, T. (2014) The i-AAA protease YME1L and OMA1 cleave OPA1 to balance mitochondrial fusion and fission. *J. Cell Biol.* **204,** 919–929

99. Abrams, A. J., Hufnagel, R. B., Rebelo, A., Zanna, C., Patel, N., Gonzalez, M. A., Campeanu, I. J., Griffin, L. B., Groenewald, S., Strickland, A. V., Tao, F., Speziani, F., Abreu, L., Schule, R., Caporali, L., La Morgia, C., Maresca, A., Liguori, R., Lodi, R., Ahmed, Z. M., Sund, K. L., Wang, X., Krueger, L. A., Peng, Y., Prada, C. E., Prows, C. A., Schorry, E. K., Antonellis, A., Zimmerman, H. H., Abdul-Rahman, O. A., Yang, Y., Downes, S. M., Prince, J., Fontanesi, F., Barrientos, A., Nemeth, A. H., Carelli, V., Huang, T., Zuchner, S., and Dallman, J. E. (2015) Mutations in SLC25A46, encoding a UGO1-like protein, cause an optic atrophy spectrum disorder. *Nat. Genet.* **47,** 926–932

100. Lee, J. Y., Kapur, M., Li, M., Choi, M. C., Choi, S., Kim, H. J., Kim, I., Lee, E., Taylor, J. P., and Yao, T. P. (2014) MFN1 deacetylation activates adaptive mitochondrial fusion and protects metabolically challenged mitochondria. *J. Cell Sci.* **127,** 4954–4963

101. Ghadially, F. N. (1985) *Diagnostic electron microscopy of tumours*, 2nd ed. Ed., Butterworths, London

102. Carneiro, F. R. G., Lepelley, A., Seeley, J. J., Hayden, M. S., and Ghosh, S. (2018) An essential role for ECSIT in mitochondrial complex I assembly and mitophagy in macrophages. *Cell Rep.* **22,** 2654–2666

103. Tirado-Velez, J. M., Benitez-Rondan, A., Cozar-Castellano, I., Medina, F., and Perdomo, G. (2012) Low-density lipoprotein cholesterol suppresses apoptosis in human multiple myeloma cells. *Ann. Hematol.* **91,** 83–88

104. Yavasoglu, I., Tombuloglu, M., Kadikoylu, G., Donmez, A., Cagirgan, S., and Bolaman, Z. (2008) Cholesterol levels in patients with multiple myeloma. *Ann. Hematol.* **87,** 223–228

105. Benatti, P., Chiaramonte, M. L., Lorenzo, M., Hartley, J. A., Hochhauser, D., Gnesutta, N., Mantovani, R., Imbriano, C., and Dolfini, D. (2016) NF-Y activates genes of metabolic pathways altered in cancer cells. *Oncotarget* **7,** 1633–1650

106. Gonsalves, W. I., Ramakrishnan, V., Hitosugi, T., Ghosh, T., Jevremovic, D., Dutta, T., Sakrikar, D., Petterson, X. M., Wellik, L., Kumar, S. K., and Nair, K. S. (2018) Glutamine-derived 2-hydroxyglutarate is associated with disease progression in plasma cell malignancies. *JCI Insight* **3,** e94543

107. Garrido, C., Gurbuxani, S., Ravagnan, L., and Kroemer, G. (2001) Heat shock proteins: endogenous modulators of apoptotic cell death. *Biochem. Biophys. Res. Commun.* **286,** 433–442

108. Lee, A. S. (2001) The glucose-regulated proteins: stress induction and clinical applications. *Trends Biochem. Sci.* **26,** 504–510

109. Tanaka, S., Uehara, T., and Nomura, Y. (2000) Up-regulation of protein-disulfide isomerase in response to hypoxia/brain ischemia and its protective effect against apoptotic cell death. *J. Biol. Chem.* **275,** 10388–10393

110. Azoitei, N., Diepold, K., Brunner, C., Rouhi, A., Genze, F., Becher, A., Kestler, H., van Lint, J., Chiosis, G., Koren, J., Frohling, S., Scholl, C., and Seufferlein, T. (2014) HSP90 supports tumor growth and angiogenesis through PRKD2 protein stabilization. *Cancer Res.* **74,** 7125–7136

111. Li, Y. H., Nagai, H., Ohno, T., Ohashi, H., Murohara, T., Saito, H., and Kinoshita, T. (2006) Aberrant DNA demethylation in promoter region and aberrant expression of mRNA of PAX4 gene in hematologic malignancies. *Leukemia Res.* **30,** 1547–1553

112. Mellado-Gil, J. M., Jimenez-Moreno, C. M., Martin-Montalvo, A., Alvarez-Mercado, A. I., Fuente-Martin, E., Cobo-Vuilleumier, N., Lorenzo, P. I., Bru-Tari, E., Herrera-Gomez, I. D., Lopez-Noriega, L., Perez-Florido, J., Santoyo-Lopez, J., Spyrantis, A., Meda, P., Boehm, B. O., Quesada, I., and Gauthier, B. R. (2016) PAX4 preserves endoplasmic reticulum integrity preventing beta cell degeneration in a mouse model of type 1 diabetes mellitus. *Diabetologia* **59,** 755–765

113. Mahbub Hasan, A. K., Ijiri, T., and Sato, K. (2012) Involvement of Src in the adaptation of cancer cells under microenvironmental stresses. *J. Signal Transduct.* **2012,** 483796

114. Eischen, C. M., Roussel, M. F., Korsmeyer, S. J., and Cleveland, J. L. (2001) Bax loss impairs Myc-induced apoptosis and circumvents the selection of p53 mutations during Myc-mediated lymphomagenesis. *Mol. Cell. Biol.* **21,** 7653–7662

115. Wu, Y., Liu, X. M., Wang, X. J., Zhang, Y., Liang, X. Q., and Cao, E. H. (2009) PIG11 is involved in hepatocellular carcinogenesis and its over-expression promotes Hepg2 cell apoptosis. *Pathol. Oncol. Res.* **15,** 411–416

116. Crivellaro, S., Carra, G., Panuzzo, C., Taulli, R., Guerrasio, A., Saglio, G., and Morotti, A. (2016) The non-genomic loss of function of tumor suppressors: an essential role in the pathogenesis of chronic myeloid leukemia chronic phase. *BMC Cancer* **16**

117. Montesi, M., Jahn, K., Bonewald, L., Stea, S., Bordini, B., and Beraudi, A. (2016) Hypoxia mediates osteocyte ORP150 expression and cell death in vitro. *Mol. Med. Rep.* **14,** 4248–4254

118. Delcourt, N., Quevedo, C., Nonne, C., Fons, P., O'Brien, D., Loyaux, D., Diez, M., Autelitano, F., Guillemot, J. C., Ferrara, P., Muriana, A., Callol, C., Herault, J. P., Herbert, J. M., Favre, G., and Bono, F. (2015) Targeted identification of sialoglycoproteins in hypoxic endothelial cells and validation in zebrafish reveal roles for proteins in angiogenesis. *J. Biol. Chem.* **290,** 3405–3417

119. Kang, B. H., Plescia, J., Dohi, T., Rosa, J., Doxsey, S. J., and Altieri, D. C. (2007) Regulation of tumor cell mitochondrial homeostasis by an organelle-specific Hsp90 chaperone network. *Cell* **131,** 257–270

120. Winter, J., Klumpe, I., Heger, J., Rauch, U., Schultheiss, H. P., Landmesser, U., and Dorner, A. (2016) Adenine nucleotide translocase 1 overexpression protects cardiomyocytes against hypoxia via increased ERK1/2 and AKT activation. *Cell Signal* **28,** 152–159

121. Lin, F. R., Kuo, H. K., Ying, H. Y., Yang, F. H., and Lin, K. I. (2007) Induction of apoptosis in plasma cells by B lymphocyte-induced maturation protein-1 knockdown. *Cancer Res.* **67,** 11914–11923

122. Lamy, L., Ngo, V. N., Emre, N. C., Shaffer A. L. 3rd, Yang, Y., Tian, E., Nair, V., Kruhlak, M. J., Zingone, A., Landgren, O., and Staudt, L. M. (2013) Control of autophagic cell death by caspase-10 in multiple myeloma. *Cancer Cell* **23,** 435–449

123. Ishida, T. (2018) Therapeutic antibodies for multiple myeloma. *Jpn. J. Clin. Oncol.* **48,** 957–963

124. Knobeloch, K. P., Wright, M. D., Ochsenbein, A. F., Liesenfeld, O., Lohler, J., Zinkernagel, R. M., Horak, I., and Orinska, Z. (2000) Targeted inactivation of the tetraspanin CD37 impairs T-cell-dependent B-cell response under suboptimal costimulatory conditions. *Mol. Cell. Biol.* **20,** 5363–5369

125. Rocha-Perugini, V., Sanchez-Madrid, F., and del Hoyo, G. M. (2016) Function and dynamics of tetraspanins during antigen recognition and immunological synapse formation. *Front. Immunol.* **6,** 653

126. God, J. M., Cameron, C., Figueroa, J., Amria, S., Hossain, A., Kempkes, B., Bornkamm, G. W., Stuart, R. K., Blum, J. S., and Haque, A. (2015) Elevation of c-MYC disrupts HLA class II-mediated immune recognition of human B cell tumors. *J. Immunol.* **194,** 1434–1445

127. Kanehisa, M., Sato, Y., Kawashima, M., Furumichi, M., and Tanabe, M. (2016) KEGG as a reference resource for gene and protein annotation. *Nucleic Acids Res.* **44,** D457–D462

57

4.2 Octenidine-based hydrogel shows anti-inflammatory and protease-inhibitory capacities in wounded human skin

Lukas Janker[2,3]*, Saskia Seiser[1]*, Nina Zila[1], Michael Mildner[1], Ana Rakita[1], Johannes Matiasek[4], Andrea Bileck[2,3], Christopher Gerner[2,3], Verena Paulitschke[1], Adelheid Elbe-Bürger[1]

1   Department of Dermatology, Medical University of Vienna, Vienna, Austria

2   Department of Analytical Chemistry, Faculty of Chemistry, University of Vienna, Vienna, Austria

3   Joint Metabolome Facility, University of Vienna and Medical University of Vienna, Vienna, Austria

4   Department of Plastic, Aesthetic and Reconstructive Surgery, St. Josef Hospital, Vienna, Austria

*   Contributed equally

Contributions to this publication:

- Performing MS measurements
- Analysis and interpretation of data
- Writing of manuscript

scientific reports

OPEN

Octenidine-based hydrogel shows anti-inflammatory and protease-inhibitory capacities in wounded human skin

Saskia Seiser[1,5], Lukas Janker[2,3,5], Nina Zila[1], Michael Mildner[1], Ana Rakita[1], Johannes Matiasek[4], Andrea Bileck[2,3], Christopher Gerner[2,3], Verena Paulitschke[1] & Adelheid Elbe-Bürger[1✉]

Octenidine dihydrochloride (OCT) is a widely used antiseptic molecule, promoting skin wound healing accompanied with improved scar quality after surgical procedures. However, the mechanisms by which OCT is contributing to tissue regeneration are not yet completely clear. In this study, we have used a superficial wound model by tape stripping of ex vivo human skin. Protein profiles of wounded skin biopsies treated with OCT-containing hydrogel and the released secretome were analyzed using liquid chromatography-mass spectrometry (LC–MS) and enzyme-linked immunosorbent assay (ELISA), respectively. Proteomics analysis of OCT-treated skin wounds revealed significant lower levels of key players in tissue remodeling as well as reepithelization after wounding such as pro-inflammatory cytokines (IL-8, IL-6) and matrix-metalloproteinases (MMP1, MMP2, MMP3, MMP9) when compared to controls. In addition, enzymatic activity of several released MMPs into culture supernatants was significantly lower in OCT-treated samples. Our data give insights on the mode of action based on which OCT positively influences wound healing and identified anti-inflammatory and protease-inhibitory activities of OCT.

Human skin has a variety of crucial functions such as serving as a barrier protecting the body from physical and chemical attack, invasion of pathogens and excessive water loss. As the primary immunological barrier to the environment, the skin is harboring several types of immune cells that participate in innate and adaptive immune responses[1,2]. Because skin is constantly exposed to potential injury, wound healing is a fundamental process for the survival of all higher organisms. Acute wound healing represents the physiological mode of wound closure and includes inflammation, blood clotting, cellular proliferation and extracellular matrix (ECM) remodeling[3,4]. In contrast, chronic wounds do not follow such a well-defined cascade, but are trapped in an inflammatory state[5]. Furthermore, such a continuously localized inflammation contributes to the pathogenesis of excessive wound healing, leading to the formation of keloids or hypertrophic scars. Pro-inflammatory cytokines have a major role in the first phases of wound healing. Interleukin (IL)-6 is enhancing the inflammatory response and induces vascular endothelial growth factor (VEGF) and IL-8 for tissue repair[6]. Further, IL-6 is favoring transition from acute to chronic inflammation as it exerts stimulatory effects on T and B cells[7]. During the remodeling phase a variety of proteolytic enzymes, such as matrix-metalloproteinases (MMPs), are active. They are capable of degrading the ECM, thus playing a major role in wound healing and tissue neomorphogenesis. MMP activity is mainly regulated via tissue inhibitors of metalloproteinases (TIMPs)[8]. In chronic wounds or wounds showing delayed wound healing frequently, an imbalance between TIMPs and MMPs has been observed[9,10]. Enhanced activity of MMPs might cause increased ECM degradation, alteration of the cytokine profile, and degradation of growth factors, culminating in delayed or absent wound closure[11].

Octenidine dihydrochloride (OCT) is a widely used antiseptic molecule with antibacterial, antifungal and partially antiviral effects[12,13]. Due to the broad pH range in which OCT is active, it is perfectly suitable for wound care[14]. Additionally, OCT has the capacity to clear bacterial biofilms in patients with chronic wounds[15]. Recent

[1]Department of Dermatology, Medical University of Vienna, Vienna, Austria. [2]Department of Analytical Chemistry, University of Vienna, Vienna, Austria. [3]Joint Metabolome Facility, University of Vienna and Medical University of Vienna, Vienna, Austria. [4]Department of Plastic, Aesthetic and Reconstructive Surgery, St. Josef Hospital, Vienna, Austria. [5]These authors contributed equally: Saskia Seiser and Lukas Janker. ✉email: adelheid.elbe-buerger@meduniwien.ac.at

studies revealed that OCT is promoting skin wound healing accompanied with improved scar quality after surgical procedures in patients[16]. Further, it has been demonstrated that OCT does neither morphologically alter skin cell architecture, nor enhance apoptosis when locally applied to superficially wounded ex vivo human skin. In addition, OCT prevents migration of epidermal Langerhans cells and inhibits the secretion of several cytokines (IL-8, IL-33, IL-10) in vitro, suggesting an anti-inflammatory capacity[17].

Although animal models have the advantage of representing a whole organism, there are major anatomical and physiological differences, making a comparison to the human system often difficult[18]. Especially wound healing shows major differences between rodents and humans, underlining the necessity of alternative wound healing models. Ex vivo human skin models are of high relevance because they provide laboratory models perhaps closest to the in vivo environment in terms of biological complexity and fidelity to human physiology. Even though we are aware that the use of ex vivo human skin models has some limitations (e.g., dependency on biological material, limitations in standardization due to donor variability, lacking the influx of biochemicals [complement proteins from the circulation] and other immune cells [natural killer cells, neutrophils, T cells], adaptive responses cannot be tested, no innervation, limited culture periods), they allow comparative assessments on the whole skin compartment of one area and cell–cell interactions[19]. Further, ex vivo skin models are ethically advantageous, because they permit experiments in human tissue that would otherwise be impossible in living individuals. They are a simple, fast, and cost-effective tool for decreasing large-scale and expensive animal testing. Because there are increasing restrictions in Europe for using animals for testing compound properties and in line with the 3Rs (reduction, refinement, and replacement of animal models), ex vivo models represent an ideal preclinical platform. Therefore, we have employed a recently established ex vivo human wound model[17,20] and a proteomic as well as ELISA-based approach to determine the protein profile of OCT-treated wounded skin, aiming to further unravel the largely unknown mechanism by which OCT might contribute to tissue regeneration and improved wound healing.

Materials and methods

Ethics statement. Abdominal skin from anonymous healthy adult female donors was obtained during plastic surgery procedures. The study was approved by the ethics committee of the Medical University of Vienna and conducted in accordance with the principles of the Declaration of Helsinki. A written informed consent was obtained from participants.

Superficial ex vivo human skin wound model using tape-stripping. Freshly isolated skin (1–2 h (hours) after surgery) was disinfected with Kodan forte (Schülke & Mayr GmbH, Austria) and tape-stripped (TS), essentially as described previously[20]. Briefly, 50 different D102-squame standard self-adhesive discs (CuDerm, USA) were applied onto excised skin on the identical area by the same operator with constant pressure for 10 s (sec). Subsequently, the TS skin was cut with a Dermatome (0.6 mm; Acculan 3Ti; Aesculap, Inc. USA) and punch biopsies (∅ 8 mm; Kai Europe GmbH, Germany) were taken from TS and non-TS (NTS) skin. The efficient removal of the *stratum corneum* was verified by routine hematoxylin and eosin (H&E) staining of TS and NTS punch biopsies.

To define if the removal efficiency of the *stratum corneum* is comparable in all positions of a TS area, or shows differences, according to potential unequally applied pressure and donor variability, abdominal skin of three donors was TS and biopsies were taken from five defined regions on the TS area (Fig. S1). H&E staining demonstrated that TS is most efficient in the inner region (= 2) compared to outer regions (= 1, 3, 4, 5) (Fig. S1). Aiming to standardize further experiments as much as possible, only biopsies of the inner region were used in this study.

Topical application of OCT and culture conditions. Before culture, OCT (octenilin wound gel, 0.05% OCT, Schülke & Mayr GmbH, Germany), or control gel (OCT-free hydrogel, Schülke & Mayr GmbH, Germany) were applied topically onto TS skin biopsies (50 microliter (μl)/biopsy). Untreated and treated TS skin biopsies were cultured in 12-well culture plates in the presence of Dulbecco´s modified eagle medium (DMEM; 500 μl/well; Gibco, Thermofisher, USA), supplemented with 10% fetal bovine serum (FBS; Gibco, Thermofisher) and 1% penicillin–streptomycin (Gibco, Thermofisher) for 48 h at 37 °C and 5% CO_2 (Heracell 150i; Thermofisher, USA). On the second day, biopsies and culture supernatants were collected and stored at − 80 °C for liquid chromatography-mass spectrometry (LC–MS) and enzyme-linked immunosorbent assays (ELISA), respectively.

Separation of skin compartments. In certain experiments, treated and untreated TS skin biopsies were washed in PBS upon 48 h of cultivation. To be able to separate the epidermis from the dermis, samples were enzymatically treated by incubation in 1.2 U/ml Dispase II (Roche Diagnostics GmbH) at 4 °C overnight. On the next day the epidermis was peeled from the dermis using forceps. Separated compartments were immediately frozen in liquid nitrogen without fixation and stored on − 80 °C for LC–MS analysis.

H&E staining. Fixed (7.5% paraformaldehyde) TS and untreated skin samples were embedded in paraffin (Sanova Pharma GmbH, Austria), cut (5 μm) with a microtome (Microm HM 335 E; GMI, USA) and stained with H&E solution according to standardized protocols.

Sample preparation and LC–MS shotgun analysis of whole TS skin biopsies. Cultured TS biopsies (female, abdomen, age range: 38–45 years, n = 5) treated with OCT, control gel and left untreated, were homogenized in 100 μl sample buffer (7.5 molar (M) urea, 1.5 M thiourea, 0.1 M dithiothreitol, 4% 3-[(3-cholamidopropyl)dimethylammonio]-1-propanesulfonate, 0.05% sodium dodecyl sulfate) using ultrasound. Protein

concentrations were premeasured using a Bradford assay. For each sample 20 µg protein was used for the in-solution digest performed according to a variation[21] of the FASP protocol[22]. Dried samples were reconstituted as previously described[23,24] in 5 µl 30% formic acid (FA) containing 4 synthetic standard peptides and diluted with 40 µl mobile phase A (97.9% H_2O, 2% ACN, 0.1% FA). Of this solution, 5 µl were injected into a Dionex Ultimate 3000 nano high performance liquid chromatography (HPLC)-system (Thermo Fisher Scientific). Peptides were concentrated on a pre-column (2 cm × 75 µm C18 Pepmap100; Thermo Fisher Scientific) at a flow rate of 10 µl/min, using mobile phase A. Subsequently, they were separated by elution from the pre-column to an analytical column (50 cm × 75 µm Pepmap100; Thermo Fisher Scientific) applying a flow rate of 300 nl/min and using a gradient of 8% to 40% mobile phase B (80% ACN, 20% H_2O, 0.1% FA), over 190 min for sample analysis. The MS analysis was performed on a QExactive classic orbitrap mass spectrometer, equipped with a nanospray ion source (Thermo Fisher Scientific), coupled to the nano HPLC system. For detection, MS scans were performed in the range from m/z 400–1400 at a resolution of 70.000 (at m/z = 200). MS/MS scans were performed choosing a top 8 method. HCD fragmentation was applied at 30% normalized collision energy and analysis in the orbitrap at a resolution of 17.500 (at m/z = 200).

LC–MS data analysis and interpretation of whole TS skin biopsies.   Analysis and interpretation of LC–MS data was performed essentially as described[21] using the open source software MaxQuant (version 1.6.3.4)[25,26] including the Andromeda search engine and the Perseus statistical analysis package[25,26]. Protein inference was achieved aligning against homo sapiens in the SwissProt Database setting the parameters (mass tolerance, missed cleavages, fixed/variable modifications, minimum of peptide identifications) as defined[21]. Label-free quantification (LFQ) revealed values for each individual protein, which were conducted for quantitative assessment of protein regulation using the Perseus statistical analysis package[27]. Proteins differentially expressed between the three treatments were evaluated via Perseus with an unpaired t-test using LFQ values of proteins for each group. Proteins with a p-value lower than 0.05 and a difference lower than − 1 or higher than + 1, corresponding to a log_2 fold change of at least 2, were considered as significant hits and were further analysed. Protein function was determined using the Uniprot database[28] as well as DAVID bioinformatics resources for gene ontology annotation[29,30].

Sample preparation and LC–MS analysis of epidermal and dermal compartments.   Cultured TS biopsies (female, abdomen, age range: 36–45 years, n = 3) treated with OCT, control gel and left untreated, were enzymatically separated into dermis and epidermis and the different compartments were independently homogenized in 100 µl lysis buffer (8 M urea, 50 mM TEAB, 5% SDS) using ultrasound. For enzymatic digestion, a protocol using the S-trap technology was employed[31]. In short, reduction and alkylation of 20 µg solubilized protein amount was achieved with 64 mM DTT and 48 mM IAA, respectively. After addition of trapping buffer (90% vol/vol Methanol, 0.1 M Triethylammonium bicarbonate), samples were loaded onto S-trap cartridges, thoroughly washed and subsequently digested using Trypsin/Lys-C Mix at 47 °C for one hour. Peptides were eluted, dried and stored at − 20 °C until LC–MS analyses. Dried samples were reconstituted in 5 µl of 30% FA containing 4 synthetic standard peptides and diluted with 40 µl of loading solvent (97.9% H_2O, 2% ACN, 0.05% trifluoroacetic acid). Of this solution, 5 µl were injected into the Dionex Ultimate 3000 nano HPLC-system (Thermo Fisher Scientific). Peptides were concentrated on a pre-column (2 cm × 75 µm C18 Pepmap100; Thermo Fisher Scientific) at a flow rate of 10 µl/min, using mobile phase A (97.9% H_2O, 2% ACN, 0.1% FA). Subsequently, they were separated by elution from the pre-column to an analytical column (50 cm × 75 µm Pepmap100; Thermo Fisher Scientific), applying a flow rate of 400 nl/min and using a gradient of 8% to 40% mobile phase B (80% ACN, 20% H_2O, 0.1% FA) over 95 min, resulting in a total LC run time of 135 min including washing and equilibration steps. Mass spectrometric analyses were accomplished using the timsTOF Pro mass spectrometer (Bruker) equipped with a captive spray ion source run at 1600 V. Furthermore, the timsTOF Pro mass spectrometer was operated in the Parallel Accumulation-Serial Fragmentation (PASEF) mode. Trapped ion mobility separation was achieved by applying a 1/k0 scan range from 0.60 to 1.60 Vs/cm² resulting in a ramp time of 166 ms. All experiments were performed with 10 PASEF MS/MS scans per cycle leading to a total cycle time of 1.88 s. MS and MS/MS spectra were recorded using a scan range (m/z) from 100 to 1700. Further, the collision energy was ramped as a function of increasing ion mobility from 20 to 52 eV and the quadrupole isolation width was set to 2 Th for m/z < 700 and 3 Th for m/z > 700.

LC–MS data analysis and interpretation of epidermal and dermal compartments.   For ion mobility mass spectrometry (IMMS) data, the software pipeline FragPipe (version 13.0) employing the search algorithm MSFragger (version 3.0)[32] and Philosopher (version 3.2.7) for peptide and protein identification statistics in combination with IonQuant (version 1.3.0) was used. Mass tolerance was set to 50 ppm and 20 ppm for MS1 and MS2, respectively. One missed cleavage was allowed. Fixed/variable modifications and peptide identification settings were set as described above. For quantification of proteins, a MaxLFQ approach with IonQuant was chosen. "Match-between-runs" (MBR) parameters were set to a retention time window of 1 min and an ion mobility window of 0.05 1/K_0. A MBR false discovery rate cut-off value of 0.01 on ion, peptide and protein level was applied. Statistical analysis of obtained results was performed with Perseus statistical analysis package (version 1.6.14.0), as described above. Proteins with a p-value lower than 0.01 and a difference lower than − 1 or higher than + 1, corresponding to a log_2 fold change of at least 2, were considered as significant hits and were further analysed. Protein function was determined using the Uniprot database as well as DAVID bioinformatics resources for gene ontology annotation.

63

Data availability. The MS proteomics data have been deposited to the ProteomeXchange Consortium via the PRIDE[33] partner repository with the dataset identifier PXD007592 and https://doi.org/10.6019/pxd007592.

ELISA. Culture plates (Nunc Immuno 96 well flat-bottom culture plate; Merck KGaA) were coated with appropriate capture human antibodies such as IL-8 (Thermo Fisher Scientific, #M108), IL-6, MMPs or TIMP-1 (R&D Systems) overnight at 4 °C or room temperature. On the next day, plates were washed with washing buffer (0.05% Tween in PBS) and blocked with blocking buffer (4% BSA, 0.5% Tween in PBS) or reagent diluent (1% BSA in PBS). Another washing step was performed, and standards and samples were pipetted on the plates in an appropriate dilution and incubated for 2 h at room temperature. After that, plates were aspirated and the respective detection antibody was applied (Thermo Fisher Scientific, #M802B; R&D Systems) and incubated for another 2 h at room temperature. Next, plates were washed again and streptavidin-horse-radish peroxidase (Thermo Fisher Scientific #34028, R&D Systems) was applied. After an incubation time of 20 to 30 min, another washing step was performed and 3,3′,5,5′-tetramethylbenzidine substrate reagent A + B (BD Biosciences, USA) was applied and incubated for 20 min. Subsequently, a stop solution (2N H_2SO_4; 50 μl/well) was added and fluorescence was measured immediately at 450 nm with a photometer (Multiskan FC Microplate Photometer; Thermofisher, USA).

Enzyme activity assay. The activity of MMPs (MMP1/2/3/7/8/9/10/12/13) in culture supernatants was measured using the Amplite Universal Fluorimetric MMP Activity Assay Kit (AAT Bioquest, USA). Supernatants were activated with 4-aminophenylmercuric acetate (2 mM) overnight. Activated supernatants and controls were pipetted in duplicates into a flat-bottom culture plate (100 μl/well; Corning 96 Well White Polystyrene Microplate; Merck KGaA) and MMP Green substrate (50 μl/well; AAT Bioquest) was added. Fluorescence intensity was monitored as kinetic measurement with a plate reader (BMG FLUOstar OPTIMA Microplate Reader; BMG Labtech Inc. USA) at Ex/Em = 490/525 nm.

Statistical analysis. ELISA data as well as results from the enzyme activity assay were analyzed using GraphPad Prism 5. An unpaired t-test was used for comparing means, respectively. The results were considered significant with *p*-values smaller than 0.05. Detailed information about statistical evaluation of LC–MS analysis and interpretation can be found in the respective method sections.

Results

OCT-treated wounded human skin shows a distinct proteomic profile compared to controls.
To uncover the protein profile of human skin cells upon wounding and OCT-treatment, a proteomic approach was chosen. Abdominal TS skin biopsies of five donors were treated with OCT, control gel or left untreated, cultivated for 48 h and subjected to LC–MS. Statistical analysis using the software packages Max-Quant and Perseus revealed a total of 2622 proteins (FDR < 0.01). Twenty-six proteins were found to be differentially regulated (FDR < 0.05) between OCT- and control gel-treated samples (Fig. 1A, Table S1) and thirty-seven proteins were differentially regulated between OCT-treated and untreated samples (Fig. 1B, Table S2). Ten proteins were differentially regulated between both, OCT-treated and untreated samples and between OCT-treated and control-treated samples (Fig. 1A,B). Additionally, sixteen proteins were differentially regulated between the untreated and control gel-treated group, showing that already application of hydrogel on the wound has an effect on the protein profile of skin cells (Table S3). Among those proteins, three proteins were also differentially regulated between OCT-treated and untreated samples and two proteins between OCT-treated and control-gel treated samples (Fig. S2). Of note, none of the ten proteins which were differentially regulated between both, OCT-treated and control gel-treated and OCT-treated and untreated samples were among the sixteen proteins differentially regulated between the untreated and control-gel-treated group, concluding that OCT indeed has a regulatory effect on respective proteins. Among significant hits, several proteins are involved in the immune response as well as wound healing and tissue regeneration (Tables S1 and S2).

OCT regulates biological processes relevant for wound healing and immune response.
Gene Ontology (GO) enrichment analysis of proteins differentially regulated in OCT-treated wounded skin was performed using DAVID Bioinformatics Resources[29,30]. We found that proteins downregulated in OCT-treated TS skin were associated with the biological functions important for wound healing (Fig. 2). Angiogenesis, collagen catabolic process, ECM disassembly as well as proteolysis were downregulated in OCT-treated TS skin compared to untreated wounded skin (Fig. 2). Proteins involved in those functions are, among others, IL-6 and members of the MMP family (MMP1, 2, 3). As anticipated, also proteins related to functions involved in inflammatory immune response, such as particular defense mechanisms were downregulated in OCT-treated wounded skin samples (Fig. 2). According to GO, IL-6 is an important representative of those functions. Together, these data suggest, that OCT reduces the inflammatory immune response and excessive collagen and ECM deposition in wounded skin. Leukocyte migration was upregulated in TS skin biopsies upon OCT treatment (Fig. 2), showing that OCT not only has suppressing capacities. Functional associations between proteins downregulated in OCT treated wounded skin samples were determined using the STRING software[34]. The analysis revealed strong functional interaction between members of the MMP family (MMP1, 2, 3) and IL-6 (Fig. S3), conforming and extending studies demonstrating that IL-6 regulates tissue MMPs[35,36].

OCT significantly reduces secretion of pro-inflammatory cytokines in wounded human skin.
Differentially regulated protein candidates in OCT-treated TS skin samples and controls were further
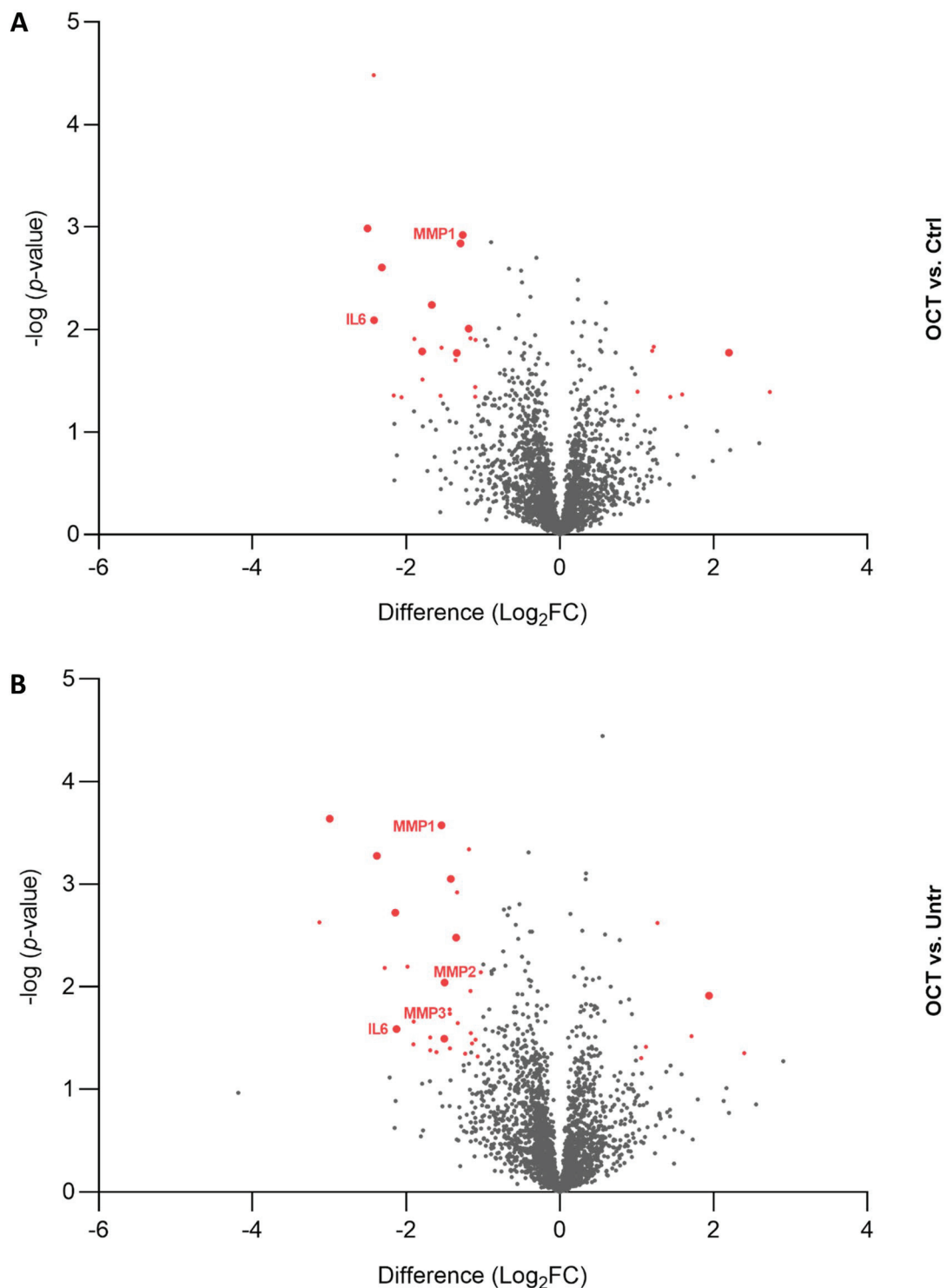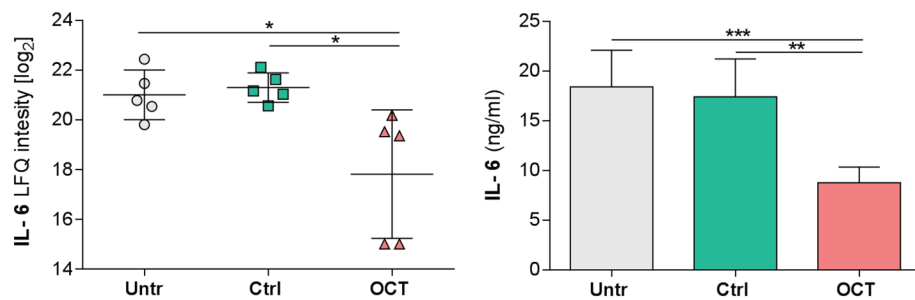
Figure 1. Proteins are differentially regulated among wounded OCT-treated skin and controls. Abdominal skin biopsies of donors (age range: 38–45 years, n = 5) were TS, treated with OCT, control gel or left untreated, cultivated for 48 h and subsequently prepared for LC–MS analysis. Volcano plots show differences in LFQ values (fold change, logarithmic scale to the base of two) on the x-axis including their corresponding *p*-values (logarithmic scale) on the y-axis. Proteins marked in red are significantly differentially regulated ($Log_2FC < -1$ = downregulated; $Log_2FC > 1$ = upregulated) in OCT treated samples compared to (**A**) control gel-treated samples or (**B**) untreated samples. Larger sized dots indicate proteins that are differentially regulated in OCT treated samples compared to both, control gel-treated samples and untreated samples. Registered proteins were further analysed. Data presented in the plots was generated performing a two-sided t-test ($p < 0.05$) using Perseus and vulcano plots were generated using Graphpad Prism. Extended information on the proteins can be found in Tables S1 and S2.

5

65
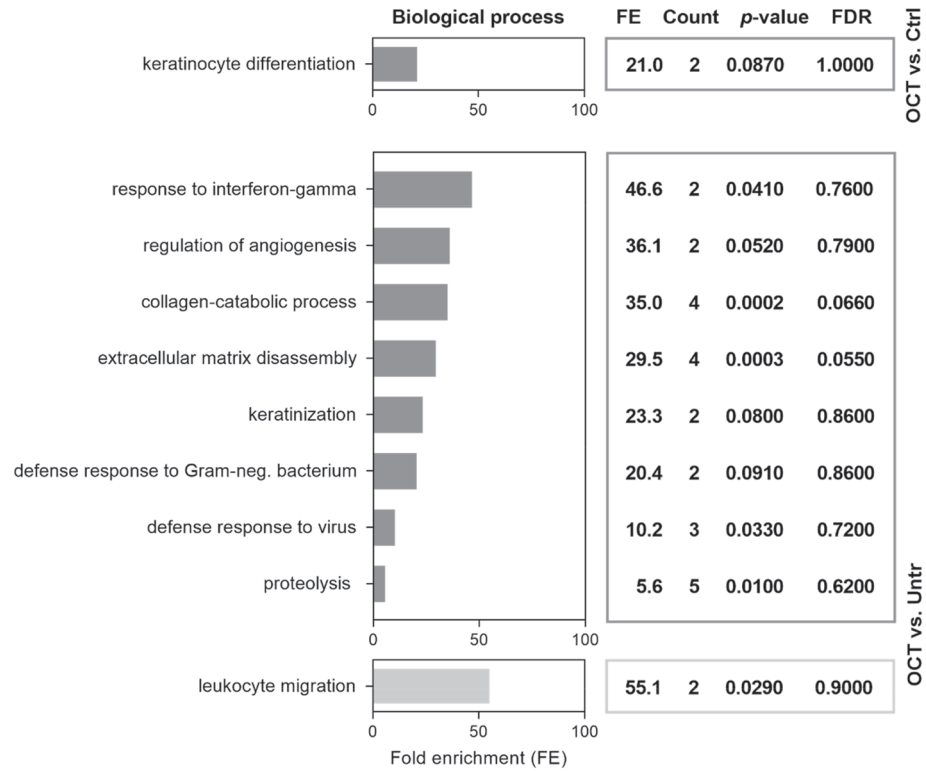
Figure 2. OCT regulates proteins involved in wound healing and immune response. Full skin biopsies of donors (age range: 38–45 years, n = 5) were TS, treated with OCT, control gel or left untreated, cultivated for 48 h and subsequently prepared for LC–MS analysis. Classification by the GO term biological process shows pathways and larger processes made up of the activities of multiple proteins. Fold enrichment values for individual GO terms, count (proteins involved in the term), *p*-value and FDR (false discovery rate, calculated using the Benjamini–Hochberg procedure), listed next to the graph, were calculated using DAVID bioinformatics resources. Biological processes downregulated in OCT-treated TS samples are shown in dark grey, processes upregulated in OCT-treated TS samples are shown in light grey.

Figure 3. OCT significantly inhibits IL-6 secretion in wounded human skin. IL-6 levels of TS human skin biopsies treated with OCT were evaluated by LC–MS and were significantly lower compared with TS biopsies which were untreated or treated with the control gel (left panel). Label-free quantification (LFQ) intensities in a logarithmic scale to the basis 2 are indicated. LFQ intensities for proteins not detected in a replicate were replaced by 15. IL-6 concentration in supernatants was tested in duplicates with an ELISA (right panel). Data in both graphs is presented as a mean ± SD (n = 5). An unpaired t-test was performed with GraphPad Prism. $*p \leq 0.05$, $**p \leq 0.01$, $***p \leq 0.001$.

quantitatively assessed by ELISA. In addition to IL-8 (Fig. S4)[17], IL-6 is another pro-inflammatory cytokine known to play a key role in acute inflammation and is pivotal for the timely resolution of cutaneous wound healing[37]. Dysregulation of IL-6 signaling can lead to either fibrosis or a failure to heal. Our LC–MS data are in line with this concept as we found significantly diminished IL-6 in OCT-treated compared to untreated or control gel-treated TS skin biopsies (Fig. 3). Analysis of culture supernatants of the same donors confirmed these

data showing significantly reduced IL-6 concentrations in OCT-treated wounded skin samples compared to controls, supporting and extending our previous conclusion that OCT has anti-inflammatory capacity (Fig. 3).

OCT downregulates release of proteases in wounded human skin.   MMPs and their inhibitors play a crucial role in all stages of wound healing by regulating ECM degradation and deposition which allows tissue remodelling as well as cell migration[38]. We found that MMP1 and MMP2 protein levels were significantly lower in the tissue and in the secretome of TS skin biopsies treated with OCT in comparison to controls (Fig. 4A). MMP3 expression and secretion levels were significantly lower only in OCT-treated wounded skin samples when compared to untreated samples (Fig. 4A). Of note, OCT treatment of TS human skin did not influence TIMP-1 expression and secretion (Fig. 4A). Importantly, supernatants of TS biopsies of the same five donors treated with OCT showed significantly lower total MMP activity than supernatants of control groups (Fig. 4B).

OCT is primarily active in the dermal compartment.   As MMPs and inflammatory cytokines are produced and secreted by many cell types[24], we next investigated whether the protease-inhibitory and anti-inflammatory action is occurring preferentially in the epidermis or dermis. To address this, TS skin biopsies of a different set of three healthy female donors, as before, were treated with OCT, control gel or left untreated and cultivated for 48 h. Physically separated epidermal and dermal compartments were then analysed with complementary instrument technology employing ion mobility gas phase separation. Statistical analysis revealed that more proteins were differentially regulated in OCT-treated TS skin samples compared to control gel-treated samples than in comparison to untreated samples. Within both groups, more proteins were differentially regulated in the dermis (OCT/Ctrl: 173; OCT/Untr: 38) than in the epidermis (OCT/Ctrl: 73; OCT/Untr: 34) (Fig. 5). Of note, the disparity between the two compartments is clearly larger when OCT-treated TS skin was compared with control gel-treated TS skin (Fig. 5). Only few proteins were differentially regulated between control gel-treated and untreated samples, in the epidermis (2) as well as dermis (6) (Table S8). Protein function was determined using the Uniprot database as well as DAVID Bioinformatics Resources. Again, among significant hits, several proteins are involved in immune response as well as wound healing (Fig. 6). In the epidermis (Fig. 6A) we found a downregulation of proteins involved in defense mechanisms in OCT-treated samples compared to untreated samples, being in conformity with the results of whole TS skin biopsy analysis (Fig. 2). In the dermis (Fig. 6B) several functions associated with wound healing were downregulated in OCT-treated samples compared to control gel-treated samples. Among them were also processes found in GO annotation results of whole TS skin biopsies (collagen catabolic process, ECM disassembly, proteolysis) (Fig. 2), which are predominantly related to members of the MMP family. Functions of all proteins significantly up- or downregulated upon OCT treatment, in both epidermis and dermis were determined using the Uniprot database (Tables S4, S5, S6, S7). Similar to data in Tables S1 and S2, significant differences were identified for MMP1 and MMP2 (Table S6) between OCT-treated and control gel-treated TS dermal samples. In addition, MMP9 was shown to be significantly downregulated in OCT-treated TS samples compared to the control (Table S6).

Discussion

In clinical practice, OCT has been shown to promote healing of chronic wounds[39–41] and to reduce the formation of hypertrophic scars in patients after abdominoplasty[16]. However, the mechanism by which OCT contributes to tissue regeneration and improved wound healing is not yet investigated in more detail. We used a mild, ex vivo human wound model to address this and applied standardization, according to sex and donor age range within one experimental set up, employing skin always from a distinct body location, defining the best TS area within a skin biopsy, and evaluating optimal skin thickness for subsequent analysis.

A detailed characterization of the protein profile of wounded and OCT-treated TS skin biopsies and controls was achieved using LC–MS. Out of 2622 identified proteins, 26 and 37 were differentially regulated between OCT- and control gel-treated samples as well as OCT-treated and untreated samples, respectively. GO annotations revealed several biological processes involved in wound healing among proteins found to be downregulated in OCT-treated skin and included ECM disassembly, collagen-catabolic process, proteolysis as well as angiogenesis. According to DAVID bioinformatics resources, proteins associated with above mentioned processes were among others, IL-6 and MMP family members. IL-6 is playing a key role in the acute phase reaction in response to immunological stress. Fetal skin, in contrast to adult skin, produces rather low levels of pro-inflammatory cytokines (IL-6, IL-8), potentially related to the immature immune status but attributing to its high regenerative capacity. Further, it has been reported that (1) exogenous IL-6 leads to scar formation of human fetal skin grafts in SCID mice[42], (2) IL-8 levels are significantly increased in slowly healing human burn wounds, (3) IL-8 decreases keratinocyte differentiation in vitro[43], and (4) fibroblasts from keloid scars show increased IL-8 levels compared with normal human fibroblasts[44]. This supports a possible contribution of IL-6 and IL-8 to pathological scar formation. Our data in this study showing significantly lower IL-6 levels in OCT-treated biopsies compared to controls extend our previously reported finding about its anti-inflammatory capacity[17]. The inhibition of IL-6 and IL-8 in OCT-treated TS skin biopsies is one possible explanation for the potency of OCT to enhance wound healing and prevent hypertrophic scar formation in vivo. MMPs are other candidates as they are capable of dissolving the basal lamina and lysis of surrounding tissue, thus facilitating proliferation and cell migration throughout acute wound healing. Dysregulation of MMP levels might lead to increased ECM degradation, alteration of the cytokine profile, and degradation of growth factors, culminating in delayed wound closure[11]. In line with this assumption is the observation that mRNA expression of MMP2 is highly increased in different types of human scar tissue when compared with normal tissue derived from the same patient[9]. Our data revealed significantly lower MMP1 and MMP2 levels in cultured wounded human skin treated with OCT in comparison to controls. In conformity with this observation, we noted a significant reduction of MMP3 for OCT-treated TS biopsies

67
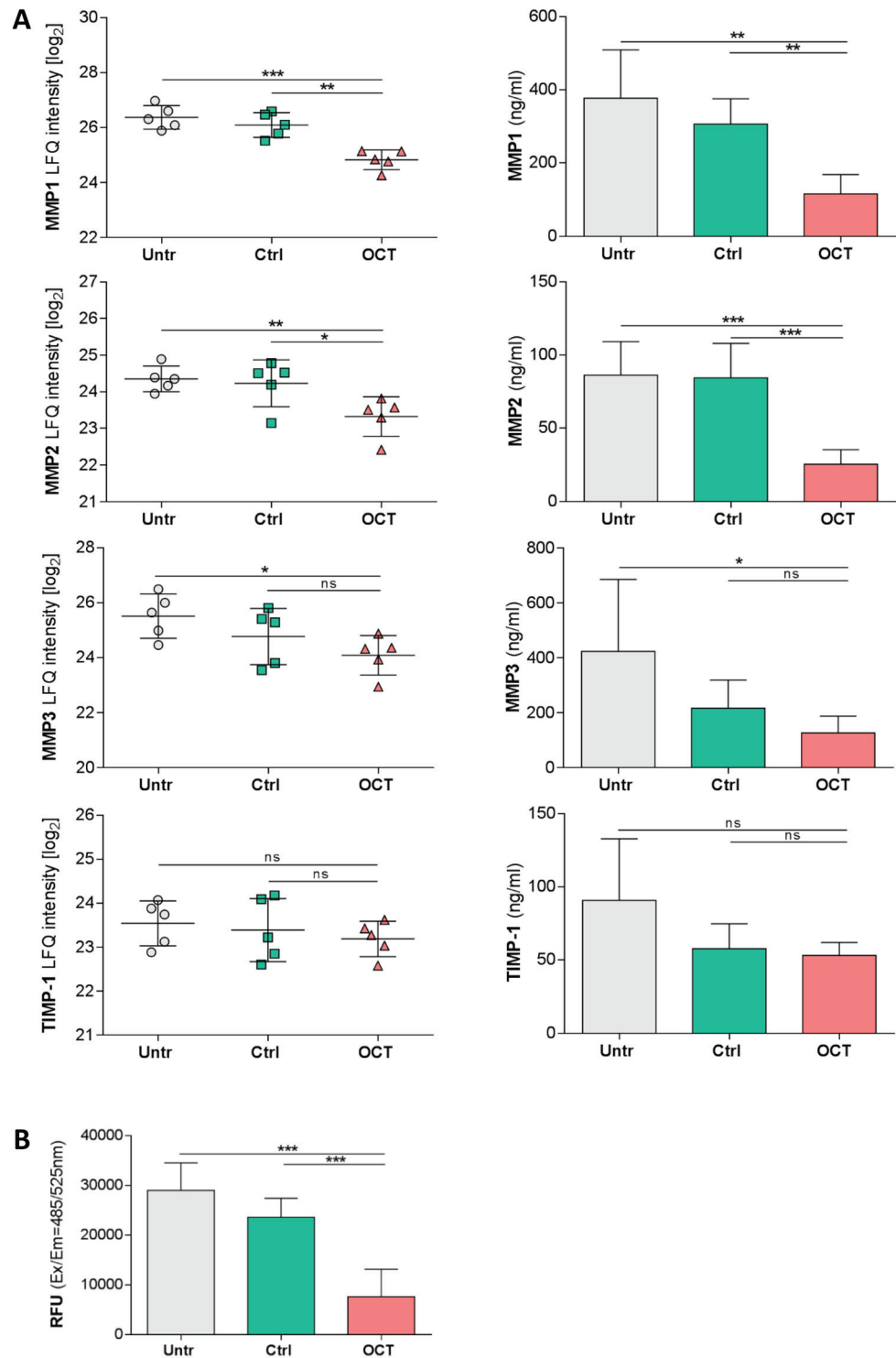
Figure 4. OCT significantly reduces secretion and activity of proteases in wounded human skin. **(A)** Indicated MMP levels, analysed by LC–MS, were significantly lower in human TS skin biopsies treated with OCT compared to biopsies which were untreated or treated with a control gel, with exception of TIMP-1, which is not affected upon OCT treatment (left panel). Label-free quantification (LFQ) intensities in a logarithmic scale to the basis 2 are indicated. LFQ intensities for proteins not detected in a replicate were replaced by 15. Proteases and a typical protease inhibitor in culture supernatants were tested in duplicates with an ELISA (right panel). **(B)** Enzymatic activity of MMPs was significantly lower in culture supernatants of OCT-treated TS human skin biopsies compared to controls (untreated, control gel-treated). Relative fluorescence units (RFU) are indicated. All data is presented as mean ± SD (n = 5). An unpaired t-test was performed with GraphPad Prism. *$p \leq 0.05$, **$p \leq 0.01$, ***$p \leq 0.001$, ns = not significant.

68
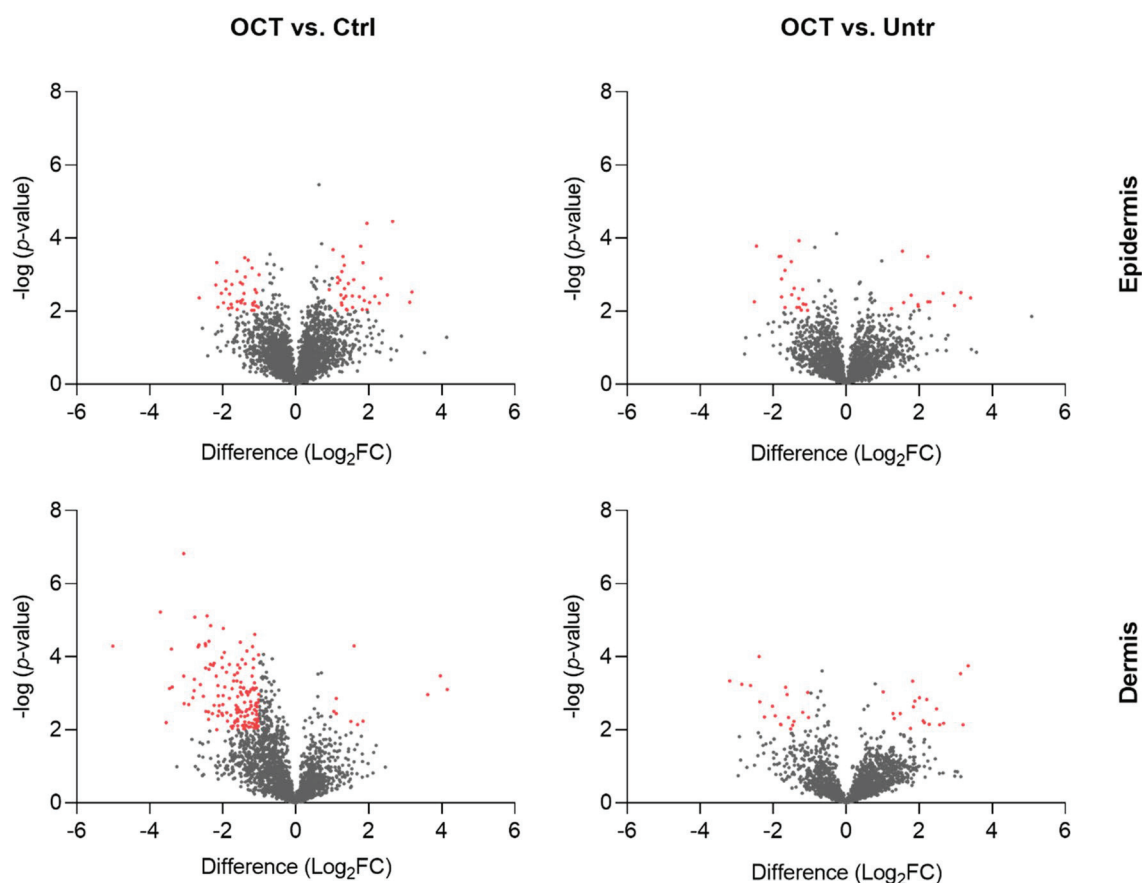
Figure 5. More proteins are significantly differentially regulated upon OCT treatment in the dermis than in the epidermis. Full skin biopsies of healthy female donors (age range: 36–44 years, n = 3) were TS, treated with OCT, control gel or left untreated and cultivated for 48 h. Subsequently, epidermis was detached from dermis and the two compartments were separately prepared for LC–MS analysis. Volcano plots show differences in LFQ values (fold change, logarithmic scale to the base of two) on the x-axis including their corresponding p-values (logarithmic scale) on the y-axis. Proteins marked in red are significantly differentially regulated ($Log_2FC < -1$ = downregulated; $Log_2FC > 1$ = upregulated) in OCT treated TS samples compared to control gel-treated TS samples or untreated TS samples. Data presented in the plots was generated performing a two-sided t-test ($p < 0.05$) using Perseus and Volcano plots were generated with Graphpad Prism using exclusively proteins with a p-value < 0.01.

when compared to untreated TS biopsies, but not with TS biopsies treated with the control gel, suggesting that application of the hydrogel on the wound already leads to a decrease of MMP3 secretion. Our further finding that MMP activity was significantly reduced in OCT-treated samples compared to controls demonstrated that OCT has indeed a regulatory effect regarding protease inhibitors. Skin fibroblasts have been demonstrated to secrete IL-6 and IL-8 in addition to several chemokines, MMPs and protease inhibitors[45]. The dermis is rich in fibroblasts suggesting that these cells may be the most relevant cell type responding to OCT treatment. The fact that OCT inhibits the release of tissue MMPs might be one further explanation of the pathological scar preventing and wound healing promoting effects of OCT in vivo. TIMP-1 is one of the major MMP inhibitors, usually significantly downregulated in chronic or slowly healing wounds[10]. As OCT did not regulate TIMP-1, as revealed by LC–MS and ELISA analysis, the exact mechanism of MMP inhibition by OCT in our model is not yet clear and remains to be further investigated.

To address which skin compartment is influenced by the topical application of OCT onto TS human skin, the epidermis and dermis were not only analyzed separately but, in addition, with a more sensitive method. Less proteins were found to be differentially regulated in OCT-treated TS epidermal samples, while we found OCT-mediated protein regulation largely in the dermis. In line with our results is the finding that OCT significantly reduces MMP1 and MMP2 compared to control gel-treated dermal TS biopsies. The discovery that MMP9 is significantly reduced in OCT-treated TS dermal samples further supports our previous finding that OCT has protease-inhibitory capacities.

Today, moist wound healing is widely accepted as the state-of-the-art in professional wound care. The high water content of hydrogels allows them to benefit cutaneous healing essentially by supporting a moist wound environment and promoting autolytic debridement[46]. We have shown in all experiments herein that the combination of a hydrogel with the antiseptic OCT provides additional immunomodulatory features compared to

69
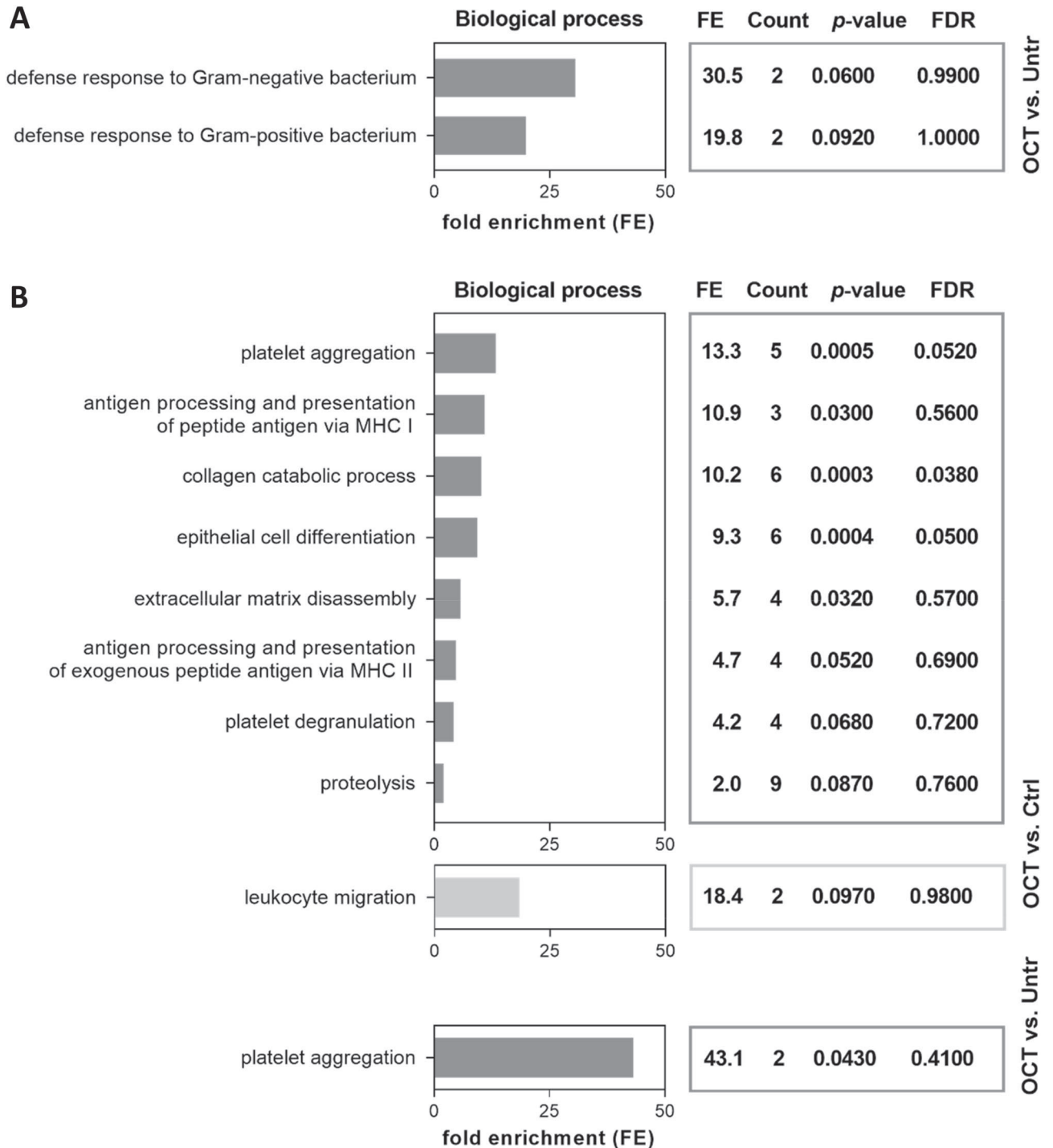
Figure 6. OCT regulates proteins involved in immune response in the epidermal compartment and proteins involved in wound healing and immune response in the dermal compartment. Full skin biopsies of donors (age range: 36–44 years, n = 3) were TS, treated with OCT, control gel or left untreated and cultivated for 48 h. Subsequently, epidermis **(A)** was detached from dermis **(B)** and the two compartments were separately prepared for LC–MS analysis. Classification by the GO term biological process shows pathways and larger processes made up of the activities of multiple proteins. Fold enrichment values for individual GO terms, count (proteins involved in the term), *p*-value and FDR (false discovery rate, calculated using the Benjamini–Hochberg procedure), listed next to the graph, were calculated using DAVID bioinformatics resources. Biological processes downregulated in OCT-treated TS samples are shown in dark grey, processes upregulated in OCT-treated TS samples are shown in light grey.
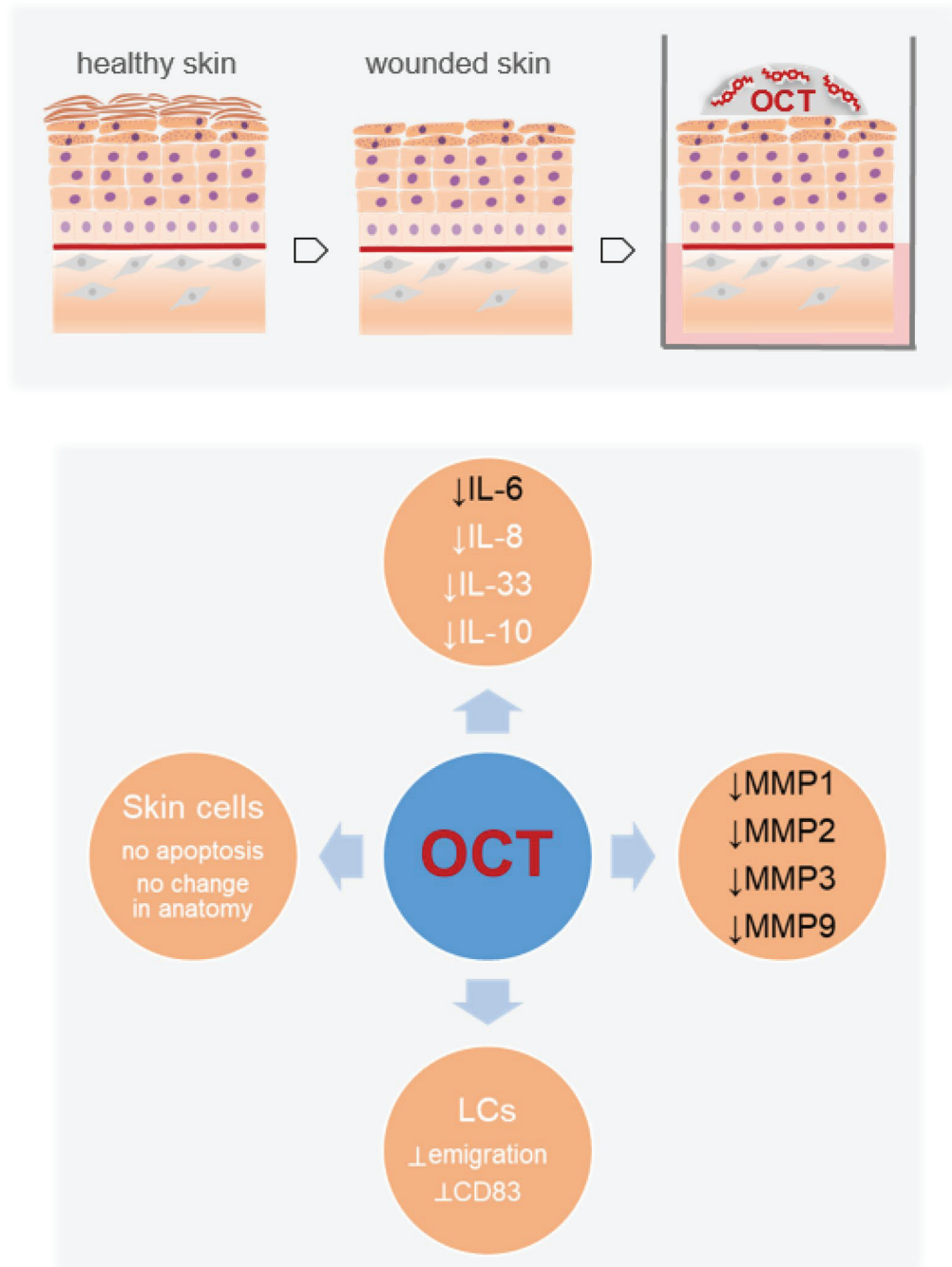
Figure 7. OCT reduces cytokines as well as protease activities in wounded human skin (this study, black font), is not apoptotic for skin cells, does not change the skin architecture and prevents the upregulation of CD83 on Langerhans cells as well as their emigration (white font)[17].

the application of the very same hydrogel without any bioactive agent. The observed local anti-inflammatory environment in TS skin samples treated with an OCT containing hydrogel can be perfectly linked to the presence of the antiseptic itself in the gel and are not the result of pure moist wound healing alone.

To conclude, our data provide further new insights into the mode of action by which OCT improves wound healing in clinical settings, as we reported anti-inflammatory and protease-inhibitory activities of OCT in wounded human skin (Fig. 7) and identified the dermal proteome as its main target.

Data availability
Data, in anonymous format (according to data protection policy in the ethics agreement) is available on reasonable request.

71

References

1. Nestle, F. O., Di Meglio, P., Quin, J.-Z. & Nickoloff, B. J. Skin immune sentinels in health and disease. *Nat. Rev. Immunol.* **9**, 679–691 (2009).
2. Quaresma, J. A. S. Organization of the skin immune system and compartmentalized immune responses in infectious diseases. *Clin. Microbiol. Rev.* **32**, e00034-18 (2019).
3. Seifert, A., Monaghan, J., Voss, R. & Maden, M. Skin regeneration in adult axolotls: a blueprint for scar-free healing in vertebrates. *PLoS ONE* **7**, e32875 (2012).
4. Richardson, R. *et al.* Adult zebrafish as a model system for cutaneous wound-healing research. *J. Investig. Dermatol.* **133**, 1655–1665 (2013).
5. Zhao, R., Liang, H., Clarke, E., Jackson, C. & Xue, M. Inflammation in chronic wounds. *Int. J. Mol. Sci.* **17**, 2085 (2016).
6. Eming, S. A., Krieg, T. & Davidson, J. M. Inflammation in wound repair: molecular and cellular mechanisms. *J. Investig. Dermatol.* **127**, 514–525 (2007).
7. Gabay, C. Interleukin-6 and chronic inflammation. *Arthritis Res. Ther.* **8**, S3 (2006).
8. Caley, M. P., Martins, V. L. C. & O'Toole, E. A. Metalloproteinases and wound healing. *Adv. Wound Care* **4**, 225–234 (2015).
9. Ulrich, D., Ulrich, F., Unglaub, F., Piatkowski, A. & Pallua, N. Matrix metalloproteinases and tissue inhibitors of metalloproteinases in patients with different types of scars and keloids. *J. Plast. Reconstr. Aesthetic Surg.* **63**, 1015–1021 (2010).
10. Auf dem Keller, U. & Sabino, F. Matrix metalloproteinases in impaired wound healing. *Metalloproteinases Med.* **2**, 1–8 (2015).
11. Martins, V. L., Caley, M. & O'Toole, E. A. Matrix metalloproteinases and epidermal wound repair. *Cell Tissue Res.* **351**, 255–268 (2013).
12. Koburger, T., Hübner, N. O., Braun, M., Siebert, J. & Kramer, A. Standardized comparison of antiseptic efficacy of triclosan, PVP-iodine, octenidine dihydrochloride, polyhexanide and chlorhexidine digluconate. *J. Antimicrob. Chemother.* **65**, 1712–1719 (2010).
13. von Rheinbaben, F. & Wolff, M. H. *Handbuch der viruswirksamen Desinfektionen* (Springer, Berlin, 2002). https://doi.org/10.1007/978-3-642-56394-2_13.
14. Metcalf, D. G., Bowler, P. G. & Hurlow, J. A clinical algorithm for wound biofilm identification. *J. Wound Care* **23**, 137–143 (2014).
15. Cutting, K. F. & Westgate, S. J. The use of wound cleansing solutions in chronic wounds. *Wounds UK* **8**, 130–133 (2012).
16. Matiasek, J. *et al.* An intra-individual surgical wound comparison shows that octenidine-based hydrogel wound dressing ameliorates scar appearance following abdominoplasty. *Int. Wound J.* **15**, 914–920 (2018).
17. Nikolić, N. *et al.* The antiseptic octenidine inhibits Langerhans cell activation and modulates cytokine expression upon superficial wounding with tape stripping. *J. Immunol. Res.* **2019**, 5143635 (2019).
18. Grada, A., Mervis, J. & Falanga, V. Research techniques made simple: animal models of wound healing. *J. Investig. Dermatol.* **138**, 2095-2105.e1 (2018).
19. Ud-Din, S. & Bayat, A. Non-animal models of wound healing in cutaneous repair: in silico, in vitro, ex vivo, and in vivo models of wounds and scars in human skin. *Wound Repair. Regen.* **25**, 164–176 (2017).
20. Tajpara, P. *et al.* Epicutaneous administration of the pattern recognition receptor agonist polyinosinic-polycytidylic acid activates the MDA5/MAVS pathway in Langerhans cells. *FASEB J.* **32**, 4132–4144 (2018).
21. Zila, N. *et al.* Proteomics-based insights into mitogen-activated protein kinase inhibitor resistance of cerebral melanoma metastases. *Clin. Proteom.* **15**, 13 (2018).
22. Wiśniewski, J. R., Zougman, A., Nagaraj, N. & Mann, M. Universal sample preparation method for proteome analysis. *Nat. Methods* **6**, 359–362 (2009).
23. Bileck, A., Kreutz, D., Muqaku, B., Slany, A. & Gerner, C. Comprehensive assessment of proteins regulated by dexamethasone reveals novel effects in primary human peripheral blood mononuclear cells. *J. Proteome Res.* **13**, 5989–6000 (2014).
24. Slany, A. *et al.* Contribution of human fibroblasts and endothelial cells to the hallmarks of inflammation as determined by proteome profiling. *Mol. Cell. Proteom.* **15**, 1982–1997 (2016).
25. Cox, J. & Mann, M. MaxQuant enables high peptide identification rates, individualized p.p.b.-range mass accuracies and proteome-wide protein quantification. *Nat. Biotechnol.* **26**, 1367–1372 (2008).
26. Cox, J. & Mann, M. 1D and 2D annotation enrichment: a statistical method integrating quantitative proteomics with complementary high-throughput data. *BMC Bioinform.* **13**, S12 (2012).
27. Tyanova, S. *et al.* The Perseus computational platform for comprehensive analysis of (prote)omics data. *Nat. Methods* **13**, 731–740 (2016).
28. UniProt Consortium. UniProt: a worldwide hub of protein knowledge. *Nucleic Acids Res.* **47**, D506–D515 (2019).
29. Huang, D. W., Sherman, B. T. & Lempicki, R. A. Systematic and integrative analysis of large gene lists using DAVID bioinformatics resources. *Nat. Protoc.* **4**, 44–57 (2009).
30. Huang, D. W., Sherman, B. T. & Lempicki, R. A. Bioinformatics enrichment tools: paths toward the comprehensive functional analysis of large gene lists. *Nucleic Acids Res.* **37**, 1–13 (2009).
31. Zougman, A., Selby, P. J. & Banks, R. E. Suspension trapping (STrap) sample preparation method for bottom-up proteomics analysis. *Proteomics* **14**, 1006–1000 (2014).
32. Kong, A. T., Leprevost, F. V., Avtonomov, D. M., Mellacheruvu, D. & Nesvizhskii, A. I. MSFragger: ultrafast and comprehensive peptide identification in mass spectrometry-based proteomics. *Nat. Methods* **14**, 513–520 (2017).
33. Vizcaíno, J. A. *et al.* 2016 Update of the PRIDE database and its related tools. *Nucleic Acids Res.* **44**, D447–D456 (2016).
34. Szklarczyk, D. *et al.* STRING v11: protein–protein association networks with increased coverage, supporting functional discovery in genome-wide experimental datasets. *Nucleic Acids Res.* **47**, D607–D613 (2019).
35. Du, G. *et al.* Induction of matrix metalloproteinase-1 by tumor necrosis factor-α is mediated by interleukin-6 in cultured fibroblasts of keratoconus. *Exp. Biol. Med.* **241**, 2033–2041 (2016).
36. Kossakowska, A. E. *et al.* Interleukin-6 regulation of matrix metalloproteinase (MMP-2 and MMP-9) and tissue inhibitor of metalloproteinase (TIMP-1) expression in malignant non-Hodgkin's lymphomas. *Blood* **94**, 2080–2089 (1999).
37. Johnson, B. Z., Stevenson, A. W., Prêle, C. M., Fear, M. W. & Wood, F. M. The role of IL-6 in skin fibrosis and cutaneous wound healing. *Biomedicines* **8**, 101 (2020).
38. Gill, S. E. & Parks, W. C. Metalloproteinases and their inhibitors: regulators of wound healing. *Int. J. Biochem. Cell Biol.* **40**, 1334–1347 (2007).
39. Hämmerle, G. & Strohal, R. Efficacy and cost-effectiveness of octenidine wound gel in the treatment of chronic venous leg ulcers in comparison to modern wound dressings. *Int. Wound J.* **13**, 182–188 (2016).
40. Alam, K., Edwards, J., Jeffery, S., Hunt, S. & Assadian, O. Safe, effective and quick: a novel treatment for burns and large wounds: clinical benefits of octenilin wound gel. *Br. J. Nurs.* **27**, 2–18 (2018).
41. Sharpe, A. *et al.* Case studies: octenidine in the management of diabetic foot ulcers. *Diabet. Foot J.* **21**, 192–197 (2018).
42. Liechty, K. W., Adzick, N. S. & Crombleholme, T. M. Diminished interleukin 6 (IL-6) production during scarless human fetal wound repair. *Cytokine* **12**, 671–676 (2000).

72

43. Iocono, J. A. *et al.* Interleukin-8 levels and activity in delayed-healing human thermal wounds. *Wound Repair. Regen.* **8**, 216–225 (2000).
44. Lim, C. P., Phan, T. T., Lim, I. J. & Cao, X. Cytokine profiling and Stat3 phosphorylation in epithelial–mesenchymal interactions between keloid keratinocytes and fibroblasts. *J. Investig. Dermatol.* **129**, 851–861 (2009).
45. Tahir, A. *et al.* Combined proteome and eicosanoid profiling approach for revealing implications of human fibroblasts in chronic inflammation. *Anal. Chem.* **89**, 1945–1954 (2017).
46. da Silva, L. P., Reis, R. L., Correlo, V. M. & Marques, A. P. Hydrogel-based strategies to advance therapies for chronic skin wounds. *Annu. Rev. Biomed. Eng.* **21**, 145–169 (2019).

Competing interests

The authors declare no competing interests.

Additional information

Supplementary Information The online version contains supplementary material available at https://doi.org/10.1038/s41598-020-79378-9.

Correspondence and requests for materials should be addressed to A.E.-B.

Reprints and permissions information is available at www.nature.com/reprints.

Publisher's note Springer Nature remains neutral with regard to jurisdictional claims in published maps and institutional affiliations.

4.3 Exploring the dermotoxicity of the mycotoxin deoxynivalenol: combined morphologic and proteomic profiling of human epidermal cells reveals alteration of lipid biosynthesis machinery and membrane structural integrity relevant for skin barrier function

Lukas Janker[3,4]*; Giorgia Del Favero[1,2]*, Benjamin Neuditschko[3,5], Julia Hohenbichler[1], Endre Kiss[2], Lydia Woelflingseder[1], Christopher Gerner[2,3,4], Doris Marko[1,2]

1   Department of Food Chemistry and Toxicology, Faculty of Chemistry, University of Vienna, Vienna, Austria
2   Core Facility Multimodal Imaging, Faculty of Chemistry, University of Vienna, Vienna, Austria
3   Department of Analytical Chemistry, Faculty of Chemistry, University of Vienna, Vienna, Austria
4   Joint Metabolome Facility, Faculty of Chemistry, University of Vienna, Vienna, Austria
5   Department of Inorganic Chemistry, Faculty of Chemistry, University of Vienna, Vienna, Austria
*   Contributed equally

Contributions to this publication:

- Performing research and MS measurements
- Analysis and interpretation of data
- Preparation of figures and writing of manuscript

BIOLOGICS

Exploring the dermotoxicity of the mycotoxin deoxynivalenol: combined morphologic and proteomic profiling of human epidermal cells reveals alteration of lipid biosynthesis machinery and membrane structural integrity relevant for skin barrier function

Giorgia Del Favero[1,2] · Lukas Janker[3,4] · Benjamin Neuditschko[3,5] · Julia Hohenbichler[1] · Endre Kiss[2] · Lydia Woelflingseder[1] · Christopher Gerner[2,3,4] · Doris Marko[1,2]

Abstract

Deoxynivalenol (vomitoxin, DON) is a secondary metabolite produced by *Fusarium* spp. fungi and it is one of the most prevalent mycotoxins worldwide. Crop infestation results not only in food and feed contamination, but also in direct dermal exposure, especially during harvest and food processing. To investigate the potential dermotoxicity of DON, epidermoid squamous cell carcinoma cells A431 were compared to primary human neonatal keratinocytes (HEKn) cells via proteome/ phosphoproteome profiling. In A431 cells, 10 µM DON significantly down-regulated ribosomal proteins, as well as mitochondrial respiratory chain elements (OXPHOS regulation) and transport proteins (TOMM22; TOMM40; TOMM70A). Mitochondrial impairment was reflected in altered metabolic competence, apparently combined with interference of the lipid biosynthesis machinery. Functional effects on the cell membrane were confirmed by live cell imaging and membrane fluidity assays (0.1–10 µM DON). Moreover, a common denominator for both A431 and HEKn cells was a significant downregulation of the squalene synthase (FDFT1). In sum, proteome alterations could be traced back to the transcription factor Klf4, a crucial regulator of skin barrier function. Overall, these results describe decisive molecular events sustaining the capability of DON to impair skin barrier function. Proteome data generated in the study are fully accessible via ProteomeXchange with the accession numbers PXD011474 and PXD013613.

Keywords Deoxynivalenol dermotoxicity · Skin barrier · Unfolded protein response mitochondrial · Klf4 transcription factor

Abbreviations

DON	Deoxynivalenol
MEM	Minimum essential medium
PMSF	Phenylmethylsulfonyl fluoride
TE	Tris EDTA
NP-40	Nonidet P-40
IAA	Iodoacetamide
FA	Formic acid
ACN	Acetonitrile
HCD	Higher collisional dissociation

Giorgia Del Favero and Lukas Janker authors contributed equally to the work.

✉ Giorgia Del Favero
giorgia.del.favero@univie.ac.at

✉ Christopher Gerner
christopher.gerner@univie.ac.at

[1] Department of Food Chemistry and Toxicology, Faculty of Chemistry, University of Vienna, Währingerstr. 38-40, 1090 Vienna, Austria

[2] Core Facility Multimodal Imaging, Faculty of Chemistry, University of Vienna, Währingerstr. 38-40, 1090 Vienna, Austria

[3] Department of Analytical Chemistry, Faculty of Chemistry, University of Vienna, Währingerstr. 38-40, 1090 Vienna, Austria

[4] Joint Metabolome Facility, Faculty of Chemistry, University of Vienna, Währingerstr. 38-40, 1090 Vienna, Austria

[5] Department of Inorganic Chemistry, Faculty of Chemistry, University of Vienna, Währingerstr. 42, 1090 Vienna, Austria

Springer

77

LFQ	Label-free quantification
PPM	Parts per million
FDR	False discovery rate
ROS	Reactive oxygen species
DCF-DA	2′,7′-Dichlorodihydrofluorescein diacetate
CYT	Cytoplasmic fraction
MOAC	Metal oxide affinity chromatography
NE	Nuclear extracts
UPR	Unfolded protein response
HEKn	Human epidermal keratinocytes, neonatal

Introduction

Skin structural integrity is essential for the maintenance of barrier function. Similarly, at cellular level, the plasma membrane represents the interface with the extracellular environment and, as such, its structure and stability are essential for cellular homeostasis. From a toxicological perspective, skin represents a highly exposed target for chemicals and toxins. For food contaminants in general and for mycotoxins in particular, dermal exposure through contaminated food commodities during harvest and processing is becoming a topic of great interest (Doi and Uetsuka 2014), and it poses concerns in addition to the classical oral administration route (Katrine et al. 2017). Among food contaminants, deoxynivalenol (DON, vomitoxin) is one of the most commonly detected mycotoxins produced by the *Fusarium species complex* (Gruber-Dorninger et al. 2016; van der Lee et al. 2015). DON is classified in the trichothecene structural group and acts at molecular level via inhibition of protein synthesis (Cundliffe et al. 1974; Ueno 1977). This event is initiated by binding to the A-site of the 60S large ribosomal subunit (Dellafiora et al. 2017; Garreau de Loubresse et al. 2014) and ultimately leads to the impairment of the peptidyl-transferase activity of the organelle. In line, the toxin extensively impairs cellular functions, and this is associated with organ-specific phenotypic manifestations (Pestka 2010a, b). As example, DON is known to impair the intestinal barrier system; it targets cell–cell-junctional proteins and mucous layer hampering in this way gut functionality (Beisl et al. 2020, 2021; Pinton and Oswald 2014; Robert et al. 2017; Wang et al. 2020).

At cutaneous level, DON sustains pro-inflammatory reactions and activates the AP-1 and NF-κB signaling cascade in vitro (Mishra et al. 2014). On these molecular premises, in vivo, DON can act as skin tumor initiator (Mishra et al. 2016) and this response is sensitive to the combined treatment with the antioxidant *N*-acetyl-cysteine and the anti-inflammatory drug celecoxib (Mishra et al. 2020a). However, much remains to be elucidated to understand the mechanisms sustaining the dermotoxic effects of DON. For instance, it was recently described how even oral intake could enhance inflammatory response in allergic dermatitis (Aihara et al. 2020). In line, accurate definition of molecular events triggered by DON is of crucial importance for the assessment of the risk associated with the cutaneous exposure through contaminated food commodities.

Epidermoid carcinoma cells A431 are routinely used as skin-derived cell model (Li et al. 2016; Smina et al. 2015). We recently demonstrated that DON impairs the capability of A431 to respond to uniaxial cell stretching and that the toxin targets several proteins essential for the maintenance of cell adhesion and morphology (Del Favero et al. 2018a). This is particularly relevant since biomechanical plasticity and adaptive response to movement are obvious essential components of the skin barrier functionality. In this study, we applied a combinatory microscopy and proteomics approach to unravel the molecular events, downstreaming from the ribosomal inhibition, toward the loss of membrane structural integrity. Proteomics profiling combined with phosphoproteomics was used to characterize the molecular signature of DON on A431 cells and to highlight the steps leading to the alteration of lipid biosynthesis machinery. Ultimately, to sustain the toxicological relevance of our findings also in non-transformed cells, we compared the effects of DON with human primary keratinocytes (HEKn) regarding proteome alterations and post-translational modifications.

Materials and methods

Cell culture

Epidermoid carcinoma cells A431 were cultivated as previously described (Del Favero et al. 2018a) in Minimum Essential Medium (MEM) with L-glutamine (4.5 g/L), 10% (*v/v*) heat-inactivated fetal bovine serum (FBS) and 1% (*v/v*) penicillin/streptomycin and maintained in controlled humidified incubators at 37 °C and 5% CO_2. Primary Epidermal Keratinocytes (HEKn; Normal, Human, Neonatal Foreskin ATCC® PCS-200-010™) were cultivated according to the specification of the supplier in Dermal Cell Basal Medium (ATCC® PCS-200-030™) including Keratinocyte Growth Kit (ATCC® PCS-200-040™). If not otherwise specified, cell culture reagents were purchased from GIBCO Invitrogen (Karlsruhe, Germany), Sigma-Aldrich Chemie GmbH (Munich, Germany), Sarstedt AG & Co (Nuembrecht, Germany), VWR International GmbH (Vienna, Austria) and Thermo Fisher Scientific GmbH (Vienna, Austria). Commercially available DON was purchased from Romer Labs (Tulln, Austria). Solid substance was dissolved in dimethyl sulfoxide (DMSO; Carl Roth GmbH, Karlsruhe, Germany) and diluted in cell culture media (1:1000). Respective

DMSO concentration (0.1%) was used as negative/solvent control (controls, CONT).

Cell fractionation

To obtain the cytoplasmic fraction, cells were lysed in isotonic lysis buffer (10 mM HEPES/NaOH, pH 7.4, 0.25 M sucrose, 10 mM NaCl, 3 mM MgCl2, 0.5% Triton X-100) supplemented with Protease and Phosphatase Inhibitor Cocktail (Sigma-Aldrich, Vienna, Austria) and 1 mM PMSF under mechanical shear stress. By centrifugation at 3500 g and 4 °C for 5 min, the cytoplasmic proteins were separated from the nucleic fraction and precipitated overnight with ice-cold ethanol at -20 °C. The remaining nuclei were thoroughly resuspended in TE–NaCl and TE–NP-40 buffer and incubated on ice. After centrifugation, the supernatant was precipitated in ethanol overnight.

Sample preparation

(i) In-gel digestion of A431 cell fractions: 50 µg of each sample were loaded on an SDS-PAGE and allowed to enter the separation gel for 0.3 cm. After that, proteins in the gel were stained by an MS-compatible silver staining procedure and the total protein amount was subjected to an established in-gel digestion protocol (Bileck et al. 2014). Upon reduction with DTT and alkylation with IAA, the proteins were digested in a two-step protocol for 14 h overnight and 4 h at 37 °C using Trypsin/Lys-C Mix (MS grade; Promega Corporation, Madison, WI). The gel pieces containing the digested peptides were extracted with an extraction buffer (1:1 mixture of 5% formic acid/ACN).

(ii) Filter-aided sample preparation of HEKn cell fractions: protein fractions were subjected to a filter-assisted proteolytic digestion with a modified version of the FASP protocol (Bileck et al. 2014; Wisniewski et al. 2009). In short, 20 µg of proteins were loaded onto a pre-wetted MWCO filter (Merck KGaA, Darmstadt, Germany) with a pore size of 10 kD, followed by reduction of disulfide bonds with dithiothreitol (DTT), alkylation with iodoacetamide (IAA) and washing steps with 50 mM ammonium bicarbonate buffer. Digestion of proteins was achieved by applying two times Trypsin/Lys-C with Mass Spec Grade quality (Promega, Mannheim, Germany), at first overnight, and in a second step for 4 h. Resulting peptides were eluted through the filter by centrifugation.

(iii) Digestion protocol with the S-trap technology (Protifi, LLC., New York; USA): 50 µg or 75 µg protein solubilized in buffer containing 5% SDS were reduced and alkylated as described above. After addition of trapping buffer (90% vol/vol Methanol, 0.1 M Triethylammonium bicarbonate) samples were loaded onto the cartridges and digested with Trypsin/Lys-C Mix at 47 °C for one hour.

Supernatants containing the collected peptides were dried before instrumental analysis.

## Phosphopeptide enrichment via metal oxide affinity chromatography (MOAC)

Enrichment was performed with tryptic digests of cytoplasmic fractions of A431 and HEKn cell lines totaling 50 µg and 75 µg, respectively. For optimal peptide recovery and purity of the samples, the digestion protocol with the S-trap technology was employed. The peptides were resuspended in Binding Buffer containing 1 M glycolic acid, 5% (vol/vol) trifluoroacetic acid (TFA), 80% (vol/vol) LC–MS grade acetonitrile and loaded onto TiO_2 Mag Sepharose beads (GE Healthcare GmbH, Solingen, Germany) preconditioned with Binding Buffer. After 30 min incubation at room temperature and three subsequent washing steps (80% vol/vol acetonitrile, 1% vol/vol TFA), phosphopeptides were eluted with 5% (vol/vol) ammonium hydroxide solution. Supernatants containing the collected peptides were dried before instrumental analysis.

LC–MS/MS analysis

Dried samples were reconstituted in 5 µL 30% FA containing 10 fmol each of four synthetic standard peptides and diluted with 40 µL mobile phase A (98% H_2O, 2% ACN, 0.1% FA). 5 µL of this solution was then injected into a Dionex Ultimate 3000 nano LC-system coupled to a QExactive orbitrap mass spectrometer equipped with a nanospray ion source (Thermo Fisher Scientific, Austria). As a pre-concentration step, peptides were loaded on a 2 cm x 100 µm C18 Pepmap100 pre-column (Thermo Fisher Scientific, Austria) at a flow rate of 10 µL/min using mobile phase A. Elution from the pre-column to a 50 cm $\times$ 75 µm Pepmap100 analytical column (Thermo Fisher Scientific, Austria) and subsequent separation was achieved at a flow rate of 300 nL/min using a gradient of 8–40% mobile phase B (80% ACN, 2% H_2O, 0.1% FA) over 90 min. For mass spectrometric detection, MS scans were performed in the range from m/z 400–1400 at a resolution of 70,000 (at $m/z = 200$). MS/MS scans of the 8 most abundant ions were achieved through HCD fragmentation at 30% normalized collision energy and analyzed in the orbitrap at a resolution of 17,500 (at $m/z = 200$).

MS data processing

Identification of proteins as well as label-free quantification (LFQ) and statistical analyses were performed using the MaxQuant 1.6.0.1 software (Cox and Mann 2008) including the Andromeda search engine (Cox et al. 2011) and the Perseus statistical analysis package, a commonly used workflow for processing and statistical assessment of
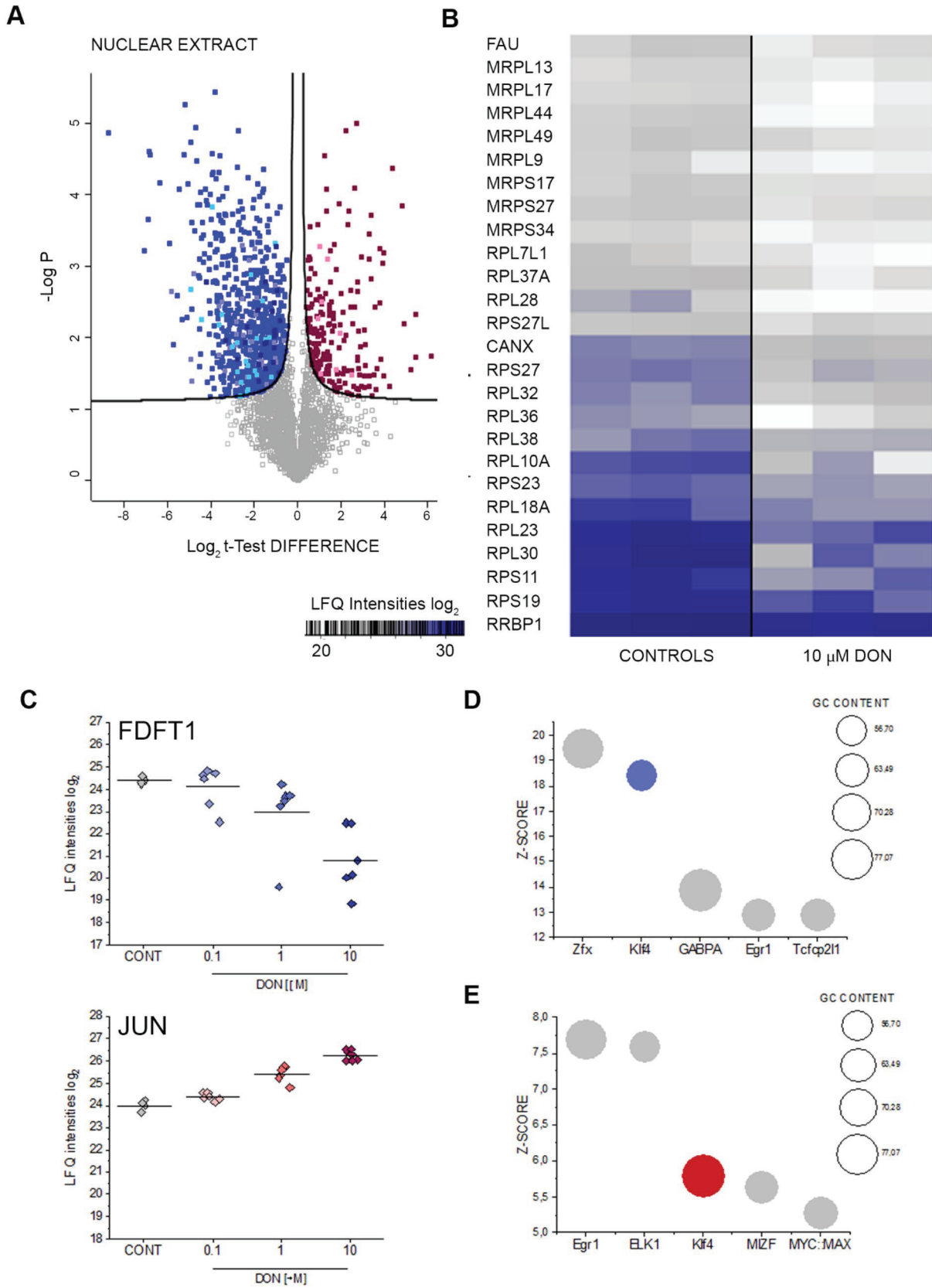
◀**Fig. 1** **a** Volcano plots depicting significant protein regulation (blue down-regulated and red up-regulated) between controls (CONT) and 10 μM DON (Nuclear Extract). Nuclear pores proteins (rose), Mitochondrial proteins (light blue), Ribonuclear proteins (violet), Ubiquitin/Proteasome (dark blue). **b** Ribosomal proteins affected by 24 h incubation with DON. **c** Concentration dependent effect of DON on squalene synthase (FDFT1) and transcription factor AP-1 component (JUN). Transcription factors associated with the proteins significantly down (**d**) and up (**e**) regulated after incubation with 10 μM DON identified by oPOSSUM search (Kwon et al. 2012)

shotgun proteomics data (Mayer et al. 2018; Tyanova et al. 2016). Proteins were identified using the UniProt database for human proteins (version 03/2018, restricted to reviewed entries only with 20,316 entries), a peptide mass tolerance of 25 ppm, an MS/MS match tolerance of 20 ppm and a maximum of two missed cleavages with trypsin as protease. Search criteria further included carbamidomethylation of cysteines as fixed modification, methionine oxidation as well as N-terminal protein acetylation as variable modifications, and a minimum of two peptide identifications per protein, at least one of them unique. Furthermore, match between runs was performed using a 1-min match time window and a 15-min alignment time window. For both, peptides and proteins, a false discovery rate (FDR) of less than 0.01 was applied; the FDR was determined by the target-decoy approach using the reversed version of the database as decoy. To determine protein groups that were significantly up- or down-regulated upon treatment, Perseus statistical analysis package was used and differences of LFQ values were calculated. LFQ values of technical duplicates were averaged and the biological replicates considered as independent. Common contaminants were removed. Changes in protein abundance values between treated and untreated cells were determined by a two-sided t test with an FDR < 0.05 and setting S0 (x-value of the hyperbolic tangent of the function separating significant events) to 0.1. Principle component analysis (PCA) results are provided in supplementary Figures S1–S2 and Figures S3–S4 for A431 and HEKn cells respectively. Data derived from bioinformatic analysis (oPOSSUM software (Ho Sui et al. 2007; Ho Sui et al. 2005; Kwon et al. 2012)) of up- and down-regulated proteins can be found in Supplementary Table 1. For the analysis of individual phosphopeptides, the software Peaks (Peaks Studio 10.0 build 20190129) was used. For the database supported search, a version of the human proteome from uniprot with 20.429 entries (October 2019) was employed. Dynamic modifications, namely N-terminal acetylation, methionine oxidation, arginine deamidation, and phosphorylation of serine, threonine and tyrosine, were taken into account. Carbamidomethylation of cysteine was considered a static modification. The maximal mass deviation of the precursor peptide was 15 ppm; the maximal fragment mass deviation was set to 0.05 Da. For phospopeptide identification, a strict

FDR of 1% was applied. For comparative analysis, a significance threshold of 15 according to Peaks and a minimum of twofold change on average were defined.

Kinase-substrate enrichment analysis was performed on site-centric quantification data obtained via MaxQuant data processing as previously described (Weiss et al. 2021). Search parameters were adjusted to additional dynamic modification of phosphorylation of serine, threonine and tyrosine. Enrichment analysis was performed on Class 1 phosphosites ($p > 0.75$) utilizing PhosphoSitePlus and NetworKIN, applying a NetworKIN score cutoff of 2, p value cutoff of 0.05 and substrate count cutoff 3.(Casado et al. 2013; Horn et al. 2014; Hornbeck et al. 2014).

Immunofluorescence

Immunolocalization experiments were performed as previously described with minor modifications (Del Favero et al. 2020). A431 cells were incubated for 24 h or 6 h hours with DON (0.1–1–10 μM) or with solvent control. At the end of the incubation, cells were fixed with pre-warmed formaldeyde (3.7%, 37 °C) and permeabilized with 0.2% Triton-X100. Blocking was perfomed with 1% Donkey serum (1 h) and targets of interest were recognized with anti-KLF4 mouse monoclonal antibody (56CT5.1.6_ab75486, Abcam), anti TOM20 mouse monoclonal antibody (F-10_sc-17764, Santa Cruz). After multiple washig steps, species-specific secondary antibodies were applied. This includes Alexa Fluor 568 Donkey anti-Rabbit (A10042) and Alexa Fluor 647 (A31571) Donkey anti-Mouse. Actin was counterstained with Alexa Fluor™ 488 Phalloidin (all from Molecular Probes, Life Technologies, Thermo Fisher Scientific, Waltham, USA). The slides were rinsed and post-fixed with 3.7% formaldehyde (10 min, RT); at the end of the postfixation, 100 mM glycine was used to mask reactive sites and slides were mounted and sealed with Roti-Mount FluoCare (Roth, Graz, Austria) with DAPI. Confocal images were acquired with a Confocal LSM Zeiss 710 equipped with ELYRA PS. 1 system and alpha plan apochromat 100X/1.46 Oil DIOC M27 objective. Image analysis was performed with ImageJ software on $n > 50$ ROI (regions of interest) randomly selected from images acquired from 3 independent datasets. Klf4 and TOM20 signals were quantified as data expressed as relative fluorescence units in comparison to controls.

Live cell imaging

For live cell imaging acquisition, CellMask™ Deep Red Plasma membrane stain (1:1000 dilution, depicted in white) was used. Cell nuclei were counterstained with Hoechst 33258 (1:1000 dilution, depicted in blue). Staining solutions were diluted in Live Cell Imaging Solution (all from
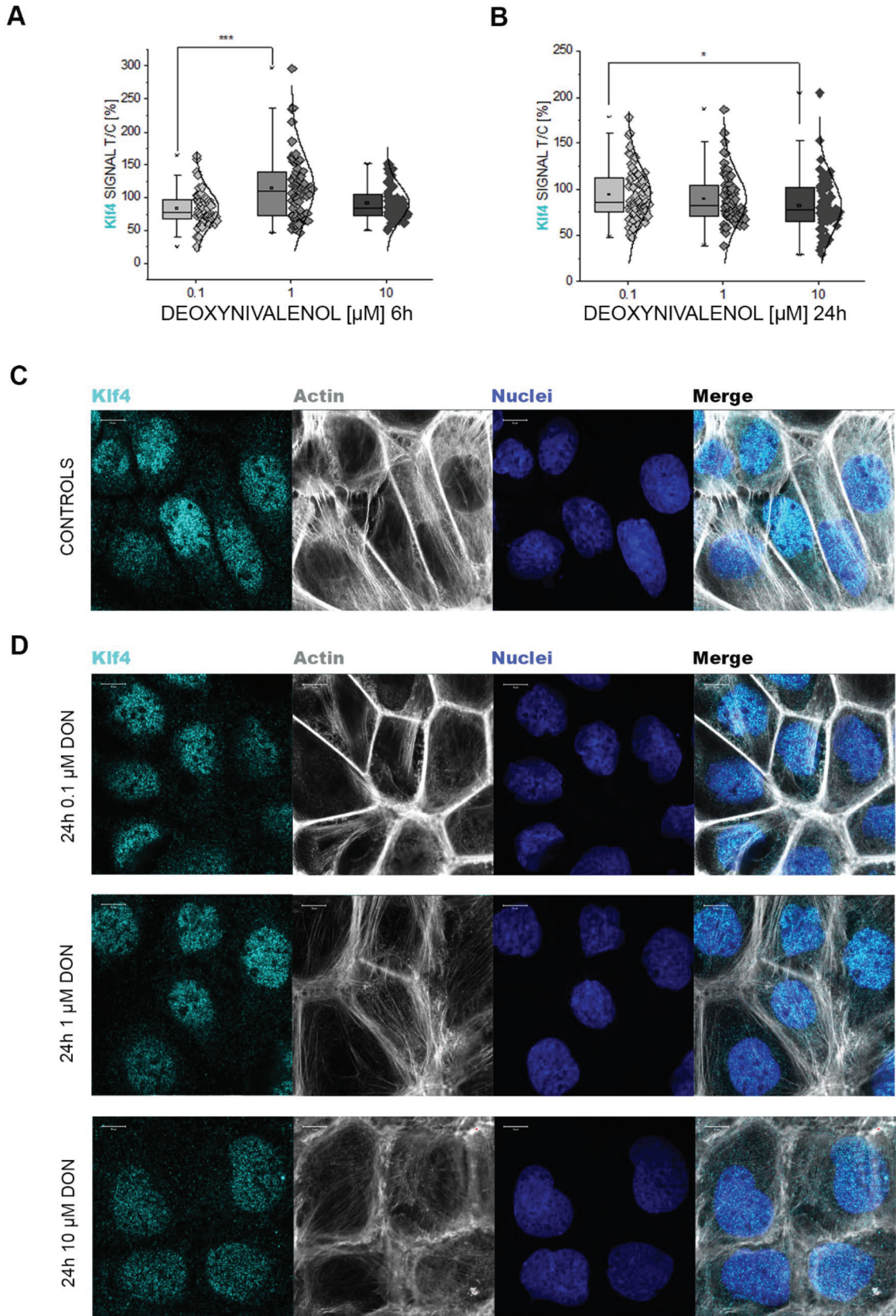
◄**Fig. 2** Immunofluorescence localization of Klf4 in A431 cells. **a** quantification of the Klf4 signal at nuclear level after 6-h incubation and **b** 24 h incubation. Data results from the quantification on n ≥ 50 ROI randomly selected from 3 independent experiments. * p < 0.05 and *** p < 0.001 at Student's *t* Test. **c** Representative images of the immunolocalization of Klf4 (light blue) and **d** after 24 h incubation with DON (0.1, 1 and 10 µM). Actin cytoskeleton is counterstained with phalloidin (depicted in gray) and cell nuclei with dapi (depicted in blue)

Molecular Probes, Life Technologies, Thermo Fisher Scientific, Waltham, USA). At the end of the incubation time, cells were washed and pre-warmed Live Cell Imaging Solution was used for the microscopy experiment. Time series were acquired with a Confocal LSM Zeiss 710 equipped with ELYRA PS. 1 using a Plan Apochromat 63X/1.4 oil objective. Filopodia were quantified using the plugin Filo-Quant for ImageJ. The cell edges and filopodia were determined for each picture either by automated analysis cross checked by step-by-step analysis to achieve representative outcomes. The quantification (Fig. 5d–h) was carried out as described by Jacquemet et al. (2017) with small adaptation. Filopodia density was calculated from the skeletonized images as the ratio of filopodia number and cell edge length for each individual picture. Analyzed datasets derived from 3 independent cell preparations.

Membrane fluidity assay

Membrane fluidity was measured adapting to the protocols from Zhang et al. (2011) and Del Favero et al. (2018b). Briefly, cells were either pre-incubated with the toxin (DON 24 h 0.1–10 µM) or challenged with the mycotoxin after the incubation with 1-pyrenedecanoic acid (PDA; Sigma Aldrich, 37 °C 1 h). Measurements were performed with Cytation3 Imaging Multi-Mode Reader (BioTek, Winooski, VT, USA) using 344 nm excitation wavelength and measuring emission at 375 nm (PDA monomeric form) and at 470 nm (PDA excimeric form). Cholesterol complexing agent methyl-beta cyclodextrin (MβCD, 10–100 µM) and H_2O_2 (100–1000 µM) were included as positive controls.

Experimental design and statistical rationale

To support statistical analysis, proteomic analyses were performed on the practical minimum of three biological replicates measured in technical duplicates per cell state (solvent controls, 0.1 µM, 1 µM and 10 µM DON, Fig. 1c, Supplementary Fig. S5). Cytoplasmic fractions and nuclear extracts were analyzed separately. For the control group of the nuclear extract fraction (Fig. 1c, Supplementary Fig. S5) one technical replicate failed and was omitted. For the identification of proteins, a false discovery rate of 0.01 was applied both at peptide and protein level. For the

calculation of significant alterations of protein abundance values, a permutation-based false discovery rate calculation applying FDR < 0.05 was applied to *t* tests of LFQ mean values. Consensus binding sites determined using the oPOSSUM software were considered significant when exceeding mean values with the addition of two standard deviations. For the selection of significantly regulated phosphopeptides, a significance threshold of a testing *p* value < 0.05 was applied.

For the data presented in Figs. 2 and 4, image analysis is the result of the quantification of at least 6 different optical fields obtained from at least three independent experiments. For the membrane fluidity assay, data are expressed as mean of 7 individually conducted experiments, comprising three technical replicates. Statistical analysis was performed applying one-way ANOVA test followed by Fisher test for pairwise comparisons (threshold values *p* < 0.05, Origin Pro 9.1G; OriginLab, Northampton, USA) or with Student's *t* Test. Graphical representation of GO terms representing biological processes and cellular components was obtained with Origin 2018b with data obtained using the DAVID Bioinformatics Resources (Huang da et al. 2009) submitting all proteins significantly up- or down-regulated, respectively. Cell lines are compared directly for the same Cellular Component or Biological Process GO Terms indicating in red the data derived from up-regulated proteins and in blue the down-regulated ones. Data used for this representation are provided in Supplementary Material Table 4.

Results

DON induced proteome alterations in A431 cells point toward regulation of transcription factor KLF4

Incubation of A431 cells with 10 µM DON triggered significant alterations of the proteome profile of the epidermoid cells. While data regarding cytoplasmic proteins were published previously (Del Favero et al. 2018a), here, we focused on nuclear extracts while adding novel data regarding the cytoplasmic proteins based on independent measurements. Out of a total of 3363 identified proteins in the nuclear extracts, 988 proteins were found significantly regulated (Fig. 1a, FDR 0.05). Among these, several ribonuclear proteins were down-regulated (Fig. 1a, b), thus confirming the ribosome as a main molecular target for DON (Cundliffe et al. 1974; Ueno 1977). Remarkably, downregulation of the ubiquitin/proteasome pathway as well as mitochondrial proteins crucial for oxidative phosphorylation (OXPHOS) was also observed (Fig. 1a) in addition to several proteins mediating lipid synthesis. To assess the specificity of this effect, dose–response experiments were performed measuring the effect of increasing
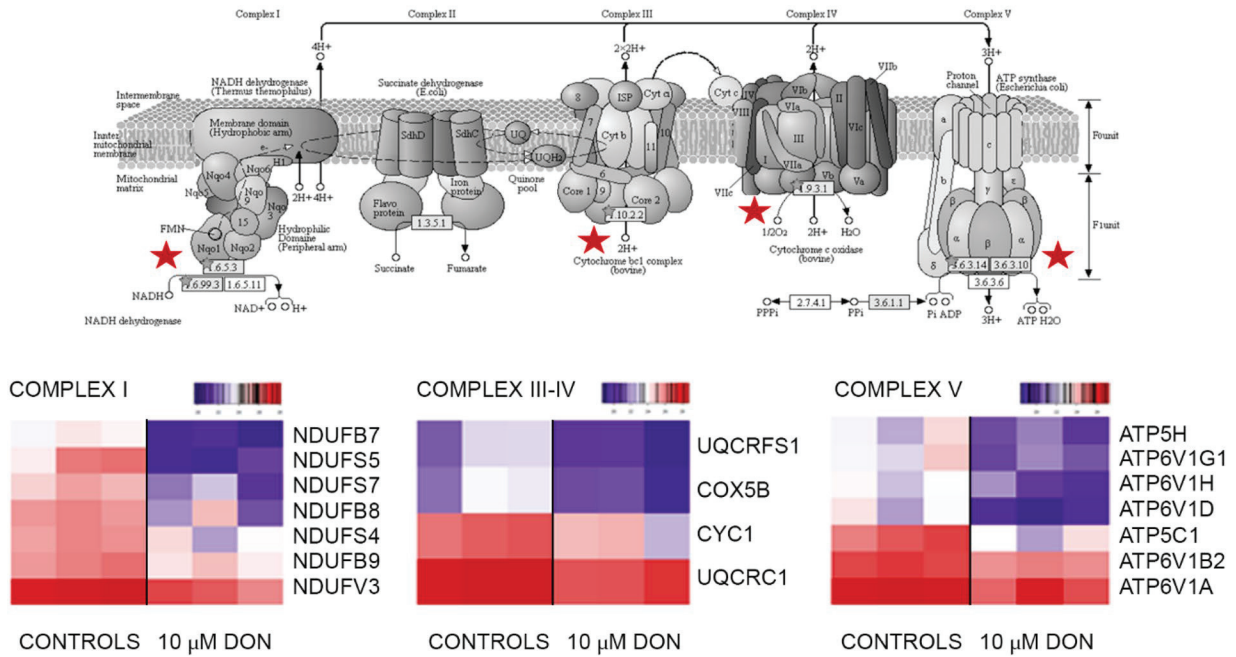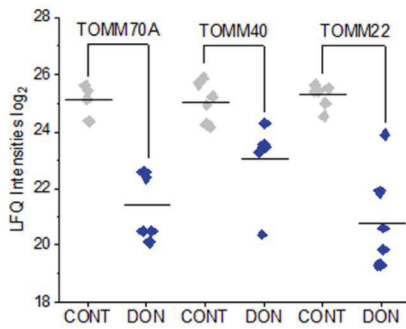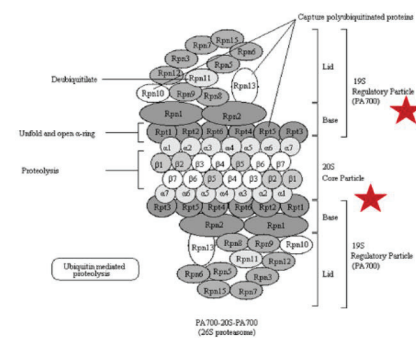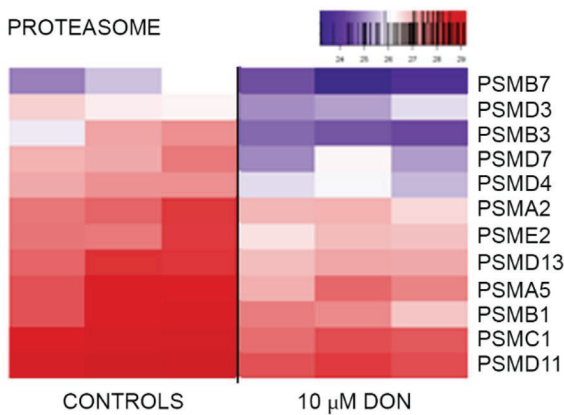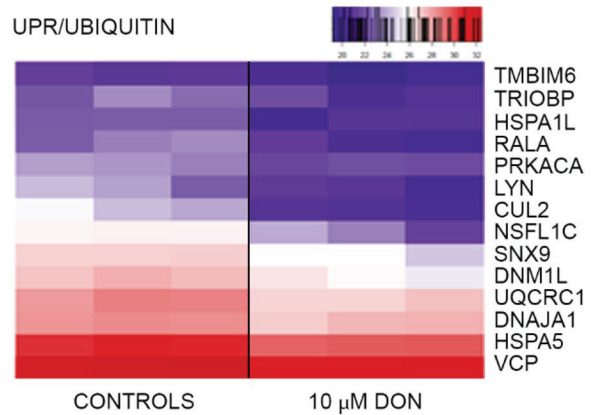
◄ **Fig. 3** Effect of DON at mitochondrial level. **a** Mitochondrial respiratory chain subunits altered by incubation with DON. Images are generated from KEGG database (Kanehisa et al. 2016, 2017; Kanehisa and Goto 2000) and reused modified with permission [KEGG Copyright Permission 200848]. Heat maps depict the proteins of the COMPLEX I, III–IV and V targeted by DON. **b** Effect of DON (blue) on the mitochondrial import proteins TOMM22/40 and 70A in comparison to controls (CONT, gray). **c** Proteasome subunits altered by incubation with DON. Images are generated from KEGG database (Kanehisa et al. 2016, 2017; Kanehisa and Goto 2000) and reused modified with permission [KEGG Copyright Permission 200848]. Red Stars indicate the subunits targeted by the mycotoxin. Heat maps depict the proteins of the proteasome (**d**) and of the ubiquitin complex (**e**) regulated by incubation with DON

concentrations of the toxin in the nuclear fraction (Fig. 1c, Supplementary Fig. S5) as well as in the cytoplasmic compartment (Supplementary Fig. S5, unreported data extracted from a previously published dataset (Del Favero et al. 2018a)). Squalene synthase (FDFT1) was found significantly regulated in a dose-dependent fashion in both subcellular fractions (Fig. 1c nuclear extracts, Supplementary Fig. S5A cytoplasmic fraction). Similar regulatory pattern could be observed for the lysosomal acid lipase/cholesteryl ester hydrolase (LIPA) and the farnesyl pyrophosphate synthase (FDPS), the mitochondrial methylmalonyl-CoA mutase (MUT, cytosolic fraction) and interferon-induced transmembrane protein 3 (IFITM3; cytosolic fraction), which were all regulated in a dose-dependent manner (Supplementary Figure S5C-H). Remarkable was also the concentration-dependent effect of the toxin on the transcription factor AP-1 (JUN, Fig. 1c) and on WWTR1 (WW domain-containing transcription regulator protein 1, Supplementary Fig. S5B). WWTR1, as component of the Hippo pathway, has been already associated with the regulation of the complex machinery governing cell adhesion and perception of mechanical forces, as well as to the development of some skin cancer types (Andl et al. 2017). Bioinformatics processing of the data with oPOSSUM software (Kwon et al. 2012) (Nuclear extracts, Fig. 1d and e, Supplementary Material Table 1) revealed the transcription factor krueppel-like factor 4 (Klf4) as a common denominator of the regulatory events triggered by DON in A431 cells. Klf4 was previously described for its role in the maintance of skin barrier function (Segre et al. 1999), hence its involvement is of great relevance for the comprehension of the dermotoxic potential of DON. Taking this as a starting point, we decided to confirm the effect of the mycotoxin on Klf4 with an independent workflow. Indeed, also with immunofluorescence and confocal imaging we could observe a concentration- and time-dependent effect of DON on the subcellular distribution of Klf4. DON increased Klf4 localization in the nuclear region after 6-h incubation (Fig. 2a) which was followed by a decrease at a longer incubation time (24 h, Fig. 2b–d).

Unfolded protein response mitochondrial induced by DON

In addition to its role in sustaining skin barrier function, Klf4 plays a central role in the regulation of metabolism and in particular mitochondrial homeostasis (Tung and Xia 2018). In line, among the most specifically challenged organelles after DON treatment, mitochondria were outstanding. More than 20 mitochondrial proteins were found significantly down-regulated (Fig. 3). Among these, there were seven members of the accessory subunits of the NADH dehydrogenase (Complex I), and four proteins of the cytochrome complex (Fig. 3a). Moreover, 7 proteins constituting the ATP synthase complex were also significantly regulated (Fig. 3a), thus confirming the central role of mitochondria and mitochondrial stress in the mechanism of action of DON (Bin-Umer et al. 2014; Ren et al. 2020). In addition to respiratory chain proteins, three mitochondrial import proteins (Wiedemann et al. 2003), namely TOMM70A, TOMM40, TOMM22 (Fig. 3b) were found significantly down-regulated. Incubation with DON reduced also the abundance of 12 protein forming the proteasome complex (Fig. 3c, d) and further 14 proteins related to ubiquitination processes (Gene Ontology), indicating overall an impairment of the protein turnover apparatus (Fig. 3e). Among these, there was bax inhibitor 1 (TMBIM6; Fig. 3e), a cytoprotective protein that exerts its function through the modulation of UPR pathway (Krajewska et al. 2011), the DnaJ homolog subfamily A member 1 (DNAJA1; Fig. 3e) that regulates protein import in the mitochondria (Radons 2016) and the heat shock protein 70 kDa like 1 (HSPA1L) that upon ATP hydrolysis allows the elimination of damaged proteins (Radons 2016). In light of the capability of DON to trigger a proteome adaption retracing the UPR-mitochondrial, we also assessed if this was mirrored in the structure of the organelles. It is well known that mitochondrial functional/energetic status is tightly related to morphology and distribution underpinning the fusion–fission equilibrium (Wakim et al. 2017). In agreement with the proteome profiling, we observed that DON dose-dependently reduced the signal generated by the immunolocalization of TOM20 (Fig. 4a and b). Moreover, after 24 h incubation, DON induced a concentration dependent disorganization of the mitochondrial network. This was visible as progressive accumulation of TOM20 signal in the perinuclear region (Fig. 4c) and culminating in almost complete fragmentation upon incubation with 10 μM DON (Fig. 4d).

Impact of DON on membrane function

Overall, both untargeted (proteomics) and targeted (microscopy) analysis supported the interpretation that DON-associated dermotoxicity could involve Klf4-related pathways.
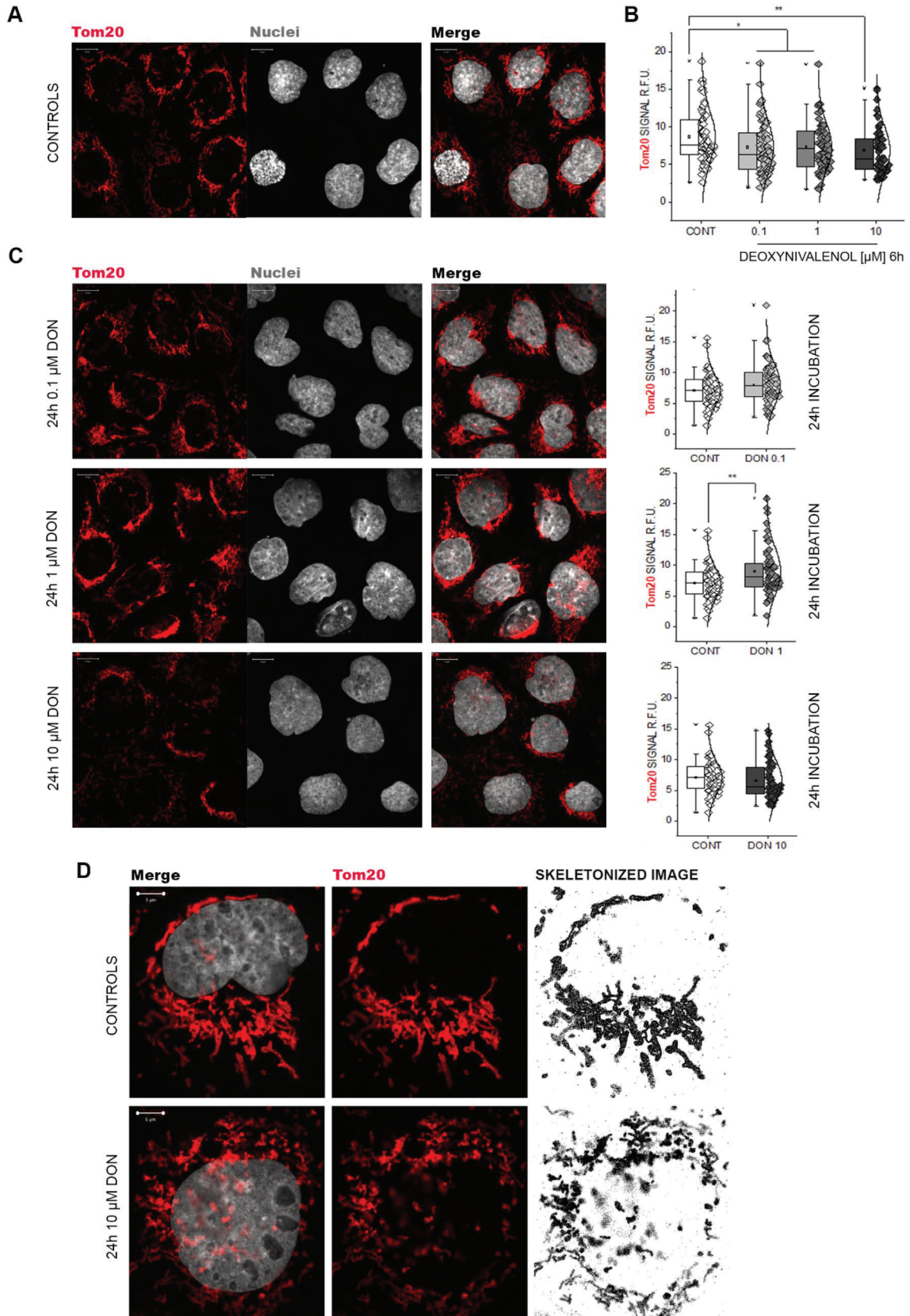
◄**Fig. 4** Immunofluorescence localization of Tom20 in A431 cells. **a** appearance of the mitochondrial protein in control conditions. **b** Tom20 signal quantification after incubation with DON for 6 h. **c** Morphology and signal quantification of Tom20 after incubation with DON for 24 h. Data results from the quantification on n ≥ 50 ROI randomly selected from 3 independent experiments, *$p < 0.05$ and **$p < 0.01$ at Student's t Test. **d** Detail of the morphological changes triggered by 10 μM DON (24 h incubation) on the mitochondrial network as compared to controls. Cell nuclei are counterstained with dapi (depicted in gray)

Once having ascertained the effect on mitochondria, we moved to verify other essential downstreaming pathways related to the activation of the transcription factor and we focused our attention on barrier function. Particularly, working with in vitro models, this can reflect on cell membrane structure and biophysical properties. DON exerted a time- and concentration-dependent effect on membrane fluidity of A431 cells (Fig. 5a). H_2O_2 added as pro-oxidant challenge failed to reproduce the effect triggered by the toxin. The cholesterol complexing agent MβCD (positive control; Fig. 5a) induced a concentration dependent decrease of the membrane fluidity of A431, confirming the performance of the assay with our cell model. Morphological evaluation of the cell membrane obtained through live cell imaging revealed prominent changes in cell membrane appearance after 1-h incubation with the toxin (10 μM; Fig. 5b) and a clear concentration-dependent effect after 24 h of incubation (Fig. 5c). Decrease of the staining intensity was accompanied by the appearance of areas of uneven accumulation of the membrane dye (CellMask), suggesting massive changes in membrane dynamics. To provide a preliminary assessment of these modulations, images were analyzed following the FILOquant workflow (Fig. 5d). Software analysis revealed homogeneous edge length in the images (Fig. 5e) and a significant decrease of the average filopodia length for the cells incubated with the lowest concentrations of the toxin (Fig. 5f; 0.1 μM DON vs CONT $p = 0.014$; 1 μM DON vs CONT $p = 0.043$ Student's t Test). Of note, an increase was detected for cells incubated with the highest concentration of DON. However, the performance of the evaluation software in this case is questioned by the apparent decrease of the CellMask signal, as well as by the uneven accumulation of the dye in cell-junctional areas. Moreover, data showed an alteration in the distribution of filopodia count (Fig. 5g, 0.1 μM DON) and a tendency on the decrease of the filopodia density (Fig. 5h).

To rule out if the effects of the mycotoxin on the cell membrane and cell membrane dynamics were associated with unspecific oxidative stress, intracellular ROS levels were determined by DCF-DA assay (Supplementary Figure S6A). Indeed, no increase in intracellular ROS levels was observed in A431 cells after cellular exposure to the toxin (max. 180 min.; Supplementary Fig. S6A). After 24 h, the

most relevant proteins typical for an oxidative stress signature, namely peroxiredoxins (Supplementary Fig. S6B nuclear extract NE and cytosolic fraction CYT), and representative members of glutathione pathway (Supplementary Fig. S6C cytosolic fraction CYT), were not regulated. However, a significant decrease/depletion in the thioredoxins pools in both nuclear and cytosolic compartment was observed (Supplementary Fig. S6D nuclear extract NE and cytosolic fraction CYT).

Effect of DON on primary epidermal keratinocytes

To expand the toxicological relevance of our findings, namely the involvement of proteins regulating cell membrane functions/barrier integrity as crucial targets downstreaming from DON-induced ribosomal inhibition, we repeated the experiments on human primary epidermal keratinocytes (HEKn). 24 h incubation with 10 μM DON induced significant regulation on more than 600 proteins out of 2977 identified proteins in the cytoplasmic fraction and more than 1600 out of 3023 identified proteins in the nuclear fraction (FDR 0.05, Supplementary Fig. S7). Bioinformatics data analysis indicated once again the transcription factor Klf4 as a key player in DON-induced response (Fig. 6a and b). In line, several proteins underpinning an involvement of skin barrier function were found disregulated (Fig. 6c, d, Supplementary Fig. S7). Similar to the A431, the squalene synthase (FDFT1) was significantly down-regulated also in the HEKn model (Fig. 6c). Among the other down-regulated proteins, cornifin-A (SPRR1A, Fig. 6c) appeared particularly meaningful in light of its function as cross-linking envelope protein for the keratinocytes (Rajagopalan et al. 2018). Similarly related to epithelial integrity were also syndecan-1 (SDC1) and galectin-3-binding protein (LGALS3BP) which mediate cytoskeleton–matrix and cell–cell adhesion (Carulli et al. 2012; Fortuna-Costa et al. 2014) (Supplementary Fig. S7C). Among the up-regulated proteins in the cytoplasmic fraction, significant regulation was observed for structural proteins like desmocollin-1 (DSC1) and keratin 18 (KRT18) (Fig. 6c and Supplementary Fig. S7C). Remarkably, several proteins sustaining an inflammatory reaction were found up-regulated, namely interleukin-1 alpha and beta (IL1A and IL1B), interleukin-36 gamma (IL36G), as well as interleukin enhancer binding factors 2 and 3 (ILF2 and ILF3; Fig. 6c and Supplementary Fig. S7). In line, data bioinformatics processing indicated the regulation of the transcription factor NF-kB in relation to the proteins up-regulated in the cytoplasmic fraction (Fig. 6a).

In the nuclear fraction, the downregulation of squalene synthase FDFT1 was confirmed and accompanied by the decrease of the long-chain-fatty-acid-CoA ligase4 (ACSL4, Fig. 6d). In parallel, downregulation of catenin alpha-1 and beta and of the epidermal growth factor receptor (EGFR)
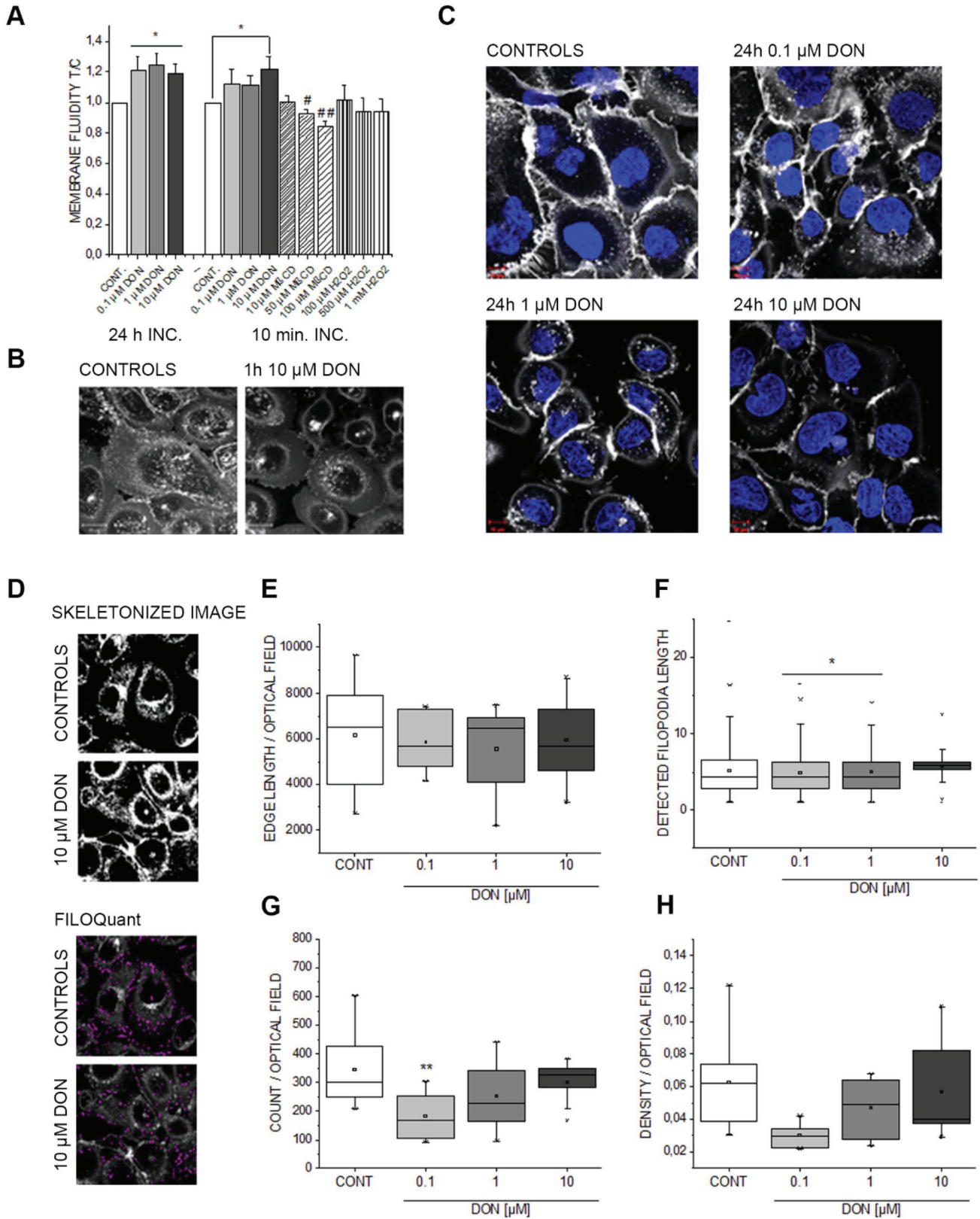
◄**Fig. 5** Effect of DON on A431 membrane. **a** Changes in membrane fluidity after 24 h incubation and 10-min exposure to DON, methyl-beta cyclodextrin (MβCD) and H_2O_2. **b** Representative pictures of cell membrane appearance after 1-h incubation with or without DON (10 μM, scale bars 20 μm). **c** Concentration dependent effect of DON on cell membrane morphology after 24 h incubation (Cell-Mask in white, Hoechst 33258 in blue) scale bars 10 μm. **d** Appearance of the images during the step-by-step analysis of filopodia using FiloQuant. **e** Edge lengths per optical field expressed as pixels of each picture. **f** Average filopodia lengths (pixels; n > 1000 filopodia/condition, * p < 0.05, Student's *t* Test). **g** Filopodia count per optical field (**$p < 0.01$, One way ANOVA). **h** Filopodia density expressed as filopodia number per edge lengths per optical field. Data are mean of at least 6 independent optical fields

was also observed (Supplementary Fig. S7D). The effect of DON on the lipid synthesis machinery of HEKn cells was evidenced also by the up-regulation of the RNA-binding protein RALY, transcriptional co-factor in cholesterol biosynthesis ((Sallam et al. 2016) Fig. 6d) and by the effect on lipocalin-1 protein (LCN1), which was described in relation to binding/transport of several lipid species (Glasgow and Abduragimovaa 2018) (Supplementary Fig. S7D). Likewise, the Ras-related protein Rab-18, which plays a role in tethering lipid droplets to the endoplasmic reticulum (Dejgaard and Presley 2019), was found up-regulated (Supplementary Fig. S7D). In line with the increase of keratin observed in the cytosolic fraction, the Fos-related antigen 2 (FOSL2) and the transcription factor JUND (binding AP-1 sites) were found up-regulated in the nuclear extract (Wurm et al. 2015) (Fig. 6d).

Comparison of the biological response triggered by DON in A431 and HEKn cells

Despite the difference in the response typical between tumor and primary cells, our data imply that the lipid synthesis and the related membrane barrier function can be considered as revevant toxicological targets for DON in both skin cell models. Data analysis through DAVID Bioinformatics Resources (Huang da et al. 2009) allowed to clearly highlight the commonalities and the differences between the response of the two cell models in terms of significantly regulated cellular components (Fig. 7a) and biological processes (Fig. 7b). For both A431 and HEKn, significant regulatory events could be traced back to the GO Terms (i) exososomes, (ii) membrane, (iii) cell junctions and (iv) focal adhesions. Interestingly, these cellular components were common denominators for down-regulated proteins in both cell types, but associated with up-regulated proteins predominantly in the primary keratinocytes. Mitochondria, as well as cell-type-specific components such as the melanosomes, were found significantly regulated for both A431 and HEKn, but prevalently associated with the negatively regulated proteins. As for the biological processes, "cell–cell adhesion" was the most

affected by the incubation with DON. This was accompanied by the regulation of several pathways connected to membrane homeostasis and cell biomechanical compliance that are essential contributors of skin integrity and barrier function (e.g., (i) cholesterol biosynthesis, (ii) Wnt signaling and (iii) endoplasmic reticulum to golgi transport). In association with the ribosomal-inhibitory potential of DON, protein folding and RNA processing were also found significantly regulated (Fig. 7b).

Phosphoproteome analysis of DON-treated A431 and HEKn cells

To deepen the understanding of the molecular events downstreaming from the incubation of DON with epidermal cells, we performed also a phosphoproteins analysis based on an affinity enrichment. As a result, out of the cytoplasmic fractions of A431 and nHEK cells, 3867 and 3474 phosphopeptides were identified (10 μM DON, FDR < 0.01; Fig. 8). Of note, one of the most reproducible phosphorylation events involved TOMM22 (Fig. 8a and b). Moreover, the dephosphorylation of YAP1 and MILK1 (MICAL-like protein 1, regulating receptor mediated endocytosis (Abou-Zeid et al. 2011)) was also observed both in A431 and HEKn (Fig. 8d). Intriguigly, the force-sensitive protein AJUBA was found regulated only in HEKn cells (Fig. 8d). Overall, 75/13 phosphopeptides derived from 55/12 phosphoproteins were found significantly regulated in A431/HEKn cells upon DON treatment (Supplementary Material Tables 2–3). Considering A431 cells, most of the significantly regulated phosphoproteins were related to cytoskeletal organization, DNA damage and repair, inflammatory response, lipid binding and membrane organization. 52 of the 75 phosphopeptides were also identified in HEKn cells, with more than 80% of them regulated similarly although without reaching significance. In HEKn cells, most regulatory events were associated with cytoskeletal organization and inflammatory response, in addition to cholesterol biosynthesis, calcium signaling and translation (Supplementary Material Tables 2–3). Here, of the 5 phosphopeptides commonly identified in A431 cells again 80% (4 peptides) were found consistently regulated. Application of a kinase substrate enrichment analysis workflow revealed a positive correlation with mTOR and NEK2 signaling in A431 cells, whereas protein kinase A and C were most prominent in HEKn cells (Supplementary Fig. S8).
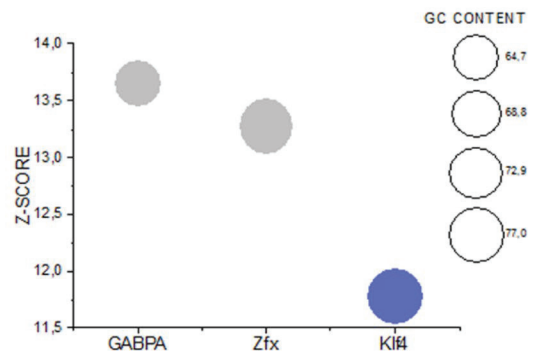
Discussion

DON is one of the most prevalent mycotoxins worldwide, but despite being studied *in depth,* it still offers novel challenges and many aspect of its toxicological profiling are
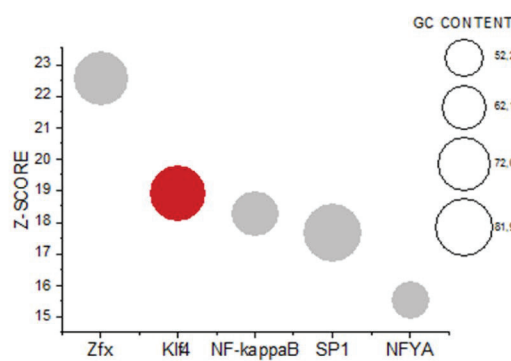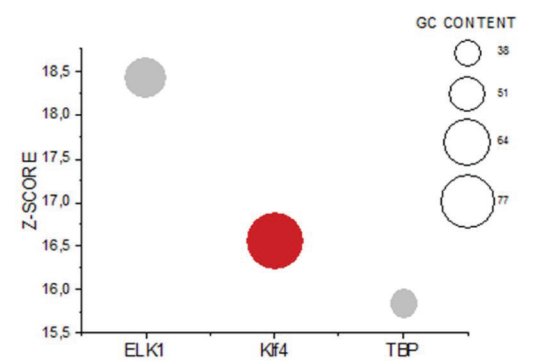
A CYTOPLASMIC FRACTION DOWN-REGULATION
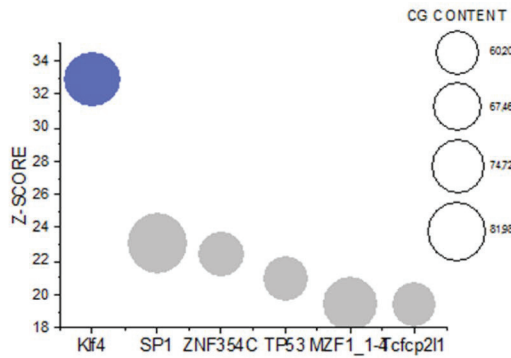
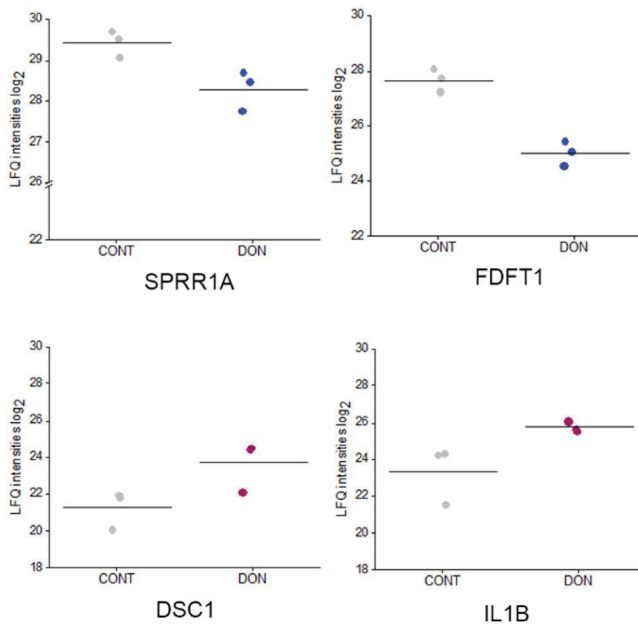**B** NUCLEAR EXTRACT DOWN-REGULATION

CYTOPLASMIC FRACTION UP-REGULATION
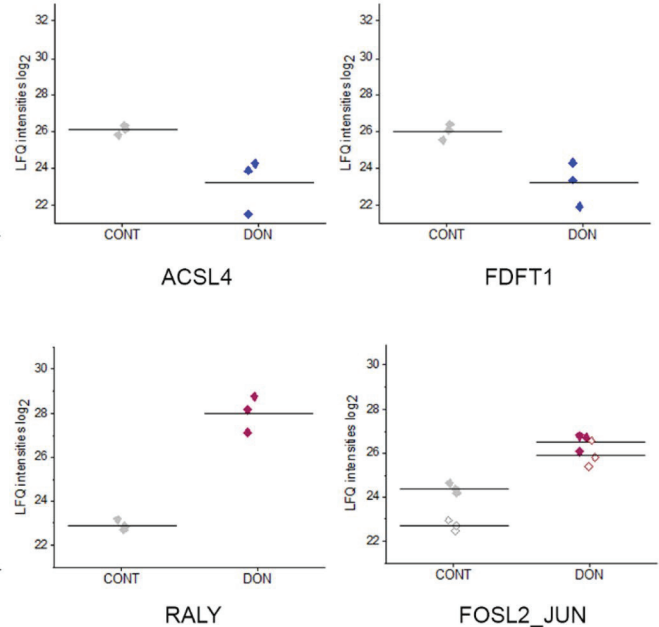
NUCLEAR EXTRACT UP-REGULATION

C

D

subject of actual research. As for other toxins, proteomic profiling after incubation with DON has been previously performed and it greatly contributed to enhance our

understanding of the molecular events sustaining the immunomodulatory function of the toxin (Nogueira da Costa et al. 2011a, b; Pan et al. 2013), as well as its effect at intestinal

◄**Fig. 6** Significant protein regulation between controls (CONT) and 10 µM DON in HEKn cells. Transcription factors associated with the proteins significantly up- and down-regulated after incubation with 10 µM DON identified by oPOSSUM Search (Kwon et al. 2012) in the cytoplasmic fraction (**a**) and nuclear extracts (**b**). **c** Selected regulated proteins in the cytoplasmic fraction: cornifin-A (SPRR1A), squalene synthase (FDFT1), desmocollin-1 (DSC-1), interleukin-1 beta (IL1B). **d** Selected regulated protein in the nuclear extract: long-chain-fatty-acid–CoA ligase 4 (ACSL4) and squalene synthase (FDFT1) RNA-binding protein Raly (RALY), Fos-related antigen 2 (FOSL2, full diamonds) and transcription factor jun-D/JUND (JUN, empty diamonds)

(Zhang et al. 2016) and hepatic levels (Smith et al. 2018). We have previously demonstrated that DON can have a quite distinctive effect on A431 cells (Del Favero et al. 2018a). It clearly affects, in the cytoplasmic compartment, proteins regulating cell adhesion, cytoskeletal membrane connection and this reflects on the capability of A431 cells to respond to mechanical stimulation (Del Favero et al. 2018a). However, the chain of molecular events leading to this loss of function, as well as the main molecular players connecting the initial ribosomal inhibition to the alteration of cell biophysical properties up to plasma membrane, remained essentially unknown. In this work, we took advantage of untargeted proteomic profiling, including phosphoproteomic analysis, to elucidate intermediate steps connecting the impairment of protein synthesis with molecular functions crucial for skin barrier maintenance.

In line with the known mechanism of action of DON, i.e. ribosomal inhibition (Cundliffe et al. 1974; Ueno 1977), incubation of A431 cells with DON triggered massive deregulation of ribosomal proteins (Fig. 1b); moreover, induction of proteins forming nuclear pore complexes supports an increase of RNA export, possibly as reaction to the ribosomal inhibition triggered by DON (Fig. 1a). Previous analysis of ribosomal-bound proteins and phosphoproteins precipitated after incubation with DON revealed that even incubation times in the order of magnitude of minutes were sufficient to significantly affect translation and protein folding (Pan et al. 2014). Similar findings were described in immune cells (Nogueira da Costa et al. 2011a). In addition, metabolic processes and energy production were also found significantly regulated (Pan et al. 2014). It was recently reported that protein turnover speed is tightly regulated, with proteins forming the mitochondrial respiratory chain being characterized by lower stability/higher turnover in comparison to ribosomal proteins (Zecha et al. 2018). In this light, a massive regulation of mitochondrial proteins upon incubation with DON can be expected (Figs. 1a and 3) and also reflects on the morphology of the organelles (Fig. 4). In addition to the effects on the mitochondrial respiratory chain (Fig. 3a), DON indeed significantly down-regulated at least three crucial proteins of the mitochondrial import machinery, namely TOMM22, TOMM40, TOMM70A

(Fig. 3b). TOMM proteins play a central role in the gate system regulating the import of nuclear-encoded proteins into the mitochondrial matrix (Chacinska et al. 2003; Rapaport et al. 1997; Wiedemann et al. 2003). Mitochondrial genes are in fact encoding for a limited number of proteins and the majority needs to be translocated into the organelles (Endo et al. 2003). Overall, alteration of protein synthesis and mitochondrial function retrace the stress signature typical for the unfolded protein response mitochondrial (UPR^{mt}). In line with the interpretation that DON could cause mitochondrial stress, phosphorylation of TOMM22 was detected in both A431 and HEKn cells (Fig. 8a, b). This event was previously associated with control of mitophagy (Kravic et al. 2018) and confirms the impact of the toxin on the turnover of the organelles as already observed in other cell types (Bin-Umer et al. 2014; Ren et al. 2020). In line, proteasomal proteins were significantly down-regulated by DON (Fig. 3c, d) as well as other members of the ubiquitination machinery (Fig. 3e). These two components are essential for the cleanup of mistargeted/misfolded proteins (Wrobel et al. 2015) and their reduction upon DON incubation mirrors the cellular stress regarding damaged protein elimination. Of note, proteasomal degradation requires ATP consumption (Finley 2009; Goldberg 2003), thus being dependent on intact mitochondrial function. Hence, it is plausible to hypothesize that DON-induced UPR might result from concomitant (i) inhibition of protein synthesis, (ii) decreased mitochondrial function and ATP production (iii) hampered/overload proteasomal system. Remarkably, UPR^{mt} is associated with increased nuclear translocation of JUN (Callegari and Dennerlein 2018) and DON triggered a concentration dependent increase of the abundance of JUN in the nuclear extract of A431 cells (Fig. 1c). In the complex landscape associated with the UPR^{mt}, vast metabolic alteration/adaptations are included (Callegari and Dennerlein 2018; Nargund et al. 2015; Oks et al. 2018). Incubation with DON triggered significant reduction of PDK1 and PDK3 (mitochondrial pyruvate dehydrogenase kinase enzymes 1 and 3), of the fatty aldehyde dehydrogenase (ALDH3A2), as well as a consistent effect on the squalene synthase (FDFT1) and other lipid synthesis-related proteins (Fig. 1, Supplementary Fig. S5). These observations imply an exstensive impairment of the lipid biosynthesis apparatus after exposure to DON and are in good agreement with previous studies describing the capability of DON to impair steroidogenesys (Cortinovis et al. 2014; Guerrero-Netro et al. 2015). In line with the effect on the lipid homeostasis, oPOSSUM engine search of the proteins significantly regulated by the mycotoxin revealed the transcription factor Klf4 as a common denominator of these effects (Fig. 1d, e) and immunofluorescence allowed to describe time and concentration dependent response of the nuclear translocation kinetics (Fig. 2). Klf4 is known to play a crucial role in the maintenance
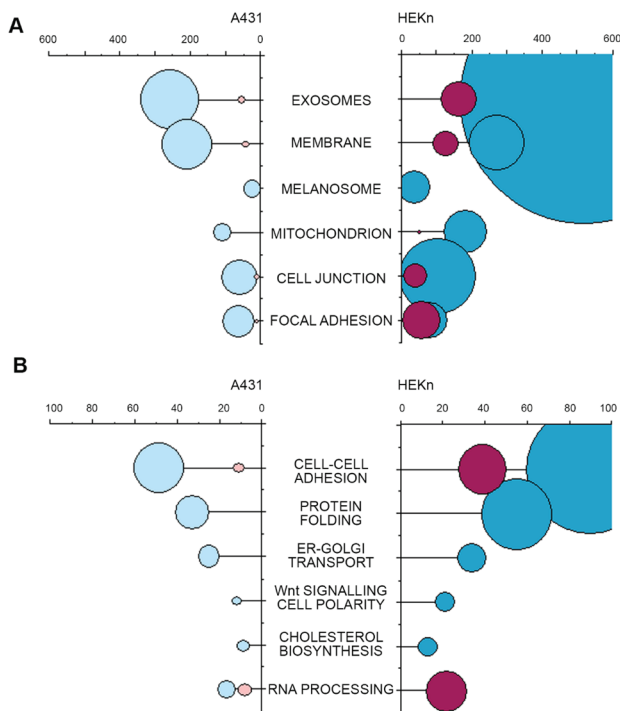
Fig. 7 A representation of DAVID functional annotation of cellular components (**a**) and biological processes (**b**) significantly regulated in A431 and HEKn in association with up-regulated proteins (red) and down-regulated proteins (blue). *X* Axes indicate the number of regulated proteins (counts) and the size of the bubbles is equivalent to –Log of the *p* value (FDR Benjamini Hochberg, Supplementary Material Table 4)

of the barrier function of the skin (Segre et al. 1999) and the validity of this result was extended also to HEKn cells (Fig. 6a, b). Obviously, the membrane plays a major role in defining cellular responses to the extracellular environment (Fuentes and Butler 2012; Lou et al. 2018). Incubation with the mycotoxin significantly altered the morphologic appearance of the cell membrane of A431 cells (Fig. 5b, c), as well as its biophysical properties measured as membrane fluidity (Fig. 5a). Filopodia also belong to membrane structures involved in cell adhesion and migration (Harel and Futerman 1993). Incubation with DON significantly altered the appearance of filopodia size and distribution (Fig. 5). In parallel, the tight junction protein TJP1 (tight junction protein ZO-1, cytosolic fraction 10 μM DON) was found up-regulated, possibly accounting for the areas of cell membrane dye (Cellmask) accumulation visible with confocal microscopy. Indeed, in response to changes of membrane fluidity and decrease of proteins necessary for filopodia formation, it cannot be excluded that other cell–cell adhesion pathways might actually be favored. It was previously described that cells can alternatively tune *N*-cadherin and filopodia, thus enhancing either cell–cell contact or migration (Kroening et al. 2010). Other proteins found regulated

in this study seem to confirm this interpretation: for instance, the Ras-related protein Ral-A (RALA; Fig. 3e) important for cell migration (Shi et al. 2006) was found significantly down-regulated in A431 cells upon incubation with DON. A similar behavior could be observed for sorting nexin 9 (SNX9, Fig. 3e) which is involved in the maintenance of cell morphology, membrane/cytoskeleton relation as well as lamellipodia formation (Hicks et al. 2015).

Of note, the effect of DON on the cell membrane could have also been mediated by direct chemical reactivity like in case of lipid peroxidation (Del Favero et al. 2020). So, the definition of the potential involvement of oxidative stress-related pathways was of crucial importance to exclude this possibility. Membrane oxidation and ROS production *per se* can account for changes of membrane biophysical properties (de la Haba et al. 2013), but without the obvious specificity of metabolic involvement. In this respect, H_2O_2, included as positive control in the membrane fluidity assay, failed to reproduce the effect mediated by the toxin (Fig. 5a). Indeed, tumor initiating effect of DON on HaCaT cells was reported to be sustained by oxidative stress (Mishra et al. 2016). However, it is known that ROS homeostasis can be altered in tumor cells as result of the malignant transformation (Del Favero et al. 2018b; Toyokuni et al. 1995; Trachootham et al. 2009), this mechanism does not seem to play a major role for A431 cells (Supplementary Fig. S6).

To better highlight the toxicological relevance of our findings also in non-tumor cells, experiments were repeated incubating HEKn primary keratinocytes. Also in this case lipid biosynthesis was influenced by the incubation with DON. For instance, the squalene synthase FDFT1 was consistently down-regulated in nuclear and cytoplasmic compartments (Fig. 6c, d). As a major difference in comparison to A431 cells, the primary keratinocytes presented a marked inflammatory response, with the up-regulation of several cytokines (Fig. 6; Supplementary Fig. S7). This result confirms previous studies on primary keratinocytes (Mishra et al. 2014) and is compatible with the PTM analysis which indicated for HEKn an increased phosphorylation of the substrates of protein kinase A and C (Supplementary Fig. S8). Most importantly, our data are coherent with in vivo studies demonstrating the central role of the inflammatory cascade, and in particular of the protein kinase C, in the dermal toxicity of DON (Mishra et al. 2020b). In line, DON induced in HEKn a significant up-regulation of the nuclear content of Fos-related antigen 2 (FOSL2) as well as of the transcription factor JUND (Fig. 6d). Both components can be traced back to the regulation of the cell redox-inflammatory response (Yin et al. 2017). Moreover, Fra-2/AP-1 interaction is crucial for terminal epidermal differentiation (Wurm et al. 2015) and it is possibly related to the increase in keratine observable in the cytoplasmic fraction (HEKn, Supplementary Fig. S7). In this respect, inhibition of cholesterol synthesis,
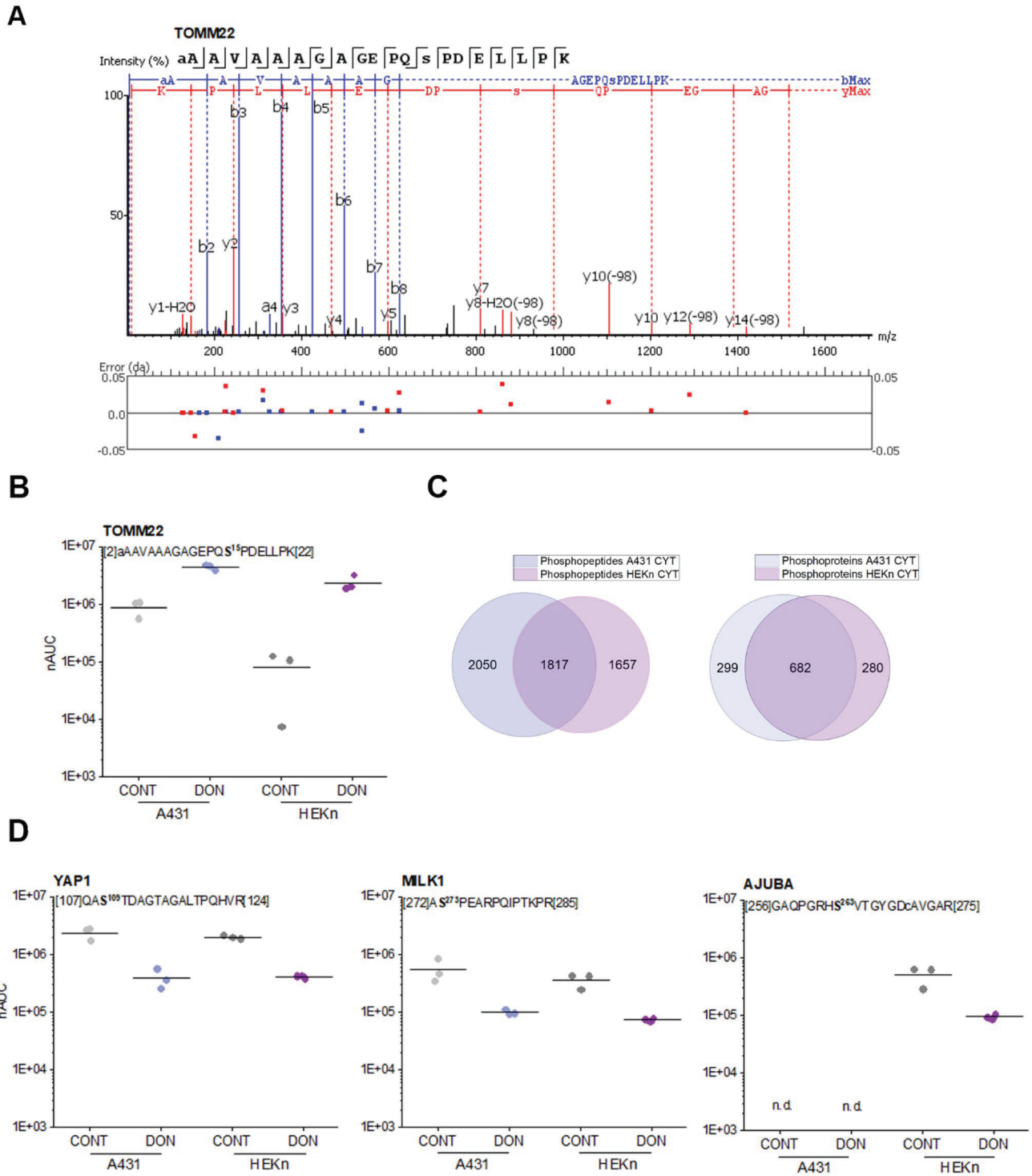
Fig. 8 Phosphoproteome analysis based on enrichment via metal oxide affinity chromatography. **a** Interpreted MS2 spectrum of the TOMM22 phosphopeptide with mass deviations observed for all matched fragment ions. **b** DON-induced phosphorylation demonstrated by the indicated phosphopeptide. The position of the peptide sequence within the protein sequence is indicated by numbers in brackets. The phosphorylated amino acid in marked in bold. nAUC, normalized area under the curve. **c** Venn diagrams depicting the number of identified phosphopeptides and phosphoproteins an A431 and HEKn cells, respectively. **d** DON-induced alterations of phosphopeptide abundance values exemplified on phosphopeptides derived from the proteins YAP1, MILK1 and AJUBA

was previously related to a loss of the cornified envelope of keratinocytes (Ponec et al. 1987) and this mirrors the balance between cornifin A (SPRR1A) and squalene synthase (FDFT1) observed in our experimental conditions (Fig. 6c). Cholesterol homeostasis in keratinocytes is also tightly connected to EGFR (Jans et al. 2004), and we observed significant down-regulation of the protein in HEKn after incubation with DON (Supplementary Fig. S7). Overall, our data pointed toward a substantial dysregulation of cell structural elements (e.g., keratin and cornifin-A) and membrane, possibly tipping the balance toward a more age-prone and "brittle" cell phenotype. This interpretation is sustained also by the morphological charachterization of A431 cells perfomed by confocal microscopy (Figs. 2 and 5). Analysis of the cellular components and biological processes regulated by DON revealed a clear prevalence in the alteration of cellular properties necessary to cope with biomechanical stimulation and respective mechanotransduction (Fig. 7). In line, mechano-sensitive transcription factors like YAP1 were also regulated (Fig. 8b). Dephosphorilation of YAP1 is associated with its activation and nuclear translocation (Totaro et al. 2018) and YAP was already described to cooperate with other transcription factors like AP-1 (up-regulated in both A431 Fig. 1c and HEKn, Fig. 6d) to orchestrate cell motility (Liu et al. 2016). Along this line, AJUBA phosphorylation seems to be crucial to ensure its effect on cell adhesion (Nola et al. 2011). AJUBA was decribed in the regulation of epithelial morphogenesis and response to tensional forces (Razzell et al. 2018) as well as in the integration of pro-inflammatory signaling (Feng and Longmore 2005), thus elegantly connecting mechanisms particularly affected in HEKn after incubation with DON (Fig. 8d).

In conclusion, we delineated a chain of events linking ribosomal inhibition, mitochondrial function, lipid metabolism to membrane structure and biophysical properties in A431 cells. Moreover, we demonstrated that lipid synthesis and cell adhesion are severely impaired by DON also in primary skin HEKn keratinocytes. From the toxicological perspective, these data represent an important insight in the biological effects of DON. In fact, considering DON to be produced by *Fusarium* spp already in the fields, this might relate to potential occupational exposure or health-related effects during harvest and food processing. Moreover, these data open new perspectives in the interpretation of the combinatory effects of DON with other toxins targeting the cell membrane, such as for instance fumonisins (Ferrante et al. 2002; Harel and Futerman 1993; Wang et al. 1991; Yoo et al. 1992), and open new intriguing questions in the evaluation of the effects of *Fusarium* toxins at cellular level.

Supplementary Information The online version contains supplementary material available at https://doi.org/10.1007/s00204-021-03042-y.

Declarations

Conflict of interest None.

References

Abou-Zeid N, Pandjaitan R, Sengmanivong L et al (2011) MICAL-like1 mediates epidermal growth factor receptor endocytosis. Mol Biol Cell 22(18):3431–3441. https://doi.org/10.1091/mbc.E11-01-0030

Aihara R, Ookawara T, Morimoto A et al (2020) Acute and subacute oral administration of mycotoxin deoxynivalenol exacerbates the pro-inflammatory and pro-pruritic responses in a mouse model of allergic dermatitis. Arch Toxicol 94(12):4197–4207. https://doi.org/10.1007/s00204-020-02875-3

Andl T, Zhou L, Yang K, Kadekaro AL, Zhang Y (2017) YAP and WWTR1: new targets for skin cancer treatment. Cancer Lett 396:30–41. https://doi.org/10.1016/j.canlet.2017.03.001

Beisl J, Pahlke G, Abeln H et al (2020) Combinatory effects of cereulide and deoxynivalenol on in vitro cell viability and

inflammation of human Caco-2 cells. Arch Toxicol. https://doi.org/10.1007/s00204-020-02658-w

Beisl J, Varga E, Braun D et al (2021) Assessing mixture effects of cereulide and deoxynivalenol on intestinal barrier integrity and uptake in differentiated human caco-2 cells. Toxins 13(3):189

Bileck A, Kreutz D, Muqaku B, Slany A, Gerner C (2014) Comprehensive assessment of proteins regulated by dexamethasone reveals novel effects in primary human peripheral blood mononuclear cells. J Proteome Res 13(12):5989–6000. https://doi.org/10.1021/pr5008625

Bin-Umer MA, McLaughlin JE, Butterly MS, McCormick S, Tumer NE (2014) Elimination of damaged mitochondria through mitophagy reduces mitochondrial oxidative stress and increases tolerance to trichothecenes. Proc Natl Acad Sci USA 111(32):11798–11803. https://doi.org/10.1073/pnas.1403145111

Callegari S, Dennerlein S (2018) Sensing the stress: a role for the UPR(mt) and UPR(am) in the quality control of mitochondria. Front Cell Dev Biol 6:31. https://doi.org/10.3389/fcell.2018.00031

Carulli S, Beck K, Dayan G, Boulesteix S, Lortat-Jacob H, Rousselle P (2012) Cell surface proteoglycans syndecan-1 and -4 bind overlapping but distinct sites in laminin alpha3 LG45 protein domain. J Biol Chem 287(15):12204–12216. https://doi.org/10.1074/jbc.M111.300061

Casado P, Rodriguez-Prados J-C, Cosulich SC, et al. (2013) Kinase-substrate enrichment analysis provides insights into the heterogeneity of signaling pathway activation in leukemia cells. Sci Signal 6(268):rs6–rs6. https://doi.org/10.1126/scisignal.2003573

Chacinska A, Rehling P, Guiard B et al (2003) Mitochondrial translocation contact sites: separation of dynamic and stabilizing elements in formation of a TOM-TIM-preprotein supercomplex. EMBO J 22(20):5370–5381. https://doi.org/10.1093/emboj/cdg532

Cortinovis C, Caloni F, Schreiber NB, Spicer LJ (2014) Effects of fumonisin B1 alone and combined with deoxynivalenol or zearalenone on porcine granulosa cell proliferation and steroid production. Theriogenology 81(8):1042–1049. https://doi.org/10.1016/j.theriogenology.2014.01.027

Cox J, Mann M (2008) MaxQuant enables high peptide identification rates, individualized p.p.b.-range mass accuracies and proteome-wide protein quantification. Nat Biotechnol 26(12):1367–72. https://doi.org/10.1038/nbt.1511

Cox J, Neuhauser N, Michalski A, Scheltema RA, Olsen JV, Mann M (2011) Andromeda: a peptide search engine integrated into the MaxQuant environment. J Proteome Res 10(4):1794–1805. https://doi.org/10.1021/pr101065j

Cundliffe E, Cannon M, Davies J (1974) Mechanism of inhibition of eukaryotic protein synthesis by trichothecene fungal toxins. Proc Natl Acad Sci USA 71(1):30–34

da Huang W, Sherman BT, Lempicki RA (2009) Systematic and integrative analysis of large gene lists using DAVID bioinformatics resources. Nat Protoc 4(1):44–57. https://doi.org/10.1038/nprot.2008.211

de la Haba C, Palacio JR, Martinez P (1828) Morros A (2013) Effect of oxidative stress on plasma membrane fluidity of THP-1 induced macrophages. Biochem Biophys Acta 2:357–364. https://doi.org/10.1016/j.bbamem.2012.08.013

Dejgaard SY, Presley JF (2019) Rab18: new insights into the function of an essential protein. Cell Mol Life Sci CMLS. https://doi.org/10.1007/s00018-019-03050-3

Del Favero G, Woelflingseder L, Janker L et al (2018a) Deoxynivalenol induces structural alterations in epidermoid carcinoma cells A431 and impairs the response to biomechanical stimulation. Sci Rep 8(1):11351. https://doi.org/10.1038/s41598-018-29728-5

Del Favero G, Zaharescu R, Marko D (2018b) Functional impairment triggered by altertoxin II (ATXII) in intestinal cells in vitro: cross-talk between cytotoxicity and mechanotransduction. Arch Toxicol. https://doi.org/10.1007/s00204-018-2317-6

Del Favero G, Hohenbichler J, Mayer RM, Rychlik M, Marko D (2020) Mycotoxin altertoxin II induces lipid peroxidation connecting mitochondrial stress response to NF-kappaB inhibition in THP-1 macrophages. Chem Res Toxicol. https://doi.org/10.1021/acs.chemrestox.9b00378

Dellafiora L, Galaverna G, Dall'Asta C (2017) In silico analysis sheds light on the structural basis underlying the ribotoxicity of trichothecenes-A tool for supporting the hazard identification process. Toxicol Lett. https://doi.org/10.1016/j.toxlet.2017.02.015

Doi K, Uetsuka K (2014) Mechanisms of mycotoxin-induced dermal toxicity and tumorigenesis through oxidative stress-related pathways. J Toxicol Pathol 27(1):1–10 https://doi.org/10.1293/tox.2013-0062

Endo T, Yamamoto H, Esaki M (2003) Functional cooperation and separation of translocators in protein import into mitochondria, the double-membrane bounded organelles. J Cell Sci 116(Pt 16):3259–3267. https://doi.org/10.1242/jcs.00667

Feng Y, Longmore GD (2005) The LIM protein Ajuba influences interleukin-1-induced NF-kappaB activation by affecting the assembly and activity of the protein kinase Czeta/p62/TRAF6 signaling complex. Mol Cell Biol 25(10):4010–4022. https://doi.org/10.1128/mcb.25.10.4010-4022.2005

Ferrante MC, Meli R, Mattace Raso G et al (2002) Effect of fumonisin B1 on structure and function of macrophage plasma membrane. Toxicol Lett 129(3):181–187

Finley D (2009) Recognition and processing of ubiquitin-protein conjugates by the proteasome. Annu Rev Biochem 78:477–513. https://doi.org/10.1146/annurev.biochem.78.081507.101607

Fortuna-Costa A, Gomes AM, Kozlowski EO, Stelling MP, Pavão MSG (2014) Extracellular galectin-3 in tumor progression and metastasis. Front Oncol. https://doi.org/10.3389/fonc.2014.00138

Fuentes DE, Butler PJ (2012) Coordinated mechanosensitivity of membrane rafts and focal adhesions. Cell Mol Bioeng 5(2):143–154. https://doi.org/10.1007/s12195-012-0225-z

Garreau de Loubresse N, Prokhorova I, Holtkamp W, Rodnina MV, Yusupova G, Yusupov M (2014) Structural basis for the inhibition of the eukaryotic ribosome. Nature 513(7519):517–522. https://doi.org/10.1038/nature13737

Glasgow BJ, Abduragimovaa AR (2018) Interaction of ceramides and tear lipocalin. Biochimica et biophysica acta. Mol Cell Biol Lipids 1863(4):399–408. https://doi.org/10.1016/j.bbalip.2018.01.004

Goldberg AL (2003) Protein degradation and protection against misfolded or damaged proteins. Nature 426(6968):895–899. https://doi.org/10.1038/nature02263

Gruber-Dorninger C, Novak B, Nagl V, Berthiller F (2016) Emerging mycotoxins: beyond traditionally determined food contaminants. J Agric Food Chem. https://doi.org/10.1021/acs.jafc.6b03413

Guerrero-Netro HM, Chorfi Y, Price CA (2015) Effects of the mycotoxin deoxynivalenol on steroidogenesis and apoptosis in granulosa cells. Reprod (Camb Engl) 149(6):555–561. https://doi.org/10.1530/rep-15-0018

Harel R, Futerman AH (1993) Inhibition of sphingolipid synthesis affects axonal outgrowth in cultured hippocampal neurons. J Biol Chem 268(19):14476–14481

Hicks L, Liu G, Ukken FP et al (2015) Depletion or over-expression of Sh3px1 results in dramatic changes in cell morphology. Biol open 4(11):1448–1461. https://doi.org/10.1242/bio.013755

Ho Sui SJ, Mortimer JR, Arenillas DJ et al (2005) oPOSSUM: identification of over-represented transcription factor binding sites in co-expressed genes. Nucl Acids Res 33(10):3154–3164. https://doi.org/10.1093/nar/gki624

Ho Sui SJ, Fulton DL, Arenillas DJ, Kwon AT, Wasserman WW (2007) oPOSSUM: integrated tools for analysis of regulatory motif over-representation. Nucleic acids research 35(Web Server issue):W245–52. https://doi.org/10.1093/nar/gkm427

Horn H, Schoof EM, Kim J et al (2014) KinomeXplorer: an integrated platform for kinome biology studies. Nat Methods 11(6):603–604. https://doi.org/10.1038/nmeth.2968

Hornbeck PV, Zhang B, Murray B, Kornhauser JM, Latham V, Skrzypek E (2014) PhosphoSitePlus, 2014: mutations, PTMs and recalibrations. Nucl Acids Res 43(D1):D512–D520. https://doi.org/10.1093/nar/gku1267

Jacquemet G, Paatero I, Carisey AF et al (2017) FiloQuant reveals increased filopodia density during breast cancer progression. J Cell Biol 216(10):3387–3403. https://doi.org/10.1083/jcb.201704045

Jans R, Atanasova G, Jadot M, Poumay Y (2004) Cholesterol depletion upregulates involucrin expression in epidermal keratinocytes through activation of p38. J Invest Dermatol 123(3):564–573. https://doi.org/10.1111/j.0022-202X.2004.23221.x

Kanehisa M, Goto S (2000) KEGG: kyoto encyclopedia of genes and genomes. Nucl Acids Res 28(1):27–30

Kanehisa M, Sato Y, Kawashima M, Furumichi M, Tanabe M (2016) KEGG as a reference resource for gene and protein annotation. Nucl Acids Res 44(D1):D457–D462. https://doi.org/10.1093/nar/gkv1070

Kanehisa M, Furumichi M, Tanabe M, Sato Y, Morishima K (2017) KEGG: new perspectives on genomes, pathways, diseases and drugs. Nucl Acids Res 45(D1):D353-d361. https://doi.org/10.1093/nar/gkw1092

Katrine KH, Jan A, Lars B et al (2017) Risks to human and animal health related to the presence of deoxynivalenol and its acetylated and modified forms in food and feed. EFSA J 15(9):e04718. https://doi.org/10.2903/j.efsa.2017.4718

Krajewska M, Xu L, Xu W et al (2011) Endoplasmic reticulum protein BI-1 modulates unfolded protein response signaling and protects against stroke and traumatic brain injury. Brain Res 1370:227–237. https://doi.org/10.1016/j.brainres.2010.11.015

Kravic B, Harbauer AB, Romanello V et al (2018) In mammalian skeletal muscle, phosphorylation of TOMM22 by protein kinase CSNK2/CK2 controls mitophagy. Autophagy 14(2):311–335. https://doi.org/10.1080/15548627.2017.1403716

Kroening S, Stix J, Keller C, Streiff C, Goppelt-Struebe M (2010) Matrix-independent stimulation of human tubular epithelial cell migration by Rho kinase inhibitors. J Cell Physiol 223(3):703–712. https://doi.org/10.1002/jcp.22079

Kwon AT, Arenillas DJ, Worsley Hunt R, Wasserman WW (2012) oPOSSUM-3: advanced analysis of regulatory motif over-representation across genes or ChIP-Seq datasets. G3 (Bethesda, Md) 2(9):987–1002. https://doi.org/10.1534/g3.112.003202

Li CC, Yu FS, Fan MJ et al (2016) Anticancer effects of cantharidin in A431 human skin cancer (Epidermoid carcinoma) cells in vitro and in vivo. Environ Toxicol. https://doi.org/10.1002/tox.22273

Liu X, Li H, Rajurkar M et al (2016) Tead and AP1 coordinate transcription and motility. Cell Rep 14(5):1169–1180. https://doi.org/10.1016/j.celrep.2015.12.104

Lou HY, Zhao W, Zeng Y, Cui B (2018) The role of membrane curvature in nanoscale topography-induced intracellular signaling. Acc Chem Res 51(5):1046–1053. https://doi.org/10.1021/acs.accounts.7b00594

Mayer RL, Schwarzmeier JD, Gerner MC et al (2018) Proteomics and metabolomics identify molecular mechanisms of aging potentially predisposing for chronic lymphocytic leukemia. Mol Cell Proteom MCP 17(2):290–303. https://doi.org/10.1074/mcp.RA117.000425

Mishra S, Tripathi A, Chaudhari BP, Dwivedi PD, Pandey HP, Das M (2014) Deoxynivalenol induced mouse skin cell proliferation and inflammation via MAPK pathway. Toxicol Appl Pharmacol 279(2):186–197. https://doi.org/10.1016/j.taap.2014.06.003

Mishra S, Tewari P, Chaudhari BP, Dwivedi PD, Pandey HP, Das M (2016) Deoxynivalenol induced mouse skin tumor initiation: Elucidation of molecular mechanisms in human HaCaT keratinocytes. Int J Cancer 139(9):2033–2046. https://doi.org/10.1002/ijc.30260

Mishra S, Divakar A, Srivastava S et al (2020a) N-acetyl-cysteine in combination with celecoxib inhibits Deoxynivalenol induced skin tumor initiation via induction of autophagic pathways in swiss mice. Free Radical Biol Med 156:70–82. https://doi.org/10.1016/j.freeradbiomed.2020.06.001

Mishra S, Srivastava S, Divakar A et al (2020b) Celecoxib reduces Deoxynivalenol induced proliferation, inflammation and protein kinase C translocation via modulating downstream targets in mouse skin. Chem Biol Interact 326:109128. https://doi.org/10.1016/j.cbi.2020.109128

Nargund AM, Fiorese CJ, Pellegrino MW, Deng P, Haynes CM (2015) Mitochondrial and nuclear accumulation of the transcription factor ATFS-1 promotes OXPHOS recovery during the UPR(mt). Mol Cell 58(1):123–133. https://doi.org/10.1016/j.molcel.2015.02.008

Nogueira da Costa A, Keen JN, Wild CP, Findlay JB (2011a) An analysis of the phosphoproteome of immune cell lines exposed to the immunomodulatory mycotoxin deoxynivalenol. Biochem Biophys Acta 1814(7):850–857. https://doi.org/10.1016/j.bbapap.2011.04.001

Nogueira da Costa A, Mijal RS, Keen JN, Findlay JB, Wild CP (2011b) Proteomic analysis of the effects of the immunomodulatory mycotoxin deoxynivalenol. Proteomics 11(10):1903–1914. https://doi.org/10.1002/pmic.201000580

Nola S, Daigaku R, Smolarczyk K et al (2011) Ajuba is required for Rac activation and maintenance of E-cadherin adhesion. J Cell Biol 195(5):855–871. https://doi.org/10.1083/jcb.201107162

Oks O, Lewin S, Goncalves IL, Sapir A (2018) The UPR(mt) Protects caenorhabditis elegans from mitochondrial dysfunction by upregulating specific enzymes of the mevalonate pathway. Genetics 209(2):457–473. https://doi.org/10.1534/genetics.118.300863

Pan X, Whitten DA, Wu M, Chan C, Wilkerson CG, Pestka JJ (2013) Global protein phosphorylation dynamics during deoxynivalenol-induced ribotoxic stress response in the macrophage. Toxicol Appl Pharmacol 268(2):201–211. https://doi.org/10.1016/j.taap.2013.01.002

Pan X, Whitten DA, Wilkerson CG, Pestka JJ (2014) Dynamic changes in ribosome-associated proteome and phosphoproteome during deoxynivalenol-induced translation inhibition and ribotoxic stress. Toxicol Sci Off J Soc Toxicol 138(1):217–233. https://doi.org/10.1093/toxsci/kft270

Pestka JJ (2010a) Deoxynivalenol-induced proinflammatory gene expression: mechanisms and pathological sequelae. Toxins 2(6):1300–1317. https://doi.org/10.3390/toxins2061300

Pestka JJ (2010b) Deoxynivalenol: mechanisms of action, human exposure, and toxicological relevance. Arch Toxicol 84(9):663–679. https://doi.org/10.1007/s00204-010-0579-8

Pinton P, Oswald IP (2014) Effect of deoxynivalenol and other Type B trichothecenes on the intestine: a review. Toxins 6(5):1615–1643. https://doi.org/10.3390/toxins6051615

Ponec M, Kempenaar J, Weerheim A, Boonstra J (1987) Differentiation of human keratinocytes: changes in lipid synthesis, plasma membrane lipid composition, and 125I-EGF binding upon administration of 25-hydroxycholesterol and mevinolin. J Cell Physiol 133(2):358–364. https://doi.org/10.1002/jcp.1041330221

Radons J (2016) The human HSP70 family of chaperones: where do we stand? Cell Stress Chaperones 21(3):379–404. https://doi.org/10.1007/s12192-016-0676-6

Rajagopalan P, Jain AP, Nanjappa V et al (2018) Proteome-wide changes in primary skin keratinocytes exposed to diesel particulate extract-A role for antioxidants in skin health. J Dermatol Sci 91(3):239–249. https://doi.org/10.1016/j.jdermsci.2018.05.003

Rapaport D, Neupert W, Lill R (1997) Mitochondrial protein import. Tom40 plays a major role in targeting and translocation of preproteins by forming a specific binding site for the presequence. J Biol Chem 272(30):18725–31

Razzell W, Bustillo ME, Zallen JA (2018) The force-sensitive protein Ajuba regulates cell adhesion during epithelial morphogenesis. J Cell Biol 217(10):3715–3730. https://doi.org/10.1083/jcb.201801171

Ren Z, Guo C, He H et al (2020) Effects of deoxynivalenol on mitochondrial dynamics and autophagy in pig spleen lymphocytes. Food Chem Toxicol Int J Pub Br Ind Biol Res Assoc 140:111357. https://doi.org/10.1016/j.fct.2020.111357

Robert H, Payros D, Pinton P, Theodorou V, Mercier-Bonin M, Oswald IP (2017) Impact of mycotoxins on the intestine: are mucus and microbiota new targets? J Toxicol Environ Health Part B Crit Rev. https://doi.org/10.1080/10937404.2017.1326071

Sallam T, Jones MC, Gilliland T et al (2016) Feedback modulation of cholesterol metabolism by the lipid-responsive non-coding RNA LeXis. Nature 534(7605):124–128. https://doi.org/10.1038/nature17674

Segre JA, Bauer C, Fuchs E (1999) Klf4 is a transcription factor required for establishing the barrier function of the skin. Nat Genet 22(4):356–360. https://doi.org/10.1038/11926

Shi J, Badri KR, Choudhury R, Schuger L (2006) P311-induced myofibroblasts exhibit ameboid-like migration through RalA activation. Exp Cell Res 312(17):3432–3442. https://doi.org/10.1016/j.yexcr.2006.07.016

Smina TP, Mohan A, Ayyappa KA, Sethuraman S, Krishnan UM (2015) Hesperetin exerts apoptotic effect on A431 skin carcinoma cells by regulating mitogen activated protein kinases and cyclins. Cell Mol Biol (Noisy-le-Grand, France) 61(6):92–99

Smith MC, Timmins-Schiffman E, Coton M et al (2018) Differential impacts of individual and combined exposures of deoxynivalenol and zearalenone on the HepaRG human hepatic cell proteome. J Proteomics 173:89–98. https://doi.org/10.1016/j.jprot.2017.11.025

Totaro A, Panciera T, Piccolo S (2018) YAP/TAZ upstream signals and downstream responses. Nat Cell Biol 20(8):888–899. https://doi.org/10.1038/s41556-018-0142-z

Toyokuni S, Okamoto K, Yodoi J, Hiai H (1995) Persistent oxidative stress in cancer. FEBS Lett 358(1):1–3. https://doi.org/10.1016/0014-5793(94)01368-B

Trachootham D, Alexandre J, Huang P (2009) Targeting cancer cells by ROS-mediated mechanisms: a radical therapeutic approach? Nat Rev Drug Discovery 8(7):579–591. https://doi.org/10.1038/nrd2803

Tung B, Xia S (2018) Kruppel-Like Factor 4 (KLF4) and its regulation on mitochondrial homeostasis. J Stem Cell Res Therapy. https://doi.org/10.4172/2157-7633.1000436

Tyanova S, Temu T, Cox J (2016) The MaxQuant computational platform for mass spectrometry-based shotgun proteomics. Nat Protoc 11(12):2301–2319. https://doi.org/10.1038/nprot.2016.136

Ueno Y (1977) Mode of action of trichothecenes. Ann Nutr Aliment 31(4–6):885–900

van der Lee T, Zhang H, van Diepeningen A, Waalwijk C (2015) Biogeography of Fusarium graminearum species complex and chemotypes: a review. Food Addit Contam Part A Chem Anal Control Expo Risk Assess 32(4):453–460. https://doi.org/10.1080/19440049.2014.984244

Vizcaino JA, Csordas A, del-Toro N, et al. (2016) 2016 update of the PRIDE database and its related tools. Nucl Acids Res 44(D1):D447-56. https://doi.org/10.1093/nar/gkv1145

Wakim J, Goudenege D, Perrot R et al (2017) CLUH couples mitochondrial distribution to the energetic and metabolic status. J Cell Sci 130(11):1940–1951. https://doi.org/10.1242/jcs.201616

Wang E, Norred WP, Bacon CW, Riley RT, Merrill AH, Jr. (1991) Inhibition of sphingolipid biosynthesis by fumonisins. Implications for diseases associated with Fusarium moniliforme. J Biol Chem 266(22):14486–90

Wang X, Li L, Zhang G (2020) A proteomic study on the protective effect of kaempferol pretreatment against deoxynivalenol-induced intestinal barrier dysfunction in a Caco-2 cell model. Food Funct 11(8):7266–7279. https://doi.org/10.1039/d0fo01579b

Weiss T, Taschner-Mandl S, Janker L et al (2021) Schwann cell plasticity regulates neuroblastic tumor cell differentiation via epidermal growth factor-like protein 8. Nat Commun 12(1):1624. https://doi.org/10.1038/s41467-021-21859-0

Wiedemann N, Kozjak V, Chacinska A et al (2003) Machinery for protein sorting and assembly in the mitochondrial outer membrane. Nature 424(6948):565–571. https://doi.org/10.1038/nature01753

Wisniewski JR, Zougman A, Nagaraj N, Mann M (2009) Universal sample preparation method for proteome analysis. Nat Methods 6(5):359–362. https://doi.org/10.1038/nmeth.1322

Wrobel L, Topf U, Bragoszewski P et al (2015) Mistargeted mitochondrial proteins activate a proteostatic response in the cytosol. Nature 524(7566):485–488. https://doi.org/10.1038/nature14951

Wurm S, Zhang J, Guinea-Viniegra J et al (2015) Terminal epidermal differentiation is regulated by the interaction of Fra-2/AP-1 with Ezh2 and ERK1/2. Genes Dev 29(2):144–156. https://doi.org/10.1101/gad.249748.114

Yin Z, Machius M, Nestler EJ, Rudenko G (2017) Activator Protein-1: redox switch controlling structure and DNA-binding. Nucl Acids Res 45(19):11425–11436. https://doi.org/10.1093/nar/gkx795

Yoo HS, Norred WP, Wang E, Merrill AH Jr, Riley RT (1992) Fumonisin inhibition of de novo sphingolipid biosynthesis and cytotoxicity are correlated in LLC-PK1 cells. Toxicol Appl Pharmacol 114(1):9–15

Zecha J, Meng C, Zolg DP, Samaras P, Wilhelm M, Kuster B (2018) Peptide level turnover measurements enable the study of proteoform dynamics. Mol Cell Proteom MCP 17(5):974–992. https://doi.org/10.1074/mcp.RA118.000583

Zhang X, Hurng J, Rateri DL, Daugherty A, Schmid-Schonbein GW, Shin HY (2011) Membrane cholesterol modulates the fluid shear stress response of polymorphonuclear leukocytes via its effects on membrane fluidity. Am J Physiol Cell Physiol 301(2):C451–C460. https://doi.org/10.1152/ajpcell.00458.2010

Zhang ZQ, Wang SB, Wang RG, Zhang W, Wang PL, Su XO (2016) Phosphoproteome analysis reveals the molecular mechanisms underlying deoxynivalenol-induced intestinal toxicity in IPEC-J2 Cells. Toxins. https://doi.org/10.3390/toxins8100270

Publisher's Note Springer Nature remains neutral with regard to jurisdictional claims in published maps and institutional affiliations.

4.4 Schwann cell plasticity regulates neuroblastic tumor cell differentiation via epidermal growth factor-like protein 8

Tamara Weiss[1,2]*, Sabine Taschner-Mandl[1]*, Lukas Janker[3,4], Andrea Bileck[3,4], Fikret Rifatbegovic[1], Florian Kromp[1], Helena Sorger[1], Maximilian O. Kauer[1], Christian Frech[1], Reinhard Windhager[1], Christopher Gerner[3,4], Peter F. Ambros[1,6], Inge M. Ambros[1]

1	St. Anna Children's Cancer Research Institute (CCRI), Vienna, Austria
2	Research Laboratory of the Department of Plastic and Reconstructive Surgery, Medical University of Vienna, Vienna, Austria
3	Department of Analytical Chemistry, University of Vienna, Vienna, Austria
4	Joint Metabolome Facility, University of Vienna & Medical University of Vienna, Vienna, Austria
5	Department of Orthopedic Surgery, Medical University of Vienna, Vienna, Austria
6	Department of Pediatrics, Medical University of Vienna, Vienna, Austria
*	Contributed equally

Contributions to this publication:

- Second author contribution
- Performing research and MS measurements
- Analysis of data
- Preparation of figures and writing of manuscript

Schwann cell plasticity regulates neuroblastic tumor cell differentiation via epidermal growth factor-like protein 8

Tamara Weiss [1,2,7], Sabine Taschner-Mandl [1,7 ✉], Lukas Janker [3,4], Andrea Bileck [3,4], Fikret Rifatbegovic [1], Florian Kromp [1], Helena Sorger [1], Maximilian O. Kauer[1], Christian Frech[1], Reinhard Windhager[5], Christopher Gerner [3,4], Peter F. Ambros[1,6] & Inge M. Ambros[1]

Adult Schwann cells (SCs) possess an inherent plastic potential. This plasticity allows SCs to acquire repair-specific functions essential for peripheral nerve regeneration. Here, we investigate whether stromal SCs in benign-behaving peripheral neuroblastic tumors adopt a similar cellular state. We profile ganglioneuromas and neuroblastomas, rich and poor in SC stroma, respectively, and peripheral nerves after injury, rich in repair SCs. Indeed, stromal SCs in ganglioneuromas and repair SCs share the expression of nerve repair-associated genes. Neuroblastoma cells, derived from aggressive tumors, respond to primary repair-related SCs and their secretome with increased neuronal differentiation and reduced proliferation. Within the pool of secreted stromal and repair SC factors, we identify EGFL8, a matricellular protein with so far undescribed function, to act as neuritogen and to rewire cellular signaling by activating kinases involved in neurogenesis. In summary, we report that human SCs undergo a similar adaptive response in two patho-physiologically distinct situations, peripheral nerve injury and tumor development.

[1] St. Anna Children's Cancer Research Institute (CCRI), Vienna, Austria. [2] Research Laboratory of the Department of Plastic and Reconstructive Surgery, Medical University of Vienna, Vienna, Austria. [3] Department of Analytical Chemistry, University of Vienna, Vienna, Austria. [4] Joint Metabolome Facility, University of Vienna & Medical University of Vienna, Vienna, Austria. [5] Department of Orthopedic Surgery, Medical University of Vienna, Vienna, Austria. [6] Department of Pediatrics, Medical University of Vienna, Vienna, Austria. [7] These authors contributed equally: Tamara Weiss, Sabine Taschner-Mandl. ✉ email: sabine.taschner@ccri.at

Schwann cells (SCs) are the principal glia of the peripheral nervous system and evolve in close contact with neurons into peripheral nerve fibers. Reciprocal signaling between SCs and neurons regulates the survival, fate decisions, and differentiation of both cell types, but also influences their behavior in regenerative and pathological conditions[1–6]. Hence, understanding the molecular mechanisms underlying SC-neuron interaction is of utmost interest to develop effective treatment strategies for injuries and pathologies of the peripheral nervous system.

Despite being necessary for correct nerve development, SCs earned recognition because of their plasticity that allows differentiated SCs, further called adult SCs, to transform into a dedicated repair cell after peripheral nerve injury. The process is referred to as adaptive cellular reprogramming and includes profound transcriptional and morphological changes[7–9]. This phenotypical switch is mediated by dedifferentiation causing the regain of immature/precursor SC properties followed by re-differentiation into a repair-specific state[10]. The resulting repair SC phenotype is characterized by the re-expression of markers known to be upregulated in SCs during development, and by distinct repair functions and repair-associated ligands distinguishing repair SCs from adult SCs or developing SCs[11–13]. Those repair functions comprise the degradation of myelin debris, attraction of phagocytes, the formation of regeneration tracks for axon guidance, and the expression of cell surface proteins and trophic (neuroprotective and neuritogenic) factors promoting axon survival and re-growth[9,10,14–16]. We have recently provided a comprehensive transcriptomic and proteomic characterization of human repair SCs demonstrating that SCs isolated from excised peripheral nerves adopt the same repair-related phenotype and function in culture as in nerve tissue explants. These included the expression of master transcriptional regulators, such as JUN, as well as myelinophagy, phagocytosis, and antigen processing and presentation via MHC-II[17]. Importantly, transcriptomic signatures of primary repair-related SC cultures indicated the expression of a variety of neurotrophins and neuritogens and, thus, present an ideal in vitro model to study processes involving nerve repair and neuronal differentiation[17].

Interestingly, a prevalent stromal SC population is found in usually benign-behaving subtypes of peripheral neuroblastic tumors[18,19]. Peripheral neuroblastic tumors originate from trunk neural crest-derived sympathetic neuroblasts[20,21] and are categorized in neuroblastomas (NBs), ganglioneuroblastomas (GNBs), and ganglioneuromas (GNs) that represent a spectrum from NBs, the most aggressive form, to GNs, the most benign form, and GNBs, which exhibit various elements of both[20,22–24]. NB and GN subtypes are associated with distinct genomic alterations and strikingly different morphologies[20,22]. In general, NBs consist of un- or mostly poorly differentiated tumor cells and cancer-associated fibroblasts[25], whereas GNs are composed of differentiated, ganglionic-like tumor cells scattered within a dominant SC stroma[19,26]. The content of SC stroma was early recognized as a valuable prognostic factor as it correlates with the degree of tumor cell differentiation and a favorable outcome[19]. The ganglionic-like tumor cells also extend numerous neuritic processes that form entangled bundles surrounded by ensheathing stromal SCs[26]. This ganglion-like organoid morphology was assumed to arise from a bi-potent neoplastic neuroblastic precursor cell capable to differentiate along a neuronal and glial lineage[27]. Hence, an active role of stromal SCs in peripheral neuroblastic tumors has been neglected due to their supposed neoplastic origin.

Of note, we and others provided evidence for a non-tumor background of stromal SCs[1,28]. In a detailed immunohistochemical study, it was shown that the earliest appearance of stromal SCs is confined to the tumor blood vessels and connective tissue septa and not intermingled within the tumor as a clonal origin would imply[28]. Furthermore, we demonstrated the absence of numerical chromosomal aberrations in stromal SCs, while adjacent ganglionic-like tumor cells possessed a typical aneuploid genome[1,29,30]. These surprising findings argue against the hitherto presumed model of GNB/GN development based on a bi-potent neoplastic cell and support that the tumor cells are able to attract adult SCs from the nervous environment to the tumor.

In detaching the origin of stromal SCs in GNB/GN from a neoplastic cell, we realized how little we know about their nature. What is the cellular state of stromal SCs? How do they affect GNB/GN development? And why are they not manipulated by the tumor cells to support tumor progression but are associated with a benign tumor behavior/biology? We and others have shown that the aggressiveness of NB cell lines, derived from high-risk metastatic NBs, can be reduced upon exposure to SCs and their secreted factors[31–35]. Accordingly, a mouse study comparing intra- or extra-fascicularly grown tumor xenografts confirmed that NBs within the nervous environment were infiltrated by SCs and developed a less aggressive tumor phenotype[36]. However, a comprehensive analysis to assess the origin and functional characteristics of stromal SCs in tumors is still missing.

Based on the inherent plasticity of adult SCs and the yet unresolved nature of SC stroma, we speculate that GNB/GN development could be the result of a reactive/adaptive response of SCs to peripheral neuroblastic tumor cells similar to injured nerve cells. Thus, we here compared the cellular state of stromal SCs in GNs to repair SCs in injured nerves by transcriptome profiling of human GN and human injured nerve tissues. Moreover, we analyzed the effect of human primary repair-related SCs and their secreted factors on genetically diverse NB cells in co-culture studies and identified a promising candidate factor of therapeutic potential for aggressive NBs and peripheral nerve injuries.

Results

Transcriptome profiling revealed that ganglioneuromas contain stromal Schwann cells with a nerve repair-associated gene expression signature. To assess the cellular state of stromal SCs, we performed a comprehensive transcriptomic analysis involving human tissues of SC stroma-rich GNs, SC stroma-poor NBs, and repair SC-containing injured nerves, alongside with cultures of primary human repair-related SCs and human NB cell lines (Supplementary Table 1). Immunofluorescence stainings of respective tissue sections for SC marker S100B determined a prevalent SC population of about 84% in injured nerves (Fig. 1a, Supplementary Fig. 1a), and of about 76% in GNs (Fig. 1b) as well as the almost complete absence of SCs in NBs (Fig. 1c, Supplementary Fig. 1a). Co-staining with neurofilament heavy polypeptide (NF200), an intermediate filament protein associated with mature neurons[37], marked axons in injured nerves that have mostly disintegrated after the degeneration period of 7 days (Fig. 1a). NF200 also stained ganglionic-like tumor cells with abundant neuritic processes in GNs (Fig. 1b). In line with the un- or poorly-differentiated state of tumor cells in NBs, hardly any NF200 signals were detected in NB tumor samples (Fig. 1c). Human repair-related SC cultures have been isolated according to our established protocol[38] and were positive for S100B, and showed the typical parallel alignment (Fig. 1d). Cultured NB cell lines highly expressed the neuronal ganglioside GD2 (Fig. 1e) that is characteristically found on tumor cells in NBs (Supplementary Fig. 1b) and only on some ganglionic-like tumor cells in GNs (Supplementary Fig. 1c).

Hierarchical clustering and principal component analysis of obtained RNA-seq data showed that biological samples derived
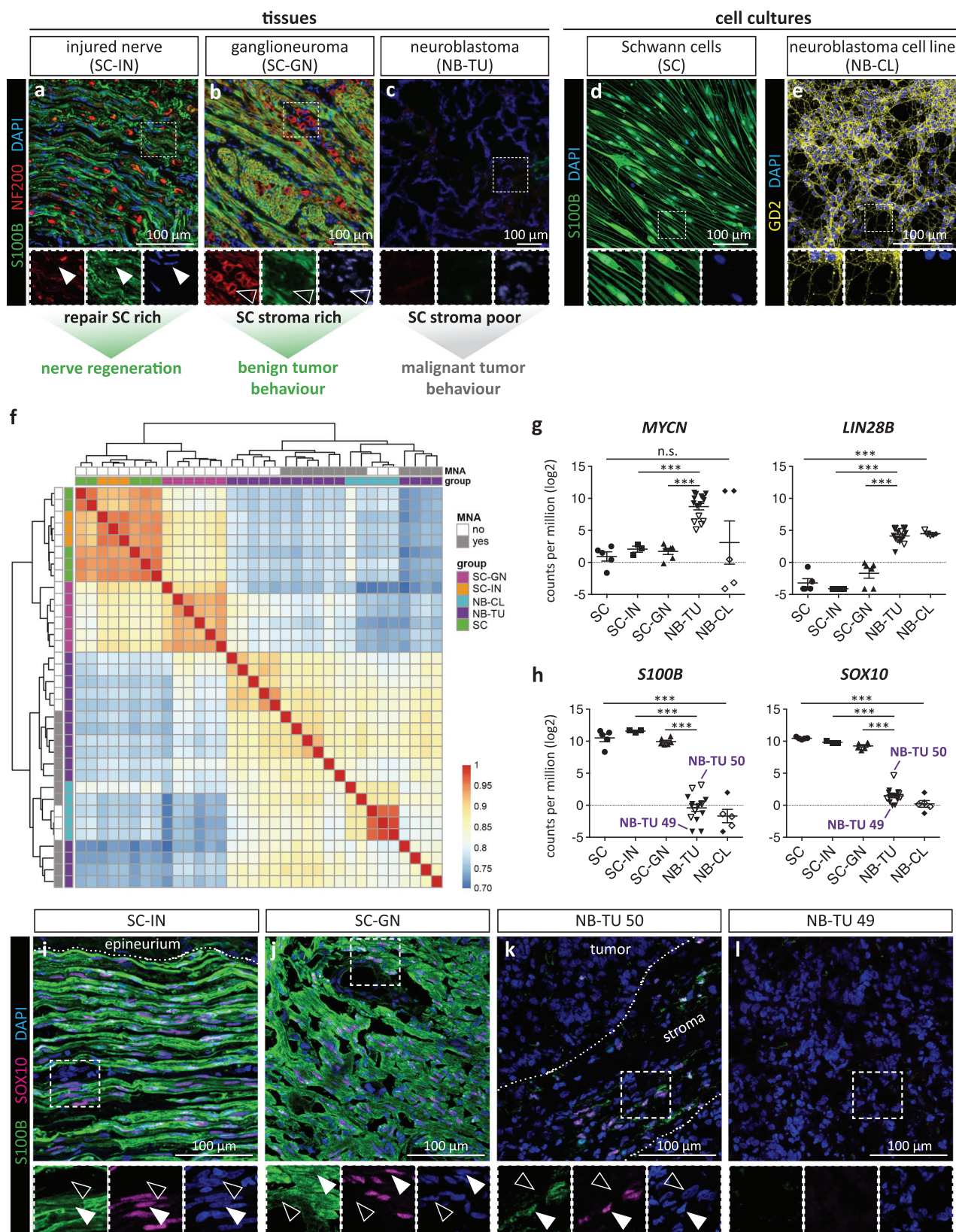
from the same tissue or cell type cluster together and that primary SCs and SC-containing tissues, i.e. injured nerves and GNs, differ from NB cell lines and NB tumors (Fig. 1f). To further confirm tissue/cell identity, we validated the expression of genes associated with either NBs, such as the miRNA suppressor *LIN28B* and the transcription factor *MYCN*[39,40], or the SC lineage, such as *S100B*

and transcription factor *SOX10*[10]. Indeed, expression of *LIN28B* was significantly higher in NBs and NB cell lines, and the *MYCN* expression level reflected the presence or absence of *MYCN* amplifications in NB cell lines and tumors (Fig. 1g, Supplementary Table 2&3). Of note, amplification of the *MYCN* oncogene is associated with an aggressive NB tumor behavior and poor

103

Fig. 1 Transcriptome analysis of repair SCs in injured nerves, stromal SCs in ganglioneuromas, neuroblastomas, primary repair-related SCs, and neuroblastoma cell cultures. a–e Tissues and cell cultures used for transcriptomic analysis. Representative immunostainings of cryosections of (**a**) injured nerve fascicle tissue (SC-IN) with S100B positive repair SCs (filled arrowheads) and NF200 positive axonal residues, (**b**) ganglioneuroma tissue (SC-GN) with S100B positive stromal SCs and NF200 positive ganglionic-like tumor cells (lined arrowheads), and (**c**) neuroblastoma tissue (NB-TU) with NF200 negative tumor cells and no SC stroma. Stainings were performed on three independent specimen per analyzed tissue. Representative immunostainings of (**d**) human primary repair-related Schwann cells (SC) positive for S100B, and (**e**) the neuroblastoma short-term cell cultures (NB-CL) CLB-Ma positive for GD2. S100B and GD2 stainings are routinely performed to characterize respective cell types. **f** RNA-seq data of SCs ($n = 5$ biological replicates from 4 donors), NB-CLs ($n = 5$ biological replicates from 3 donors), SC-GN ($n = 6$), SC-INs ($n = 3$) and NB-TU ($n = 15$) illustrated as cluster heatmap of sample-to-sample distances; computed using the Pearson correlation coefficient. Red and blue colors indicate high and low similarity between samples, respectively. Expression level of genes associated with (**g**) aggressive NBs: *MYCN* and *LIN28*, and (**h**) SCs: *S100B* and *SOX10*. Empty symbols indicate *MYCN* non-amplified, full symbols indicate *MYCN* amplified (MNA) NB-TUs and NB-CLs. *** q-value ≤ 0.001; Data are depicted as mean ± SD. Representative immunostainings of tissue cryosections of (**i**) SC-IN, (**j**) SC-GN, (**k**) NB-TU 50, and (**l**) NB-TU 49 stained for S100B, SOX10, and DAPI; filled arrowheads indicate S100B⁺/SOX10⁺ SCs, lined arrowheads indicate S100B⁻/SOX10⁻ cells. Stainings were performed on three independent specimen per analyzed tissue.

outcome[41]. The SC specific genes *S100B* and *SOX10* were significantly and strongly expressed in primary SCs, injured nerves, and GNs (Fig. 1h). Immunofluorescence stainings on tissue sections acknowledged that SOX10 positive cell nuclei correspond to S100B positive repair SCs in injured nerves (Fig. 1i, Supplementary Fig. 2a) and stromal SCs in GNs (Fig. 1j, Supplementary Fig. 2b). Moreover, the elevated level of *SOX10* mRNA found in NB-TU 50 could be ascribed to a high proportion of infiltrating stroma containing S100B and SOX10 positive SCs (Fig. 1k, Supplementary Fig. 2c), while the sections analyzed from other NB tumors such as NB-TU 49 lacked S100B and SOX10 positive cells and mRNA (Fig. 1l, Supplementary Fig. 2d).

We next defined the characteristic expression signatures of GNs and injured nerves, that both possessed a predominant SC content (Supplementary Fig. 1a), by selecting for genes significantly up-regulated (q-value > 0.05; $|\log2FC| > 1$) in GNs versus NBs, and injured nerves versus NBs. In this way, we excluded genes also present in NBs and enriched for genes characteristic for repair SCs in injured nerves and stromal SCs in GNs. Then, we compared the identified expression signatures associated with stromal SCs and repair SCs, which showed an overlap in 2755 genes (q-value > 0.05; $|\log2FC| > 1$) (Fig. 2a). Functional annotation analysis of these stromal/repair SC genes revealed pathways and gene ontology terms that could be grouped into distinct functional competences. Importantly, these functions reflected the main tasks of human repair SCs involving axon guidance, lipid/myelin degradation/metabolism, basement membrane formation/ECM (re-)organization, phagocyte attraction, and a MHC-II mediated immune regulation (Fig. 2b)[10,14,17,42]. To examine whether the expression of MHC-II is not the sole result of tissue resident immune cells, but indeed attributed to repair and stromal SCs, we stained respective tissue sections for HLA-DR and S100B. The images showed that injured nerves and GNs were highly positive for HLA-DR (Supplementary Fig. 3a,b), whereas HLA-DR staining signals were mainly restricted to the stromal portion and only scattered within the tumor cell portion of NBs (Supplementary Fig. 3c,d). Indeed, HLA-DR was expressed by S100B⁺ repair SCs in injured nerves (Supplementary Fig. 3a) as well as stromal SCs in GNs (Supplementary Fig. 3b) in addition to HLA-DR⁺/S100B⁻ immune cells (Supplementary Fig. 3a-d).

A possible repair-associated cell state of stromal SCs should be reflected by key signatures of both, developing/dedifferentiated SCs and repair-specific SCs. Accordingly, the repair/stromal SC enriched gene set included genes characteristic for SCs during development and after injury such as transcription factors *JUN*, *SOX2*, *ZEB2*, and *RUNX2* (Supplementary Fig. 4a), and receptors *NGFR*, *ERBB3*, *GFRA1*, and *CADH19*[13,43–45]. Notably, we also detected significant levels of *GDNF*, *LIF*, *SHH*, *CLCF1*, *BTC*, *CCL2*, and *UCN2* (Fig. 2c) that were reported to be exclusively expressed by repair SCs and not by adult or developing SCs[11–13] (Supplementary Fig. 4b). Moreover, *JUN* is the key transcription

factor determining the repair identity of SCs by up-regulating repair-specific target genes such as *SHH* and *GDNF*[13,46]. Hence, we performed immunofluorescence stainings for SOX10 and JUN on nerve and GN tissue sections, which confirmed that SOX10⁺ nuclei of both, repair SCs and stromal SCs were positive for JUN (Fig. 2d-f, Supplementary Fig. 5a,b). In line with the transcriptomic data, JUN was also expressed by SOX10⁻ cells such as ganglionic-like tumor cells in GNs (Fig. 2e, Supplementary Fig. 5b) and tumor cells in NBs (Fig. 2f,g, Supplementary Fig. 5c,d).

Functional annotation analysis of GN characteristic genes that were not shared with injured nerves revealed an enrichment of gene ontology terms implicated in innate immunity, inflammation as well as T- and B-cell receptor signaling pathways (Supplementary Table 5). Immunofluorescence stainings for CD3 and S100B verified the presence of CD3⁺ T-cells within the S100B⁺ SC stroma in GNs (Supplementary Fig. 6a), while CD3⁺ T-cells were only sparsely detected in the tumor cell portion of NBs (Supplementary Fig. 6b,c). In turn, genes characteristic for injured nerves not shared with GNs were assigned to gene ontology terms for the endoplasmatic reticulum, the Golgi apparatus, vesicle coating and transport, protein transport and binding, as well as acetylation and protein N-linked glycosylation (Supplementary Table 6). Those annotations suggest an active protein modification and transport machinery in repair SCs.

Taken together transcriptome profiling demonstrate that the expression signature shared by stromal SCs in GNs and repair SCs in injured nerves contain distinct nerve repair-associated genes and functions.

Direct contact to repair-related Schwann cells promotes alignment and neurite out-growth of neuroblastoma cells. Since we identified a repair SC-associated gene expression signature in stromal SCs, we used a co-culture model to analyze how NB cells react to repair-related SCs in vitro (Fig. 3a). Therefore, we used human primary SCs cultures as a model, as these have been shown to reflect all major characteristics of repair SCs[17]. SC cultures (passage 1) characterized by the expression of S100B, SOX10, and the intermediate filament vimentin (VIME) were used for experimentation (Fig. 3b). SCs were co-cultured with a well established human NB cell line (CLB-Ma) and short-term cultured patient-derived NB cells (STA-NB-6) alongside controls of SCs and NB cells cultured alone for 11 days. As a qualitative read-out, we established an immunofluorescence staining panel, which identified NB cells by GD2 expression and SCs by S100B expression. After 11 days, CLB-Ma and STA-NB-6 cell controls showed their typical morphology of clustered cell bodies with short, randomly extended neuritic processes (Fig. 3c,d). However, in the co-cultures with SCs, NB cells had aligned along the bipolar SC extensions and increased the length of neuritic
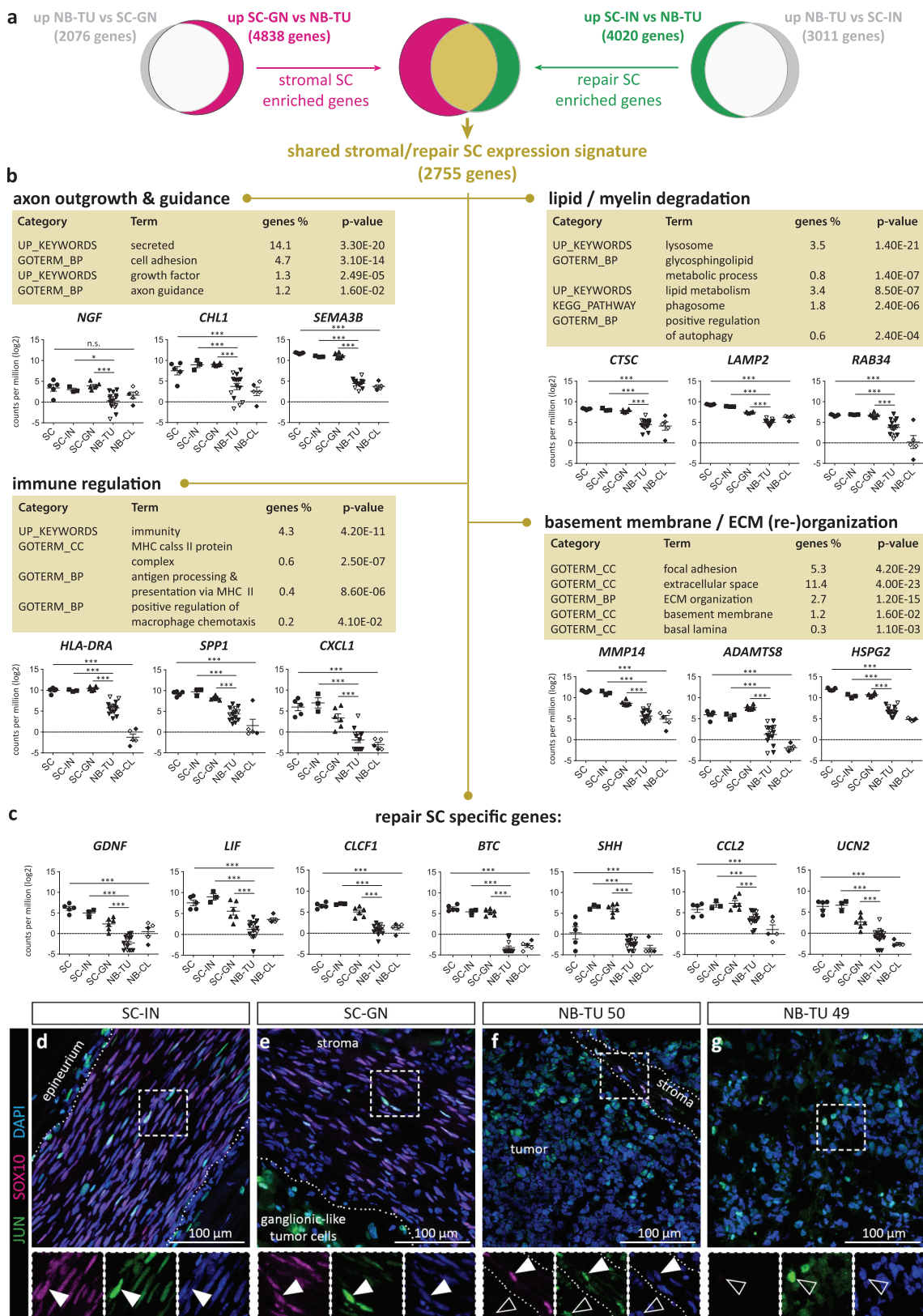
processes, predominantly in close contact with the SC surface (Fig. 3e,f,g,h arrows). Quantification of neurite length and alignment confirmed a significant increase of the mean neurite length (Fig. 3i) and neurite alignment (Fig. 3j) in co-cultures. These results suggest that the contact to human repair-related SCs induces a directed neuritic out-growth of NB cells in vitro.

Repair-related Schwann cells induce neuronal differentiation of neuroblastoma cells independent of direct cell–cell contact. We next aimed to dissect the effect of repair-related SCs on NB cells and distinguish signaling effects between cell bound and secreted molecules. Therefore, we refined the co-culture setting and used flow cytometry as a quantitative read-out. NB cells were either seeded in

105

Fig. 2 Transcriptome profiling and functional annotation analysis of genes shared by stromal SCs in ganglioneuroma tissue and repair SCs in injured nerve tissue. a Venn diagrams illustrate the number of significantly regulated genes (q-value > 0.05; |log2FC| > 1) of stromal SCs (SC-GN, n = 6 independent biological replicates) and repair SCs (SC-IN, n = 3) containing tissues compared to neuroblastoma tumor tissue (NB-TU, n = 15), respectively, and the overlap in genes shared by stromal and repair SCs (q-value > 0.05; |log2FC| >1). **b** The DAVID database [37] was used for functional annotation analysis of the 2755 gene set shared by stromal and repair SCs. KEGG pathways, functional categories (UP_KEYWORDS) and gene ontology terms (GOTERM) for biological processes (BP) and cellular compartments (CC) were manually grouped to functions such as axon outgrowth and guidance, lipid/myelin degradation, immune regulation and basement membrane/ECM (re-) organization. The expression of representative genes for each group (**b**) and the expression of specific repair SC genes (**c**) is shown for all samples; SCs (n = 5 biological replicates from 4 donors), NB-CLs (n = 5 biological replicates from 3 donors), SC-GN (n = 6), SC-INs (n = 3) and NB-TU (n = 15). Empty symbols indicate *MYCN* non-amplified NB-TUs and NB-CLs. Data are depicted as mean ± SD; *** q-value ≤ 0.001, ** q-value ≤ 0.01, * q-value ≤ 0.05, n.s. not significant. Representative immunostainings of tissue cryosections of (**d**) SC-IN, (**e**) SC-GN, (**f**) NB-TU 50, and (**g**) NB-TU 49 stained for JUN, SOX10, and DAPI; filled arrowheads indicate JUN$^+$/SOX10$^+$ SCs, lined arrowheads indicate JUN$^+$/SOX10$^-$ cells. Stainings were performed on three independent specimen per analyzed tissue.

direct contact with SCs or in a trans-well insert placed above SC cultures allowing diffusion of soluble molecules and reciprocal signaling. The refined co-culture set-up is illustrated in Fig. 4a.

In order to functionally validate whether isolated repair-related SCs reenact their key ability of regulating neuronal differentiation on NB cells in vitro, three well-established human NB cell lines (SH-SY5Y, IMR5, CLB-Ma) and two short-term NB cell cultures (STA-NB-6, STA-NB-10) covering the genetic spectrum of NBs, were co-cultured in direct and indirect contact with SCs. After 8 and 16 days, the cultures were analyzed by flow cytometry. The differentiation panel discriminated GD2$^-$/S100B$^+$ SCs and GD2$^+$/S100B$^-$ NB cells and included the neuronal differentiation marker NF200 (gating strategy Supplementary Fig. 7a). We found that NF200 expression was significantly upregulated in the *MYCN* non-amplified STA-NB-6 and SH-SY5Y NB cells after 16 days of direct contact to repair-related SCs (Fig. 4b). Of note, all NB cell lines, except STA-NB-10, showed a significant increase in NF200 expression at day 16 when co-cultured in the trans-wells without direct contact (Fig. 4b). We also noticed that the presence or absence of *MYCN* amplification in the analyzed NB cells correlated with their responsiveness to SCs (Fig. 4b). The mean fluorescence intensity histograms of NF200 further revealed that the basal NF200 expression level varied among the analyzed NB cells from low, as in CLB-Ma cells (Fig. 4c, CTRL), to highest in STA-NB-6 cells (Fig. 4d, CTRL). They also demonstrated that the increase in NF200 expression after co-culture was either due to the occurrence of a NF200$^+$ subpopulation, e.g. in CLB-Ma cells (Fig. 4c, co-cultured), or an overall elevated expression, e.g. in STA-NB-6 cells (Fig. 4d, co-cultured). These findings were confirmed by qualitative assessment of NF200 expression by immunofluorescence stainings of co-cultures compared to controls of CLB-Ma cells (Fig. 4e,f) and STA-NB-6 cells (Fig. 4g,h).

To analyze whether the increase in neuronal differentiation is SC specific, we co-cultured STA-NB-6 and SH-SY5Y cells, which showed the strongest response to SCs, with immortalized human fibroblasts (iFBs) and cancer associated FBs (CAFs). After 16 days, the NF200 expression of both NB cell cultures was either unaffected or even significantly decreased upon direct and indirect contact with iFBs (Supplementary Fig. 8a) or CAFs (Supplementary Fig. 8b).

Taken together, the results demonstrate that primary repair-related SCs and/or their secreted factors are sufficient to induce neuronal differentiation of aggressive NB cell lines and primary NB cultures in vitro.
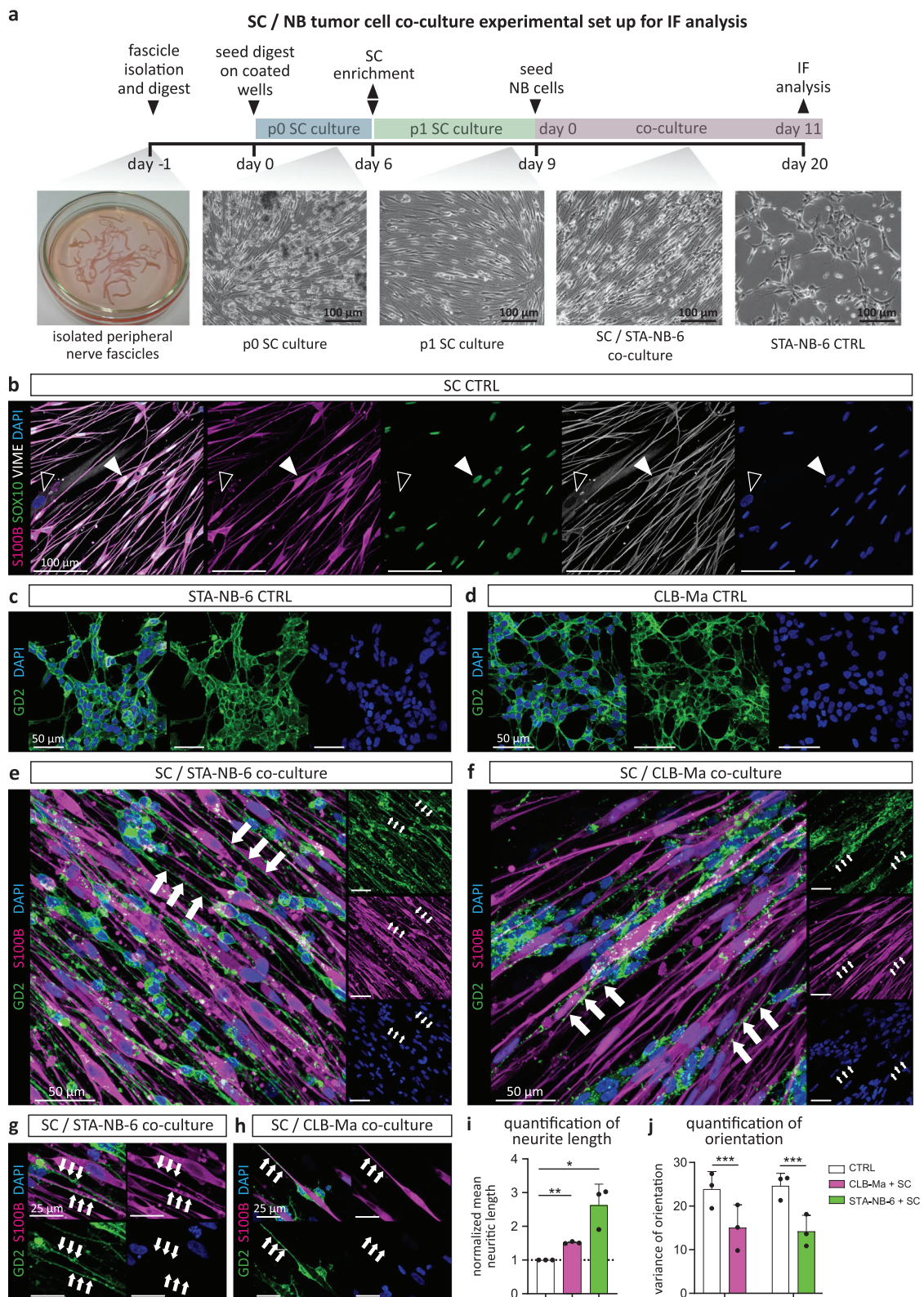
Repair-related Schwann cells impair proliferation and increase apoptosis of neuroblastoma cells. As cellular differentiation is accompanied by cell cycle arrest, we next determined the proliferation rate of NB cells by EdU incorporation in combination with DNA content analysis after direct and trans-well co-culture with SCs (gating strategy Supplementary Fig. 7b). Notably, after 16 days of direct SC contact the number of NB cells in the

S-phase was strongly reduced in all tested NB cell cultures (Fig. 5a). The proliferation rate of trans-well co-cultures was also significantly decreased in all NB cells, except STA-NB-10, but less pronounced as upon direct contact (Fig. 5a). The strongest anti-proliferative effects were detected in *MYCN* non-amplified STA-NB-6 and SH-SY5Y cells, as well as *MYCN* amplified IMR5 cells (Fig. 5a). Representative FACS plots illustrated the reduction of proliferation in CLB-Ma cells (Fig. 5b) and almost absent proliferation in STA-NB-6 cells (Fig. 5c) after 16 days of co-culture. This was also visualized by immunofluorescence stainings of co-cultures compared to controls of CLB-Ma cells (Fig. 5d,e) and STA-NB-6 cells (Fig. 5f,g) including the proliferation marker Ki67. In contrast, direct or indirect co-cultures with iFBs and CAFs did not influence the proliferation rate of STA-NB-6 and SHSY-5Y cells (Supplementary Fig. 7c,d).

In addition to increased differentiation and impaired proliferation, also cell death contributes to the decrease of tumor cells during GN development. Hence, we performed a terminal deoxynucleotidyl transferase dUTP nick end labeling (TUNEL) assay in combination with immunofluorescence staining for GD2 and S100B to detect apoptotic NB cells in control and co-cultures (Supplementary Fig. 9a,b). Quantitative evaluation showed that the apoptosis rate of both, *MYCN* non-amplified STA-NB-6 and *MYCN* amplified CLB-Ma cells, was increased about 10% at day 11 after direct co-culture (Supplementary Fig. 9c).

These findings show that direct and/or indirect contact to repair-related SCs decreased proliferation and elevated apoptosis of NB cells. As observed for neuronal differentiation, the *MYCN* amplification status correlated with the responsiveness of NB cells to SCs and revealed STA-NB-6 as the strongest and STA-NB-10 as the weakest SC-responsive NB cell cultures tested.

Stromal and repair Schwann cells express EGFL8, which is able to induce neurite outgrowth and neuronal differentiation of neuroblastoma cells. After demonstrating a pro-differentiating and anti-proliferative impact of human primary repair-related SCs on NB cells in vitro, we next aimed to identify the factors able to mediate these effects. Therefore, we interrogated the set of transcripts shared by repair SCs in injured nerve tissue and stromal SCs in GN tissue for the expression of secreted factors. Factors of interest were prioritized according to literature research and whether associated receptors, if known, were expressed by NBs. The shared secretome of repair and stromal SCs included neurotrophins such as *NGF*, *BDNF* and *GDNF* that confirmed the validity of our approach (Fig. 6a). In addition, we identified further highly expressed factors of interest such as *IGFBP6*, *FGF7* and *EGFL8* (Fig. 6a). IGFBP-6 was previously reported to inhibit the growth of SH-SY5Y cells[47] and FGF7 is involved in neuromuscular junction development[48], but both factors were not yet associated with SCs. Notably, EGFL8 was recently described by us as a potential factor involved in nerve

106

a SC / NB tumor cell co-culture experimental set up for IF analysis

isolated peripheral nerve fascicles | p0 SC culture | p1 SC culture | SC / STA-NB-6 co-culture | STA-NB-6 CTRL

b SC CTRL

c STA-NB-6 CTRL

d CLB-Ma CTRL

e SC / STA-NB-6 co-culture

f SC / CLB-Ma co-culture

g SC / STA-NB-6 co-culture

h SC / CLB-Ma co-culture

i quantification of neurite length

j quantification of orientation

CTRL / CLB-Ma + SC / STA-NB-6 + SC

regeneration but with yet unknown function[17]. Other neurotrophic factor transcripts, such as *PTN*, highly expressed in stromal but not in repair SCs, and *CNTF*, expressed in repair but not in stromal SCs, were included in the panel of candidate factors as transcripts of their putative receptors were present in NBs (Supplementary Fig. 10).

In order to validate the effect of a set of 8 candidate factors, the recombinant proteins NGF, BDNF, GDNF, CNTF, PTN, FGF7,

IBP6 and EGFL8 were added to the SC-weakly-responsive STA-NB-10 and SC-strongly-responsive STA-NB-6 cells. Proliferation and neuronal differentiation were monitored by flow cytometry after 16 days of exposure to respective factors. As suspected, the factors had less impact on the SC-weakly-responsive STA-NB-10 cells, however, NGF and EGFL8 caused a significant anti-proliferative effect (Fig. 6b). In contrast, the SC-strongly-responsive STA-NB-6 cells were significantly impaired in

Fig. 3 Establishment of a co-culture model to validate the effect of repair-related SCs on neuroblastoma cells in vitro. a Scheme of SC isolation, SC culture, and SC/NB cell co-culture. Representative immunofluorescence images of (**b**) a human primary repair-related SC culture stained for S100B, SOX10, vimentin (VIME), and DAPI; filled arrowheads indicate a S100B$^+$/SOX10$^+$/VIME$^+$ SC, lined arrowheads indicate a S100B$^-$/SOX10$^-$/VIME$^+$ fibroblast. Stainings were performed on three independent SC cultures. Representative immunostainings of GD2$^+$ STA-NB-6 (**c**) and CLB-Ma (**d**) NB cell controls as well as of (**e–h**) STA-NB-6 or CLB-Ma cells co-cultured with SCs at day 11. Arrows indicate extended neuritic processes aligned along SCs. Stainings were performed on NB cell controls and co-cultures with SCs derived from three independent donors per cell line. Quantification of (**i**) neurite length of STA-NB-6 ($p = 0.0452$) and CLB-Ma ($p = 0.002$) cells co-cultured with SCs compared to NB cell controls without SCs. Data are depicted as normalized mean neurite length ± SD ($n \geq 300$ cells over 6 images per condition over 3 independent experiments). Statistical test: repeated measures ANOVA and Dunnett's multiple comparison test. **j** Quantification of alignment of STA-NB-6 ($p < 0.0001$) and CLB-Ma ($p < 0.0001$) cells co-cultured with SCs compared to NB cell controls without SCs. Variance of orientation (variance of deviation of main cell orientation) ± SD; a value of 0 corresponds to perfect alignment; (180 datapoints in each 3 images over 3 independent experiments); For each pair of measurements (control and co-culture), a Levene test was applied to test for equal variances; *** p-value ≤ 0.001, ** p-value ≤ 0.01, * p-value ≤ 0.05.

proliferation and showed increased neuronal differentiation after treatment with either NGF, EGFL8, BDNF, CNTF, PTN or GDNF (Fig. 6c). Notably, the effect of EGFL8 was concentration dependent and comparable to NGF, one of the most potent neurotrophins known so far (Fig. 6d). EGFL8 also acted pro-differentiating on CLB-Ma and SH-SY5Y cells, while an anti-proliferative effect was only observed in the latter (Fig. 6e). Phase contrast images illustrated the reduction of cell number and longer neuritic processes (Fig. 6f). Compared to untreated controls, STA-NB-6 cells showed a significant increase of neurite length after NGF- and EGFL8-treatment (Fig. 6g).

These findings demonstrate that EGFL8, a protein so far only described in thymocyte development[49], has a neuritogenic function able to enhance neuronal differentiation and/or to impair proliferation of aggressive NB cells.

EGFL8 gene expression level in neuroblastomas correlates with increased patient survival. As EGFL8 exerted anti-tumor activity on NB cells in vitro, we next assessed whether *EGFL8* expression levels in peripheral neuroblastic tumors may correlate with the clinical outcome. Analysis of the overall patient survival according to *EGFL8* gene expression was performed using the *R2: Genomics Analysis and Visualization platform*. Two different datasets, comprising 649 and 283 tumor specimens, respectively, demonstrated an over 90% and 70%, respectively, 5-year overall survival probability for patients with high *EGFL8* expression, but less than 60% and 40%, respectively, for patients with low *EGFL8* expression (Fig. 6h & Supplementary Fig. 11 a,b). Information about the stromal SC content of the included tumor specimens was not available. These data show that *EGFL8* expression correlates with increased patient survival, which could be due to its neuritogenic effect on peripheral neuroblastic tumor cells.

The EGFL8 protein is significantly elevated in ganglioneuromas compared to neuroblastomas and expressed by repair Schwann cells and stromal Schwann cells. To verify whether the high *EGFL8* gene expression detected in GNs is reflected by the EGFL8 protein level, we performed high-resolution mass spectrometry analysis of SC stroma-rich GNs, SC stroma-poor NBs, as well as primary NB cultures and evaluated this data set together with our existing proteomic data set comprising repair SC-containing injured nerve tissue as well as primary repair-related SC cultures[17]. The results demonstrated a significantly higher abundance of the EGFL8 protein in injured nerves and GNs when compared to NBs (Fig. 7a). In addition, the protein levels of EGFL8 in primary cells matched their respective tissue of origin (Fig. 7a). This was confirmed by immunostaining illustrating SOX10 and EGFL8 co-expression by repair SCs in injured nerve tissue (Fig. 7b) and stromal SCs in GNs (Fig. 7c), while EGFL8 was absent on tumor cells in GN and NB primary

tumors (Fig. 7d,e). The images further showed that EGFL8 was also expressed in S100$^-$ cells, e.g. in the perineurium and blood vessel-like structures (Fig. 7a,b).

Hence, mass spectrometric analyses and immunostaining confirmed that the EGFL8 protein is highly abundant in stromal SCs in GNs and repair SC in injured nerve tissues as well as primary repair-related SC cultures.

EGFL8 protein is secreted by repair-related Schwann cells and rewires kinase-mediated signaling in neuroblastoma cells in vitro. As EGFL8 is a predicted secreted factor and recombinant EGFL8 was able to induce neuronal differentiation, we next determined whether SC-produced EGFL8 is indeed secreted and investigated its mode-of-action in NB cells. First, we co-stained primary repair-related SC cultures for EGFL8 and membranous nerve growth factor receptor (NGFR), a marker associated with immature/repair SCs. EGFL8 showed an intracellular staining pattern with accumulation of positive signals in clusters of different sizes (Fig. 7f). 3D analysis illustrated EGFL8 positive vesicular structures embedded within the cytoplasm beneath the NGFR$^+$ SC membrane (Supplementary Movie 1). In addition, we performed WB analysis for EGFL8 on cell lysates of human primary SCs, STA-NB-6 and SH-SY5Y cells, and conditioned culture medium (supernatants) of respective cultures (Fig. 7g, Supplementary Fig. 12). A GST-tagged recombinant EGFL8 protein was used as positive control. EGFL8 has an expected mass of 32 kDa, accordingly, the antibody detected the GST-tagged (GST corresponding to 26 kDa) recombinant EGFL8 protein at around 58 kDa in positive controls. In all four SC whole cell lysates, two bands were visible at around 32 and 37 kDa and three SC samples showed an additional band at around 55 kDa. In three out of four analyzed SC supernatants, prominent bands were detected at 37 kDa, which could indicate that the secreted EGFL8 protein underwent posttranslational modifications.

Second, we addressed the down-stream signaling of EGFL8 in NB primary cultures. As no data currently exist on EGFL8 receptor or signaling in human or any other mammalian cells, we employed an unbiased global- and phospho-proteomics approach in EGFL8-responsive STA-NB-6 versus non-responsive STA-NB-10 NB cells in a time-resolved manner. In total we identified 6385 and 6122 proteins expressed by STA-NB-6 and STA-NB-10 cells, respectively (Supplementary data 1). 6.408 and 6.133 sites were found phosphorylated corresponding to 1.851 and 1.820 proteins in STA-NB-6 and STA-NB-10, respectively (Supplementary Data 2). While STA-NB-6 showed a clear trajectory in the phospho-proteome upon 15 towards 60 min EGFL8 exposure (Supplementary Fig. 13a), a more diffuse dynamics was observed in STA-NB-10 (Supplementary Fig. 14a). As the most pronounced change was evident after 15 min, we focused on this time point and performed kinase enrichment analysis (KSEA), revealing a significant activation (enrichment z-score ≥ 1, $p \leq 0.05$, substrate cutoff ≥ 3) of 11 kinases in STA-NB-6 and 18 kinases in STA-NB-10 (Fig. 7h,
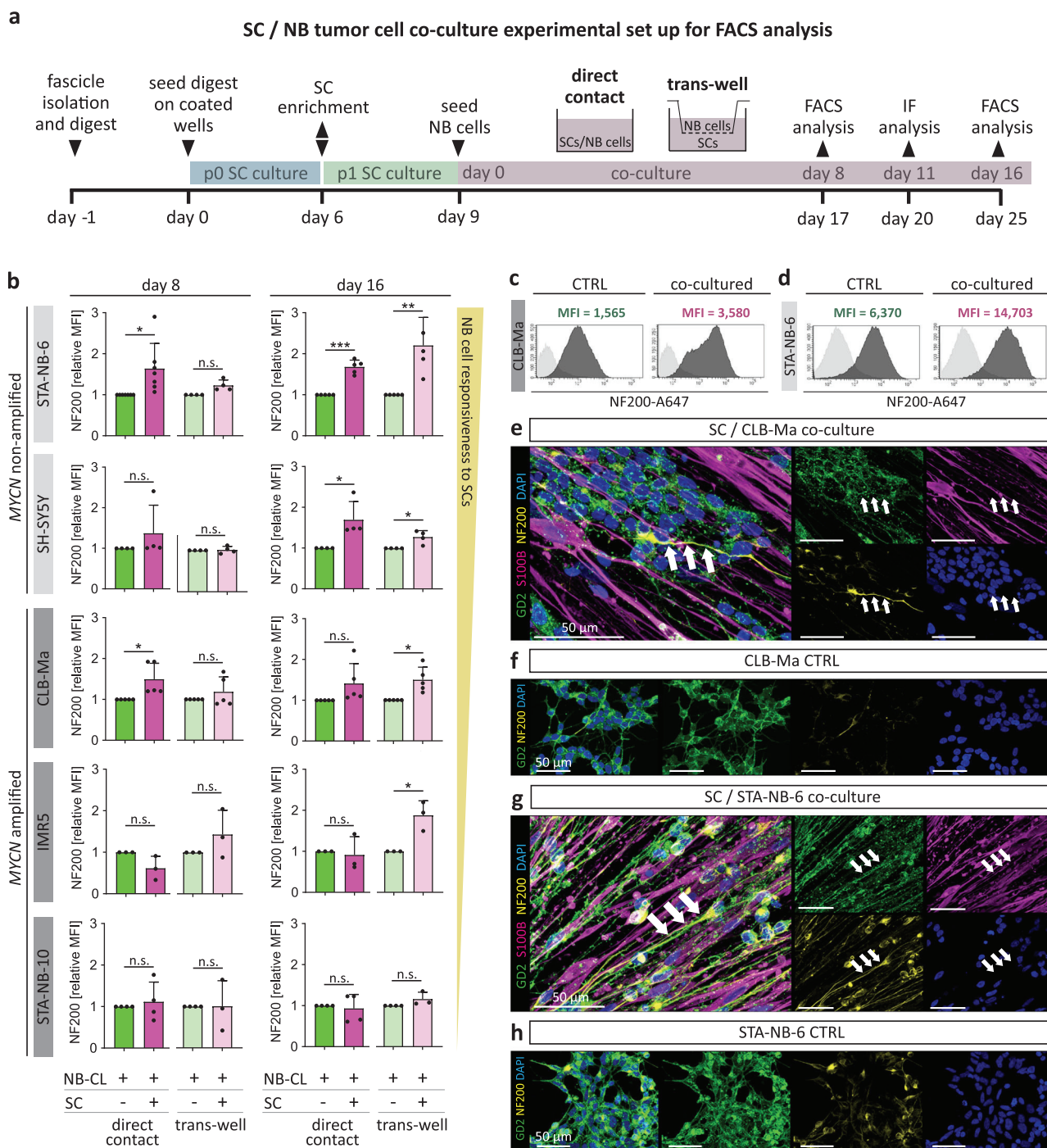
Fig. 4 Neuronal differentiation analysis of neuroblastoma cell lines in response to repair-related SCs in vitro. a Refined SC/NB cell co-culture set up including direct and trans-well co-cultures. Three NB cell lines and two NB cell short-term cultures were co-cultured with primary repair-related SCs and NF200 expression levels were analyzed by flow cytometry (FACS) and immunofluorescence (IF). **b** Bar diagrams show the normalized mean fluorescence intensity (MFI) of NF200 ± SD in GD2$^+$/S100B$^-$ NB cells upon direct co-cultures (STA-NB-6, $p = 0.033$; SH-SY5Y, $p = 0.363$; CLB-Ma, $p = 0.048$; IMR5, $p = 0.146$; STA-NB-10, $p = 0.666$) and trans-well co-cultures (STA-NB-6, $p = 0.042$; SH-SY5Y, $p = 0.816$; CLB-Ma, $p = 0.331$; IMR5, $p = 0.331$; STA-NB-10, $p = 0.988$) with SCs at day 8 as well as direct co-cultures (STA-NB-6, $p = 0.001$; SH-SY5Y, $p = 0.049$; CLB-Ma, $p = 0.132$; IMR5, $p = 0.762$; STA-NB-10, $p = 0.713$) and trans-well co-cultures (STA-NB-6, $p = 0.017$; SH-SY5Y, $p = 0.041$; CLB-Ma, $p = 0.023$; IMR5, $p = 0.050$; STA-NB-10, $p = 0.242$) with SCs at day 16. STA-NB-6: day 8 direct co-culture $n = 7$, trans-well $n = 4$, day 16 direct co-culture $n = 5$, trans-well $n = 4$; SH-SY5Y: $n = 4$; CLB-Ma: $n = 5$; IMR5: $n = 3$; STA-NB-10: direct co-culture $n = 4$; trans-well $n = 3$. A paired two-tailed Student's t-test comparing against the control was performed. n refers to the number of independent experiments; * $p \leq 0.05$; ** $p \leq 0.01$; *** $p \leq 0.001$; n.s. not significant. Representative FACS histograms show the unstained controls (light grey) and the MFI of NF200 in control and co-cultured (**c**) CLB-Ma and (**d**) STA-NB-6 cells (dark grey) at day 16. FACS gating strategy is detailed in Supplementary Fig. 7a. Representative IF images of co-cultured CLB-Ma cells (**e**) and STA-NB-6 (**g**) cells stained for NF200, S100B, GD2 and DAPI at day 11 of direct co-culture and respective NB cell controls stained for GD2, NF200, and DAPI (**f**, **h**); arrows indicate long neuritic processes of NB cells strongly positive for NF200 in co-cultures. Stainings were performed on NB cell controls and corresponding co-cultures with SCs derived from three independent donors.

109
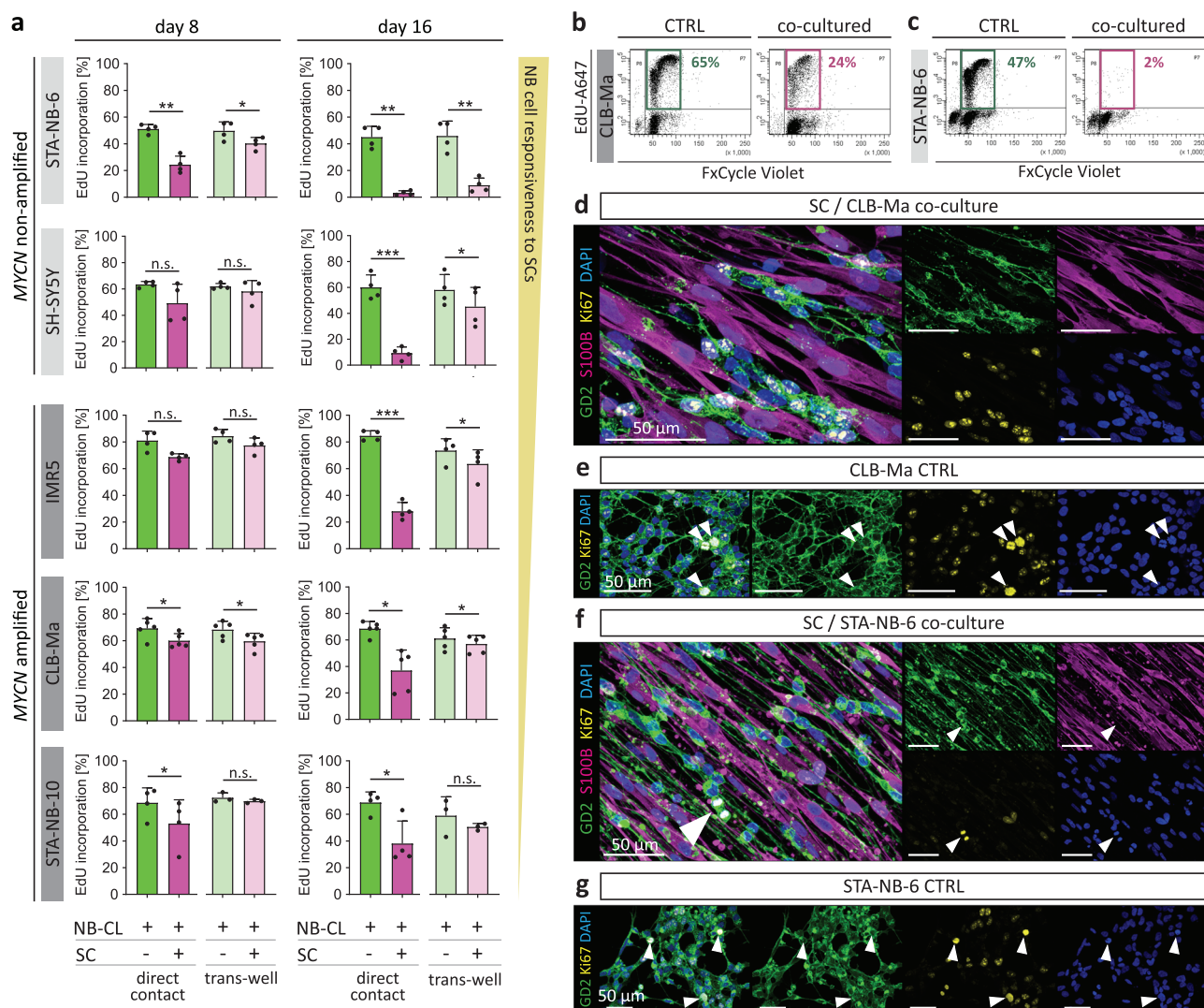
Fig. 5 Proliferation analysis of neuroblastoma cell lines after direct and indirect contact to repair-related SCs in vitro. Three NB cell lines and two NB cell short-term cultures were co-cultured with primary repair-related SCs and their proliferation rates were analyzed by FACS and IF. **a** Bar diagrams show the mean percentage of EdU-incorporation ± SD in GD2$^+$/S100B$^-$ NB cells upon direct co-cultures (STA-NB-6, $p = 0.008$; SH-SY5Y, $p = 0.139$; CLB-Ma, $p = 0.025$; IMR5, $p = 0.073$; STA-NB-10, $p = 0.023$) and trans-well co-cultures (STA-NB-6, $p = 0.006$; SH-SY5Y, $p = 0.401$; CLB-Ma, $p = 0.032$; IMR5, $p = 0.051$; STA-NB-10, $p = 0.209$) with SCs at day 8 as well as direct co-cultures (STA-NB-6, $p = 0.003$; SH-SY5Y, $p = 0.001$; CLB-Ma, $p = 0.019$; IMR5, $p = 0.001$; STA-NB-10, $p = 0.037$) and trans-well co-cultures (STA-NB-6, $p = 0.015$; SH-SY5Y, $p = 0.042$; CLB-Ma, $p = 0.039$; IMR5, $p = 0.028$; STA-NB-10, $p = 0.472$) with SCs at day 16; STA-NB-6: $n = 4$; SH-SY5Y: $n = 4$; CLB-Ma: $n = 5$; IMR5: $n = 4$; STA-NB-10: direct co-cultures $n = 4$, trans-well cultures $n = 3$; A paired two-tailed Student's t-test comparing against the control was performed. * $p \leq 0.05$; ** $p \leq 0.01$; *** $p \leq 0.001$. Representative FACS plots illustrate EdU incorporation and the DNA content of control and co-cultured NB cells (**b**) CLB-Ma and (**c**) STA-NB-6 at day 16; the marked EdU$^+$/FxCycleViolet$^+$ cells are in the S-Phase of cell cycle. FACS gating strategy is detailed in Supplementary Fig. 7b. n refers to the number of independent experiments. Representative IF images of co-cultured CLB-Ma (**d**) and STA-NB-6 (**f**) cells stained for Ki67, S100B, GD2 and DAPI at day 11 of direct co-culture and respective NB cell controls stained for GD2, Ki67, and DAPI (**e**, **g**); arrows indicate NB cells undergoing mitosis. Stainings were performed on NB cell controls and corresponding co-cultures with SCs derived from three independent donors.
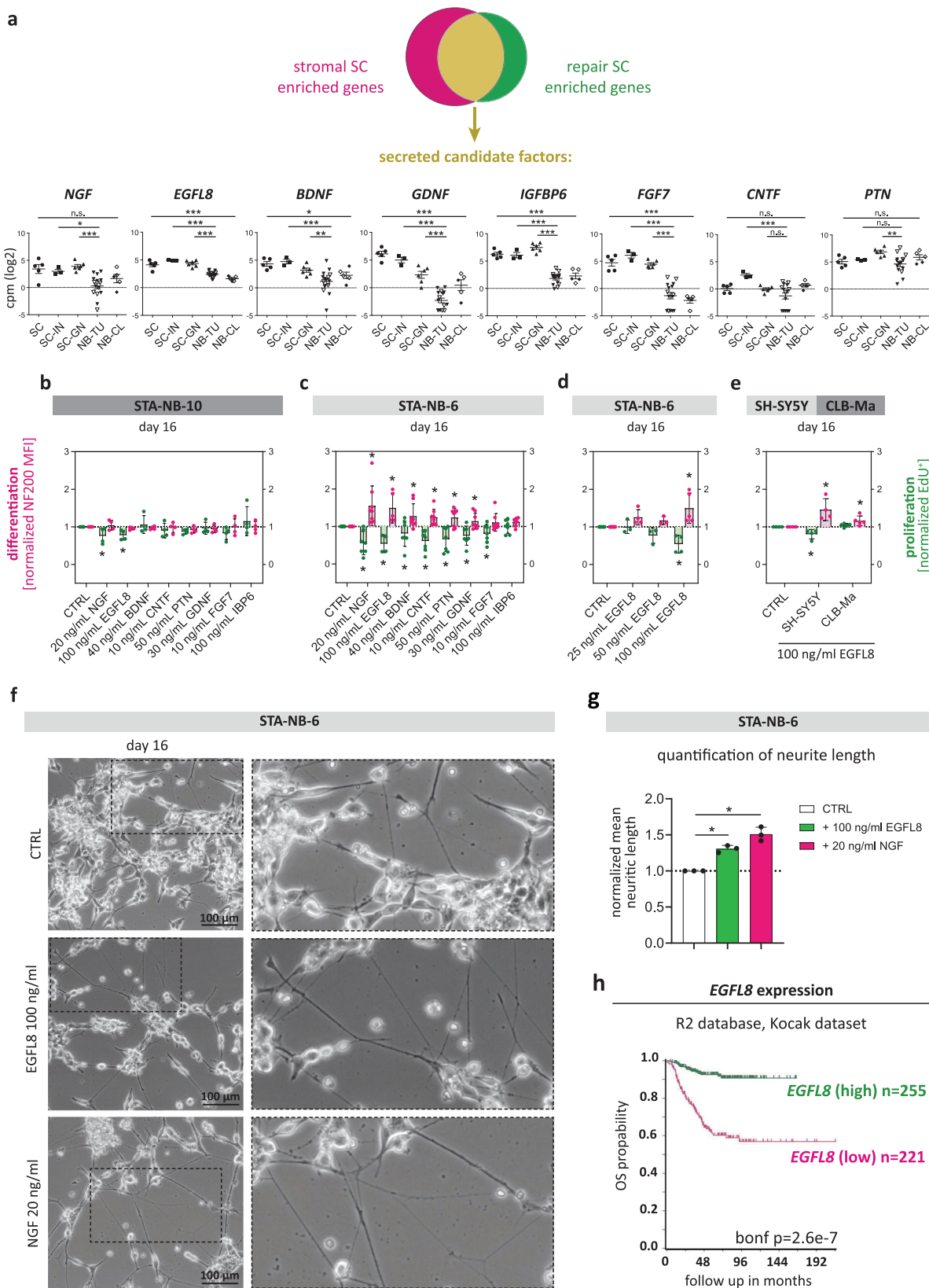
Supplementary Data 3, Supplementary Fig. 15). Kinases activated in STA-NB-6 and counter- or not regulated in STA-NB-10, such as HIPK1, p38β/MAPK11, ERK5/MAPK7, SGK1 and TLK2, and their substrates, e.g. PML, PAK2 or NDRG2, present key components of the EGFL8-induced signaling network (Fig. 7h, Supplementary Data 3 and 4, Supplementary Fig. 13-15).

In line with the predicted secretion of EGFL8, we here show that EGFL8 is present in vesicular structures within the cytoplasm and released in the medium of cultured human repair-related SCs. Further, we demonstrate that EGFL8 addition leads to a rapid (within 15 min) and specific phosphorylation of substrates of e.g. HIPK1, p38b/MAPK11, ERK5/MAPK7 only in EGFL8

responsive STA-NB-6, but not in the non-responsive STA-NB-10 short-term NB cell cultures, providing evidence for dynamic changes in the kinome associated with neuronal differentiation triggered by EGFL8.

Discussion

This study presents a comparative analysis of human repair SCs in injured nerves and stromal SCs in GNs that builds upon previous efforts to delineate the role of SCs in nerve regeneration and the tumor microenvironment[1,17,31]. By investigating human tissues and primary cultures with deep RNA-sequencing, high-

resolution mass spectrometry, and confocal imaging, we reveal a similar cellular state and functional competences of repair SCs and stromal SCs. Our comprehensive approach identified EGFL8 as a neuritogenic factor expressed by repair SCs and stromal SCs, which highlights matricellular proteins as tissue active components involved in regenerative and pathological responses of SCs

in the peripheral nervous system. Focusing on the interaction of tumor cells and SCs, we developed a co-culture model combined with a flow cytometry-based read-out demonstrating that NB cells react to repair-related SCs in a similar fashion as peripheral neurons upon injury. Moreover, the established co-culture model is broadly applicable and contributes to the ongoing research in

111

Fig. 6 Neuronal differentiation and anti-proliferative effects of secreted factors shared by stromal and repair SCs. a Expression levels of chosen candidate factors *NGF, EGFL8, BDNF, GDNF, IGFBP6, FGF7, CNTF* and *PTN* shown for primary repair-related SCs (SC, *n* = 5 biological replicates from 4 donors), repair SC rich injured nerve fascicle tissue (SC-IN, *n* = 3 biological replicates), SC stroma rich GN tissue (SC-GN, *n* = 6 biological replicates), NB tissue (NB-TU, *n* = 15 biological replicates) and NB short-term cell cultures (NB-CL, *n* = 5 biological replicates from 3 donors). Empty symbols indicate *MYCN* non-amplified NB-TUs and NB-CLs. Data are depicted as mean ± SD; *** *q* ≤ 0.001, ** *q* ≤ 0.01, * *q* ≤ 0.05. **b–e** FACS analyses of neuronal differentiation (NF200 MFI) and proliferation (EdU incorporation) of NB cells treated with recombinant candidate proteins compared to untreated NB cell controls (CTRL) after 16 days of culture; data are shown as normalized mean values ± SD; n refers to the number of independent experiments; * *p* ≤ 0.05. Proliferation levels (green) of (**b**) SC-weak responsive STA-NB-10 exposed to recombinant candidate proteins NGF (*p* = 0.107), EGFL8 (*p* = 0.042), BDNF (*p* = 0.636), CNTF (*p* = 0.390), PTN (*p* = 0.026), GDNF (*p* = 0.671), FGF7 (*p* = 0.128), and IBP6 (*p* = 0.486) compared to CTRLs (all *n* = 4) and (**c**) SC-strong responsive STA-NB-6 exposed to recombinant candidate proteins NGF (*p* = 0.009), EGFL8 (*p* = 0.030), BDNF (*p* = 0.197), CNTF (*p* = 0.009), PTN (*p* = 0.033), GDNF (*p* = 0.042), FGF7 (*p* = 0.935), and IBP6 (*p* = 0.082) compared to CTRLs (all *n* = 7, except EGFL8 *n* = 4) at concentrations as indicated. Differentiation levels (magenta) of (**b**) SC-weak responsive STA-NB-10 exposed to recombinant candidate proteins NGF (*p* = 0.567), EGFL8 (*p* = 0.099), BDNF (*p* = 0.252), CNTF (*p* = 0.783), PTN (0.153), GDNF (*p* = 0.335), FGF7 (*p* = 0.934), and IBP6 (*p* = 0.926) compared to CTRLs (all *n* = 4) and (**c**) SC-strong responsive STA-NB-6 exposed to recombinant candidate proteins NGF (*p* = 0.022), EGFL8 (*p* = 0.049), BDNF (*p* = 0.050), CNTF (*p* = 0.014), PTN (*p* = 0.025), GDNF (*p* = 0.100), FGF7 (*p* = 0.015), and IBP6 (*p* = 0.232) compared to CTRLs (all *n* = 8, except EGFL8 *n* = 5). **d** Proliferation levels (green) of STA-NB-6 cells exposed to 25ng/ml EGFL8 (*n* = 3, *p* = 0.978), 50 ng/ml EGFL8 (*n* = 3, *p* = 0.196), and 100 ng/ml EGFL8 (*n* = 4, *p* = 0.030) compared to CTRLs (*n* = 4). Differentiation levels (magenta) of STA-NB-6 cells exposed to 25ng/ml EGFL8 (*n* = 4, *p* = 0.087), 50 ng/ml EGFL8 (*n* = 3, *p* = 0,106), and 100 ng/ml EGFL8 (*n* = 5, *p* = 0.049) compared to CTRLs (*n* = 5). **b–e** Statistical test: One way ANOVA or mixed effects model and adjustments for multiple testing was performed. **e** Proliferation (green) and differentiation (magenta) levels of SH-SY5Y cells after treatment with 100 ng/ml EGFL8 (proliferation: *p* = 0.050, differentiation: *p* = 0.050) compared to CTRLs (both *n* = 4, paired, two-tailed Student's t-test) and CLB-Ma cells after treatment with 100 ng/ml EGFL8 (proliferation: *p* = 0.116, differentiation: *p* = 0.046) compared to CTRLs (both *n* = 5, paired, two-tailed Student's t-test); **f** Representative bright field images of STA-NB-6 cells at day 16 cultured in the absence (CTRL) or presence of 100 ng/ml EGFL8 or 20 ng/ml NGF (*n* = 3). Enlargements illustrate the neuritic processes of STA-NB-6 cells in CTRL as well as EGFL8- and NGF-treated cultures. **g** Quantification of neurite length of STA-NB-6 cells treated with 20 ng/ml NGF (*p* = 0.004) or 100 ng/ml EGFL8 (0.006) compared to untreated CTRLs. Data are depicted as normalized mean neurite length ± SD (*n* = 6 images per treatment over 3 independent biological replicates); Statistical test: repeated measures ANOVA and Dunnett's multiple comparison test; * *p*-value ≤ 0.05. **h** Kaplan-Meier survival plot show the overall survival (OS) probability of patients grouped according to high and low *EGFL8* expression in primary tumors at diagnosis. Data were derived from the Kocak dataset (GSE45547) of the R2 Genomics Analysis and Visualization platform (https://r2.amc.nl) (see also Supplementary Fig. 11).

the field of regenerative medicine as well as cancer research aiming to elucidate the interplay of human SCs with different (tumor) cell populations.

The development of mostly benign-behaving peripheral neuroblastic tumors is hallmarked by an increasing stromal SC population and tumor cell differentiation along the sympathetic neuronal lineage. Since previous studies demonstrated that stromal SCs unlikely descend from tumor cells[1,28,30], we aimed to understand their origin and cellular state. The accumulation of publications supporting adult SCs as a highly plastic cell type urged us to investigate whether this reactive/adaptive potential plays a role in GNB/GN development.

The inherent SC plasticity is impressively demonstrated after peripheral nerve injury, where adult SCs undergo substantial expression and morphological changes to adapt their cellular functions to the needs of nerve repair[7,9,13,17]. In this study, transcriptome profiling elucidated a similar expression signature of stromal SCs in GNs and repair SCs in injured nerves as demonstrated by nerve repair-associated genes and functions. SC stroma development in peripheral neuroblastic tumors indeed exhibits parallels to the nerve injury-induced transformation of adult SCs into a repair cell identity, which is defined by two characteristics.

The first characteristic is the re-expression of genes associated with precursor/immature SCs that enables them to exit their differentiated cell state, re-enter the cell cycle, and gain an increased migratory capacity[10,50,51]. These features match the morphological observation of stromal SCs entering tumors through migration along blood vessels and connective tissue septa and the augmentation of SC stroma over time[28]. The expression of genes associated with a pre-myelin developmental stage of stromal SCs could also explain why the long axonal processes of ganglionic-like tumor cells in GNs are not myelinated[26].
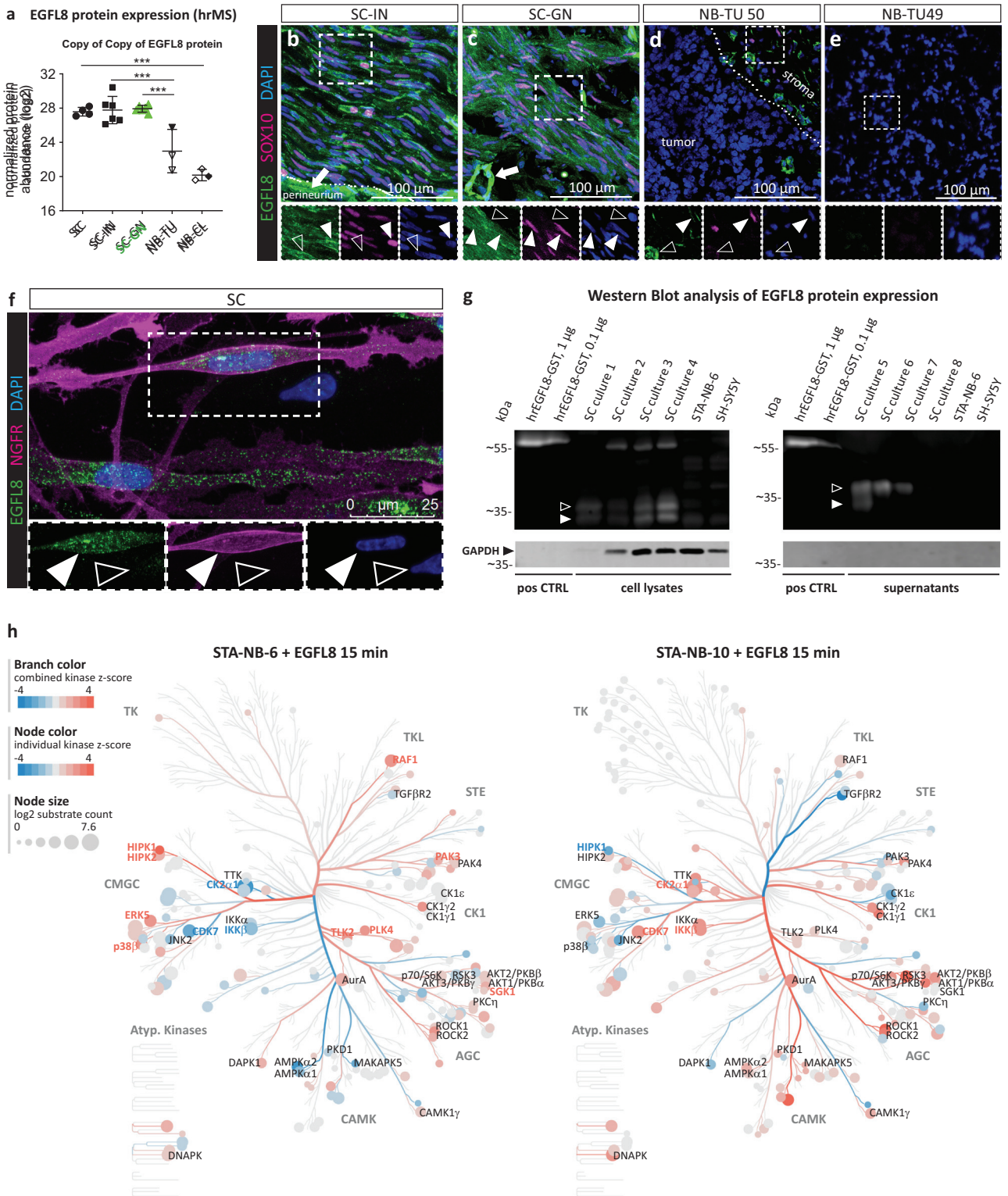
The second characteristic of repair SCs is the acquisition of repair-specific functions including myelin clearance, macrophage recruitment, upregulation of MHC-II, formation of regeneration

tracks and expression of neurotrophic factors that support axon re-growth and guidance[7,9,14,16,17]. It is important to empathize that these competences are not shared by developing SCs or adult, i.e. differentiated, SCs. Previous studies identified the specific upregulation of ligands such as *GDNF* and *SHH* in repair SCs[12,13] and a recently published single-cell RNA-sequencing analysis comparing neonatal, uninjured (adult) and injured mouse peripheral nerves now provides further genes exclusively expressed by SCs upon injury. As the majority of them were present in the herein described enriched gene sets of human repair SCs and stromal SCs (see Fig. 2c), a contribution of mesenchymal stem cells or other precursors differentiating into Schwann-like stromal cells during GNB/GN development is unlikely.

Taken together, these findings assign the cellular state of stromal SCs to adult SCs that underwent a phenotypical switch as occurring after nerve damage and supports a repair-related cellular state of stromal SCs in GNs. Moreover, the progressing death of differentiating and differentiated neuroblastoma cells (ganglionic-like tumor cells) and resulting axon degeneration observed in GNBs/GNs[52] could supply stromal SCs with cues that trigger the repair-like state and explain why it does not diminish over time. As a consequence, stromal SCs could continuously exert nerve repair-associated functions in the microenvironment that are responsible for a benign tumor development.

Recognizing stromal SCs as possible facilitators of nerve repair-associated functions in the tumor microenvironment prompts the question how these functions could affect the behavior of tumor cells. We here show that stromal SCs share the expression of several neurotrophins and axon-guiding proteins with repair SCs in damaged nerves. Hence, neuronal differentiation-inducing cues derived from stromal SCs could be responsible for the differentiation of tumor cells into ganglionic-like cells during GNB/GN development. We modeled the interaction of SCs and NB cells in functional co-culture experiments, where we exposed genetically diverse NB cell lines and short-term primary NB cultures, derived from

a EGFL8 protein expression (hrMS)

g Western Blot analysis of EGFL8 protein expression

h STA-NB-6 + EGFL8 15 min   STA-NB-10 + EGFL8 15 min

aggressive high-risk NBs, to human primary repair-related SCs. Both, the direct contact to SCs and the in-direct contact to the SCs' secretome, were sufficient to induce neuronal differentiation and to impair proliferation of NB cells. Of note, this anti-tumor effect could be replicated by replacing SCs with recombinant neurotrophic factors discovered within the repair/stromal SC secretome.

In addition to their influence on neuroblastic tumor cells, stromal SCs also hold a considerable potential to modulate the tumor microenvironment. We found that stromal SCs express MHC-II, which is in line with other studies that reported the capacity of SCs to express MHC-II in (auto-) inflammatory or infectious neuropathies[53–56]. We also discovered that stromal SCs express potent chemokines and confirmed the presence of macrophages and T-cells in GNs, which is in accordance with the increasing reports about the immunomodulatory potential of SCs[17,56–61]. Furthermore, the shared expression signature of

113

Fig. 7 EGFL8 protein expression analysis and kinome activation. a High-resolution mass spectrometry (hrMS) data of EGFL8 protein expression levels in primary repair-related SCs (SC, $n = 4$ biological replicates), injured nerve tissue (SC-IN, $n = 6$ biological replicates from 3 donors), SC stroma-rich ganglioneuromas (SC-GN, $n = 6$ biological replicates), SC stroma-poor neuroblastomas (NB-TU, $n = 3$) and neuroblastoma short term cell cultures (NB-CL, $n = 3$); lined symbols indicate *MYCN* non-amplified NB-TUs and NB-CLs; *** $p \leq 0.001$; Data are depicted as mean ± SD. One-way ANOVA and Tukey's multi-comparison test was performed: SC vs. NB-TU adjusted $p = 0.0006$; SC vs. NB-CL $p < 0.0001$; SC-IN vs. NB-TU $p < 0.0001$; SC-IN vs. NB-CL $p < 0.0001$; SC-GN vs. NB-TU $p = 0.0004$; SC-GN vs. NB-CL $p < 0.0001$; Representative immunostaining of tissue cryosections of (**b**) SC-IN, (**c**) SC-GN, (**d**) NB-TU 50, and (**e**) NB-TU 49 stained for EGFL8, SOX10, and DAPI; filled arrowheads indicate EGFL8$^+$/SOX10$^+$ SCs, lined arrowheads indicate EGFL8$^-$/SOX10$^-$ cells. Stainings were performed on three independent specimen per analyzed tissue. **f** Representative immunostaining of a repair-related SC culture stained for NGFR, EGFL8, and DAPI. The enlargement shows the SC body with membranous NGFR staining and intracellular EGFL8 signals within vesicle-like structures (filled arrowheads); the lined arrowheads indicate a NGFR$^-$/EGFL8$^-$ fibroblast. A video of z-stacks visualizing the intracellular location of EGFL8 signals is available in Supplementary Movie 1. Stainings were performed on three independent SCs cultures. **g** Western blots show EGFL8 protein bands in primary repair-related SC lysates ($n = 4$) and supernatants ($n = 4$) but not in NB cell line STA-NB-6 and SH-SY5Y lysates and supernatants; filled white arrowheads indicate bands of about 32 kDa, the proposed molecular weight of EGFL8, lined white arrowheads indicate bands of ~37 kDa that could represent the EGFL8 protein with posttranscriptional modifications. Human recombinant (hr) EGFL8 (32 kDa) with a GST-tag (26 kDa) was used as positive control. Note that EFGL8 was detected via chemiluminescence and GAPDH via immunofluorescence on the same blot; full scans are available in Supplementary Fig. 12. **h** Phospho-proteomics upon 15 min EGFL8 treatment of EGFL8-responsive STA-NB-6 and non-responsive STA-NB-10 cells ($n = 3$ independent biological replicates). Kinase tree depicts kinases significantly enriched for substrate phosphorylation as compared to untreated control; for kinases with a cut-off ≥ 3 substrates; z-score ≥ 1; $p \leq 0.05$ kinase names are shown next to the node. For complete kinome trees see Supplementary Fig. 13b and 14b. Kinase families are labeled in grey; Kinases significantly enriched (red) or de-enriched (blue) in STA-NB-6 and not regulated or counter-regulated in STA-NB-10 are labeled in bold. Statistical test: kinase-substrate enrichment analysis of class 1 phosphosites ($p > 0.75$) utilizing PhosphoSitePlus and NetworKIN was performed, applying a NetworKIN score cutoff of 2, p-value cutoff of 0.05 and substrate count cutoff 3.

stromal/repair SCs contained basement membrane components and ECM remodelers such as metalloproteinases and matricellular proteins. Stromal SCs could therefore recruit and interact with immune cells, as well as execute tissue remodeling functions in the tumor environment with the original goal to rebuild an organized nerve structure similar to repair SCs upon nerve injury.

Taken together, the nerve repair-like phenotype equips stromal SCs with different strategies to influence their environment. Stromal SCs could either directly induce neuronal differentiation of peripheral neuroblastic tumor cells or indirectly manipulate the tumor microenvironment via immunomodulation and ECM remodeling responsible for a favorable tumor development.

Here, we introduce the matricellular protein EGFL8 as neuritogen. EGFL8 shares similar domains and molecular weight with EGFL7, which was described to induce neural stem cell differentiation[62,63]. We demonstrated high expression of the EGFL8 protein by repair SCs and stromal SCs and its secretion by repair-related SCs in vitro. Moreover, *EGFL8* expression in peripheral neuroblastic tumors correlated with an increased patient survival. We provide evidence for a neuritogenic function of human EGFL8, a protein of so far unknown function, as its recombinant form was sufficient to induce neuronal differentiation of NB cells at similar efficacy as NGF. Further, our comprehensive map of the activated kinome at baseline and upon EGFL8 stimulation delineates the down-stream signaling dynamics in NB cells. EGFL8 addition leads to specific phosphorylation of HIPK1, p38β/MAPK- and ERK5/MAPK7-substrates only in the sensitive cell line STA-NB-6, but not in the insensitive STA-NB-10. While ERK and MAPK are well established key nodes transmitting neurotrophic/neuritogenic signals[64], HIPK1, SGK1 and TLK2 have not been implicated in peripheral neuronal differentiation yet. Interestingly, the re-wiring of cellular signaling by EGFL8 converged at known regulators of neurogenesis, such as PML, NDRG2 and PAK2[65–67], corroborating the role of EGFL8 as neuritogenic factor. It will be interesting to elaborate the common and unique roles of EGFL8 in the concert of neurotrophic factors.

The discovery of EGFL8 as neuritogen underlines the increasingly recognized impact of matricellular proteins in injury response and pathological conditions[68–71]. Stromal SCs and repair SCs also shared the expression of other matricellular proteins such as *SPARC*, *SPP1* (osteopontin) and *CCN3* (*NOV*).

Notably, SC stroma-derived SPARC was previously reported to suppress NB progression by inhibiting angiogenesis and introducing changes in the ECM composition[72], suggesting that stromal/repair SCs are a source of various matricellular proteins that foster neuronal differentiation.

The plastic potential of adult SCs is a double-edged sword. While essential for nerve repair, recent studies point out its adverse effect in neuropathies and epithelial cancer progression[56,73]. Here, we demonstrate a favorable impact of SC plasticity on peripheral neuroblastic tumor cells as it manifests in SC stroma during the development of benignly behaving GNB/GN. The cellular similarities between stromal SCs and repair SCs suggest that stromal SCs are able to exert nerve repair-associated functions in the tumor microenvironment. Exploiting the strategies repair/stromal SCs use to generate a neuronal (re-)differentiation supporting environment could therefore hold a valuable therapeutic potential.

The prerequisite for a possible treatment approach is the susceptibility of aggressive NBs to SCs. We and others have previously investigated the effect of SCs and their secreted factors on aggressive NB cell lines. These studies confirmed that SCs are able to induce neuronal differentiation and impair the growth of NB cells, which were derived from SC-stroma poor high-risk NBs[31,32,34–36,74,75]. The confirmation that aggressive NB cells, although lacking the ability to attract SCs, are still responsive to SCs, offers essentially two therapeutic options[23], 1) including SC-derived factors as anti-tumor agents[1,76] and 2) the induction of SC stroma in aggressive NBs. Furthermore, identifying how the repair SC state can be sustained is also of high value for the field of regenerative medicine, since one of the main reasons for axonal regeneration failure after injury is the deterioration of repair SCs over time[46,77]. Thus, the more detailed knowledge about the molecular processes involved in GNB/GN development and nerve regeneration is promising to enrich treatment approaches for both nerve repair and aggressive NBs.

In conclusion, our study demonstrates that the cellular state of stromal SCs in GNs shares key features with repair SCs in injured nerves. This finding provides essential insight into GNB/GN development as it suggests that the inherent plasticity allows adult SCs to react to peripheral neuroblastic tumor cells in a similar way as to injured neurons. As a consequence, stromal SCs could exert repair-associated functions that shape an anti-tumor

microenvironment and induce neuronal differentiation of tumor cells responsible for a benign tumor behavior. Among the factors released by SCs, we identified the matricellular protein EGFL8 and report its neuritogenic effect on neuroblastic tumor cells. EGFL8 mediated neuronal differentiation through broad kinase activation including and beyond p38β/MAPK and ERK signaling, might hold considerable treatment possibilities for the therapy of aggressive NBs and patho-physiological conditions compromising peripheral nerve integrity.

Methods

Human material. The collection and research use of human peripheral nerve tissues and human tumor specimen was conducted according to the guidelines of the Council for International Organizations of Medical Sciences (CIOMS) and World Health Organisation (WHO) and has been approved by the Ethikkommission Medizinische Universität Wien (EK2281/2016 and 1216/2018). Informed consent has been obtained from all patients or parents/guardians/legally authorized representatives participating in this study. The informed consent for obtaining peripheral nerve tissue covers the use of left over materials from medically indicated surgery for research purposes directed towards studying growth inhibition of aggressive neuroblastoma cells by human SC signals. The age-adapted informed consent for the CCRI Biobank covers the use of left over materials from medically necessary surgery or biopsy, which, after completion of routine diagnostic procedures, is biobanked (EK1853/2016) and available for research purposes, including genetic analysis, that are further specified in EK1216/2018: to conduct genetic, proteomic, imaging analysis and cell cultivation.

Neuroblastoma cell lines and primary cultures are available upon request. Primary Schwann cell cultures and tumor tissues are limited materials and therefore cannot be provided.

Human peripheral nerve explants and primary Schwann cell cultures. Human peripheral nerves were collected during reconstructive surgery, amputations or organ donations of male and female patients between 16 and 70 years of age. The ex vivo nerve injury model as well as the isolation procedure and culture conditions of primary human SCs have been performed as previously described[17,38]. Briefly, fascicles were pulled out of nerve explants and digested overnight using 1.25 U/ml Dispase II, 0.125% Collagenase type IV and 3mM calcium chloride. The fascicle-derived cell suspension was seeded on PLL/laminin coated dishes and cultured in SC expansion medium (SCEM: MEMα GlutaMAX™, 1% Pen/Strep, 1 mM sodium pyruvate, 25 mM HEPES, 10 ng/mL hu FGF basic, 10 ng/mL hu Heregulin-β1, 5 ng/mL hu PDGF-AA, 0.5% N2 supplement, 2 μM forskolin and 2% FCS. Cells of the initial seeding represent passage 0 (p0). Half of the medium was changed twice a week. When the cultures reached approx. 80% confluence, contaminating fibroblasts were depleted by exploiting their ability to adhere more rapidly to plastic. Enriched passage 1 (p1) SC cultures of about 96% purity, as determined via positivity for the SC marker S100B, were used for experimentation. For the ex vivo nerve injury model, about 1.5 cm long human nerve fascicles were subjected to an ex vivo degeneration period of 8 days in SCEM + 10% FCS at 37 °C (= injured nerve fascicle). During that time, axons degenerate and SCs adapt the repair phenotype within the explant[17]. Phase contrast microscopy images were generated using a Zeiss Axiovert 40C with the pixelink application version AL/A6XX.

Neuroblastoma/ganglioneuroma tissue, neuroblastoma cell lines and patient-derived short-term cultures. Tumor specimen from diagnostic NB tumors and GN tumors have been collected during surgery or biopsy for diagnostic purposes and left-overs were cryopreserved until analysis. Cryosections of GN tissue were analyzed for SC stroma rich areas identified by H+E-staining, immmuno-fluorescence staining for SC marker S100B, and confirmed by a pathologist. The corresponding tumor region was excised using a scalpel blade and cryopreserved until RNA and protein extraction. The immunostaining analyses of cryosections were performed on three independent specimen per analyzed tissue, e.g. GN cryosections stained from three patients were stained for S100B, SOX10 and DAPI.

The used NB cell lines are derived from biopsies or surgical resection of aggressively behaving NB tumors of patients suffering from high-risk metastatic NBs. In-house established, short-term cultured primary NB cells STA-NB-6, -7 -10 and -15 as well as well-established NB cell lines SK-N-SH, SH-SY5Y, IMR5 and CLB-Ma were cultured in MEMα complete (MEMα GlutaMAX™, 1% Pen/Strep, 1 mM sodium pyruvate, 25 mM HEPES and 10% FCS). The NB cell lines, primary NB cultures and NB tumors differ in their genomic background including *MYCN*-amplification status. An overview of NB cell[78–84], primary NB cultures as well as NB and GN tumor characteristics is provided in Supplementary Tables 1 and 2.

The co-culture model of primary Schwann cells and neuroblastoma cell lines or short-term cultured neuroblastoma cells. NB cell lines or short term NB cultures (STA-NB-6, STA-NB-10, IMR5, SH-SY5Y and CLB-Ma) were co-cultured with enriched human p1 SCs from at least 3 independent donors. First, SCs were seeded in PLL/laminin coated wells of a 6-well plate in SCEM. At day 1 and day 2,

half of the media was exchanged with MEMα complete. At day 3, total media was changed to MEMα complete and NB cells were seeded directly to the p1 SC cultures as well as in PLL/laminin coated trans-wells (24 mm Inserts, 0.4 μm polyester membrane, COSTAR) placed above SC cultures, alongside with respective controls. Two third of the media was changed twice a week and one day prior to FACS analyses on day 8 and day 16.

For IF analysis, SCs from 3 independent donors were co-cultured with STA-NB-6 or CLB-Ma NB cell lines in coated wells of an 8-well chamber slide (Ibidi), respectively, alongside with controls for 11 days.

Proliferation and differentiation FACS panels. All antibody details are listed in Supplementary Table 3. If not stated otherwise, all steps of the staining procedures were performed on ice. The following antibodies have been conjugated to fluorochromes using commercially available kits according to the manufacturer´s instructions: anti-S100B has been conjugated to FITC (FLUKA) using Illustra NAP-5 columns (GE Healthcare), anti-GD2 (ch14:18, kindly provided by Professor Rupert Handgretinger, Department of Hematology/Oncology, Children's University Hospital, Tübingen, Germany) has been conjugated to AF546 using the AlexaFluor® 546 protein labeling kit (Molecular probes) and anti-NF200 has been conjugated to AF647 using the AlexaFluor® 647 protein labeling kit (Molecular probes).

Untreated SC and NB cell cultures, co-cultures or NB cultures stimulated with recombinant neuritogenic factors (Supplementary Table 3) were detached using Accutase (LifeTechnologies) and washed with FACS-buffer (1x PBS containing 0.1% BSA and 0.05% NaAzide). For the differentiation FACS panel, cells were incubated with GD2-AF546 for 20 min, washed once with FACS-buffer and fixed using Cytofix/Cytoperm (BD Biosciences) in the dark for 20 min. After washing with 1x perm/wash (BD), cells were stained with anti-S100B-FITC and NF200-A647 for 20 min. Cells were washed in 1x perm/wash and analyzed immediately at the FACSFortessa flow cytometer equipped with flow cytometer equipped with 5 lasers (355, 405, 488, 561 and 640 nm) and the FACSDiva software version 8.0 (both BD). For the proliferation FACS panel, 1 μM EdU was added to cultures for about 15 h. Cells were detached, washed and fixed in Roti-Histofix 4% for 20 min at RT. Permeabilization and EdU detection was carried out using the Click-iT EdU Alexa Fluor 647 Flow Cytometry Assay Kit (Thermo Fisher Scientific, C10419) according to the manufacturer's manual. Additional extracellular/intracellular staining was performed with GD2-A546 and anti-S100B-FITC antibodies in 1x saponin-based perm/wash for 30 min. After washing, cells were resuspended in 1x saponin-based perm/wash, 1 μl of FxCycle Violet (LifeTechnologies) DNA dye was added and samples were analyzed immediately at the FACSFortessa.

Immunofluorescence staining and confocal image analysis. All antibody details are listed in Supplementary Table 3. If not stated otherwise, the staining procedure was performed on RT and each washing step involved three washes with 1x PBS for 5 min. Primary antibodies against extracellular targets were diluted in 1x PBS containing 1% BSA and 1% serum; primary antibodies against intracellular targets were diluted in 1x PBS containing 1% BSA, 0.1% TritonX-100 and 1% serum. Briefly, thawed tissue cryosections or grown SC/NB cell co-cultures were fixed with Roti-Histofix 4% (ROTH) for 20 min at 4 °C, washed, and blocked with 1x PBS containing 1% BSA and 3% serum for 30 min. Cells and tissue sections were incubated with primary antibodies against extracellular targets, washed and incubated with appropriate secondary antibodies for 1h. Samples were then again fixed with Roti-Histofix 4% for 10 min. After washing, cells were permeabilized and blocked with 1x PBS containing 0.3% TritonX-100 and 3% serum for 10 min. When required, TUNEL staining was performed after permeabilization according to the manufacturer's protocol (PROMEGA). Samples were then incubated with primary antibodies against intracellular targets, washed and incubated with the appropriate secondary antibodies for 1h. Finally, samples were incubated with 2 μg/mL DAPI in 1x PBS for 2 min, washed and embedded in Fluoromount-G mounting medium (SouthernBiotech). Images were acquired with a confocal laser scanning microscope (Leica Microsystems, TCS SP8X) using Leica application suite X version 1.8.1.13759 or or LAS AF Lite version 4.0 software (Leica). Confocal images are shown as maximum projection of total z-stacks and brightness and contrast were adjusted in a homogenous manner using the Leica LAS AF software (Leica Microsystems).

Quantification of neurite length and alignment. The ImageJ plugin NeuronJ[85] was used to quantify the mean length of extended neurites by NB cells either on phase contrast images or immunofluorescence images between treated NB cells (co-culture with SCs, or exposure to EGFL8) and untreated NB cell controls (n = 3); at least two images were analyzed per condition. To evaluate the orientation (alignment) of NB cells after co-culture with SCs compared to NB cell cultured alone (n = 3), three GD2 stained immunofluorescence images per condition were analyzed with the ImageJ plugin OrientationJ *Measure* function [http://bigwww.epfl.ch/demo/orientation/], that calculates a distribution of pixels' orientations (varying from -90 to 90 degrees) per image. In order to merge information of all images per condition, the calculated distributions of orientations were mean-normalized resulting in a mean NB cell orientation of 0 degrees. To obtain a measure distinguishing the NB cell alignment between control and co-cultures, the

variance of the merged distributions was calculated (zero variance would reflect a perfect alignment). For each pair of measurements (control and co-culture), a Levene test[86] was applied to test for equal variances.

RNA isolation, RNA sequencing and gene expression analysis. Fresh frozen SC stroma-rich areas derived from diagnostic GNs (SC-GN, $n = 6$) were homogenized with the gentleMACS Dissociator (Miltenyi) using 1 mL of TRIzol per sample and the predefined RNA-01 gentleMACS program. RNA isolation was performed with the miRNeasy micro kit (Qiagen) following the manufacturer's protocol. Quantity and integrity of extracted RNA were assessed by the Qubit RNA HS Assay Kit (Life Technologies) and the Experion RNA StdSens Assay Kit (BioRad), respectively. 30 ng total RNA (RQI ≥ 8) was used for library preparation following the NEBNext Ultra RNA Library Prep Kit for Illumina protocol (New England BioLabs) with the Poly(A) mRNA Magnetic Isolation Module (New England BioLabs). After cDNA synthesis, the library was completed in an automated way at the EMBL Genomics Core Facility (Heidelberg, Germany). RNA-Seq was performed at the Illumina HiSeq 2000 platform and corresponding Illumnia software (Illumina HiSeq Control software version 2.2.38, RTA version 1.18.61, HiSeq serial number HWI-ST999 and 50 bp-single-end reads were generated); basecalling was done with Illumina bcl2fastq-1.8.4.

The generated data were bioinformatically analyzed together with our previously published transcriptomic data sets of human primary SCs (SC, $n = 5$ samples from 4 donors), human injured fascicle explants (SC-IN, $n = 3$) and NB cells STA-NB-6 (analyzed in three biological replicates), STA-NB-7 and STA-NB-15 (NB-CL, $n = 6$ from 3 donors)[17], SC-rich areas of ganglioneuroma (SC-GN, $n = 6$) and diagnostic, untreated stage 4 NBs (NB-TU, $n = 15$)[87]. Respective GEO identifiers can be found in Supplementary Table 4.

Short read sequencing data was quality checked using FASTQC v0.11.5 (http://www.bioinformatics.babraham.ac.uk/projects/fastqc) and QoRTs v1.1.8[88] and then aligned to the human genome hs37d5 (ftp://ftp.1000genomes.ebi.ac.uk/) using the STAR aligner v2.5.3a[89] yielding a minimum of 11.6 million aligned reads in each sample. Further analysis was performed in R v3.4.1 statistical environment using Bioconductor v3.5 packages[90]. Count statistics for Ensembl (GRCh37.75) genes were obtained by the "featureCounts" function (package "Rsubread") and differential expression analysis was performed by edgeR and voom[91,92]. For differential gene expression analysis only genes passing a cpm (counts per gene per million reads in library) cut-off of 1 in more than two samples were included. All p-values were corrected for multiple testing by the Benjamini-Hochberg method. Genes with an adjusted q-value < 0.05 and a log2 fold change > 1 ($|\log 2FC| > 1$) were referred to as 'significantly regulated' and used for functional annotation analysis via DAVID database[93].

Western Blot analysis. All antibody details are listed in Supplementary Table 3. Western blot analysis was performed as previously described[94,95]. 1x TBS-T was used for all washing steps that were performed three times for 5 min after each antibody incubation. Briefly, frozen cell aliquots were thawed, pelleted and lysed by addition of RIPA buffer. Culture media were centrifuged at 300 g for 10 min at 4 °C to remove cellular debris. The supernatants were mixed with −20 °C EtOH (1:5), precipitated at −20 °C for 20 h, centrifuged at 4000xg for 40 min at 4 °C and the dried pellet was lysed by addition of RIPA buffer. Protein extracts were stored in Protein LoBind tubes (Eppendorf) at −80 °C. Protein concentrations were determined via Bradford assay (BioRad). Protein extracts were mixed with SDS-loading buffer, denatured for 5 min at 95 °C, separated on a 10% SDS/PAA gel and blotted onto methanol-activated Amersham Hybond-P PVDF membranes. Membranes were blocked using 1x T-BST with 5% w/v nonfat dry milk for 30 min and incubated with anti-EGFL8 followed by HRP-conjugated secondary antibody. The blots were developed using the WesternBright Quantum detection kit (Advansta) and visualized with the FluorChemQ imaging system (Alpha Innotech, San Leandro, USA). Subsequently, membranes were incubated with anti-GAPDH followed by IRdye680T labeled secondary antibody. Blots were analyzed using the Odyssey imaging system (Licor) and the Odyssey software v3.0.

Protein isolation, high-resolution mass spectrometry and expression analysis. Fresh frozen diagnostic GN-derived SC stroma-rich areas (SC-GN, $n = 6$), diagnostic high-risk NB tumors (NB-TU, $n = 3$) as well as low-passage NB cells STA-NB-7, STA-NB-2 and STA-NB-10 (NB-CL, $n = 3$) were used for proteomic analysis (see Supplementary Table 1 & 2 for tumor and cell line characteristics). Protein isolation from cells and tissue, mass spectrometry sample preparation and liquid chromatography-mass spectrometry (LC-MS) has been carried out[17,96], all samples were measured in two technical replicates. LC-MS/MS analyses were performed using a Dionex Ultimate 3000 nano LC-system coupled to a QExactive orbitrap mass spectrometer with software TUNE version 2.5-204201/2.5.0.2042 and Chromeleon version 6.0 (all Thermo Fisher Scientific).

For the identification and label free quantification of proteins, the MaxQuant software package (version 1.6.1.0)[97] was used[98]. The human UniProt database (version 03/2018, restricted to reviewed entries only) with 20316 entries was used for the search, and the false discovery rate (FDR) was set to 0.01 on both peptide and protein level. The alignment time window was set to 1 min, with a match time window of 5 min. The four data matrices obtained as described above were loaded

into Perseus software (version 1.6.7.0), followed by filtering those analytes that were present in at least 70% of samples in at least one group[99]. Next, data were log 2 transformed, and missing values were replaced by normally distributed random numbers with a set width of 0.3 and a downshift of 1.8. A two sided t-test was applied for statistical significance testing with number of randomizations set to 250, the FDR threshold was set to 0.05 and the S0 value to 0.1. The data were analysed together with previously generated proteomic data set of human primary SCs and human injured fascicle explants[17].

Phosphoproteomics. EGFL8-treated (100 ng/mL) and untreated cell lines were lysed with 4% SDC buffer containing 100 mM Tris-HCL (pH 8.5) to the cells. The lysate was collected and heat-treated at 95 °C for 5 min. Three biological replicates were performed for each cell line.

For the phosphopeptide enrichment, a slightly modified protocol of the EasyPhos workflow was applied[100]. Briefly, a total of 200 µg protein was used for the enrichment procedure. Protein reduction using 100 mM TCEP and alkylation using 400 mM 2-CAM with subsequent enzymatic digestion with Trypsin/Lys-C mixture (1:100 Enzyme to Substrate ratio) at 37 °C for 18 h was performed. The solution containing the peptides was mixed with enrichment buffer containing 48% TFA (vol/vol) and 8mM Potassium dihydrogen phosphate. Samples were incubated with 3mg TiO2 Titansphere beads (GL Sciences) for 5 min at 40 °C with subsequent washing and elution from StageTips with 40% ACN and 5% Ammonium hydroxide solution. Samples were dried and reconstituted in 15 µL MS loading buffer containing 97.7% H2O, 2% ACN and 0.3% TFA.

For the global proteome, a digestion protocol S-trap technology was employed[101]. In short, proteins were solubilized in buffer containing 5% SDS with subsequent reduction and alkylation using 64 mM DTT and 48 mM IAA, respectively. After addition of trapping buffer (90% vol/vol methanol, 0.1 M triethylammonium bicarbonate) samples were loaded onto S-trap cartridges and digested with Trypsin/Lys-C Mix at 37 °C for 2 h. Supernatants containing the collected peptides were dried. Dried peptide samples were reconstituted in 5 µL 30% formic acid (FA) containing 10 fmol of 4 synthetic standard peptides each and diluted with 40 µL mobile phase A (99.9% H2O, 0.1% FA). LC-MS/MS analyses were performed using a Dionex Ultimate 3000 nano LC-system (Thermo Fisher Scientific) coupled to a timsTOF pro mass spectrometer (Bruker Daltonics). 10 and 5 µL of phosphopeptide enriched and global proteome samples, respectively, were loaded on a 2 cm x 100µm C18 Pepmap100 pre-column (Thermo Fisher Scientific) at a flow rate of 10 µL/min using mobile phase A. Afterwards, peptides were eluted from the pre-column to a 25 cm x 75 µm 25cm Aurora Series emitter column (Ionopticks) at a flow rate of 300 nL/min and separation was achieved using a gradient of 8% to 40% mobile phase B (79.9% acetonitrile, 20% H2O, 0.1% FA) over 90 min.

Data analysis was performed using MaxQuant 1.6.17.0[97] employing the Andromeda search engine was used for protein identification against the UniProt Database (version 12/2019 with 20 380 entries) allowing a mass tolerance of 20ppm for MS spectra and 40ppm for MS/MS spectra, a FDR < 0.01 and a maximum of 2 missed cleavages. Furthermore, search criteria included carbamidomethylation of cysteine as fixed modification and methionine oxidation, N-terminal protein acetylation as well as phosphorylation of serine, threonine and tyrosine as variable modifications. For the interpretation of phosphoproteomics data, a kinase-substrate enrichment analysis of class 1 phosphosites ($p > 0.75$) utilizing PhosphoSitePlus and NetworKIN was performed, applying a NetworKIN score cutoff of 2, p-value cutoff of 0.05 and substrate count cutoff 3[102–104]. For the visualization of enriched kinases in context of the global kinome, the application Coral was used[105].

Statistical analyses. If not mentioned otherwise, Excel 2016 and GraphPad Prism 8 was used for statistical analysis. Values were given as means ± SD of at least 3 independent biological samples or independent biological replicates. For paired analyses a Student's t-test, for parametric analysis of multiple conditions one-way ANOVA and Tukey's multiple comparisons post-hoc test was performed. p-values ≤ 0.05 were considered significant.

Reporting Summary. Further information on research design is available in the Nature Research Reporting Summary linked to this article.

Data availability

All data sets produced and used in this study are available in public repositories as listed in Supplementary Table 4. RNA-sequencing datasets were uploaded to the gene expression omnibus (GEO) repository (https://www.ncbi.nlm.nih.gov/geo/) with the dataset identifiers GSE90711, GSE94035, GSE147635, the Kocak dataset GSE45547 and NRC dataset GSE85047 are publicly available. The mass spectrometry global and phosphospho-proteomics data have been deposited to the ProteomeXchange Consortium (http://proteomecentral.proteomexchange.org) via the PRIDE partner repository[106] with the dataset identifier PXD018267 and PXD022217 and are publicly available. Source data are provided with this paper.

Code availability

No custom codes have been developed in this study.

References

1. Ambros, I. M. et al. Role of ploidy, chromosome 1p, and Schwann cells in the maturation of neuroblastoma. *N. Engl. J. Med* **334**, 1505–1511 (1996).
2. Mirsky, R. et al. Schwann cells as regulators of nerve development. *J. Physiol. Paris* **96**, 17–24 (2002).
3. Furlan, A. & Adameyko, I. Schwann cell precursor: a neural crest cell in disguise? *Dev. Biol.* **444**, S25–s35 (2018). **Suppl 1**.
4. Monk, K. R., Feltri, M. L. & Taveggia, C. New insights on Schwann cell development. *Glia* **63**, 1376–1393 (2015).
5. Nave, K. A. Myelination and the trophic support of long axons. *Nat. Rev. Neurosci.* **11**, 275–283 (2010).
6. Syroid, D. E. et al. Cell death in the Schwann cell lineage and its regulation by neuregulin. *Proc. Natl Acad. Sci. USA* **93**, 9229–9234 (1996).
7. Jessen, K. R., Mirsky, R & Lloyd, A. C. Schwann Cells: Development and Role in Nerve Repair. *Cold Spring Harb. Perspect. Biol.* **7**, a020487 (2015).
8. Jessen, K. R., Mirsky, R. & Arthur-Farraj, P. The Role of Cell Plasticity in Tissue Repair: Adaptive Cellular Reprogramming. *Dev. Cell* **34**, 613–620 (2015).
9. Gomez-Sanchez, J. A. et al. After Nerve Injury, Lineage Tracing Shows That Myelin and Remak Schwann Cells Elongate Extensively and Branch to Form Repair Schwann Cells, Which Shorten Radically on Remyelination. *J. Neurosci.* **37**, 9086–9099 (2017).
10. Jessen, K. R. & Mirsky, R. The repair Schwann cell and its function in regenerating nerves. *J. Physiol.* **594**, 3521–3531 (2016).
11. Toma J. S., et al. Peripheral Nerve Single-Cell Analysis Identifies Mesenchymal Ligands that Promote Axonal Growth. *eNeuro* **7**, (2020).
12. Fontana, X. et al. c-Jun in Schwann cells promotes axonal regeneration and motoneuron survival via paracrine signaling. *J. Cell Biol.* **198**, 127–141 (2012).
13. Arthur-Farraj, P. J. et al. c-Jun reprograms Schwann cells of injured nerves to generate a repair cell essential for regeneration. *Neuron* **75**, 633–647 (2012).
14. Gomez-Sanchez, J. A. et al. Schwann cell autophagy, myelinophagy, initiates myelin clearance from injured nerves. *J. Cell Biol.* **210**, 153–168 (2015).
15. Jang, S. Y. et al. Autophagic myelin destruction by schwann cells during wallerian degeneration and segmental demyelination. *Glia* **64**, 730–742 (2016).
16. Tofaris, G. K., Patterson, P. H., Jessen, K. R. & Mirsky, R. Denervated Schwann cells attract macrophages by secretion of leukemia inhibitory factor (LIF) and monocyte chemoattractant protein-1 in a process regulated by interleukin-6 and LIF. *J. Neurosci.* **22**, 6696–6703 (2002).
17. Weiss, T. et al. Proteomics and transcriptomics of peripheral nerve tissue and cells unravel new aspects of the human Schwann cell repair phenotype. *Glia* **64**, 2133–2153 (2016).
18. Shimada, H. et al. Terminology and morphologic criteria of neuroblastic tumors: recommendations by the International Neuroblastoma Pathology Committee. *Cancer* **86**, 349–363 (1999).
19. Shimada, H. et al. Histopathologic prognostic factors in neuroblastic tumors: definition of subtypes of ganglioneuroblastoma and an age-linked classification of neuroblastomas. *J. Natl Cancer Inst.* **73**, 405–416 (1984).
20. Brodeur, G. M. Neuroblastoma: biological insights into a clinical enigma. *Nat. Rev. Cancer* **3**, 203–216 (2003).
21. Nakagawara, A. Neural crest development and neuroblastoma: the genetic and biological link. *Prog. Brain Res.* **146**, 233–242 (2004).
22. Ambros, P. F. et al. Regression and progression in neuroblastoma. Does genetics predict tumour behaviour? *Eur. J. Cancer* **31A**, 510–515 (1995).
23. Brodeur, G. M. & Bagatell, R. Mechanisms of neuroblastoma regression. *Nat. Rev. Clin. Oncol.* **11**, 704–713 (2014).
24. Okamatsu, C. et al. Clinicopathological characteristics of ganglioneuroma and ganglioneuroblastoma: A report from the CCG and COG. *Pediatr. Blood Cancer* **53**, 563–569 (2009).
25. Zeine, R. et al. Presence of cancer-associated fibroblasts inversely correlates with Schwannian stroma in neuroblastoma tumors. *Mod. Pathol.* **22**, 950–958 (2009).
26. Scheithauer B. W., Woodruff J. M., Erlandson R. A. *Atlas of Tumor Pathology: Tumors of the Peripheral Nervous System*. American Registry of Pathology (1999).
27. Mora, J. et al. Neuroblastic and Schwannian stromal cells of neuroblastoma are derived from a tumoral progenitor cell. *Cancer Res.* **61**, 6892–6898 (2001).
28. Katsetos, C. D. et al. The stromal Schwann cell during maturation of peripheral neuroblastomas. Immunohistochemical observations with antibodies to the neuronal class III beta-tubulin isotype (beta III) and S-100 protein. *Clin. Neuropathol.* **13**, 171–180 (1994).
29. Ambros, I. M., Brunner, C., Abbasi, R., Frech, C. & Ambros, P. F. Ultra-High Density SNParray in Neuroblastoma Molecular Diagnostics. *Front Oncol.* **4**, 202 (2014).
30. Ambros, I. M. et al. Proof of the reactive nature of the Schwann cell in neuroblastoma and its clinical implications. *Prog. Clin. Biol. Res.* **385**, 331–337 (1994).
31. Ambros, I. M. et al. Neuroblastoma cells provoke Schwann cell proliferation in vitro. *Med. Pediatr. Oncol.* **36**, 163–168 (2001).
32. Chlenski, A. et al. SPARC is a key Schwannian-derived inhibitor controlling neuroblastoma tumor angiogenesis. *Cancer Res.* **62**, 7357–7363 (2002).
33. Crawford, S. E. et al. Thrombospondin-1 is a major activator of TGF-beta1 in vivo. *Cell* **93**, 1159–1170 (1998).
34. Huang, D. et al. Schwann cell-conditioned medium inhibits angiogenesis. *Cancer Res.* **60**, 5966–5971 (2000).
35. Kwiatkowski, J. L., Rutkowski, J. L., Yamashiro, D. J., Tennekoon, G. I. & Brodeur, G. M. Schwann cell-conditioned medium promotes neuroblastoma survival and differentiation. *Cancer Res.* **58**, 4602–4606 (1998).
36. Liu, S. et al. Cross-talk between Schwann cells and neuroblasts influences the biology of neuroblastoma xenografts. *Am. J. Pathol.* **166**, 891–900 (2005).
37. Trojanowski, J. Q., Walkenstein, N. & Lee, V. M. Expression of neurofilament subunits in neurons of the central and peripheral nervous system: an immunohistochemical study with monoclonal antibodies. *J. Neurosci.* **6**, 650–660 (1986).
38. Weiss, T., Taschner-Mandl, S., Ambros, P. F. & Ambros, I. M. Detailed Protocols for the Isolation, Culture, Enrichment and Immunostaining of Primary Human Schwann Cells. *Methods Mol. Biol.* **1739**, 67–86 (2018).
39. Lastowska, M. et al. Comprehensive genetic and histopathologic study reveals three types of neuroblastoma tumors. *J. Clin. Oncol.* **19**, 3080–3090 (2001).
40. Molenaar, J. J. et al. Sequencing of neuroblastoma identifies chromothripsis and defects in neuritogenesis genes. *Nature* **483**, 589–593 (2012).
41. Brodeur, G. M. Molecular basis for heterogeneity in human neuroblastomas. *Eur. J. Cancer* **31A**, 505–510 (1995).
42. Bunge, M. B., Williams, A. K. & Wood, P. M. Neuron-Schwann cell interaction in basal lamina formation. *Dev. Biol.* **92**, 449–460 (1982).
43. Quintes, S. et al. Zeb2 is essential for Schwann cell differentiation, myelination and nerve repair. *Nat. Neurosci.* **19**, 1050–1059 (2016).
44. Wu, L. M. et al. Zeb2 recruits HDAC-NuRD to inhibit Notch and controls Schwann cell differentiation and remyelination. *Nat. Neurosci.* **19**, 1060–1072 (2016).
45. Hung, H. A., Sun, G., Keles, S. & Svaren, J. Dynamic regulation of Schwann cell enhancers after peripheral nerve injury. *J. Biol. Chem.* **290**, 6937–6950 (2015).
46. Jessen, K. R. & Mirsky, R. The Success and Failure of the Schwann Cell Response to Nerve Injury. *Front Cell Neurosci.* **13**, 33 (2019).
47. Seurin, D., Lassarre, C., Bienvenu, G. & Babajko, S. Insulin-like growth factor binding protein-6 inhibits neuroblastoma cell proliferation and tumour development. *Eur. J. Cancer* **38**, 2058–2065 (2002).
48. Fox, M. A. et al. Distinct target-derived signals organize formation, maturation, and maintenance of motor nerve terminals. *Cell* **129**, 179–193 (2007).
49. Subhan, F. et al. Epidermal growth factor-like domain 8 inhibits the survival and proliferation of mouse thymocytes. *Int J. Mol. Med* **32**, 952–958 (2013).
50. Clements, M. P. et al. The Wound Microenvironment Reprograms Schwann Cells to Invasive Mesenchymal-like Cells to Drive Peripheral Nerve Regeneration. *Neuron* **96**, 98–114 e117 (2017).
51. Jessen, K. R. & Arthur-Farraj, P. Repair Schwann cell update: Adaptive reprogramming, EMT, and stemness in regenerating nerves. *Glia* **67**, 421–437 (2019).
52. Li, Y. & Nakagawara, A. Apoptotic cell death in neuroblastoma. *Cells* **2**, 432–459 (2013).
53. Cadoni, A., Zicca, A. & Mancardi, G. L. Schwann cell expression of HLA-DR antigen in peripheral neuropathies. *Lancet* **2**, 1281–1282 (1986).
54. Mancardi, G. L. et al. HLA-DR Schwann cell reactivity in peripheral neuropathies of different origins. *Neurology* **38**, 848–851 (1988).
55. Yoshiba, N., Yoshiba, K., Iwaku, M. & Ozawa, H. Immunohistochemical localizations of class II antigens and nerve fibers in human carious teeth: HLA-DR immunoreactivity in Schwann cells. *Arch. Histol. Cytol.* **61**, 343–352 (1998).
56. Meyer Zu Horste, G. et al. Expression of antigen processing and presenting molecules by Schwann cells in inflammatory neuropathies. *Glia* **58**, 80–92 (2010).
57. Baetas-da-Cruz, W. et al. Schwann cells express the macrophage mannose receptor and MHC class II. Do they have a role in antigen presentation? *J. Peripher Nerv. Syst.* **14**, 84–92 (2009).
58. Bergsteinsdottir, K., Kingston, A., Mirsky, R. & Jessen, K. R. Rat Schwann cells produce interleukin-1. *J. Neuroimmunol.* **34**, 15–23 (1991).
59. Hartlehnert, M. et al. Schwann cells promote post-traumatic nerve inflammation and neuropathic pain through MHC class II. *Sci. Rep.* **7**, 12518 (2017).

117

60. Ydens, E. et al. The neuroinflammatory role of Schwann cells in disease. *Neurobiol. Dis.* **55**, 95–103 (2013).
61. Martyn, G. V., Shurin, G. V., Keskinov, A. A., Bunimovich, Y. L. & Shurin, M. R. Schwann cells shape the neuro-immune environs and control cancer progression. *Cancer Immunol. Immunother.* **68**, 1819–1829 (2019).
62. Fitch, M. J., Campagnolo, L. & Kuhnert, F. Stuhlmann H. Egfl7, a novel epidermal growth factor-domain gene expressed in endothelial cells. *Dev. Dyn.* **230**, 316–324 (2004).
63. Schmidt, M. H. et al. Epidermal growth factor-like domain 7 (EGFL7) modulates Notch signalling and affects neural stem cell renewal. *Nat. Cell Biol.* **11**, 873–880 (2009).
64. Chao, M. V. Neurotrophins and their receptors: a convergence point for many signalling pathways. *Nat. Rev. Neurosci.* **4**, 299–309 (2003).
65. Yu, J. H. et al. Restoration of promyelocytic leukemia protein-nuclear bodies in neuroblastoma cells enhances retinoic acid responsiveness. *Cancer Res.* **64**, 928–933 (2004).
66. Shin, E. Y. et al. Phosphorylation of p85 beta PIX, a Rac/Cdc42-specific guanine nucleotide exchange factor, via the Ras/ERK/PAK2 pathway is required for basic fibroblast growth factor-induced neurite outgrowth. *J. Biol. Chem.* **277**, 44417–44430 (2002).
67. Takahashi, K., Yamada, M., Ohata, H., Honda, K. & Yamada, M. Ndrg2 promotes neurite outgrowth of NGF-differentiated PC12 cells. *Neurosci. Lett.* **388**, 157–162 (2005).
68. Alford, A. I. & Hankenson, K. D. Matricellular proteins: Extracellular modulators of bone development, remodeling, and regeneration. *Bone* **38**, 749–757 (2006).
69. Chiodoni, C., Colombo, M. P. & Sangaletti, S. Matricellular proteins: from homeostasis to inflammation, cancer, and metastasis. *Cancer Metastasis Rev.* **29**, 295–307 (2010).
70. Murphy-Ullrich, J. E. & Sage, E. H. Revisiting the matricellular concept. *Matrix Biol.* **37**, 1–14 (2014).
71. Bornstein, P. & Sage, E. H. Matricellular proteins: extracellular modulators of cell function. *Curr. Opin. Cell Biol.* **14**, 608–616 (2002).
72. Chlenski, A. et al. SPARC expression is associated with impaired tumor growth, inhibited angiogenesis and changes in the extracellular matrix. *Int J. Cancer* **118**, 310–316 (2006).
73. Deborde, S. & Wong, R. J. How Schwann cells facilitate cancer progression in nerves. *Cell Mol. Life Sci.* **74**, 4405–4420 (2017).
74. Crawford, S. E. et al. Pigment epithelium-derived factor (PEDF) in neuroblastoma: a multifunctional mediator of Schwann cell antitumor activity. *J. Cell Sci.* **114**, 4421–4428 (2001).
75. Pajtler, K. W. et al. Neuroblastoma in dialog with its stroma: NTRK1 is a regulator of cellular cross-talk with Schwann cells. *Oncotarget* **5**, 11180–11192 (2014).
76. Brodeur, G. M. Schwann cells as antineuroblastoma agents. *N. Engl. J. Med* **334**, 1537–1539 (1996).
77. Höke, A. Mechanisms of Disease: what factors limit the success of peripheral nerve regeneration in humans? *Nat. Clin. Pract. Neurol.* **2**, 448–454 (2006).
78. Combaret, V. et al. Sensitive detection of numerical and structural aberrations of chromosome 1 in neuroblastoma by interphase fluorescence in situ hybridization. Comparison with restriction fragment length polymorphism and conventional cytogenetic analyses. *Int J. Cancer* **61**, 185–191 (1995).
79. Fischer, M. & Berthold, F. Characterization of the gene expression profile of neuroblastoma cell line IMR-5 using serial analysis of gene expression. *Cancer Lett.* **190**, 79–87 (2003).
80. Momoi, M., Kennett, R. H. & Glick, M. C. A membrane glycoprotein from human neuroblastoma cells isolated with the use of a monoclonal antibody. *J. Biol. Chem.* **255**, 11914–11921 (1980).
81. Biedler, J. L., Helson, L. & Spengler, B. A. Morphology and growth, tumorigenicity, and cytogenetics of human neuroblastoma cells in continuous culture. *Cancer Res.* **33**, 2643–2652 (1973).
82. Biedler, J. L., Roffler-Tarlov, S., Schachner, M. & Freedman, L. S. Multiple neurotransmitter synthesis by human neuroblastoma cell lines and clones. *Cancer Res.* **38**, 3751–3757 (1978).
83. Ambros, I. M. et al. Neuroblastoma cells can actively eliminate supernumerary MYCN gene copies by micronucleus formation–sign of tumour cell revertance? *Eur. J. Cancer* **33**, 2043–2049 (1997).
84. Stock, C. et al. Genes proximal and distal to MYCN are highly expressed in human neuroblastoma as visualized by comparative expressed sequence hybridization. *Am. J. Pathol.* **172**, 203–214 (2008).
85. Meijering, E. et al. Design and validation of a tool for neurite tracing and analysis in fluorescence microscopy images. *Cytom. A* **58**, 167–176 (2004).
86. Olkin I. Contributions to Probability and Statistics: Essays in Honor of Harold Hotelling. Stanford University Press (1960).
87. Rifatbegovic, F. et al. Neuroblastoma cells undergo transcriptomic alterations upon dissemination into the bone marrow and subsequent tumor progression. *Int J. Cancer* **142**, 297–307 (2018).
88. Hartley, S. W. & Mullikin, J. C. QoRTs: a comprehensive toolset for quality control and data processing of RNA-Seq experiments. *BMC Bioinforma.* **16**, 224 (2015).
89. Dobin, A. et al. STAR: ultrafast universal RNA-seq aligner. *Bioinformatics* **29**, 15–21 (2013).
90. Gentleman, R. C. et al. Bioconductor: open software development for computational biology and bioinformatics. *Genome Biol.* **5**, R80 (2004).
91. Law, C. W., Chen, Y., Shi, W. & Smyth, G. K. voom: Precision weights unlock linear model analysis tools for RNA-seq read counts. *Genome Biol.* **15**, R29 (2014).
92. Ritchie, M. E. et al. limma powers differential expression analyses for RNA-sequencing and microarray studies. *Nucleic Acids Res.* **43**, e47 (2015).
93. Huang da, W., Sherman, B. T. & Lempicki, R. A. Systematic and integrative analysis of large gene lists using DAVID bioinformatics resources. *Nat. Protoc.* **4**, 44–57 (2009).
94. Bogen, D. et al. The genetic tumor background is an important determinant for heterogeneous MYCN-amplified neuroblastoma. *Int J. Cancer* **139**, 153–163 (2016).
95. Taschner-Mandl, S. et al. Metronomic topotecan impedes tumor growth of MYCN-amplified neuroblastoma cells in vitro and in vivo by therapy induced senescence. *Oncotarget* **7**, 3571–3586 (2016).
96. Groessl, M. et al. Proteome profiling of breast cancer biopsies reveals a wound healing signature of cancer-associated fibroblasts. *J. Proteome Res.* **13**, 4773–4782 (2014).
97. Cox, J. & Mann, M. MaxQuant enables high peptide identification rates, individualized p.p.b.-range mass accuracies and proteome-wide protein quantification. *Nat. Biotechnol.* **26**, 1367–1372 (2008).
98. Neuditschko, B. et al. The Challenge of Classifying Metastatic Cell Properties by Molecular Profiling Exemplified with Cutaneous Melanoma Cells and Their Cerebral Metastasis from Patient Derived Mouse Xenografts. *Mol. Cell Proteom.* **19**, 478–489 (2020).
99. Tyanova, S. et al. The Perseus computational platform for comprehensive analysis of (prote)omics data. *Nat. Methods* **13**, 731–740 (2016).
100. Humphrey, S. J., Karayel, O., James, D. E. & Mann, M. High-throughput and high-sensitivity phosphoproteomics with the EasyPhos platform. *Nat. Protoc.* **13**, 1897–1916 (2018).
101. HaileMariam, M. et al. S-Trap, an Ultrafast Sample-Preparation Approach for Shotgun Proteomics. *J. Proteome Res.* **17**, 2917–2924 (2018).
102. Casado, P. et al. Kinase-substrate enrichment analysis provides insights into the heterogeneity of signaling pathway activation in leukemia cells. *Sci. Signal* **6**, rs6 (2013).
103. Hornbeck, P. V., Zhang, B., Murray, B., Kornhauser, J. M. & Latham, V. Skrzypek E. PhosphoSitePlus, 2014: mutations, PTMs and recalibrations. *Nucleic Acids Res.* **43**, D512–D520 (2015).
104. Horn, H. et al. KinomeXplorer: an integrated platform for kinome biology studies. *Nat. Methods* **11**, 603–604 (2014).
105. Metz, K. S. et al. Coral: Clear and Customizable Visualization of Human Kinome Data. *Cell Syst.* **7**, 347–350.e341 (2018).
106. Vizcaíno, J. A. et al. ProteomeXchange provides globally coordinated proteomics data submission and dissemination. *Nat. Biotechnol.* **32**, 223–226 (2014).

Author contributions

T.W. and S.T.-M. planned experiments, performed research, analyzed and interpreted data and wrote the manuscript; H.S., A.B., L.J. and F.R. performed research and analyzed data; F.K. analyzed data; C.F. and M.K. developed bioinformatics tools and analyzed data; C.G. analyzed and interpreted data; R.W. provided essential material; P.F.A., I.M.A., and S.T.-M. conceptualized the project; P.F.A. and I.M.A interpreted data; all authors reviewed the manuscript.

Competing interests

The authors declare no conflict of interest.

4.5 Multi-omics empowered deep phenotyping of ulcerative colitis

Lukas Janker[1], Dina Schuster[1], Patricia Bortel[1], Gerhard Hagn[1], Julia Brunmair[1], Samuel Meier-Menches[1, 2], Johanna C. Mader[1], Astrid Slany[1], Andrea Bileck[2], Christian Madl[3], Lukas Unger[4], Barbara Hennlich[3], Barbara Weitmayr[5], Giorgia Del Favero[6], Dietmar Pils[7], Tobias Pukrop[8], Nikolaus Pfisterer[3], Thomas Feichtenschlager[3], Christopher Gerner[1, 2]

1   Department of Analytical Chemistry, University of Vienna, Vienna, Austria

2   Joint Metabolome Facility, University of Vienna & Medical University of Vienna, Vienna, Austria

3   Krankenanstalt Rudolfstiftung, 4. Interne Abteilung, Vienna, Austria

4   Division of General Surgery, Department of Surgery, Medical University of Vienna, Vienna, Austria

5   Institut für Pathologie und Mikrobiologie, Klinik Landstraße, Vienna, Austria

6   Core Facility Multimodal Imaging, Faculty of Chemistry University of Vienna, Vienna, Austria

7   Joint Metabolome Facility, University of Vienna & Medical University of Vienna, Vienna, Austria

8   Joint Metabolome Facility, University of Vienna & Medical University of Vienna, Vienna, Austria

Contributions to this publication:

- Planning of research and writing of application for ethical approval
- Performing research and MS measurements
- Analysis and interpretation of data
- Preparation of figures and writing of manuscript

Multi-omics empowered deep phenotyping of ulcerative colitis

Lukas Janker[1], Dina Schuster[1], Patricia Bortel[1], Gerhard Hagn[1], Julia Brunmair[1], Samuel M. Meier-Menches[1, 2], Johanna C. Mader[1], Astrid Slany[1], Andrea Bileck[1,2], Christian Madl[3], Lukas Unger[4], Barbara Hennlich[3], Barbara Weitmayr[3], Giorgia Del Favero[5], Dietmar Pils[6], Tobias Pukrop[7], Nikolaus Pfisterer[3], Thomas Feichtenschlager[3], Christopher Gerner[1, 2]*

[1] Department of Analytical Chemistry, Faculty of Chemistry, University of Vienna, Waehringer Straße 38, 1090 Vienna, Austria

[2] Joint Metabolome Facility, University and Medical University of Vienna, Waehringer Straße 38, 1090 Vienna, Austria

[3] Institute of Pathology and Microbiology, Krankenanstalt Rudolfstiftung, Vienna, Austria.

[4] Division of General Surgery, Department of Surgery, Medical University of Vienna, Währinger Gürtel 18-20, Vienna, Austria

[5] Core Facility Multimodal Imaging, Faculty of Chemistry University of Vienna, Waehringer Straße 38, 1090 Vienna, Austria

[6] Department of Obstetrics and Gynaecology, Medical University of Vienna, Spitalgasse 23, 1090 Vienna, Austria

[7] Department of Internal Medicine III, Hematology and Oncology, University Hospital Regensburg, Regensburg, Germany

* Correspondence: christopher.gerner@univie.ac.at

123

Abstract

Objective: Ulcerative colitis (UC) is a chronic disease with rising incidence and unclear etiology. The application of mass spectrometry-based analysis methods shall support the establishment of systemic molecular biomarker signatures providing status information with regard to individual UC pathomechanisms.

Design: UC pathomechanisms were assessed by proteome profiling of human tissue specimen, obtained from five distinct colon locations each of 12 patients. Systemic disease-associated alterations were investigated in a cross-sectional setting by mass spectrometry-based multi-omics analyses comprising proteins, metabolites and eicosanoids of plasma obtained from UC patients during disease and upon remission in comparison to healthy controls.

Results: Tissue proteome profiling identified colitis-associated activation of neutrophils, macrophages, B- and T-cells, fibroblasts, endothelial cells and platelets, and indicated hypoxic stress, as well as a general downregulation of mitochondrial proteins accompanying the establishment of apparent wound healing-promoting activities including scar formation. While the immune cells mainly contributed pro-inflammatory proteins, the colitis-associated epithelial cells, fibroblasts, endothelial cells and platelets predominantly formed anti-inflammatory and wound healing-promoting proteins. Blood plasma proteomics indicated chronic inflammation and platelet activation, whereas plasma metabolomics identified disease-associated deregulation of bile acids, eicosanoids and gut microbiome-derived metabolites. Upon remission, several, but not all, molecular candidate biomarker levels recovered to normal levels. These findings may indicate that pathomechanisms related to gut functions, gut microbiome status, microvascular damage and metabolic dysregulation associated with hypoxia may not resolve uniformly during remission.

Conclusions: This study integrates and expands the knowledge about local and systemic effects of UC and identifies biomarker profiles related to molecular UC pathomechanisms.

Introduction

Ulcerative colitis (UC), an inflammatory bowel disease (IBD), is characterized by ascending inflammation of the large intestine with intermittent cycles of active inflammation and asymptomatic periods.[1] With an early disease onset at around 30 years of age and increasing incidence rates in developed countries (24.3/100,000 in Europe; 19.2/100,000 in North America), UC is becoming an increasing and severe health risk for millions of people.[2, 3] Due to the chronic inflammation, UC patients suffer from an increased risk of colorectal cancer as well as thromboembolic complications.[4-6] The chronicity of UC accompanied with life-long non-curative treatment of symptoms is challenging, as patients are treated based on symptom subsets and their severity in an iterative scheme[1, 7-10], which has not fundamentally changed for the past two decades.[5, 11, 12] Often used metrics including the Ulcerative Colitis Disease Activity Index (UCDAI) and MAYO-score are reliant on multiple clinical observations, invasive and non-invasive in nature, as well as on the compliance of patients subjective measures in form of patient-reported outcomes, so called PRO reports.[13, 14] A vast effort was put into the elucidation of disease driving genetic factors including genome-wide association studies, but to the best of our knowledge, no definitive causal links could be established yet.[15] MHC locus HLA Class II alleles as well as the multidrug resistance gene *MDR1* have been implicated as possible genetic susceptibility factors.[16-18] Studies focusing on the genetic landscape of the second main type of IBD, namely Crohn's Disease (CD), found, in contrast to UC, evidence of causal effects of single nucleotide polymorphisms with biological plausibility and dose-response effects independently verified by multiple studies.[19-22] The abovementioned points strengthen the theory of involvement of environmental factors and other possible post-genomic related influence factors such as the general composition and functional state of the proteome, metabolome and microbiome. Even for malignant diseases where genetic instability determines disease progression, post-genomic analysis tools can provide deeper insights into molecular mechanisms of progression and escalation.[23] Recent studies[24, 25] provide insights into potential pathophysiologic mechanisms of UC, showing for example the influence of the microbiome and its compositional alterations before and after diagnosis with UC[26], the activation of the innate immune system monitored on a proteome wide scale[27], or general compositional changes in the metabolome[28, 29] or microbiome dependent co-metabolome.[30, 31] Although these findings are leading UC related research into a more molecularly focused direction, there are still pathophysiological processes, which remain to be unveiled. Studies focusing on *post hoc* analysis of serological markers for the discrimination of clinically relevant cohorts showed the limitations of established marker molecules, and demonstrated the need for comprehensive screening and combination of data on multiple "omics" levels.[32, 33] In the presented study, we thus aimed to investigate pathophysiological aberrations *in situ*. We present an in-depth analysis of intra-individual colonic proteome alterations during active UC in a spatially resolved manner. The parallel analysis of plasma samples, allowing to identify systemic disease-associated alterations, was performed by the combination of an extensive panel of biomolecules ranging from amino acids to lipids, including eicosanoids and plasma proteins. An additional case-control study with UC patients in remission was performed in order to investigate remission-associated normalization of biomarker profiles. Thus, we demonstrate that specific colitis-associated

biomarkers were still deregulated at a time when no more symptoms were reported and those indicate possible determinants for chronicity. The present multi-omics analyses provide a deep molecular phenotyping of UC disease manifestation, pointing at novel therapeutic targets and presenting biomarker candidates that may be validated in prospective clinical trials.

Material and Methods

A more detailed description of the methodology can be found in the Supplementary Materials and Methods.

Study design and population

The presented case-control study includes patients from the age of 18 and above diagnosed with ulcerative colitis (UC), either in active or remission state, as well as healthy control patients, as described in Figure 1A. Patient information regarding clinical data from active and remission patients, as well as age distribution in regard to healthy controls can be found in Supplementary Tables S1, S2 and Suppl. Figure S1. Exclusion criteria for active UC patients included pancolitis, remission status according to MAYO-Score, infections, colon resection or colectomy as well as colitis indeterminata. Exclusion criteria for remission UC patients included infections, colitis indeterminata as well as colon resection or colectomy. Patients with active UC underwent a routine colonoscopy for the assessment of the local inflammatory status including fecal calprotectin and assignment of MAYO-Score.[13] Colon biopsies were classified into three categories ranging from non-inflamed over surrounding/mildly inflamed to inflamed. Classification was based on histological findings of inflammatory features (Supplementary Figure S2. For the monitoring of systemic events happening during the pathogenesis of UC, blood plasma was collected from each patient cohort. The study was approved by the ethics commission of the city of Vienna with votum EK 18-193-0918. All patients gave informed consent.

Sample collection and processing

Colon biopsies of colonic subsections from active UC patients were taken, washed with PBS and immediately frozen at -80°C or processed for subsequent histologic examination. Blood was drawn from all three cohorts, processed into blood plasma and frozen following a strict time regimen. A detailed description of the methodology can be found in the Supplementary Materials and Methods.

Statistical data analysis

Proteomics data was analyzed with MaxQuant (version 1.6.17.0).[34] Eicosanoid spectra were compared with reference spectra from the Lipid Maps depository library and subsequently integrated using the TraceFinderTM software package (version 4.1).[35] Targeted metabolomics data validation and evaluation was performed with the software supplied with the MxP® Quant 500 Kit (MetIDQ-Oxygen-DB110-3005). For the analysis of causal networks between inflamed and non-inflamed tissue, the software CausalPath with standard parameter settings and pre-processed LFQ intensity values (Supplementary Table S3) was utilized.[36] Additional statistical analysis was performed utilizing Perseus (version 1.6.14.0), Microsoft Excel and GraphPad Prism (version 6.07).

127

Omics data were integrated in R using N-integration discriminant analysis with DIABLO (Data Integration Analysis for Biomarker discovery, R-package mixOmics 6.18.0,[37]) and an own developed method using Gaussian Graphs Models Selection (R-package GGMselect 0.1-12.4, CIT2) for analytes reduction via sub-network generation and Principal Component representation. Subsequently partial correlations of significantly deregulated single analytes with analyte sub-network representations were performed.[38]

Results

Rationale and presentation of the study design.

After informed consent, five colon biopsy samples from different locations were obtained from each of the 12 patients suffering from active ulcerative colitis (clinical parameters are provided in Supplementary data). The tissue samples were categorized via histological findings into "inflamed", "surrounding" and "non-inflamed" (Figure 1A, Suppl. Figure S1). Blood plasma was collected from a total of 16 acute UC patients, including the 12 patients that underwent biopsy, as well as other 12 UC patients after successful remission (clinical parameters are provided in Supplementary data and Supplementary Tables S7, S8). Blood plasma from 11 healthy donors served as controls. Each plasma sample was analyzed with regard to proteins, metabolites and eicosanoids using three different mass spectrometry-based analysis methods (Figure 1A). Tissue proteome analysis was conducted to provide insight into disease-associated pathomechanisms, and plasma samples from the same patients were analyzed to investigate whether local changes were indicated by systemic plasma profiles (Figure 1B).

Tissue proteomics reveals molecular patterns associated with local UC pathomechanisms.

The analysis of a total of 60 tissue biopsy samples resulted in the identification of 4,579 proteins (at least two peptides per protein, FDR < 0.01 at protein and peptide level, at least 5 independent identifications in at least one tissue category per protein, Supplementary Table S3) and various protein regulatory events distinguishing the three pre-defined tissue categories (Figure 2A, Supplementary Table S4). PCA separated "inflamed" versus "non-inflamed", while the surrounding tissue samples were found dispersed across the other two groups (Figure 2B). It is fair to expect alterations of the cell type composition when comparing such tissue categories. Thus, differentially regulated proteins (FDR < 0.01) were attributed in a first step to different cell types according to expression specificity. In a subsequent step, functional cell activation markers were considered as described previously,[39-41] in addition to protein regulatory events pointing to characteristic pathomechanisms (Figure 2C, Supplementary data, Supplementary Table S5).

The inflammation-associated upregulation of VIM accompanied by a downregulation of KRT18 (Figure 2A, Supplementary Table S1) indicated a relative increase of mesenchymal cells at the cost of parenchymal cells. This interpretation was corroborated by a dominance of neutrophil-, macrophage- and fibroblast-specific proteins among the most strongly upregulated proteins in inflamed tissue (Figure 2A, C). Several epithelial proteins known to be induced upon inflammation such as REG4, PLA2G2A and GREM1 were found upregulated. In contrast, epithelial proteins characteristic for colon functions such as mucus formation were downregulated, including CLCA1, SLC4A4 and CEACAM7, suggesting a profound functional state switch of these cells. Actually, mitochondrial proteins were found to be the protein group most consistently downregulated, which is compatible with this notion (Figure 2A, C).

129

Characteristic marker proteins (Figure 2C, Supplementary Table S2, Supplementary data – tissue marker proteins) strongly indicated the inflammatory activation of neutrophils (LTF, ELANE and PRTN3), macrophages (LYZ, IFI16), B lymphocytes (CD40, CD79A, BTK) and T lymphocytes (LSP1, PTPRC and FGL2). This inflammatory signature was further corroborated by a marked interferon response (MX1, GBP2, ISG20) and apparent local complement activation (C2, C3, CFI). However, platelet activation, potentially promoted by FBLN1 and CD40 and evidenced by PECAM1, PDGFRA and PDGFRB, indicated an onset of wound healing activities already during acute UC. This interpretation was supported by an increased abundance of several TGF-beta induced proteins derived from macrophages (e.g. TNC, AIF1), fibroblasts (COL4A2, FBLN5, PXDN) and epithelial cells (e.g. SERPINB5, GREM1, MUC12) in addition to markers for mucosal healing (e.g. MFGE8, MGAT1, TIGAR) and other anti-inflammatory proteins such as SERPINB8, IL1RN and APCS. Furthermore, a proteome signature pointing to hypoxia (CSRP2, AQP1, LIMS1) may be causally related to angiogenesis, indicated by EFEMP1, ANGPTL2, VCAM1, and scar formation, indicated by MXRA5, COL1A1 and FN1 (Figure 2C). The downregulation of enzymes essential for beta-oxidation such as ACOX1, ACSF2 and ECI2 may also indicate a functional state switch of tissue functions potentially resulting in a loss of energy-demanding detoxification capabilities mediated by UGT1A8, UGT2A3, SLC6A2 and others.

Investigation of the tissue proteomics data using causal path analysis (Materials and Methods) indicated a hub function of the metabolic key transcription factor MAX (Figure 2D), which has also been linked to a hypoxia-induced metabolic switch promoting glycolysis above beta-oxidation.[42]

UC pathomechanisms also affect systemic molecular plasma profiles.

Proteins, eicosanoids and metabolites were analyzed in plasma samples derived from healthy controls, patients suffering from acute colitis, as well as UC patients in remission using three different LC/MS-based analysis strategies comprising 293, 72 and 494 distinct molecules (Figure 3A, Supplementary Tables S6, S7, S8), respectively. Unsupervised PCA of identified proteins separated the remission group from the healthy group, whereas the PCA of metabolomics and eicosanoid analyses separated active disease patients from healthy controls (Figure 3B). Each kind of analysis delivered significant regulatory events as displayed in volcano plots (Figure 3C) and listed in Supplementary Tables S4-S6. The application of analytes-set analyses and Data Integration Analysis, as described in Materials and Methods, further improved the separation capabilities and suggested molecular profiles associated with the clinical phenotype (Figure 4A, B). Further unsupervised hierarchical clustering of blood-borne molecules listed several biomarker candidates and separated the patient groups quite well, with some intersection between the active colitis and the remission group (Figure 4B). Figure 4C shows a molecular network of correlated regulated analytes and sub-networks generated from an integrative analyses approach comparing patients in remission with healthy controls.

In an independent approach for data interpretation, molecules deregulated in plasma of UC patients were screened manually searching for potential biomarkers related to

pathomechanisms evidenced by tissue proteomics. Molecules were discriminated based on significant alterations within one or two, out of two, group comparisons (active UC versus control and remission versus control, Figure 3A). Proteome profiling identified the liver-derived acute phase proteins CRP and SAA1 indicative for acute inflammation (Figure 3C). The proteins ITGA2B, FBLN1 and VCL are strongly expressed by platelets and indicate platelet involvement in UC.[43] The detected upregulation of PTGDS, catalyzing the formation of the platelet aggregation inhibiting the eicosanoid PGD_2[44] and described to be upregulated upon injury,[45] may represent a systemic response to onset of wound healing and thromboembolism – a characteristic risk for UC patients.

Eicosanoid analyses showed that the neutrophil-derived inflammation marker PGE_2 and 5S-HETE were consistently detected but not found to be differentially regulated. The prostaglandin PGD_2, described to be involved in the protection of the gut mucosa and promoting regeneration, was actually found downregulated.[46] In contrast, the mainly platelet-derived lipoxygenase product 12S-HETE, the lipid peroxidation marker 11-HETE [47] as well as the anti-inflammatory molecules 11-HEPE, 12-HEPE and 14-HDoHE were found significantly upregulated (Figure 3C). The latter molecules were previously described to be associated with a neutrophil's eicosanoid class switch characteristic for N2.[48] Thus, rather anti-inflammatory contributions from platelets and neutrophils apparently dominated the UC-associated plasma eicosanoid profile.

Notably, metabolomics analyses detected the downregulation of several amino acids including ornithine. This observation may indicate reduced amino acid uptake via the gut epithelial cells in colitis patients. Increased levels of propionylcarnitine, potentially accumulating upon mitochondrial dysfunction, and a loss of aconitic acid, an essential citric acid cycle component, may relate to mitochondrial stress consistent with the notion of a mitochondrial loss (Figure 2A). Increased plasma cystine levels may relate to oxidative stress,[49] a characteristic consequence of mitochondrial stress. The broad downregulation of the primary bile acid glycocholic acid and the secondary bile acids deoxycholic acid, glycodeoxycholic acid and glycolithocholic acid may indicate a loss of lipid synthesis or reduced lipid uptake. Various metabolites formed with the contribution of the gut microbiome such as p-cresol sulfate, hippuric acid, 3-indol propionic acid and indoxyl sulfate were found significantly decreased, indicating a loss of gut microbiome activities. Sarcosine, which has been described as oncometabolite due to its implications with hypoxia and mitochondrial stress,[50] was found upregulated in patients with remission as well as in patients with active disease.

Several metabolic alterations may be directly related to altered levels of associated enzymes detected by tissue proteomics. Along with many other mitochondrial proteins, ACO2 was found downregulated in inflamed tissue regions, as well as cytoplasmic ACO1. This may relate to the systemic downregulation of aconitic acid mentioned above. CYP27A1, another mitochondrial enzyme presently found downregulated in inflamed tissue, catalyzes the first biosynthetic step of bile acid synthesis, and may thus relate to the above-described downregulation of bile acids. LPCAT1, an enzyme found significantly upregulated in

inflamed tissue samples, was described to be upregulated upon gut microbiome dysregulation.[51] The main substrates consumed by LPCAT1, lysophosphatidylcholines (n=14 distinct molecules) were found significantly downregulated in the plasma of colitis patients. This may promote the formation of platelet activating factors (PAFs) as described by us previously[52] resulting in calcium mobilization reinforcing chronic inflammation.

Recovery pattern of UC biomarkers upon remission indicates unresolved disease processes.

Remission from acute UC was assessed with clinical parameters such as calprotectin and CRP levels in addition to several other clinical parameters (Supplementary data – UC remission patient cohort) and subjective reports regarding relief of symptoms. Only patients showing full remission were included. Remarkably, through comparison of control, remission and active UC plasma samples, we identified some candidate biomarkers not recovering back to healthy control levels, suggesting that some UC pathomechanisms may prevail after clinical remission (Figure 4D). On the one hand, the levels of bile acids CA, DCA, DCDA and IndSO$_4$ and the gut microbiome-derived metabolites 3IPA and 3IAA were found close to normal values during remission, potentially indicating efficient recovery of gut functions such as lipid extraction and gut microbiome metabolism (Figure 4D, marked red). In contrast, sarcosine, the inflammation-associated molecules SAA1, 11S-HETE and the platelet-associated proteins ITGA2B and ENO1 hardly returned to normal levels, potentially indicating difficulties for the re-establishment of a normal homeostasis (Figure 4D, marked green). Indeed, several molecules involved in chronic inflammation (e.g. SAA4 and PGE2) and other pathomechanisms such as deregulated lipid uptake or hypoxia (e.g. GUDCA and hypoxanthine) were found even more deregulated upon remission when compared to the active disease states (Figure 4D, marked blue).

Discussion

This study realized deep molecular phenotyping of UC pathomechanisms focusing on tissue proteomics and multi-omics blood plasma analyses. Tissue proteomics not only confirmed many known characteristics of UC such as neutrophil invasion and neutrophil extracellular trap as well as scar formation, but also painted a comprehensive picture of acute and chronic events.

As expected, many pro-inflammatory factors were released by tissue-resident immune cells including neutrophils, macrophages, B-cells and T-cells (Figure 2, Supplementary data). However, during inflammation, the resulting formation of oxidized lipids, together with TGF-beta and the administration of antiphlogistic drugs may initiate a functional switch of neutrophils and macrophages to a regenerative phenotype designated as N2 and M2, as characterized previously.[48, 53] Several molecules characteristic for M2 such as TNC and AIF1 were found strongly upregulated in the acutely inflamed tissue samples, indicating the presence of polarized macrophages. Remarkably, no inflammation-associated molecules derived from fibroblasts were found upregulated in the inflamed tissue samples, whereas many TGF-beta induced proteins were found upregulated, pointing to a predominance of wound-healing activities of fibroblasts. A similar observation was made regarding epithelial cells. Several TGF-beta induced proteins such as SERPINB5 and SERPINB8, as well as proteins associated with mucosal healing such as MFGE8, MGAT1 and TIGAR (Figure 2, Supplementary data) were found upregulated in inflamed tissue samples. Furthermore, the apparent involvement of platelets also points to wound-healing activities. Thus, the present data suggested regenerative processes mainly contributed by endothelial cells, fibroblasts, platelets and epithelial cells to occur during active inflammation. This temporal coincidence represents a hallmark of chronic inflammation, suggesting that unresolved regulatory signaling mechanisms may prevail.[54] The observed tissue regeneration efforts seem to remain somewhat unsuccessful, as the clinical phenotype shows delayed recovery and a high risk for inflammation-relapse. This raises the question, which molecular mechanisms might account for this. The following model may provide an explanation.

Recent evidence suggests that a lack of vagal nerve activities,[55] a corresponding chronic shortage of blood supply of the guts and apparent microbiome dysregulations may contribute to ulcerative colitis initiation.[56] Therefore, a lack of energy-demanding mucus formation in addition to mucus degradation by pathogenic microorganisms could account for increased exposure of epithelial cells to bacterial endotoxins, eventually triggering immune cell invasion. Exaggerated neutrophil activities may cause tissue damage,[57] most notably microvascular damage further promoting a lack of oxygen supply. Epithelial cells will suffer from both, neutrophil-induced tissue destruction and a lack of oxygen required for high energy demanding activities such as mucus synthesis, transcellular transport and detoxification. Apparently, a strong angiogenic and wound-healing response is accompanying these events, potentially orchestrated by platelets activated at the surface of microvascular damage sites. Platelets are a highly plausible source for TGF-beta, apparently accounting for a large number of specific protein regulatory events currently observed in inflamed tissue

samples.[58] Several mechanisms may feed into a potential vicious cycle (Figure 4E). It is reasonable to speculate that scar formation during early provisional tissue regeneration is accompanied by a decrease in mucus formation as fibroblasts are unable to secrete mucus. More neutrophil-induced tissue damage may thus promote more scar tissue and thus less mucus formation, less detoxification capability and more vulnerability to endotoxins. Hypoxia, promoted by a lack of vagal nerve activities in addition to damaged microvessels, may further attract neutrophils,[59] promoting an exaggerated response. An eventual functional switch to N2 may shut down 5-LOX, thus no longer promoting highly desirable phagocytotic activities of macrophages. Hypoxia may also cause mitophagy and attenuate energy-demanding processes. Continuous anti-inflammatory treatment as typically applied for UC patients may also affect stromal cells and thus interfere with regenerative mechanisms in a not yet fully understood fashion.[60]

The presently described biomarker candidates may serve as proxies for functional aberrations and thus indicate unresolved pathomechanisms in patients after remission. Successful treatment seems to recover major primary gut functions, as suggested by the corresponding biomarker levels in patients after remission. The apparent normalization of the acute inflammation marker CRP and the eicosanoid 11-HEPE supports this interpretation (Figure 4D). However, the chronic inflammation marker SAA1, the platelet activation markers ITGA2B and ENO1 and the radical stress marker 11S-HETE remain deregulated. Sarcosine, also belonging to this group, may relate to a still attenuated mitochondrial metabolism.

It seems to us that a prevalence of innate immune system-derived pathogen defense mechanisms above tissue regeneration may generally promote chronic diseases. Similar observations were reported by us with regard to chemical hepatocarcinogenesis promoted by inadequately activated Kupffer cells,[61] and a lack of cartilage regeneration due to apparent pathogen defense activities of neutrophils.[62]

In summary, the application of a multi-omics analysis strategy allowed us to relate systemic blood-borne proteins, metabolites and lipids to local UC pathomechanisms with potential synergistic prognostic power. Prospective clinical studies are needed to test whether the present biomarker candidates will be able to fulfill our expectation regarding prognostic power supporting a more individualized colitis treatment strategy.

Legend to Figures

Figure 1: Study design supporting the discovery of functional biomarker. **(A)** Patient cohort and general sampling strategy. Patients with active UC (top, n=12 for complete tissue and plasma series, n=4 only plasma available) providing tissue (n=5 per patient) and plasma samples. Blood plasma samples from UC patients in remission (n=12), as well as healthy controls (n=11) were collected. Based on histological classification, tissue samples were categorized into non-inflamed (n=24), surrounding (n=20) and inflamed (n=16) tissue. **(B)** Schematic overview regarding pathophysiological processes taking place in different compartments. Blood microvessels supply the mesenchymal interstitium separated from the mucus-forming parenchyme via a basal membrane. Disease progression (left to right) associated with microvascular damage, invasion of immune cells, breakdown of the basal membrane, loss of epithelial cells and increased access of inflammation-inducing bacteria are depicted, together with the presently applied complementary analysis strategies.

Figure 2: Tissue proteomics identifies pathomechanisms characteristic for UC. (A) Volcano plots illustrating comparisons of differentially abundant proteins in tissue samples according to histological graded categories. Proteins highlighted correspond to neutrophil granulocytes/macrophages (red), epithelial/fibroblast cells (blue) and mitochondria (green). VIM and KRT18 are highlighted as orange triangle or square, respectively. Axis were scaled according to extend of regulation, with anchor points as dotted lines at -log p-value of 1.5 (horizontal) and log2 fold change of -2 and 2 (vertical). **(B)** Principal component analysis of tissue proteomics dataset, each point representing a single colon biopsy. PC1 is plotted against PC3, allowing a complete separation of non-inflamed sections from inflamed sections (dotted line), with surrounding sections in between. **(C)** Heatmap of selected proteins of interest involved in pathophysiological processes. Color coding of gene names with red and green relates to pro-inflammatory (PI) and anti-inflammatory (AI) properties of the given protein, respectively. LFQ intensity values were z-score normalized and averaged for inflammation related grouping. **(D)** Causal-path analysis results of comparison from inflamed vs. non-inflamed tissue. Protein modules, colored from blue (lower expression) to red (higher expression), linked via direct positive (green) or negative (red) connectors form nodes of uniformly regulated proteins which are combined in hubs. For the calculation of significant causal connected regulation events, standard parameters were employed.

Figure 3: Multi-omics analysis of blood plasma. **(A)** Pie charts indicating significant regulations of proteins, eicosanoids, and metabolites derived from plasma samples. Number of experimentally determined analytes per molecule class are depicted in the middle of the respective pie chart circle. Statistical testing was performed employing a two-sided t-test (p=0.05) for the comparison between 1) UC Active versus Healthy Control and 2) UC Remission versus Healthy control. Number of analytes only significantly regulated in one of those comparisons are depicted in orange (+), analytes significantly regulated in both comparisons are depicted in red (++). **(B)** Principal component analysis of in Figure 3a illustrated datasets. Individual dots represent individual patients. 95% confidence intervals of patient cohorts are highlighted via respective coloring of areas in the plot. PCA of plasma

135

proteins allows separation of Healthy Controls from UC Remission patients over both axis (dotted line), PCA of plasma metabolites as well as eicosanoids allowed separation of Healthy Controls from UC Active patients via PC1 (dotted lines). **(C)** Volcano plots of comparative data analysis as indicated. Significant protein regulatory events (-log p-value=1.5) between patient cohorts are highlighted in blue (down-regulation) and red (up-regulation). Selected protein candidates (left box) CRP, SAA1, ITGA2B, FBLN1, VCL and PTGDS are annotated from 1 to 6, respectively. Eicosanoid candidates (middle box) PGE2, 11-HETE, 11-HEPE, 12-HEPE, 5S-HETE, 14-HDoHE and PGD2 are annotated from 1 to 7, respectively. Metabolite candidates (right box) ornithine, aconitic acid, cystine, glycocholic acid, deoxycholic acid, glycodeoxycholic acid, glycolithocholic acid, trigonelline, p-cresol sulfate, hippuric acid, 3-indol propionic acid, indoxyl sulfate and sarcosine are annotated from 1 to 13, respectively.

Figure 4: Data Integration Analysis and prognostic biomarker candidates. **(A)** Heatmap of plasma analytes (proteins, eicosanoids, and metabolites), selected by Data Integration Analysis for Biomarker discovery (DIABLO) implemented in the R-package mixOmics including information on age and sex. Eight proteins, six eicosanoids, 26 metabolites, age, and sex were selected for the first component (shown in a) and 14, six, and five, respectively, and age were selected for the second component. **(B)** Correlation plots of the first components of the DIABLO analysis using the selected analytes of each analyte type given above, color coded as in (a): green, healthy control; blue, patients in remission; and red, patients with active disease. **(C)** Network of correlated significant analytes and significant analyte sub-networks generated from an integrative analyses approach (for details see Materials and Methods) comparing patients in remission with healthy controls. Single analytes are given with their names, sub-networks of analytes are represented by their first (PC1) and sometimes second components (PC2, connected by dashed lines) and named "P" for proteins, "E" for eicosanoids, and "M" for metabolites. The second component is used if the first component represents less than 75% of the variance. The number of summarized analytes in each sub-network is indicated by the number of pie pieces in each node. The colors of the nodes and – in case of summarized sub-networks – the pie pieces of the nodes represent the log2 fold-changes between patients in remission and healthy controls, with colors in red as higher in patients with remission. If the borders of the pie pieces of the nodes representing sub-networks are in solid lines, the corresponding component is also significantly associated with the comparison of patients in remission and healthy controls. The color of the edges indicates the pairwise partial Pearson correlations between analytes and/or the Principal Component representations of the sub-networks (cut-off: $|R| > 0.6$). **(D)** Z-scores of analytes sorted according their behavior in the trajectory healthy control (green) -
> patients in remission (blue) -> patients with acute disease (red). Green highlighted are analytes which do not normalize in patients in remission, red highlighted are analytes which get close to normal during remission, and blue highlighted are analytes which show an exceptional behavior, i.e. either the value of healthy controls is in-between the other two categories (GUDCA) or the values of healthy controls and patients in remission are at the edges and the values in patients with acute disease are in-between. **(E)** Illustration of

pathophysiological mechanisms driving UC disease chronicity and proposed interconnected network depicting malicious cascades resulting in a "vicious circle".

Supplementary information

Supplementary Materials and Methods

Supplementary data
   1.) Supplementary Figure S1: Age and gender distribution of UC patients.
   2.) Supplementary Figure S2: Histologic assessment of colon tissue samples.
   3.) Justification of marker proteins identified by tissue proteomics
   4.) Visualization of clinical parameters of UC patients

Supplementary Table S1: Clinical data of UC patient cohort
Supplementary Table S2: Clinical data of UC remission cohort
Supplementary Table S3: Colon tissue proteome analysis results listing LFQ values
Supplementary Table S4: Colon tissue proteome analysis volcano data matrices for 1-inflamed versus non-inflamed; 2- inflamed versus surrounding, 3- surrounding versus non-inflamed.
Supplementary Table S5: z-scores for heatmap in Figure 2
Supplementary Table S6: Plasma proteome analysis results listing LFQ values
Supplementary Table S7: Plasma eicosanoid analysis results listing nAUC values
Supplementary Table S8: Plasma metabolome analysis results listing μM concentration values

Author contributions:

Conceptualization: LJ, DS, NP, TF, CG

Methodology: NP, TF, CG

Investigation: LJ, DS, PB, GH, JB, SMMM, JCM, AB, BH, BW

Data processing and interpretation: LJ, DS, SMMM, AS, AB, GDF, DP, TP, CG

Visualization: LJ, PB, GH

Project administration: DS, CM, NP, CG

Supervision: TF, CG

Writing – original draft: LJ, CG

Writing – review & editing: LJ, DS, AB, SMMM, LU, CG

Data and materials availability

The mass spectrometry proteomics data comprising both tissue and plasma analyses have been deposited to the ProteomeXchange Consortium (http://proteomecentral.proteomexchange.org) via the PRIDE partner repository (PMID: 30395289) with the dataset identifier PXD030775.

Competing interests

Authors declare that they have no competing interests.

References

1. Fumery M, Singh S, Dulai PS, et al. Natural History of Adult Ulcerative Colitis in Population-based Cohorts: A Systematic Review. Clin Gastroenterol Hepatol 2018;16:343-356 e3.

2. Cosnes J, Gower-Rousseau C, Seksik P, et al. Epidemiology and natural history of inflammatory bowel diseases. Gastroenterology 2011;140:1785-94.

3. Molodecky NA, Soon IS, Rabi DM, et al. Increasing incidence and prevalence of the inflammatory bowel diseases with time, based on systematic review. Gastroenterology 2012;142:46-54 e42; quiz e30.

4. Linson EA, Hanauer SB. Epidemiology of Colorectal Cancer in Inflammatory Bowel Disease - the Evolving Landscape. Curr Gastroenterol Rep 2021;23:16.

5. Rubin DT, Ananthakrishnan AN, Siegel CA, et al. ACG Clinical Guideline: Ulcerative Colitis in Adults. Am J Gastroenterol 2019;114:384-413.

6. Zezos P, Kouklakis G, Saibil F. Inflammatory bowel disease and thromboembolism. World J Gastroenterol 2014;20:13863-78.

7. Feuerstein JD, Isaacs KL, Schneider Y, et al. AGA Clinical Practice Guidelines on the Management of Moderate to Severe Ulcerative Colitis. Gastroenterology 2020;158:1450-1461.

8. Chen JH, Andrews JM, Kariyawasam V, et al. Review article: acute severe ulcerative colitis - evidence-based consensus statements. Aliment Pharmacol Ther 2016;44:127-44.

9. Hanauer SB. Medical therapy for ulcerative colitis 2004. Gastroenterology 2004;126:1582-92.

10. Hanauer SB, Sparrow M. Therapy of ulcerative colitis. Curr Opin Gastroenterol 2004;20:345-50.

11. Peyrin-Biroulet L, Sandborn W, Sands BE, et al. Selecting Therapeutic Targets in Inflammatory Bowel Disease (STRIDE): Determining Therapeutic Goals for Treat-to-Target. Am J Gastroenterol 2015;110:1324-38.

12. Ungaro R, Colombel JF, Lissoos T, et al. A Treat-to-Target Update in Ulcerative Colitis: A Systematic Review. Am J Gastroenterol 2019;114:874-883.

13. Schroeder KW, Tremaine WJ, Ilstrup DM. Coated oral 5-aminosalicylic acid therapy for mildly to moderately active ulcerative colitis. A randomized study. N Engl J Med 1987;317:1625-9.

14. Sutherland LR, Martin F, Greer S, et al. 5-Aminosalicylic acid enema in the treatment of distal ulcerative colitis, proctosigmoiditis, and proctitis. Gastroenterology 1987;92:1894-8.

15. Cho JH, Weaver CT. The genetics of inflammatory bowel disease. Gastroenterology 2007;133:1327-39.

16. Hanauer SB. Update on the etiology, pathogenesis and diagnosis of ulcerative colitis. Nat Clin Pract Gastroenterol Hepatol 2004;1:26-31.

17. Bonen DK, Cho JH. The genetics of inflammatory bowel disease. Gastroenterology 2003;124:521-36.

18. Ahmad T, Marshall S, Jewell D. Genotype-based phenotyping heralds a new taxonomy for inflammatory bowel disease. Curr Opin Gastroenterol 2003;19:327-35.

19. Tabor HK, Risch NJ, Myers RM. Candidate-gene approaches for studying complex genetic traits: practical considerations. Nat Rev Genet 2002;3:391-7.

20.   Hugot JP, Chamaillard M, Zouali H, et al. Association of NOD2 leucine-rich repeat variants with susceptibility to Crohn's disease. Nature 2001;411:599-603.

21.   Ogura Y, Bonen DK, Inohara N, et al. A frameshift mutation in NOD2 associated with susceptibility to Crohn's disease. Nature 2001;411:603-6.

22.   Hampe J, Cuthbert A, Croucher PJ, et al. Association between insertion mutation in NOD2 gene and Crohn's disease in German and British populations. Lancet 2001;357:1925-8.

23.   Janker L, Mayer RL, Bileck A, et al. Metabolic, Anti-apoptotic and Immune Evasion Strategies of Primary Human Myeloma Cells Indicate Adaptations to Hypoxia. Mol Cell Proteomics 2019;18:936-953.

24.   Schniers A, Goll R, Pasing Y, et al. Ulcerative colitis: functional analysis of the in-depth proteome. Clin Proteomics 2019;16:4.

25.   Schniers A, Anderssen E, Fenton CG, et al. The Proteome of Ulcerative Colitis in Colon Biopsies from Adults - Optimized Sample Preparation and Comparison with Healthy Controls. Proteomics Clin Appl 2017;11.

26.   Galipeau HJ, Caminero A, Turpin W, et al. Novel Fecal Biomarkers That Precede Clinical Diagnosis of Ulcerative Colitis. Gastroenterology 2021;160:1532-1545.

27.   Bennike TB, Carlsen TG, Ellingsen T, et al. Neutrophil Extracellular Traps in Ulcerative Colitis: A Proteome Analysis of Intestinal Biopsies. Inflamm Bowel Dis 2015;21:2052-67.

28.   Gallagher K, Catesson A, Griffin JL, et al. Metabolomic Analysis in Inflammatory Bowel Disease: A Systematic Review. J Crohns Colitis 2021;15:813-826.

29.   Sugihara K, Morhardt TL, Kamada N. The Role of Dietary Nutrients in Inflammatory Bowel Disease. Front Immunol 2018;9:3183.

30.   Ridlon JM, Kang DJ, Hylemon PB. Bile salt biotransformations by human intestinal bacteria. J Lipid Res 2006;47:241-59.

31.   Lloyd-Price J, Arze C, Ananthakrishnan AN, et al. Multi-omics of the gut microbial ecosystem in inflammatory bowel diseases. Nature 2019;569:655-662.

32.   Alper A, Zhang L, Pashankar DS. Correlation of Erythrocyte Sedimentation Rate and C-Reactive Protein With Pediatric Inflammatory Bowel Disease Activity. J Pediatr Gastroenterol Nutr 2017;65:e25-e27.

33.   Langhorst J, Boone J, Lauche R, et al. Faecal Lactoferrin, Calprotectin, PMN-elastase, CRP, and White Blood Cell Count as Indicators for Mucosal Healing and Clinical Course of Disease in Patients with Mild to Moderate Ulcerative Colitis: Post Hoc Analysis of a Prospective Clinical Trial. J Crohns Colitis 2016;10:786-94.

34.   Cox J, Mann M. MaxQuant enables high peptide identification rates, individualized p.p.b.-range mass accuracies and proteome-wide protein quantification. Nat Biotechnol 2008;26:1367-72.

35.   Fahy E, Sud M, Cotter D, et al. LIPID MAPS online tools for lipid research. Nucleic Acids Res 2007;35:W606-12.

36.   Babur O, Luna A, Korkut A, et al. Causal interactions from proteomic profiles: Molecular data meet pathway knowledge. Patterns (N Y) 2021;2:100257.

37.   Rohart F, Gautier B, Singh A, et al. mixOmics: An R package for 'omics feature selection and multiple data integration. PLoS Comput Biol 2017;13:e1005752.

38.   Bekos C, Muqaku B, Dekan S, et al. NECTIN4 (PVRL4) as Putative Therapeutic Target for a Specific Subtype of High Grade Serous Ovarian Cancer-An Integrative Multi-Omics Approach. Cancers (Basel) 2019;11.

39. Groessl M, Slany A, Bileck A, et al. Proteome profiling of breast cancer biopsies reveals a wound healing signature of cancer-associated fibroblasts. J Proteome Res 2014;13:4773-82.

40. Slany A, Bileck A, Kreutz D, et al. Contribution of Human Fibroblasts and Endothelial Cells to the Hallmarks of Inflammation as Determined by Proteome Profiling. Mol Cell Proteomics 2016;15:1982-97.

41. Slany A, Paulitschke V, Haudek-Prinz V, et al. Determination of cell type-specific proteome signatures of primary human leukocytes, endothelial cells, keratinocytes, hepatocytes, fibroblasts and melanocytes by comparative proteome profiling. Electrophoresis 2014;35:1428-38.

42. Pan T, Liu J, Xu S, et al. ANKRD22, a novel tumor microenvironment-induced mitochondrial protein promotes metabolic reprogramming of colorectal cancer cells. Theranostics 2020;10:516-536.

43. Huang J, Swieringa F, Solari FA, et al. Assessment of a complete and classified platelet proteome from genome-wide transcripts of human platelets and megakaryocytes covering platelet functions. Sci Rep 2021;11:12358.

44. Zhou Y, Shaw N, Li Y, et al. Structure-function analysis of human l-prostaglandin D synthase bound with fatty acid molecules. FASEB J 2010;24:4668-77.

45. Nelson AM, Loy DE, Lawson JA, et al. Prostaglandin D2 inhibits wound-induced hair follicle neogenesis through the receptor, Gpr44. J Invest Dermatol 2013;133:881-9.

46. Ajuebor MN, Singh A, Wallace JL. Cyclooxygenase-2-derived prostaglandin D(2) is an early anti-inflammatory signal in experimental colitis. Am J Physiol Gastrointest Liver Physiol 2000;279:G238-44.

47. Guido DM, McKenna R, Mathews WR. Quantitation of hydroperoxy-eicosatetraenoic acids and hydroxy-eicosatetraenoic acids as indicators of lipid peroxidation using gas chromatography-mass spectrometry. Anal Biochem 1993;209:123-9.

48. Muqaku B, Pils D, Mader JC, et al. Neutrophil Extracellular Trap Formation Correlates with Favorable Overall Survival in High Grade Ovarian Cancer. Cancers (Basel) 2020;12.

49. Fu X, Cate SA, Dominguez M, et al. Cysteine Disulfides (Cys-ss-X) as Sensitive Plasma Biomarkers of Oxidative Stress. Sci Rep 2019;9:115.

50. Beyoglu D, Idle JR. Metabolic Rewiring and the Characterization of Oncometabolites. Cancers (Basel) 2021;13.

51. Liu Y, Yang C, Zhang Z, et al. Gut Microbiota Dysbiosis Accelerates Prostate Cancer Progression Through Increased LPCAT1 Expression and Enhanced DNA Repair Pathways. Front Oncol 2021;11:679712.

52. Muqaku B, Eisinger M, Meier SM, et al. Multi-omics Analysis of Serum Samples Demonstrates Reprogramming of Organ Functions Via Systemic Calcium Mobilization and Platelet Activation in Metastatic Melanoma. Mol Cell Proteomics 2017;16:86-99.

53. Gundacker NC, Haudek VJ, Wimmer H, et al. Cytoplasmic proteome and secretome profiles of differently stimulated human dendritic cells. J Proteome Res 2009;8:2799-811.

54. Lawrence T, Gilroy DW. Chronic inflammation: a failure of resolution? Int J Exp Pathol 2007;88:85-94.

55. Stavely R, Rahman AA, Sahakian L, et al. Divergent Adaptations in Autonomic Nerve Activity and Neuroimmune Signaling Associated With the Severity of Inflammation in Chronic Colitis. Inflamm Bowel Dis 2022.

56.   Fang J, Wang H, Zhou Y, et al. Slimy partners: the mucus barrier and gut microbiome in ulcerative colitis. Exp Mol Med 2021;53:772-787.

57.   Ricevuti G. Host tissue damage by phagocytes. Ann N Y Acad Sci 1997;832:426-48.

58.   Haudek VJ, Slany A, Gundacker NC, et al. Proteome maps of the main human peripheral blood constituents. J Proteome Res 2009;8:3834-43.

59.   Rudloff S, Bileck A, Janker L, et al. Dichotomous Responses to Chronic Fetal Hypoxia Lead to a Predetermined Aging Phenotype. Mol Cell Proteomics 2022;21:100190.

60.   Tahir A, Bileck A, Muqaku B, et al. Combined Proteome and Eicosanoid Profiling Approach for Revealing Implications of Human Fibroblasts in Chronic Inflammation. Anal Chem 2017;89:1945-1954.

61.   Lorenz O, Parzefall W, Kainzbauer E, et al. Proteomics reveals acute pro-inflammatory and protective responses in rat Kupffer cells and hepatocytes after chemical initiation of liver cancer and after LPS and IL-6. Proteomics Clin Appl 2009;3:947-67.

62.   Ribitsch I, Bileck A, Egerbacher M, et al. Fetal Immunomodulatory Environment Following Cartilage Injury-The Key to CARTILAGE Regeneration? Int J Mol Sci 2021;22.
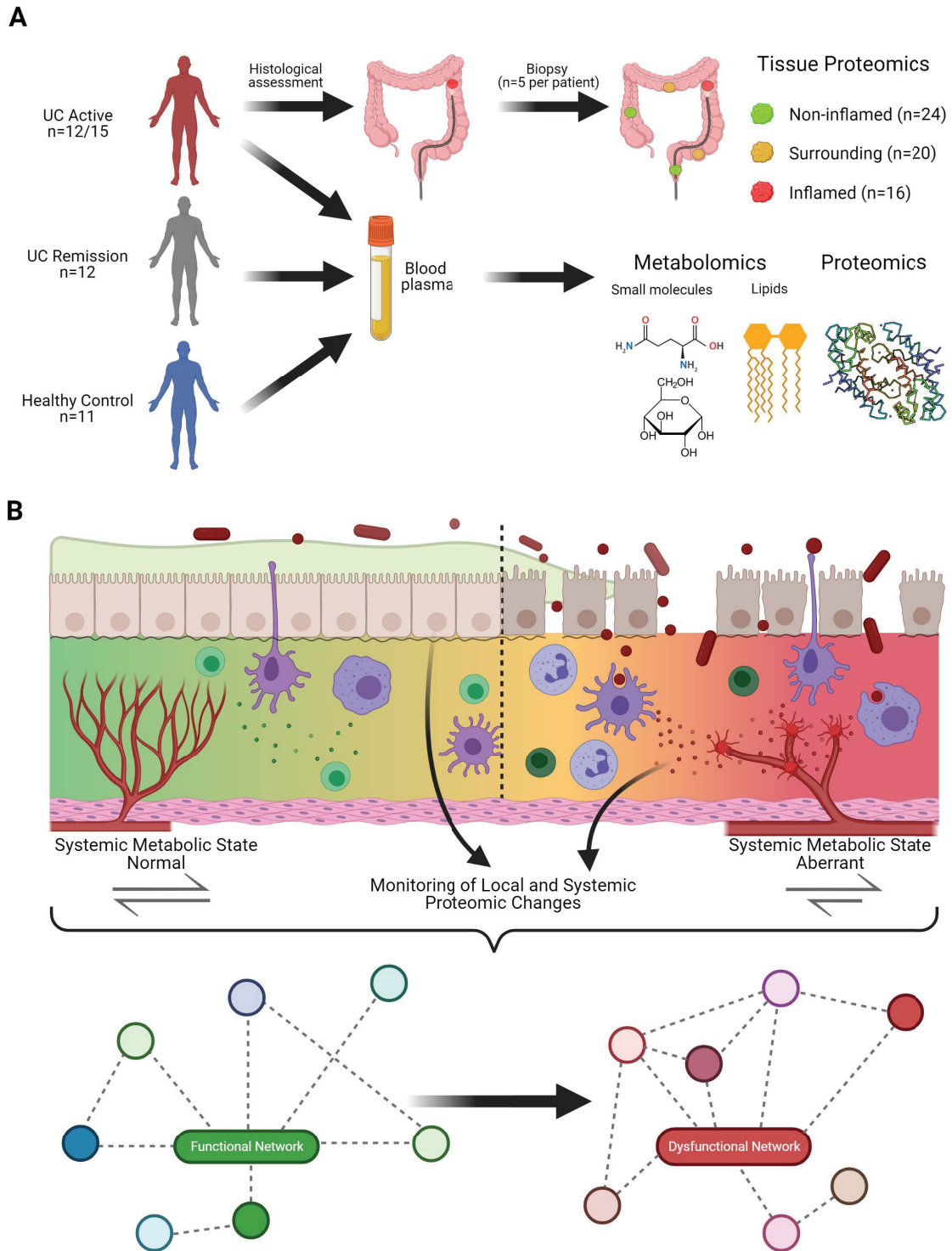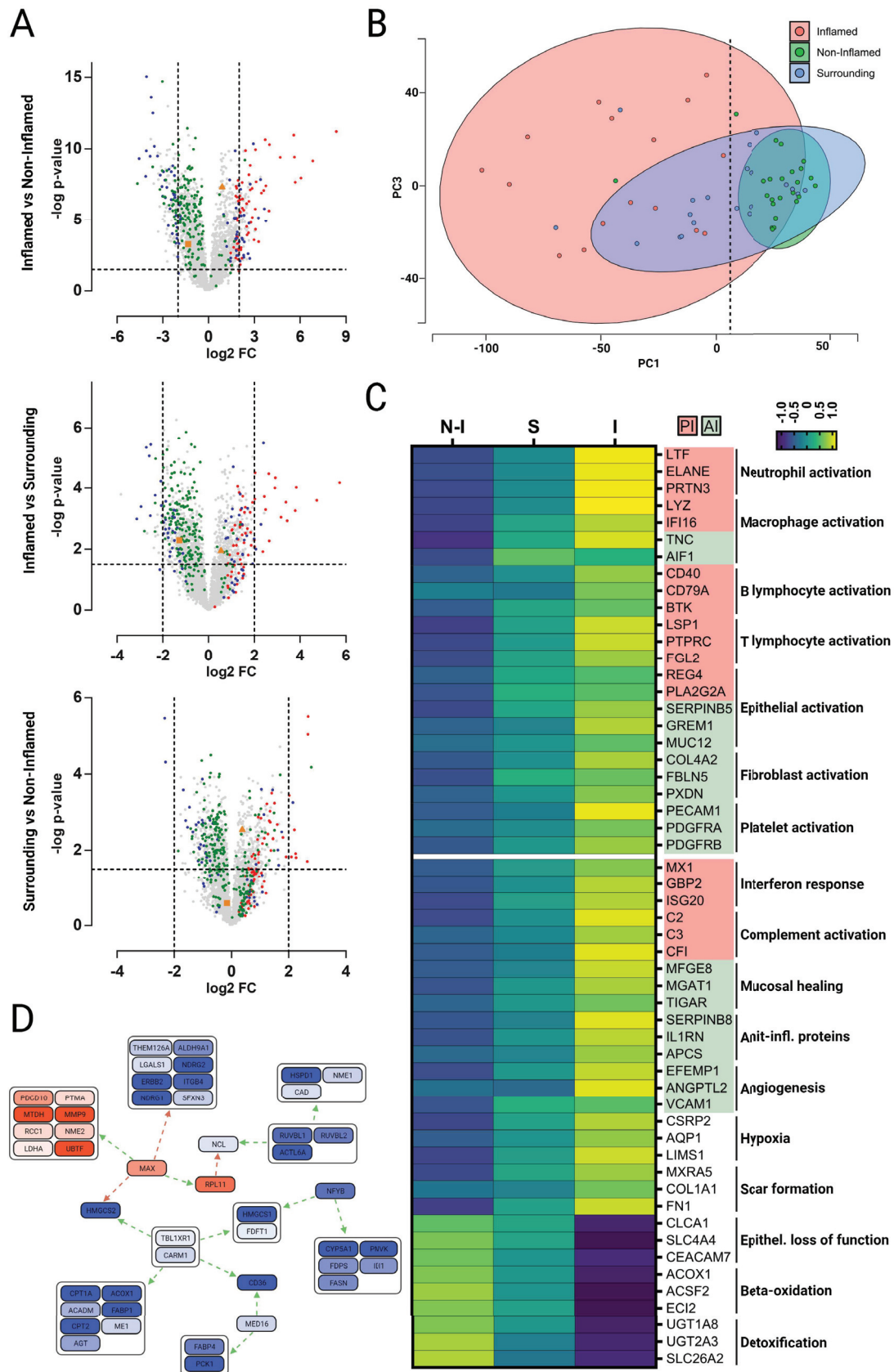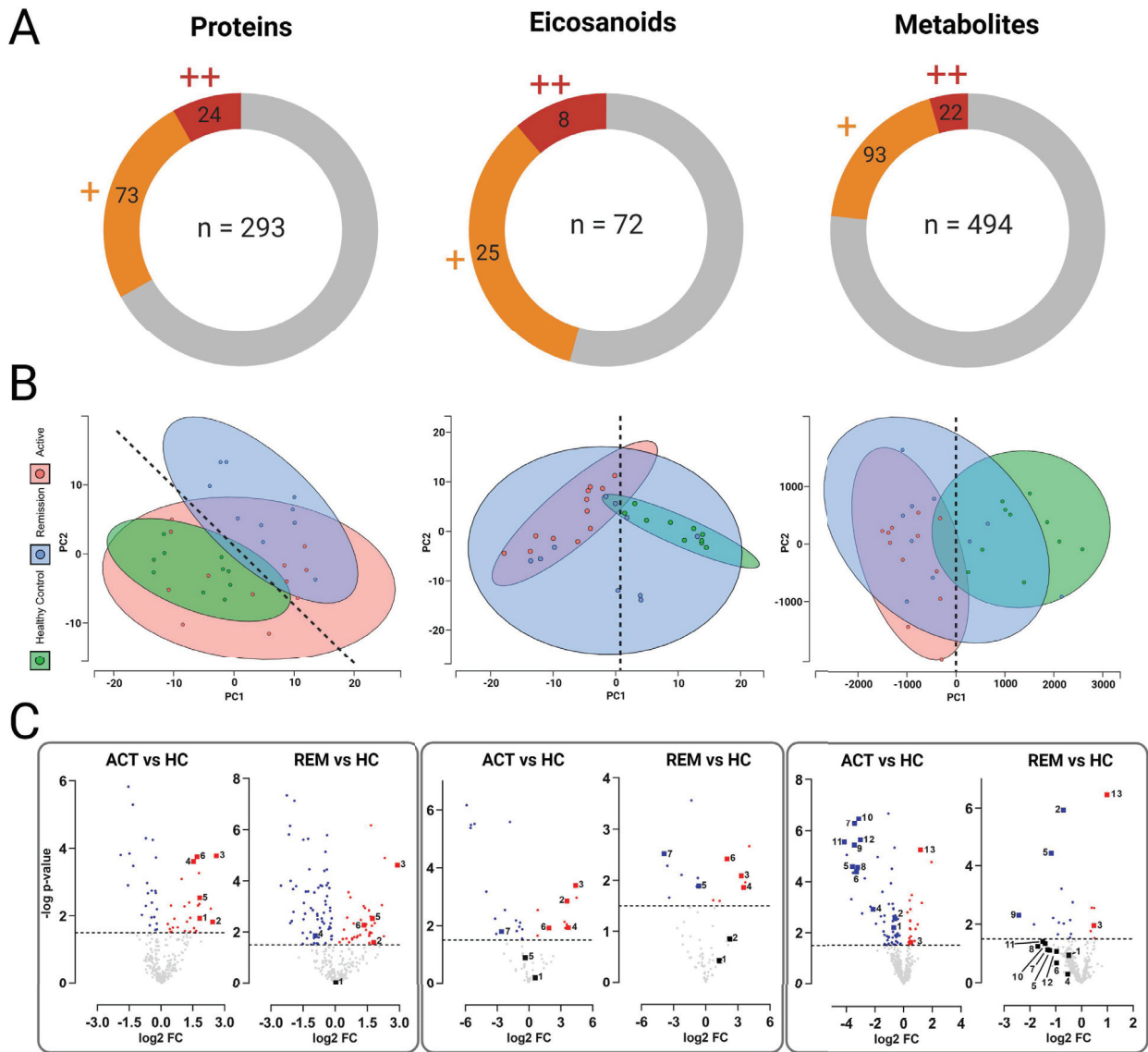
Figure 1
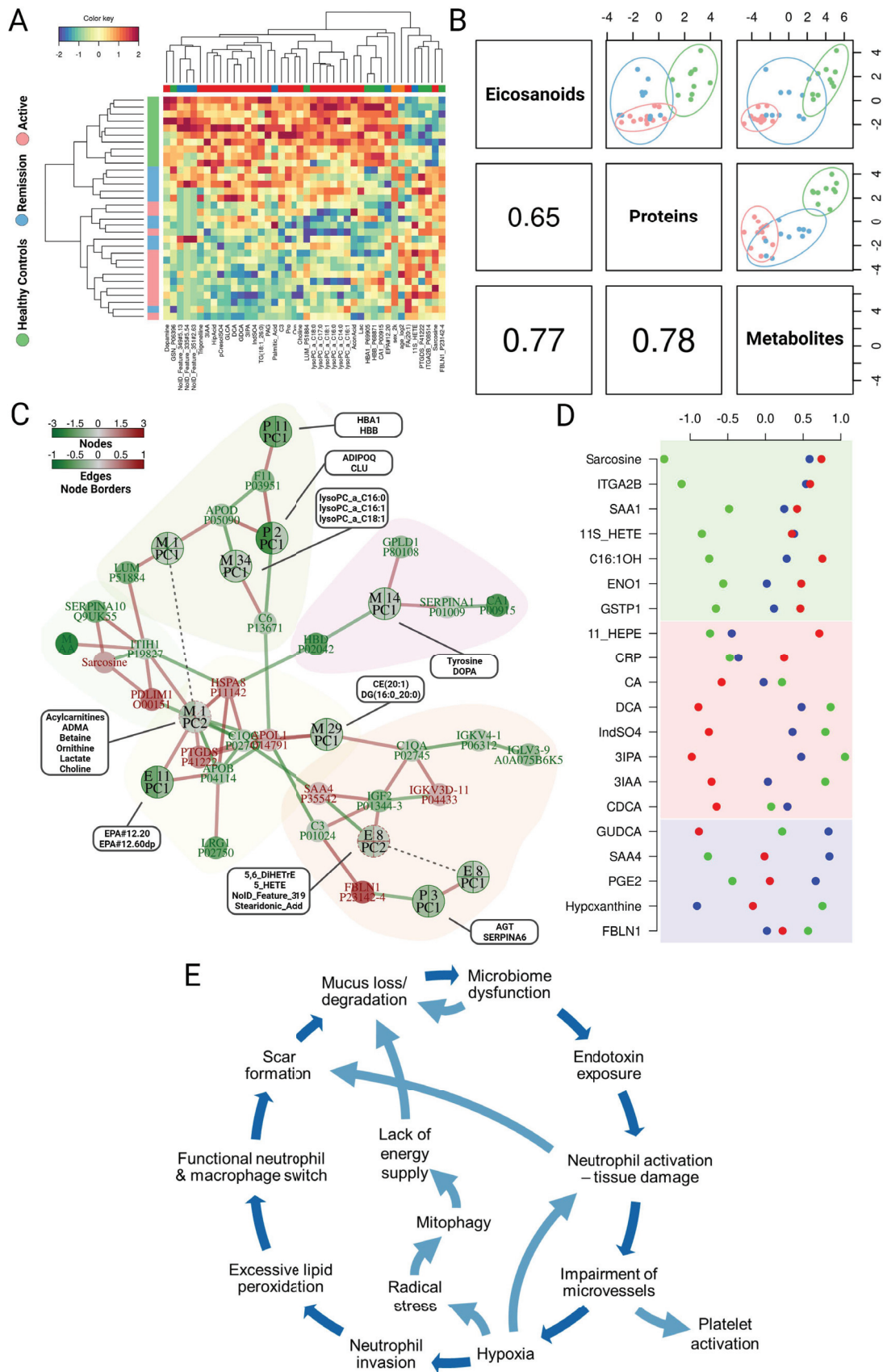
Figure 2

Figure 3

Figure 4

5 Conclusion

The in this thesis presented studies show, each in a unique way, the importance of post-genomic methods in conjunction with complementary methods to depict relevant (patho-) physiological processes in complex biological systems.

In the first study, proteome profiling data strongly support that adaptation of multiple myeloma (MM) cells to hypoxia accompanies myeloma disease progression. The data clearly reproduced established knowledge on myeloma cells, but also present novel findings and causal relations of relevant pathways taking place in these tumor cells. Importantly, it seems that strategies exploited by myeloma cells to allow survival and proliferation, including immune evasion mechanisms and metabolic adaptations, are more dependent on the disease state than on the genetic background. This study may thus support the development of improved stratification and anti-myeloma treatment strategies. (see p.149 - work 2)

The second study focuses on octenidine dihydrochloride (OCT) and its effects on wound healing in an *ex vivo* setting. In clinical practice, OCT has been shown to promote healing of chronic wounds and to reduce the formation of hypertrophic scars in patients after abdominoplasty. However, the mechanism by which OCT contributes to tissue regeneration and improved wound healing was not yet investigated in more detail. Proteomics analysis of OCT-treated skin wounds revealed significant lower levels of key players in tissue remodeling as well as reepithelization after wounding such as pro-inflammatory cytokines and matrix-metalloproteinases when compared to controls. Utilizing MS based methods in this study allowed the comprehensive profiling of proteome alterations in a controlled *ex vivo* setting, also demonstrating the power of state-of-the-art ion mobility separation. (see p.149 - work 3)

In the third study we explored the dermotoxicity of a mycotoxin called deoxynivalenol employing, in addition to global proteome profiling, a phosphoproteomics analysis to elucidate signalling events taking place in an *in vitro* setting. We delineated a chain of events linking ribosomal inhibition, mitochondrial function, lipid metabolism to membrane structure and biophysical properties in A431 cells. Moreover, we demonstrated that lipid synthesis and cell adhesion are severely impaired by DON also in primary skin HEKn keratinocytes. Moreover, these data open new perspectives in the interpretation of the combinatory effects of DON with other toxins targeting the cell membrane, such as for instance fumonisins, and open new intriguing questions in the evaluation of the effects of Fusarium toxins at cellular level. (see p.149 - work 5)

The fourth study discussed in this thesis tackles the topic of Schwann cell plasticity and how it regulates neuroblastic tumor cell differentiation, with a special focus on EGFL8. Further developing our phosphoproteomics pipeline, we profiled intricate phosphorylation directed signalling networks around EGLF8, a neuritogenic factor relevant in neuroblastic tumors. We could show that EGFL8 mediates neuronal differentiation through broad kinase activation

including and beyond p38β/MAPK and ERK signaling. This might hold considerable treatment possibilities for the therapy of aggressive NBs and (patho) physiological conditions compromising peripheral nerve integrity.

In the fifth and last study of this thesis, we aimed to better understand and profile molecular postgenomic signatures relevant for disease escalation and remission of ulcerative colitis via multi-omics analysis of plasma samples, accompanied by in-depth proteome profiling of colon tissue samples from acute patients. We could demonstrate the application of a multi-omics analysis strategy allowed us to relate blood-borne proteins, metabolites, and lipids to disease-associated pathomechanisms with some potential prognostic power.

To summarize the in this thesis presented studies, the application of unbiased MS based methods can aid the understanding of mostly postgenomically driven biological processes in complex systems and reveal novel aspects. Furthermore, the versatility of said methods enabled the application to a diverse set of important scientific questions, once more demonstrating the power of mass spectrometry-based research.

6 Scientific Contributions

6.1 List of Publications

1. Janker, L. *et al.* Multi-omics empowered deep phenotyping of ulcerative colitis. *medRxiv* 2022.05.25.22275502 (2022).

2. Janker, L. *et al.* Metabolic, Anti-apoptotic and Immune Evasion Strategies of Primary Human Myeloma Cells Indicate Adaptations to Hypoxia*. *Mol Cell Proteomics* 18, 936–953 (2019).

3. Janker, L. & Seiser, S. *et al.* Octenidine-based hydrogel shows anti-inflammatory and protease-inhibitory capacities in wounded human skin. *Sci Rep* 11, 32 (2021).

4. Weiss, T. *et al.* Schwann cell plasticity regulates neuroblastic tumor cell differentiation via epidermal growth factor-like protein 8. *Nat Commun* 12, 1624 (2021).

5. Janker, L. & Favero, G. D. *et al.* Exploring the dermotoxicity of the mycotoxin deoxynivalenol: combined morphologic and proteomic profiling of human epidermal cells reveals alteration of lipid biosynthesis machinery and membrane structural integrity relevant for skin barrier function. *Arch Toxicol* 95, 2201–2221 (2021).

6. Janker, L. & Rebay-Salisbury, K. *et al.* Child murder in the Early Bronze Age: proteomic sex identification of a cold case from Schleinbach, Austria. *Archaeol Anthrop Sci* 12, 265 (2020).

7. M, M.-M., Samuel *et al.* A Proteomic Platform Enables to Test for AML Normalization In Vitro. *Front Chem* 10, 826346–826346 (2022).

8. Rebay-Salisbury, K. *et al.* Gendered burial practices of early Bronze Age children align with peptide-based sex identification: A case study from Franzhausen I, Austria. *J Archaeol Sci* 139, 105549 (2022).

9. Bileck, A. *et al.* Inward Outward Signaling in Ovarian Cancer: Morpho-Phospho-Proteomic Profiling Upon Application of Hypoxia and Shear Stress Characterizes the Adaptive Plasticity of OVCAR-3 and SKOV-3 Cells. *Front Oncol* 11, 746411–746411 (2022).

10. Brunmair, J. *et al.* Finger sweat analysis enables short interval metabolic biomonitoring in humans. *Nat Commun* 12, 5993 (2021).

11. Rudloff, S. *et al.* Dichotomous responses to chronic fetal hypoxia lead to a predetermined aging phenotype. *Mol Cell Proteomics* 21, 100190 (2021).

12. Niederstaetter, L. *et al.* Eicosanoid Content in Fetal Calf Serum Accounts for Reproducibility Challenges in Cell Culture. *Biomol* 11, 113 (2021).

13. Gerner, M. C. *et al.* Packed red blood cells inhibit T-cell activation via ROS-dependent signaling pathways. *J Biological Chem* 296, 100487 (2021).

14. Unterleuthner, D. *et al.* Cancer-associated fibroblast-derived WNT2 increases tumor angiogenesis in colon cancer. *Angiogenesis* 23, 159–177 (2020).

15. Ribitsch, I. *et al.* Fetal Immunomodulatory Environment Following Cartilage Injury—The Key to CARTILAGE Regeneration? *Int J Mol Sci* 22, 12969 (2021).

16. Pany-Kucera, D. *et al.* Social Relations, Deprivation and Violence at Schleinbach, Lower Austria. Insights from an Interdisciplinary Analysis of the Early Bronze Age Human Remains. *Archaeol Austriaca* Band 104/2020, 13–52 (2020).

17. Neuditschko, B. *et al.* The Challenge of Classifying Metastatic Cell Properties by Molecular Profiling Exemplified with Cutaneous Melanoma Cells and Their Cerebral Metastasis from Patient Derived Mouse Xenografts*. *Mol Cell Proteomics* 19, 478–489 (2020).

18. Favero, G. D. *et al.* Structural Similarity with Cholesterol Reveals Crucial Insights into Mechanisms Sustaining the Immunomodulatory Activity of the Mycotoxin Alternariol. *Cells* 9, 847 (2020).

19. Gerner, M. C. *et al.* Proteome Analysis Reveals Distinct Mitochondrial Functions Linked to Interferon Response Patterns in Activated CD4+ and CD8+ T Cells. *Front Pharmacol* 10, 727 (2019).

20. Kreutz, D. *et al.* Curcumin exerts its antitumor effects in a context dependent fashion. *J Proteomics* 182, 65–72 (2018).

21. Favero, G. D. *et al.* Deoxynivalenol induces structural alterations in epidermoid carcinoma cells A431 and impairs the response to biomechanical stimulation. *Sci Rep-uk* 8, 11351 (2018).

22. Zila, N. *et al.* Proteomics-based insights into mitogen-activated protein kinase inhibitor resistance of cerebral melanoma metastases. *Clin Proteom* 15, 13 (2018).

6.2 List of Oral Presentations

„Mass spectrometry-based analysis of peptides from human tooth enamel: a new perspective for archaeological and anthropological studies"

- Wien – Vortragsreihe „Neue Bioarchäologische Forschungen" – BAG/ÖAW (2020)

„Identifying key players responsible for local and systemic changes in colonic tissue and plasma samples of ulcerative colitis patients"

- Salzburg – Austrian Proteomics and Metabolomics Research Symposium (2019)

„Deoxynivalenol and A431 epidermoid squamous carcinoma cells: proteomic profiling reveals the pathways connecting ribosomal inhibition with a loss of function of the cell membrane"

- Wien – 30th MassSpec-Forum Vienna (2019)

„Eicosanoids as underestimated molecular players relevant for tumor biology and mechanisms of metastasis"

- Tel Aviv – Vienna-Tau collaboration on: melanoma brain metastasis (2018)

„Curcumin exerts its antitumor effects in a context dependent fashion"

- Wien – ASAC–JunganalytikerInnenforum (2018)
- Rom – Second International Meeting on Anakoinosis (2018)

6.3 List of Poster Presentations

„Deoxynivalenol and A431 epidermoid squamous carcinoma cells: proteomic profiling reveals the pathways connecting ribosomal inhibition with a loss of function of the cell membrane"

- Heidelberg – Proteomics in Cell Biology and Disease Mechanisms – EMBL (2019)

„Proteome profiling of epidermoid carcinoma cells A431 exposed to deoxynivalenol: steps toward the understanding of the potential for dermal toxicity"

- Wien – The Austrian Proteomics and Metabolomics Research Symposium APMRS (2018)

„In-depth proteome-profiling to evaluate a novel combinatory metronomic treatment for therapy-resistant multiple myeloma patients"

- Dublin – HUPO - Human Proteome Organization World Congress (2017)
- Graz – APRS: Austrian Proteomics and Metabolomics Research Symposium (2017)